

DEVELOPMENT AND CHARACTERIZATION OF NOBLE METAL INTEGRATED
POLYMERIC MEMBRANE REACTORS FOR THREE-PHASE HYDROGENATION
REACTIONS

by

JOHN PAUL STANFORD

B.S., University of Iowa, 2010

B.A., University of Iowa, 2010

AN ABSTRACT OF A DISSERTATION

submitted in partial fulfillment of the requirements for the degree

DOCTOR OF PHILOSOPHY

Department of Chemical Engineering
College of Engineering

KANSAS STATE UNIVERSITY
Manhattan, Kansas

2016

Abstract

Catalytic membrane reactors are a class of reactors that utilize a membrane to selectively deliver reactants to catalysts integrated in the membrane. The focus of this research has been on developing and characterizing polymeric catalytic membranes for three-phase hydrogenation reactions, where the membrane functions as a gas/liquid phase contactor allowing selective delivery of hydrogen through the membrane to reach catalytic sites located on the liquid side of the membrane. The benefit of conducting three-phase reactions in this manner is that delivering hydrogen through the membrane to reach catalytic sites avoids the necessity of hydrogen dissolution and diffusion in the liquid phase, which are both inherently low and often described as causing mass-transfer and reaction rate limitations for the reactive system.

This work examines two types of membrane reactor systems, porous polytetrafluoroethylene and asymmetric Matrimid membranes, respectively, for the ruthenium catalyzed aqueous phase hydrogenation of levulinic acid. The highly hydrophobic PTFE material provides an almost impermeable barrier to the liquid phase while allowing hydrogen gas to freely transport through the pores to reach catalytic sites located at the liquid/membrane interface. Catalytic rates as a function of hydrogen pressure over the range 0.07 to 5.6 bar are presented and shown to be higher than those of a packed bed reactor under similar reaction conditions. An increasing catalytic benefit was obtained operating at temperatures up to 90 °C, which is attributed to increased hydrogen permeability and avoidance of the decreasing solubility of hydrogen in water with increasing temperature. The membrane reactor was shown to be stable with no decrease in catalytic activity over 200 hours of operation. The Matrimid membrane reactor work demonstrates the feasibility of applying an integrally-skinned asymmetric membrane for an aqueous phase hydrogenation reaction and focuses on the impact that membrane hydrogen

permeance and catalyst loading have on catalytic activity. The non-porous nature of the separating layer in the Matrimid membrane allowed successful operation up to 150 °C. The overall catalytic rates were approximately an order of magnitude lower than those achieved in the PTFE membrane reactor system due primarily to significantly lower hydrogen permeances, nevertheless rates were still higher than control experiments.

This work also focuses on characterizing Matrimid/solvent thermodynamic relationships for a variety of organic solvents, looking at sorption, diffusion, and polymer relaxation behavior in thin films ranging from 0.1 to 2.0 μm in thickness using quartz crystal microbalance techniques. Diffusion coefficients at infinite dilution for water and C1-C6 alcohols are given as a function of van der Waals molar volume and a clear dependency is shown ranging from 2E-11 to 6.5E-13 cm^2/s for water and hexanol, respectively, for 0.26 μm thick films. Diffusion coefficients for all studied vapor penetrants displayed a marked dependence on thickness spanning approximately two orders of magnitude for each respective vapor penetrant over the range 0.1 to 1.0 μm . Chemically cross-linking Matrimid is a method to mitigate some of the relatively high sorption and swelling behavior exhibited in the presence of sorbing species. An in-depth analysis on the vapor phase ethylenediamine cross-linking of Matrimid films and its impact on diffusion, sorption, and relaxation is also described.

DEVELOPMENT AND CHARACTERIZATION OF NOBLE METAL INTEGRATED
POLYMERIC MEMBRANE REACTORS FOR THREE-PHASE HYDROGENATION
REACTIONS

by

JOHN PAUL STANFORD

B.S., University of Iowa, 2010
B.A., University of Iowa, 2010

A DISSERTATION

submitted in partial fulfillment of the requirements for the degree

DOCTOR OF PHILOSOPHY

Department of Chemical Engineering
College of Engineering

KANSAS STATE UNIVERSITY
Manhattan, Kansas

2016

Approved by:

Major Professor
Mary E. Rezac

Copyright

JOHN PAUL STANFORD

2016

Abstract

Catalytic membrane reactors are a class of reactors that utilize a membrane to selectively deliver reactants to catalysts integrated in the membrane. The focus of this research has been on developing and characterizing polymeric catalytic membranes for three-phase hydrogenation reactions, where the membrane functions as a gas/liquid phase contactor allowing selective delivery of hydrogen through the membrane to reach catalytic sites located on the liquid side of the membrane. The benefit of conducting three-phase reactions in this manner is that delivering hydrogen through the membrane to reach catalytic sites avoids the necessity of hydrogen dissolution and diffusion in the liquid phase, which are both inherently low and often described as causing mass-transfer and reaction rate limitations for the reactive system.

This work examines two types of membrane reactor systems, porous polytetrafluoroethylene and asymmetric Matrimid membranes, respectively, for the ruthenium catalyzed aqueous phase hydrogenation of levulinic acid. The highly hydrophobic PTFE material provides an almost impermeable barrier to the liquid phase while allowing hydrogen gas to freely transport through the pores to reach catalytic sites located at the liquid/membrane interface. Catalytic rates as a function of hydrogen pressure over the range 0.07 to 5.6 bar are presented and shown to be higher than those of a packed bed reactor under similar reaction conditions. An increasing catalytic benefit was obtained operating at temperatures up to 90 °C, which is attributed to increased hydrogen permeability and avoidance of the decreasing solubility of hydrogen in water with increasing temperature. The membrane reactor was shown to be stable with no decrease in catalytic activity over 200 hours of operation. The Matrimid membrane reactor work demonstrates the feasibility of applying an integrally-skinned asymmetric membrane for an aqueous phase hydrogenation reaction and focuses on the impact that membrane hydrogen

permeance and catalyst loading have on catalytic activity. The non-porous nature of the separating layer in the Matrimid membrane allowed successful operation up to 150 °C. The overall catalytic rates were approximately an order of magnitude lower than those achieved in the PTFE membrane reactor system due primarily to significantly lower hydrogen permeances, nevertheless rates were still higher than control experiments.

This work also focuses on characterizing Matrimid/solvent thermodynamic relationships for a variety of organic solvents, looking at sorption, diffusion, and polymer relaxation behavior in thin films ranging from 0.1 to 2.0 μm in thickness using quartz crystal microbalance techniques. Diffusion coefficients at infinite dilution for water and C1-C6 alcohols are given as a function of van der Waals molar volume and a clear dependency is shown ranging from 2E-11 to 6.5E-13 cm^2/s for water and hexanol, respectively, for 0.26 μm thick films. Diffusion coefficients for all studied vapor penetrants displayed a marked dependence on thickness spanning approximately two orders of magnitude for each respective vapor penetrant over the range 0.1 to 1.0 μm . Chemically cross-linking Matrimid is a method to mitigate some of the relatively high sorption and swelling behavior exhibited in the presence of sorbing species. An in-depth analysis on the vapor phase ethylenediamine cross-linking of Matrimid films and its impact on diffusion, sorption, and relaxation is also described.

Table of Contents

List of Figures	xii
List of Tables	xxi
List of Abbreviations	xxii
Acknowledgements.....	xxiii
Chapter 1 - Introduction and Background	1
1.1. Introduction.....	1
1.2. Membranes and transport theory	2
1.3. Membrane reactors.....	7
1.4. Levulinic acid hydrogenation	11
1.5. Polymer/penetrant thermodynamics	14
1.5.1. Equilibrium sorption	14
1.5.2. Kinetic sorption.....	15
1.6. Quartz crystal microbalance	15
1.7. Polymer cross-linking	17
1.8. Dissertation structure	17
Chapter 2 - Aqueous Phase Hydrogenation of Levulinic Acid using a Porous Catalytic Membrane Reactor*.....	19
2.1. Abstract.....	19
2.2. Introduction.....	20
2.2.1. Membrane reactor background	20
2.2.2. Levulinic acid hydrogenation background.....	22
2.3. Materials and methods	23
2.3.1. Materials	23
2.3.2. Catalytic membrane preparation.....	24
2.3.3. TEM and SEM sample preparation and imaging.....	24
2.3.4. Reactor process	25
2.3.5. Levulinic acid hydrogenation	26
2.4. Results and discussion	26
2.4.1. Membrane characterization.....	26

2.4.1.1.	Gas transport	26
2.4.1.2.	Water transport.....	27
2.4.1.3.	Membrane morphology and catalyst characterization	29
2.4.2.	Catalytic activity	31
2.4.2.1.	Effect of pressure	31
2.4.2.2.	Effect of temperature	38
2.4.2.3.	Additional polymer layer on PTFE membrane surface	41
2.4.2.4.	Membrane reactor longevity.....	44
2.4.2.5.	Suggested future system improvement	45
2.5.	Conclusions.....	45
 Chapter 3 - Ruthenium Integrated Matrimid Membrane Reactor for the Aqueous Phase		
	Hydrogenation of Levulinic Acid.....	47
3.1.	Abstract.....	47
3.2.	Introduction.....	48
3.2.1.	Polymeric membrane reactors.....	48
3.2.2.	Levulinic acid hydrogenation	50
3.3.	Materials and Methods.....	51
3.3.1.	Materials	51
3.3.2.	Catalytic membrane preparation	51
3.3.3.	Reactor process	53
3.3.4.	Levulinic acid hydrogenation	53
3.3.5.	SEM and TEM sample preparation and imaging.....	54
3.4.	Results and Discussion	54
3.4.1.	Membrane and catalyst characterization.....	54
3.4.1.1.	Membrane morphology and gas transport properties	54
3.4.1.2.	Catalyst loading	56
3.4.2.	Reaction results.....	61
3.4.2.1.	Effect of membrane properties.....	61
3.4.2.2.	Permeate analysis.....	65
3.4.2.3.	Effect of catalyst location	67
3.4.2.4.	Catalytic improvement and scale-up.....	70

3.5. Conclusions.....	72
Chapter 4 - Kinetic and Equilibrium Sorption of Organic Liquids and Vapors in Matrimid*	74
4.1. Abstract.....	74
4.2. Introduction.....	75
4.2.1. Background.....	75
4.2.2. Quartz crystal microbalance (QCM) measurement, calculation, and error	76
4.3. Experimental.....	78
4.3.1. Materials	78
4.3.2. Equilibrium liquid sorption.....	78
4.3.3. Kinetic vapor sorption.....	79
4.3.4. Calculations.....	80
4.4. Results and discussion	82
4.4.1. Equilibrium liquid sorption.....	82
4.4.2. Equilibrium vapor sorption.....	84
4.4.3. Penetrant-induced T_g depression.....	86
4.4.4. Kinetic vapor sorption.....	87
4.4.4.1. Diffusion	87
4.4.4.2. Polymer relaxation	93
4.4.5. Thickness dependence on diffusion and relaxation	94
4.5. Conclusions.....	96
Chapter 5 - Effect of Vapor Phase Ethylenediamine Cross-linking of Matrimid on Alcohol Vapor Sorption and Diffusion	98
5.1. Abstract.....	98
5.2. Introduction.....	99
5.2.1. Polymeric membranes and cross-linking	99
5.3. Experimental.....	101
5.3.1. Materials	101
5.3.2. Quartz crystal film coating.....	101
5.3.3. Ethylenediamine (EDA) vapor-phase cross-linking	102
5.3.4. Kinetic vapor sorption and calculations.....	102
5.4. Results and Discussion	102

5.4.1.	Ethylenediamine (EDA) cross-linking kinetics	102
5.4.2.	Equilibrium vapor sorption	104
5.4.3.	Kinetic vapor sorption.....	107
5.4.3.1.	Diffusion case analysis	107
5.4.3.2.	Diffusion	109
5.4.3.3.	Polymer relaxation	113
5.5.	Conclusions.....	115
Chapter 6 - Future Work.....		117
6.1.	Introduction.....	117
6.2.	Mixed matrix Matrimid membrane surface hydrophobization for aqueous phase membrane reactor applications	117
6.3.	Complexation-induced phase separation formed composite membrane with dense skin layer loaded with catalyst ions for membrane reactor application	120
6.4.	Conversion of fructose to desirable hydrogenated products using ionic liquid solvents in membrane reactor	123
6.5.	Kinetic and equilibrium sorption of liquid and vapor penetrants in P84, PBI, and blended polymers using QCM	128
6.6.	Controlling polymer swelling and cross-linking initiation to produce membranes with different molecular weight cut-offs	129
6.7.	Effect of pH on catalytic activity and membrane permeability	130
Chapter 7 - Conclusions.....		132
References.....		134
Appendix A - Additional Information for Chapter 2		148
Appendix B - Additional Information for Chapter 3		151
Appendix C - Vapor Pressures of Levulinic Acid and γ -valerolactone.....		153
Appendix D - Additional Information for Chapter 4.....		154
Appendix E - MATLAB Code used in Chapter 4 Data Analysis		194
Appendix F - Membrane reactor and QCM sorption system images		198

List of Figures

Figure 1-1 - Top view of isotropic, porous PTFE membrane with 0.05 μm pore size. The fibers and pores extend 25 μm normal to this surface view and are uniform in composition throughout the entire thickness.	3
Figure 1-2 - Cross-sectional view of anisotropic, asymmetric polymeric membrane with a thin, dense separating layer and a porous support layer.....	4
Figure 1-3 - Schematic of transport mechanisms in porous (convective) and dense layer membranes (solution-diffusion).....	5
Figure 1-4 - Membrane reactor methods of flow and catalyst contact. (A) indicates dissolution of substrate species A and hydrogen in the membrane undergoing reaction with the homogeneously dispersed catalyst in the membrane bulk. (B) indicates a liquid solution containing dissolved substrate species A and hydrogen that undergo hydrogenation as they pass through the pores of the membrane that contain the catalyst. (C) indicates the membrane acting as a liquid/gas phase contactor with the catalyst coated on the liquid phase surface of the membrane. Hydrogenation reaction occurs as hydrogen permeates the membrane and reaches the catalytic sites.	9
Figure 1-5 - Levulinic acid (LevA) hydrogenation to gamma-valerolactone (GVL).....	11
Figure 2-1 - Membrane reactor process schematic. Shaded areas indicate liquid phase while white areas indicate gas phase.	25
Figure 2-2 - Water flux through ePTFE membrane ($A = 13.8 \text{ cm}^2$) as a function of temperature. A 1.4 bar nitrogen cross-flow at a rate of 10 mL/min was applied to the permeate side of the membrane to facilitate permeate collection.	28
Figure 2-3 - Water flux through Matrimid modified ePTFE membrane ($A = 13.8 \text{ cm}^2$) as a function of Matrimid coating. There is a modest water flux decline as the Matrimid coating increases. All indicated fluxes were collected at 70 $^{\circ}\text{C}$ with a 1.3 bar gas cross-flow at 10 mL/min.....	29
Figure 2-4 - GVL production at cross-flow hydrogen pressures ranging from 0.7 to 5.6 bar. Reaction conditions: temperature = 60 $^{\circ}\text{C}$, 930 μg Ru, 60 mL of 3 wt% LevA in water. One membrane was utilized for all of the above experiments and each pressure was tested in increasing succession from 0.7 to 5.6 bar and then returned to 0.7 bar for the final ~20 h of	

experimentation to demonstrate continued catalytic activity. The (x) data points indicate the repeated 0.7 bar experiment.....	32
Figure 2-5 - GVL rate of production as a function of hydrogen pressure. PBR calculated rate data shown for comparison. Reaction conditions same as those in Figure 2-4. MR (○), PBR (- - -). Error bars calculated using error propagation in membrane reactor measurements.....	33
Figure 2-6 - Ratio of membrane reactor rate to calculated packed bed reactor rate, as a function of hydrogen pressure. It is evident that a maximum rate ratio is obtained above 0.7 bar of hydrogen pressure. Error bars calculated using error propagation in membrane reactor measurements.....	34
Figure 2-7 - (L) Depiction of porous membrane situated between liquid and gas phases. Shown to visualize how dispersed catalyst particles may be located in some combination of gas and liquid environments. (R) MR (membrane reactor) control experiment performed with H ₂ dissolved in liquid phase and circulated over membrane, rather than delivered through the membrane as in typical experiments.....	36
Figure 2-8 - Membrane reactor, PBR, and membrane reactor control experiment rates. Reaction conditions: temperature = 60 °C, 930 μg Ru, H ₂ pressure = 1.4 bar, 60 mL of 3 wt% LevA in water. Error bars calculated using error propagation in membrane reactor measurements.....	36
Figure 2-9 - Inferred depth of aqueous phase penetration into porous PTFE membrane reactor approximated by comparing catalytic rate of control experiment and calculated PBR [27].	38
Figure 2-10 - GVL production at temperatures from 50 to 90 °C in membrane reactor. Reaction conditions: hydrogen pressure = 1.4 bar, 930 μg Ru, 60 mL 3 wt% LevA in water.	39
Figure 2-11 - GVL production rates as a function of temperature for membrane reactor (○) and calculated PBR (- - -). Reaction conditions same as those in Figure 2-10. Error bars calculated using error propagation in membrane reactor measurements.....	40
Figure 2-12 - Ratio of membrane reactor GVL hydrogenation rate to calculated packed bed reactor rate, or "catalytic benefit", as a function of temperature. Error bars calculated using error propagation in membrane reactor measurements.....	41
Figure 2-13 - Arrhenius plot of the natural log of the apparent rate constant, k, as a function of 1000/T from 50 to 90 °C. k is given in units of mol ^{0.5} L ^{0.5} / g _{Ru} h.	41

Figure 2-14 - GVL production with additional polymer layer on catalytic surface of ePTFE membrane. Reaction conditions: temperature = 70 °C, hydrogen pressure = 1.4 bar, 930 μg Ru, 60 mL of 3 wt% LevA in water..... 43

Figure 2-15 - GVL rate of production for each Matrimid modified ePTFE membrane. Data text labels indicate Matrimid coating solution wt%, and unmodified refers to an unmodified ePTFE membrane. All membranes were coated with the same amount of RuCl₃ in ethanol solution, however the depth penetration may be different for each membrane because of the Matrimid surface addition. Reaction conditions same as those in Figure 2-14. 43

Figure 2-16 - GVL rate of production over extended time period. Reaction conditions: temperature = 50 °C, H₂ pressure = 1.4 bar, Ru mass = 930 μg, ePTFE membrane. The left y-axis shows the GVL mass production as a function of time and the right y-axis shows the calculated instantaneous rate as a function of time. This plot demonstrates the catalytic stability of the membrane reactor and suggests no loss of catalytic activity over 200 hours of continuous operation. (○) indicates GVL mass and (□) indicates the calculated instantaneous reaction rate, dm/dt..... 44

Figure 3-1 - Schematic representation of asymmetric polymeric membrane with dispersed Ru coating on the dense surface used for the aqueous phase hydrogenation of levulinic acid (LevA) to gamma-valerolactone (GVL). 50

Figure 3-2 - RuCl₃ in ethanol spin-coated Matrimid membranes. Low loading (0.025 M) and high loading (0.20 M) hydrogen reduced membranes are shown with indicated regions of good and poor catalyst dispersion. 53

Figure 3-3 - SEM image of asymmetric Matrimid membrane showing a porous support layer approximately 60 μm thick on the right of the image transitioning to a completely dense layer on the left of the image. Not evident is the dispersed Ru layer located on the exterior of the membrane dense surface and calculated to be on the order of 10 nm. 55

Figure 3-4 - Hydrogen permeance of Ru coated membranes used in hydrogenation reaction experiments. Hydrogen and nitrogen permeances measured at 35 °C. Dashed line indicates ideal selectivity of Matrimid for hydrogen over nitrogen at 35 °C [95]. The legend values refer to the Ru loading in μg/cm² and ‘Flipped’ refers to the flipped configuration experiments described in Section 3.4.2.3..... 56

Figure 3-5 - Ru loading as a function of the coating solution molarity measured by quartz crystal microbalance (QCM) using Matrimid coated quartz crystals. Error bar indicates one standard deviation for five independent measurements for each coating solution molarity. 57

Figure 3-6 - Photographs of Ru (reduced) coated Matrimid membrane surfaces for each loading density. A clear visual difference in the amount of catalyst loaded is apparent. Loading amounts are those determined from QCM analysis. 57

Figure 3-7 - Ru surface loading as determined by energy dispersive x-ray spectroscopy of coated membrane surfaces. The Ru loading was determined from the ratio of Ru to C and O atoms and is therefore given in arbitrary units. Error bars indicate one standard deviation of four independent measurements of the 0.2 mol/L coated surface. 58

Figure 3-8 - Roughness (RMS) of Ru (reduced) coated Matrimid membrane surface as a function of Ru loading determined by AFM measurements. Error bars represent one standard deviation for seven independent measurements of one sample. 59

Figure 3-9 - SEM images of 8.8 and 4.5 $\mu\text{g}/\text{cm}^2$ Ru loaded membrane surfaces. The higher loaded surface displays a more continuous layer of catalyst whereas the lesser loaded surface is more fractured or 'island-like'. 60

Figure 3-10 - TEM images of Ru coated Matrimid surface. It is apparent that there is a 'base' layer of 2.7 ± 0.8 nm Ru particles with intermediate and larger agglomerates of Ru (10-100 nm) dispersed on the membrane surface. 61

Figure 3-11 - Reaction rate as a function of membrane hydrogen permeance as tested with pure hydrogen at 35 °C before use in the reaction. The legend values refer to the Ru loading for each membrane in $\mu\text{g}/\text{cm}^2$. Reaction conditions: T = 120 °C and H₂ pressure = 2 bar. 63

Figure 3-12 - Schematic representation of normal and control experiments. The gas phase permeate stream is N₂ for the control experiment instead of H₂. 63

Figure 3-13 - Reaction rate dependency on membrane hydrogen permeance as a function of Ru mass loading. The lower the Ru mass loading, the more efficient the membrane reactor utilizes hydrogen that permeates through the membrane. 64

Figure 3-14 - Reaction rate as a function of Ru mass loading on the dense surface layer of the membrane. Although the higher catalyst loading produces more overall GVL, normalizing the reaction rate by the catalyst mass present reveals that lessening the loading improves the

efficiency of the system in terms of catalytic rate per unit catalyst mass. Reaction conditions: T = 120 °C and H ₂ pressure = 2 bar.	65
Figure 3-15 - LevA permeate molar flux as a function of membrane H ₂ permeance under reaction conditions. The “No catalyst” data point was obtained using a feed concentration of 1 wt% LevA and 0.1 wt% GVL in water with an uncoated dense film with an H ₂ permeance of 0.6 GPU.....	66
Figure 3-16 - GVL permeate molar flux as a function of membrane H ₂ permeance under reaction conditions. The “No catalyst” data point was obtained using a feed concentration of 1 wt% LevA and 0.1 wt% GVL in water with an uncoated dense film with an H ₂ permeance of 0.6 GPU.....	67
Figure 3-17 - Reaction rate as a function of H ₂ pressure for the 'flipped' membrane reactor configuration. Δ indicates a catalyst loading of 8.8 μg/cm ² and □ indicates 2.3 μg/cm ² . The filled symbol ▲ indicates that the same membrane was used for both experiments run in succession for 24 hours each without exposing the membrane to air. The membranes used in this plot had an H ₂ permeance of 7 GPU. Reaction temperature was 120 °C.	69
Figure 3-18 - Reaction rate comparison of 'normal' and 'flipped' membrane reactor configurations for low and high catalyst loadings. Experimental conditions: T = 120°C and H ₂ pressure = 2 bar.	70
Figure 3-19 - This plot is an extrapolation of observed catalytic trends in terms of membrane H ₂ permeance and Ru loading. The trends were determined over experimental ranges of 1 to 12 GPU for H ₂ permeance and 1.1 to 8.8 μg/cm ² for Ru loading. The contour lines represent GVL production rates in units of g _{GVL} /h.	71
Figure 3-20 - This plot presents the same extrapolated catalytic trends as those shown in Figure 3-19, but here the contour lines represent catalyst mass normalized rates given in units of g _{GVL} /h*g _{Ru}	72
Figure 4-1 - Repeat unit of Matrimid 5218 polyimide.	76
Figure 4-2 - QCM Vapor Sorption Setup – FC denotes ‘flow controller’ and quartz crystal holder contains polymer coated crystal in an o-ring sealed cell with appropriate electrodes for QCM control. Dashed line indicates components were submerged in temperature controlled (±0.05 °C) water bath.....	80

Figure 4-3 - Ethanol sorption in Matrimid for an activity step change from 0.1 to 0.2 at $t = 0$ over a 12 h time period displayed to exemplify model parameter definitions and the associated approximate time intervals used. 82



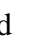
Figure 4-4 - Equilibrium liquid sorption of indicated chemical species in Matrimid at 30 °C. * and ** indicate values taken from literature references at 35 °C and 25 °C, respectively [91,105]. Note that the y-axis ranges over 2 orders of magnitude for the chemical species listed. Species are approximately organized into three groups: alkanes , alcohols , and other organics . Exact values of mass of solute sorbed per mass of polymer can be found in Supporting Information Table A1..... 83

Figure 4-5 - Vapor sorption for 12 h intervals in Matrimid at 30 °C for 0.1 chemical activity step changes. Values listed at an activity of 1 are taken from equilibrium liquid sorption of dense Matrimid films. All film thicknesses were 0.26 μm ($\pm 0.015 \mu\text{m}$). Error bars omitted for clarity. The standard deviation of six independent measurements of methanol isotherms was at most 5 % of the average value for each 0.1 activity increment..... 85

Figure 4-6 - Vapor sorption for 48 h intervals in Matrimid at 30 °C for 0.2 chemical activity step changes. Values listed at an activity of 1 are taken from equilibrium liquid sorption of dense Matrimid films. Film thicknesses ranged from 0.26 to 0.40 μm . See Figure 5 caption for error discussion..... 86

Figure 4-7 - T_g depression as calculated by Chow's model (—) and Fox equation (- - -) using sorption isotherm data. It is stressed that these calculations are estimates..... 87

Figure 4-8 - Thermodynamically corrected vapor diffusion coefficients in Matrimid at 30 °C as a function of chemical activity. All initial film thicknesses were 0.26 μm ($\pm 0.015 \mu\text{m}$). Error bars omitted for clarity. See Appendix C for error analysis, which places approximately ± 25 % error on the diffusion coefficient values reported. Lines added for visual aid..... 88

Figure 4-9 - Diffusion coefficients at infinite dilution for the indicated chemical species in Matrimid at 30 °C as a function of van der Waals molar volume. All film thicknesses were 0.26 μm ($\pm 0.015 \mu\text{m}$). Error bars represent one standard deviation for 15 independent samples for methanol sorption. See Supporting Information for expanded error discussion. 89

Figure 4-10 - Ethanol sorption profile for 0.1 chemical activity steps every 12 h at 30 °C. Film thickness = 0.278 μm 90

Figure 4-11 - Initial short-time interval for each 0.1 activity step change for ethanol sorption. $\Delta t = 1$ second. (- - -) represents fit BH equation. D_F signifies the Fickian or transport diffusion coefficient. D_{TC} signifies the thermodynamically corrected diffusion coefficient. It was determined that the sorption data for activity change 0 to 0.1 exhibited Case II diffusion, so coefficients are not reported for that interval.....	90
Figure 4-12 - Propanol sorption profile for 0.2 chemical activity steps every 48 h at 30 °C.	91
Figure 4-13 - Deborah number as a function of chemical activity calculated using regressed diffusion coefficients and relaxation parameters. All film thicknesses were 0.26 μm ($\pm 0.015 \mu\text{m}$).	94
Figure 4-14 - Diffusion coefficients at infinite dilution for the indicated chemical species at 30 °C as a function of film thickness. The filled symbols (●) represent diffusion coefficients for water in Matrimid at 35 °C taken from [121] for comparison to thick film values. An expanded view of this plot is found in Appendix C.....	96
Figure 5-1 - Matrimid monomeric units cross-linked showing formation of amide groups linking the chains with ethylenediamine.	100
Figure 5-2 - Mass of EDA per mass of Matrimid polymer as a function of cross-linking agent (EDA vapor) exposure time at 20, 25 and 30 °C as measured with QCM. The dashed line indicates the calculated ratio of the molecular weights of one molecule of EDA per one monomer of Matrimid.	104
Figure 5-3 - Vapor pressures of ethylenediamine (EDA) [142] and water for comparison.	104
Figure 5-4 - Vapor sorption isotherms for 0.2 chemical activity steps with 48 hours at each activity at 30 °C. (—) indicates unmodified Matrimid film and (- - -) indicates EDA cross-linked (2 h EDA vapor exposure) Matrimid film.	106
Figure 5-5 - Ethanol sorption in EDA cross-linked Matrimid films with thickness $0.30 \pm 0.03 \mu\text{m}$ at 30 °C for films with varying durations of 20 °C EDA vapor exposure.	107
Figure 5-6 - Hexanol sorption for 0.2 to 0.4 activity step change in unmodified Matrimid. The value of the parameter $n = 0.85$, which is indicative of anomalous diffusion. It is noted that the y-axis is only 0.2 for this interval indicating the rest of the sorption for this activity step change was due to penetrant induced polymer relaxation.	109
Figure 5-7 - Hexanol sorption for 0.2 to 0.4 activity step change in EDA cross-linked Matrimid (2 h vapor exposure). The value of the parameter $n = 0.5$, which is indicative of Fickian	

diffusion. It is noted that the y-axis is only 0.1 for this interval indicating the rest of the sorption for this activity step change was due to penetrant induced polymer relaxation. .. 109

Figure 5-8 - Thermodynamically corrected diffusion coefficients for indicated species in Matrimid as a function of chemical activity at 30 °C. All film thicknesses were 0.26±0.015 μm, except heptanol, which is marked with an * indicating a film thickness of 0.46 μm. The heptanol calculated diffusion coefficients were multiplied by 0.5 as suggested by the thickness dependence on diffusion coefficients presented in Chapter 4 for the difference between 0.26 and 0.46 μm. 111

Figure 5-9 - Thermodynamically corrected diffusion coefficients for the indicated species in EDA cross-linked (2 h vapor exposure) Matrimid films of thickness 0.45±0.05 μm at 30 °C. 112

Figure 5-10 - Diffusion coefficients at infinite dilution for water and C1-C7 alcohols plotted at their respective van der Waals molar volumes for unmodified (●) and EDA cross-linked (○) Matrimid films at 30 °C. The unmodified films were 0.26±0.015 μm and the cross-linked films were 0.45±0.05 μm in thickness. This difference in thickness was accounted for by multiplying the originally calculated cross-linked diffusion coefficients by 0.5 as suggested by the thickness dependence trend presented in Chapter 4. Error bars determined by varying thickness and time by expected uncertainties when performing the diffusion calculation, which produced a larger error than the standard deviation of three independent experiments and consequently determined diffusion coefficients. 112

Figure 5-11 - Relaxation parameter, k_R , as a function of chemical activity for unmodified (—) and EDA cross-linked (- - -) Matrimid films at 30 °C. 114

Figure 5-12 - Relaxation parameter, k_R , at infinite dilution of water and C1-C7 alcohols plotted at their respective van der Waals molar volume for unmodified (●) and EDA cross-linked (○) Matrimid films at 30 °C. 115

Figure 6-1 - Perfluorinated octyltrichlorosilane (FOTS) used for attachment to titania, alumina, or silica nanoparticles in dense layer of membrane to increase hydrophobicity. 118

Figure 6-2 - Schematic representation of membrane consisting of a porous Matrimid layer with a hydrophobized nanoparticle loaded dense layer of Matrimid. 120

Figure 6-3 - Complexation-induced phase separation composite membrane image and schematic. Image taken from [145]. 122

Figure 6-4 - Metal loaded dense layer of CIPS composite membrane. Image taken from [145].
..... 123

Figure 6-5 - Ruthenium coated membrane before and after use in aqueous phase hydrogenation
of HMF reaction..... 124

Figure 6-6 - Membrane used in membrane reactor with [EMIM]OAc as solvent. Matrimid
dissolved in the ionic liquid at 90 °C..... 126

Figure 6-7 – Schematic of polymer matrix swollen to different extents and cross-linked in the
swollen state effectively ‘locking’ in the relative expanded volume elements within the
matrix. (—) are the polymer chains and (- - -) indicates cross-linking..... 130

List of Tables

Table 1-1 – Levulinic acid hydrogenation with Ru catalyst under various reaction conditions...	13
Table 2-1 - Gas transport properties at 25 °C	27
Table 4-1 – Diffusion-relaxation model terms.....	81
Table 4-2 - Solvents for Matrimid. These listed chemicals dissolved films of Matrimid at the indicated temperature.....	84
Table 6-1 - Viscosity of select ionic liquids and other liquids for comparison.	125

List of Abbreviations

C1-C6 (or C7) alcohols – Methanol through hexanol (heptanol), all of the normal isomeric form.

CSTR – Continuously stirred tank reactor

D – Diffusion coefficient (often discussed in relation to penetrant in polymer diffusion coefficient)

D_0 – Infinite dilution diffusion coefficient

DCM – Dichloromethane

De – Deborah number

EDA – Ethylenediamine

EDS – Energy dispersive x-ray spectroscopy

GPU – Gas permeation unit

GVL – gamma-valerolactone (also γ -valerolactone)

HMF – 5-hydroxymethylfurfural

IL – Ionic liquid

LevA – Levulinic acid

MR – Membrane reactor

PBR – Packed bed reactor

PTFE (or ePTFE) – Polytetrafluoroethylene (or expanded polytetrafluoroethylene)

SEM – Scanning electron microscopy

TEM – Tunneling electron microscopy

T_g – Glass transition temperature

THF – Tetrahydrofuran

QCM – Quartz crystal microbalance

XL – X-linked or cross-linked (referring to chemically cross-linked polymer chains)

Acknowledgements

I would like to acknowledge my advisor Dr. Mary Rezac and co-advisor Dr. Peter Pfromm for supporting me as a graduate student and helping me to find and develop my skills and knowledge as a research scientist. I would also like to acknowledge all of the members of the Rezac-Pfromm research group that I have worked with since arriving at K-State, namely Fan Zhang, Ronald Michalsky, Alexandru Avram, Sebastian Wendel, Leslie Schulte, Michael Wales, Matthew Young, Liz Boyer, Michael Heidlage, Shuzhen Qui, Yixiao Li, and Jared Carson. I also show my appreciation to the undergraduate research assistants and REU students I have had the pleasure to work with while at K-State and that have made contributions to my research projects, David Madden, Andrew Betzen, Jared Carson, Lydia Watton, Lauren McDonald, Anne Maier, and Michelle Soto.

I would like to acknowledge the funding sources that made much of this research possible, including the National Science Foundation Grant: From Crops to Commuting: Integrating the Social, Technological, and Agricultural Aspects of Renewable and Sustainable Biorefining (I-STAR); NSF award number: DGE-0903701 and the USDA NIFA award number 2011-67009-20055.

Chapter 1 - Introduction and Background

1.1. Introduction

As the universe progresses according to the second law of thermodynamics, the homogeneous distribution of all matter and energy, it seems there is nothing that can be done to avoid this fate. Although, in isolated systems within the universe, we may temporarily delay the inevitable ultimate thermal and chemical equilibrium by storing energy and selectively separating matter into useful partitions. Indeed, it is by this very principle that the unique conditions over many millennia on our planet have allowed natural selection to proceed to our very existence and contemplation of its eventual finality. A crucial phenomenon that brought about and continues to allow our moderately comfortable existence is selective permeation through semipermeable barriers, or membranes. If one grants a little liberty to this interpretation, one begins to see membranes everywhere, ranging from the earth's magnetosphere that selectively allows some of the radiation from the sun to reach our planet's surface while repelling many of the charged particles that would quickly strip our planet of its atmosphere, to our lungs that selectively extract oxygen from the atmosphere while expelling accumulated carbon dioxide from our bloodstream, to the complex cellular membrane that regulates the transport of nutrients into and waste products out of the cell, to the man-made membranes that purify our drinking water, perform hemodialysis for the nearly half million patients with kidney failure in the US alone [1], and remove inerts and impurities from the 25 trillion cubic feet of natural gas produced in the US per year [2].

The importance and ubiquity of membranes in the natural world and in our industrial society can be substantiated with many other examples, but suffice it to say there is a large amount of further benefit and potential for understanding and developing membrane technology. The focus of this research is on the development and characterization of polymeric membranes for

applications in three-phase reactors. The general focus is to utilize the membrane as a combined catalyst interface and gas/liquid phase contactor allowing selective permeation of gaseous or liquid reactants to catalytic sites.

1.2. Membranes and transport theory

A membrane is any material that selectively allows transport of one chemical species while inhibiting that of another. Depending on the type of membrane, the separation mechanism may be based on the relative size, charge, or solubility and diffusivity of the species in contact with the membrane. The driving force for transport for any chemical species is the difference in chemical potential of a species i , $\mu_i = \frac{\partial G}{\partial N_i}$, across the membrane. Unless there is a mechanical barrier preventing transport, such as the physical size of a species being larger than the available pore diameter, the system will move towards equilibrium, or minimization of the free energy for all involved chemical species, $\sum_{i=1}^n \mu_i dN_i = dG = 0$.

Two common methods for classifying membranes are by composition/structure and separation size/application. The three major types of membrane composition are polymer, ceramic, and metal, or some combination thereof. Biological membranes present an entirely different class of membranes and research field, and are consequently not included in any of this research. Classification by size of separation or intended application include: microfiltration, ultrafiltration, nanofiltration, reverse osmosis, pervaporation, and gas separation. The micro (10 μm – 600 nm), ultra (600 – 20 nm), and nanofiltration (20 – 0.1 nm) membranes are all porous in nature with the classification based on the size of the pores with approximate ranges given in parentheses [3]. Reverse osmosis, pervaporation, and gas separation membranes all contain a dense, i.e. non-porous, layer that performs the actual separation. The structure of a membrane can be isotropic, anisotropic, composite layers, or a completely dense layer. Isotropic membranes have

a uniform structure throughout the entire thickness, while anisotropic membranes consist of either multiple layers (composite) or a porous support layer that transitions to a very thin, completely dense layer (asymmetric). Considering the flux through a membrane is inversely proportional to separating layer thickness, anisotropic membranes are desirable in the sense that the separating layer is of minimal thickness. The type of membrane of focus in Chapter 2 is an isotropic, porous polytetrafluoroethylene (PTFE) membrane with 0.05 μm pore size, as shown in Figure 1-1. The type of membrane discussed in Chapter 3 is an anisotropic, asymmetric Matrimid membrane, an example of which is shown in Figure 1-2.

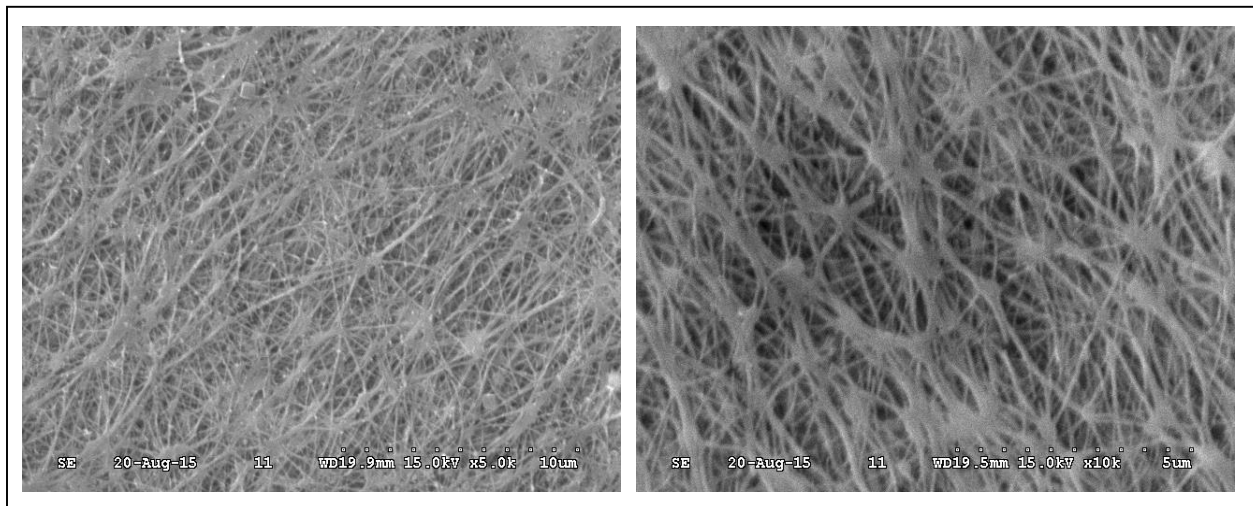


Figure 1-1 - Top view of isotropic, porous PTFE membrane with 0.05 μm pore size. The fibers and pores extend 25 μm normal to this surface view and are uniform in composition throughout the entire thickness.

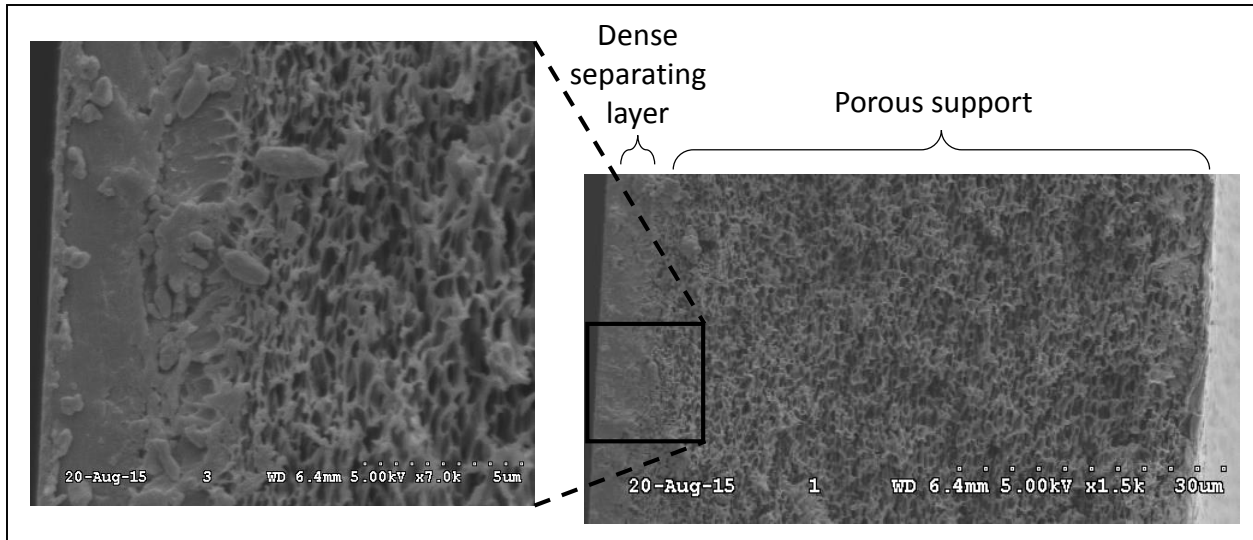


Figure 1-2 - Cross-sectional view of anisotropic, asymmetric polymeric membrane with a thin, dense separating layer and a porous support layer.

Transport through a membrane can occur by convective transport, as in porous membranes, or by the solution-diffusion mechanism in the dense layer of an asymmetric or composite membrane. An intermediate regime known as Knudsen diffusion occurs when the pore size approaches that of the mean free path length of the permeating species. Figure 1-3 shows a schematic of convective, or Poiseuille, flow in a porous membrane and diffusion based permeation in a dense layer membrane.

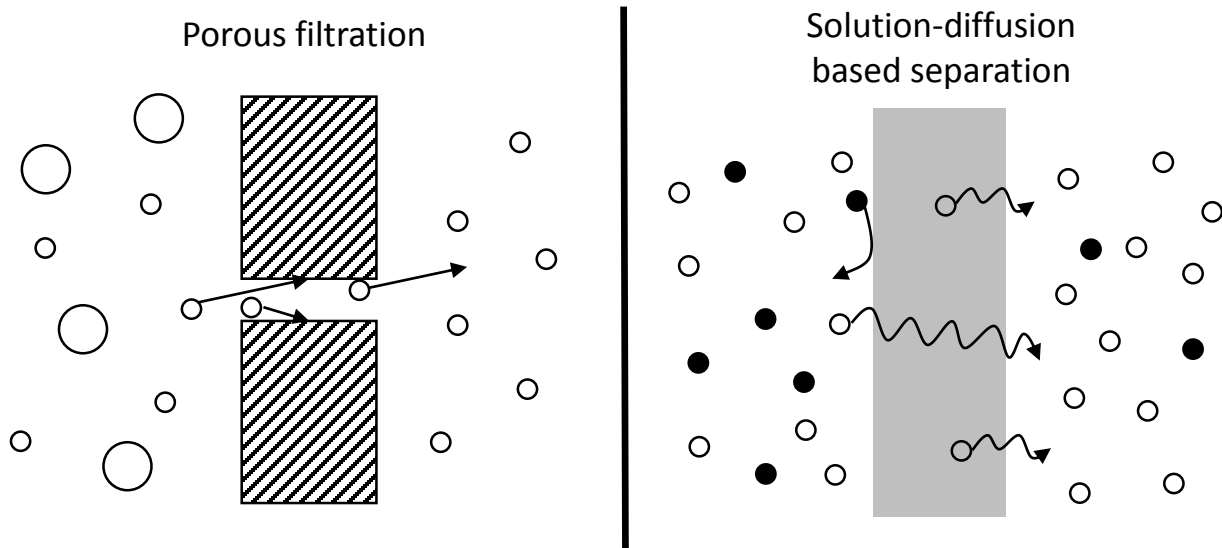


Figure 1-3 - Schematic of transport mechanisms in porous (convective) and dense layer membranes (solution-diffusion).

The mathematical description of flux, J_i , through a porous membrane in the simplest form is given by Darcy's law,

$$J_i = K' c_i \frac{dp}{dx} \quad (1-1)$$

where dp/dx is the pressure gradient across the membrane, c_i is the concentration of permeating species i in the membrane, and K' is a coefficient encompassing parameters associated with the relative permeability of the porous membrane, including area, thickness, viscosity of permeating species, and the nature of the pores. Flux, J_i , through a dense layer membrane is mathematically given as Fick's first law,

$$J_i = -D_i \frac{dc_i}{dx} \quad (1-2)$$

where dc_i/dx is the concentration gradient of species i across the membrane and D_i is the diffusion coefficient of species i in the membrane material. Integrating Equation (1-2) gives

$$J_i = \frac{D_i (c_{i_0(m)} - c_{i_l(m)})}{l} \quad (1-3)$$

where the c with subscripts $0(m)$ and $l(m)$ represent the concentrations of species i on each respective side of the membrane cross-section yet still within the membrane material and l is the cross-sectional thickness. If we consider gas separation specifically, the expression for flux analogous to Equation (1-3) is given as

$$J_i = \frac{P_i(p_{i_0} - p_{i_l})}{l} \quad (1-4)$$

where p_i is the partial pressure of species i at each respective side of the membrane cross-section, 0 and l . P_i is referred to as the permeability coefficient and is equal to the product of the diffusion coefficient, D_i and the sorption coefficient, K_i . Alternatively, P_i is often just referred to as the permeability of i in the membrane material and is correspondingly equal to the product of diffusivity and solubility, yielding the well-known expression $P = DS$. The permeability of a species i in a dense membrane can be thought of as the product its relative mobility in the material, or diffusion coefficient, and the amount of i that can solubilize in the membrane material, or sorption coefficient. Equation (1-4) is identical to the flux of condensable vapors through a dense membrane, as in pervaporation, but with p_i representing the vapor pressure of the condensable species i . The permeability $P = DS$ expression is also the same for condensable vapors, and Chapters 4 and 5 show results for experimentally independently determined D and S values for short-chain alcohol (C1-C6) vapor permeation in Matrimid and ethylenediamine cross-linked Matrimid, respectively.

A final useful expression often encountered in membrane research is the selectivity for permeation of species i over species j through a membrane, given as

$$\alpha_{i/j} = \frac{P_i}{P_j} = \frac{D_i}{D_j} \frac{S_i}{S_j} \quad (1-5)$$

where the selectivity for i over j is simply a ratio of their respective permeabilities in the dense membrane material. The ‘defect-free’ quality of a membrane is often interpreted as the extent that the ratio of observed permeation rates of species i and j , or selectivity, deviates from the ideal selectivity, where ideal refers to the ratio of permeation rates determined in a substantially thick dense film considered to have no defects and be uniform in cross-sectional thickness. For the reader interested in rigorous derivations of Equations (1-1) through (1-5), the underlying mathematical and thermodynamic assumptions made in each case, and overviews of membrane separations in general, please refer to [3-5].

1.3. Membrane reactors

As global demand for oil grows and reserves lessen, alternative sources for sustainable fuels and chemicals are needed. Biomass based feedstock offers a sustainable alternative, but conversion possibilities and technologies must be further realized to offer practical and economically viable sources of production. Catalytic membrane reactors afford an alternative and potentially more efficient method for performing three-phase heterogeneous chemical reactions. Traditional three-phase reactors often present mass transfer limitations, namely relatively large diffusional distances to reach catalytic sites exacerbated by low gas solubility in the liquid phase. Hydrogen availability at the catalytic sites is often the rate limiting step for hydrogenation reactions [6]. Membrane reactors can alleviate the inherent mass transfer limitations by directly and abundantly supplying gas to the catalytic sites located on the membrane surface, which acts as a gas/liquid phase contactor, and thus lessen the necessity for higher gas phase pressures.

Traditional three-phase reactors may be homogeneous or heterogeneous, and examples of both include trickle-bed, fixed-bed, slurry, stirred-tank, and bubble-column [7-9]. Membrane reactors have the advantage of being heterogeneous, thus eliminating the need for catalyst

separation. The catalyst phase of the membrane reactor may be integrated onto the surface or distributed/impregnated throughout the entire membrane. Excellent reviews on membrane reactors, their history and development, and their applications in catalysis and separations have been written by Vankelecom [10], Vital and Sousa [11], Dittmeyer [12], and Gryaznov [13]. In the work described in Chapters 2 and 3 the membrane functions as a liquid/gas phase contactor with the utilized catalyst located at the liquid/membrane interface where the hydrogen permeates through the membrane to reach the catalytic sites.

There are some examples in the literature of hydrogenation reactions in membrane reactors on a variety of reactions, but most notable are the differences in the location of the catalyst particles and the intended transport of the substrate for hydrogenation, as shown in Figure 1-4. The methods of substrate transport include: (A) diffusion in the dense membrane layer, (B) convective flow through membrane pores, or (C) convective cross-flow in contact with the catalytically active surface of the membrane.

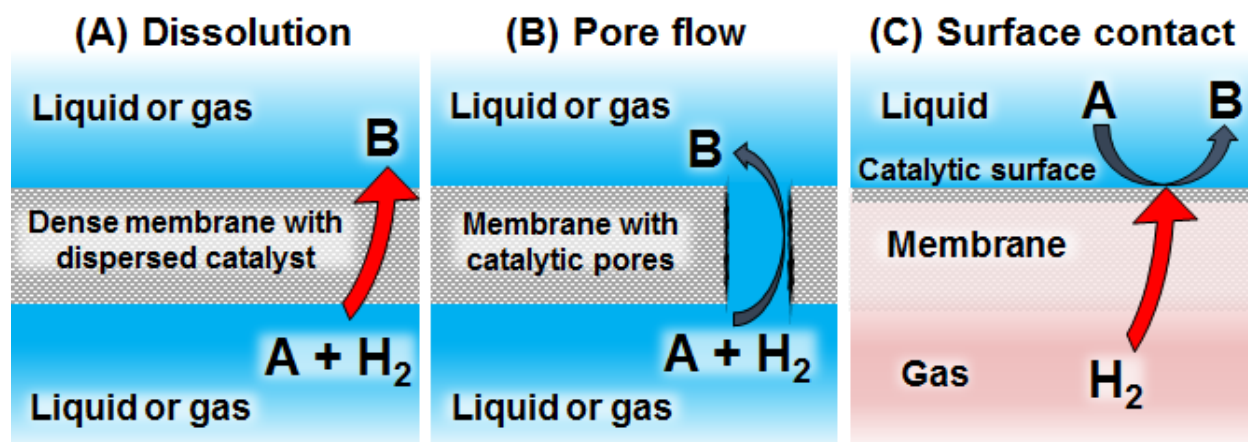


Figure 1-4 - Membrane reactor methods of flow and catalyst contact. (A) indicates dissolution of substrate species A and hydrogen in the membrane undergoing reaction with the homogeneously dispersed catalyst in the membrane bulk. (B) indicates a liquid solution containing dissolved substrate species A and hydrogen that undergo hydrogenation as they pass through the pores of the membrane that contain the catalyst. (C) indicates the membrane acting as a liquid/gas phase contactor with the catalyst coated on the liquid phase surface of the membrane. Hydrogenation reaction occurs as hydrogen permeates the membrane and reaches the catalytic sites.

The dissolution method (A) more specifically occurs when diffusion in the dense layer of the membrane is utilized for reactions where the membrane is substantially permeable to both the substrate and hydrogen. This was shown in the work of [14,15] where the gas phase hydrogenation of propylene and propyne occurred over palladium dispersed through a 4.4 μm dense layer of PDMS. The pore flow method (B) of catalyst/substrate contact was demonstrated with the partial hydrogenations of cyclooctadiene, octyne, phenylacetylene, and geraniol using a polyacrylic acid cross-linked membrane where the hydrogen (40 bar) was premixed in the liquid phase [16]. The motivation of this work was to control the flow characteristics and contact time with the catalyst and therefore the selectivity and conversion of the partial hydrogenation reactions. Another example utilizing membrane pore flow was in the hydrogenation of sunflower oil with a polyamideimide membrane with platinum and palladium catalysts [17]. Again, it was sought to control the selectivity (cis vs. *trans* fatty acid) of the reaction by controlling the flow and residence time in the pores.

The surface contact method (C) of membrane reactor function is demonstrated when convective cross-flow of the substrate across the catalytically active surface of the membrane occurs, while hydrogen, with a much higher permeability in the membrane material, is supplied from the opposite side. Examples of this method are seen in the work performed on the partial hydrogenation of soybean oil where the oil was circulated across the catalytic surface coated on the dense layer of the asymmetric polymeric membrane and hydrogen supplied from the porous support side of the membrane [18-20]. The membrane reactor in this work was shown to produce significantly less trans fats than traditional slurry reactors under similar reaction conditions. It was also shown to have increasingly greater selectivity for *cis* fats at higher temperatures where hydrogen starvation at catalytic sites is exacerbated by lower hydrogen solubility in the liquid phase. Another example of a membrane reactor operating with cross-flow over a catalytic surface is seen in a porous polypropylene hollow fiber membrane with palladium catalyst for the removal of dissolved oxygen from water [21]. Even though the membrane was porous, the hydrophobicity of polypropylene allowed the membrane to act as an impermeable barrier to water while allowing hydrogen to easily reach the catalytic sites. This method of membrane reactor operation is similar to the research described in Chapter 2 where a porous, yet highly hydrophobic polytetrafluoroethylene (PTFE) membrane was used to maintain an aqueous liquid phase on one side of the membrane while allowing hydrogen to permeate and reach ruthenium catalyst on the liquid phase surface. The surface contact method of membrane reactor function is advantageous for our aqueous phase hydrogenation system, because the separation of the gas and liquid phases allows the interfacial catalyst particles to be in simultaneous proximity with gas phase hydrogen and the liquid phase organic reactant. In contrast, the dissolution (A) and pore flow (B) methods of membrane reactor function still operate with liquid phase dissolved hydrogen. The low

solubility and slower diffusion of hydrogen in the liquid phase are hypothesized to no longer be rate limiting constraints in the surface contact (C) method of operation, thus allowing far lower hydrogen pressures to be utilized in comparison to (A), (B), and other traditional three-phase reactors.

1.4. Levulinic acid hydrogenation

The reaction studied for the membrane reactor applications described in Chapters 2 and 3 is the aqueous-phase hydrogenation of levulinic acid using ruthenium as a catalyst, as shown in Figure 1-5. Levulinic acid is derived from the acid-catalyzed hydrolysis of cellulose proceeding through the reaction pathway of glucose, 5-hydroxymethylfurfural (HMF), to levulinic acid (LevA) [22-25]. This reaction was chosen as a model reaction for study in our membrane reactor applications because nearly all references indicate >99 % selectivity for the product gamma-valerolactone.

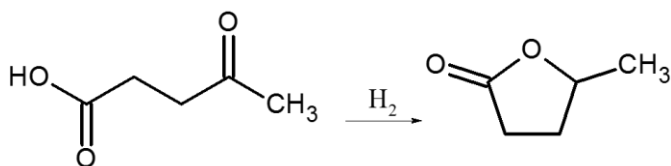


Figure 1-5 - Levulinic acid (LevA) hydrogenation to gamma-valerolactone (GVL)

Levulinic acid is considered a “Top 10” biobased platform chemical and several approaches to its chemical transformation can be found in the literature [26]. Although several catalysts, supports, and solvents have been investigated for the hydrogenation of levulinic acid, many researchers agree that ruthenium is the most effective noble metal catalyst for its aqueous phase hydrogenation [27-32].

The extensive range of reaction conditions, catalyst supports, and catalyst location (heterogeneous vs. homogeneous) make a direct comparison challenging, but most literature either directly or indirectly cites mass of gamma-valerolactone (GVL) produced per unit of time per mass

of catalyst. This value is usually termed catalytic rate or sometimes described as catalytic ‘productivity’ and ranges from the order of one to about one thousand depending on the system. However, two of the short-comings of describing the catalytic rate in this manner include the use of catalyst mass rather than available catalyst or number of catalytic sites, and the lack of normalizing for temperature and pressure. Nevertheless, it does allow a first approximation to comparing the various catalytic systems. Table 1-1 displays the catalytic rate for levulinic acid hydrogenation for a variety of catalytic systems and reaction conditions referenced from literature. Not listed are reaction solvent, catalyst dispersion, catalyst additives/promotors, catalyst support, and heterogeneous vs. homogeneous, which are assumed to be the main factors contributing to the over three orders of magnitude range of rates obtained.

Table 1-1 – Levulinic acid hydrogenation with Ru catalyst under various reaction conditions.

H ₂ pressure (bar)	Temperature (°C)	Rate (g _{GVL} /h*g _{Ru})	Reference
0.3	60	2.9	*
1	265	12	[33]
1.3	120	5.0	**
1.3	60	8.4	*
1.3	70	15	*
1.3	90	47	*
5	60	3.8	[27]
5	80	15	[34]
5	130	19	[35]
5	50	64	[36]
5	70	99	[36]
5.6	60	7.4	*
10	100	25	[37]
12	25	7.8	[29]
12	130	120	[29]
24	50	46	[28]
30	70	9.0	[31]
35	100	20	[38]
35	100	160	[39]
40	200	3.6	[32]
40	130	5000	[40]
45	150	1050	[41]
50	140	130	[42]
50	30	170	[43]
50	70	310	[43]
67	140	55	[44]
150	160	10600	[39]

Note: References with a * or ** represent the work with membrane reactors described in Chapters 2 and 3, respectively.

1.5. Polymer/penetrant thermodynamics

1.5.1. Equilibrium sorption

Gas, liquid, and vapor sorption and diffusion in polymers has been an active area of research for several decades with a large variety of penetrant sorption, diffusion, and polymer behaviors observed [45-51]. Experimental techniques for exploring these phenomena include standard gravimetry, magnetic suspension balance [49], quartz spring microbalance (QSM) [52], FTIR-ATR [48], quartz crystal microbalance (QCM) [53,54], NMR [55], time-lag permeation [56], and pressure decay (PD) [57].

Sorption in glassy polymers is often described according to the dual sorption model where there are two primary contributions to overall sorption, a Henry's law type sorption in the equilibrium free volume of the polymer and a Langmuir sorption process that occurs in the excess free volume that exists between polymer chains [58,59]. The dual sorption model is empirically based and gives good qualitative agreement for many polymer/gas systems. A more recently proposed model for sorption in glassy polymers is the non-equilibrium lattice fluid (NELF) model [60], which is based on the lattice fluid model for polymer/penetrant systems at equilibrium originally developed by Sanchez and Lacombe [61]. The NELF model has no adjustable parameters and is entirely predictive for penetrant solubility in the polymer if pseudo-equilibrium volumetric data are available. The dual sorption and NELF are just two of many models available for describing sorption of gases and vapors in polymers, and although no equilibrium modeling of the polymer/penetrant systems was attempted in this dissertation, the data could certainly be extended for such work.

1.5.2. Kinetic sorption

Diffusion in glassy polymers depends on the molecular size and shape of the penetrant, the thermal motions possible in the polymer chains, and any interactions that occur between penetrant and polymer. Generally, thermal motion in glassy polymers is restricted, so diffusion coefficients are lower than those in rubbery polymers and liquids. Glassy polymers are known to undergo swelling or plasticization behavior for many penetrants. The glass transition temperature can be overcome if sufficient swelling occurs in the polymer, i.e. the presence of sufficient amounts of swelling penetrants allows the polymer backbone chains to become ‘unfrozen’ from their glassy state and undergo thermal motions, which in turn leads to increased sorption and changing penetrant mobility. Berens and Hopfenberg observed that in glassy polymers undergoing swelling behavior there appeared to be two kinetic sorption events occurring, a rapid initial Fickian sorption followed by a much slower non-Fickian sorption phase where the polymer chains were slowly relaxing and consequently allowing continued sorption of penetrants [45]. This diffusion-relaxation model appropriately captures the kinetic sorption behavior of the C1-C6 alcohol vapors sorbing in glassy Matrimid described in Chapter 4. Chapter 5 focuses on the effect of chemically cross-linking the polymer chains and how it mitigates the swelling or relaxation behavior shown in Chapter 4.

1.6. Quartz crystal microbalance

Quartz crystal microbalance (QCM) is a technique for measuring masses down to the order of nanograms. The essence of the technique utilizes the piezoelectric property of appropriately cut quartz crystals. The piezoelectric property of materials arises from an asymmetrical arrangement of dipole moments in a crystal lattice, such that when an external pressure is applied to the lattice the dipoles reorient producing a net voltage difference across the entire material. The converse

property is also true in that applying a voltage to a piezoelectric material induces mechanical deformation. For example, when an alternating electric field is applied to electrodes attached to the faces of each side of a QCM crystal, a directional mechanical deformation, or shear oscillation, is induced in the crystal matrix [62]. The technique of utilizing the piezoelectric property of appropriately cut quartz crystal to measure thin film deposition thickness was originally described and developed by Günter Sauerbrey [63].

Quartz crystal microbalance has been explored and applied for a variety of mass-sensitive uses including high pressure gas sorption [53,54,64], vapor sorption [48,65,66], chemical sensor applications [67,68], and ligand binding [69,70]. QCM was chosen for this work for its ability to examine films with thicknesses in the range of 0.05 to 5 μm , which encompasses the range of thicknesses often observed in the dense layer of asymmetric polymeric membranes [3,5,71,72]. QCM also possesses the potential for high-throughput experimentation considering the use of inexpensive quartz crystals and the immediate availability for data collection assuming the chemical and temperature environments are appropriately controlled.

The frequency of oscillation in the crystal depends on crystal cut and thickness. Thus, each individual crystal has a unique fundamental frequency. When a thin film is deposited onto the electrodes of the crystal and is mechanically adhered, the frequency decreases in direct proportion to the deposited mass. This mathematical relation is known as the Sauerbrey equation:

$$\Delta f = \frac{2\Delta m f_0^2}{A(\mu_q \rho_q)^{1/2}} \quad (1-1)$$

where Δf is the frequency change, Δm is the mass change, f_0 is the fundamental frequency of the uncoated crystal, A is the active area of one face of the crystal, μ_q is the shear modulus of quartz (29.47 GPa), and ρ_q is the density of quartz (2.648 g/cm^3). Simplifying this relationship by

grouping all of the constants, we see that $\Delta f = C\Delta m$, and the mass of the applied film or sorbed species is easily calculated.

1.7. Polymer cross-linking

Chemically cross-linking polyimide membranes is a modification performed to suppress plasticization behavior and increase solvent resistance [73]. The increased robustness of the polyimide membranes has allowed expansion of their use into novel separation areas including solvent resistant nanofiltration, pharmaceutical manufacturing, pervaporation, and other processes that require separation of organic mixtures [74-78]. Popular cross-linking agents for polyimide membranes include a variety of diols and diamines. The diol cross-linking reaction occurs in polyimides with available carboxylic acid groups. The diamine cross-linker reacts with the imide ring in the polymer chain to form a resulting amide linkage, as shown in Figure 5-1 for the cross-linking of the polyimide Matrimid with ethylenediamine (EDA). This cross-linking reaction in Matrimid and its effect on reducing plasticization and swelling behavior in the presence of alcohol vapor is the focus of Chapter 5.

1.8. Dissertation structure

Chapter 2 of the dissertation discusses the development of catalyst integrated porous PTFE membranes for the application of the aqueous phase hydrogenation of levulinic acid. Chapter 3 extends the membrane reactor concept to catalyst coated asymmetric Matrimid membranes for the aqueous phase hydrogenation of levulinic acid. The goal of the research discussed in Chapter 3 was to examine how changing membrane transport properties and catalyst coatings impacted the reaction kinetics of the system. Chapter 4 more closely examines material properties of Matrimid, focusing on the solubility and diffusivity of a variety of organic liquid and vapor penetrants in the material and consequent polymer chain relaxation behavior using QCM as the analytical technique.

Chapter 5 extends this work by examining cross-linking Matrimid with ethylenediamine (EDA) vapor and how it impacts the diffusion, sorption, and polymer relaxation behavior for C1-C6 alcohol vapor penetrants. Chapter 6 offers recommendations for future work in the development of membrane reactors through modification of the membrane to better suit reaction conditions and extending the thermodynamic investigations of Chapters 4 and 5 to other potentially interesting membrane polymers. Chapter 7 summarizes the research performed and concludes with the major and important findings of each study.

Chapter 2 - Aqueous Phase Hydrogenation of Levulinic Acid using a Porous Catalytic Membrane Reactor*

2.1. Abstract

Membrane reactors offer an alternative approach for conducting three-phase heterogeneous chemical reactions. The membrane acts as a liquid/gas phase contactor, while also serving as the support for a solid catalyst. A significant benefit from this approach is circumvention of gas phase dissolution and diffusion in the liquid phase to reach catalytic sites. This method of gas phase mass transfer allows a significant reduction in operating pressure compared to traditional three-phase reactors that often require higher gas pressures due to low gas solubility and diffusivity in the liquid phase. The membrane reactor in this work consists of a porous expanded polytetrafluoroethylene (ePTFE) membrane with deposited Ru catalyst particles. The reaction studied is the aqueous phase hydrogenation of levulinic acid to produce γ -valerolactone. The highly hydrophobic PTFE material provides an almost impermeable barrier to the liquid phase while allowing hydrogen gas to freely transport through the pores to reach catalytic sites located at the liquid/membrane interface. The reaction kinetics displayed by the membrane reactor favorably compare to those of a packed bed reactor (PBR). In terms of hydrogen pressure the maximum catalytic benefit in comparison to the PBR is obtained at pressures greater than 0.7bar, and a more pronounced and continuously increasing catalytic benefit is obtained with increasing temperature.

*This chapter has been submitted to *Catalysis Today* and accepted for publication. doi:10.1016/j.cattod.2016.02.026

2.2. Introduction

2.2.1. Membrane reactor background

As global demand for oil grows and reserves lessen, alternative sources for sustainable fuels and chemicals are needed. Biomass based feedstock offers a sustainable alternative, but conversion possibilities and technologies must be further realized to offer practical and economically viable sources of production. Catalytic membrane reactors afford an alternative and potentially more efficient method for performing three-phase heterogeneous chemical reactions. Traditional three-phase reactors often present mass transfer limitations, namely relatively large diffusional distances to reach catalytic sites exacerbated by low gas solubility in the liquid phase. Hydrogen availability at the catalytic sites is often the rate limiting step for hydrogenation reactions [6]. Membrane reactors can alleviate the inherent mass transfer limitations by directly and abundantly supplying gas to the catalytic sites located on the membrane surface, which acts as a gas/liquid phase contactor, and thus lessen the necessity for higher gas phase pressures.

Traditional three-phase reactors may be homogeneous or heterogeneous, and examples of both include trickle-bed, fixed-bed, slurry, stirred-tank, and bubble-column [7-9]. Membrane reactors have the advantage of being heterogeneous, thus eliminating the need for catalyst separation. The catalyst phase of the membrane reactor may be integrated onto the surface or distributed/impregnated throughout the entire membrane. Excellent reviews on membrane reactors, their history and development, and their applications in catalysis and separations have been written by Vankelecom [10], Vital and Sousa [11], Dittmeyer [12], and Gryaznov [13]. In our work the membrane functions as a liquid/gas phase contactor with the utilized catalyst located at the liquid/membrane interface where the hydrogen permeates through the membrane to reach the catalytic sites.

There are some examples of hydrogenation reactions in membrane reactors in the literature on a variety of reactions, but most notable are the differences in the location of the catalyst particles and the intended transport of the substrate for hydrogenation, as shown in Figure 1-4. The methods of substrate transport include: (A) diffusion in the dense membrane layer, (B) convective flow through membrane pores, or (C) convective cross-flow contact with the catalytic active surface of the membrane, as in our work. Works demonstrating the use of the membrane in the dissolution method (A) and pore flow method (B) can be found in [14,15] and [16,17], respectively. The surface contact method (C) is demonstrated when convective cross-flow of the liquid phase substrate across the catalytically active surface of the membrane occurs, while hydrogen, with a much higher permeability in the membrane material, is supplied from the opposite side. Examples of this method are seen in the work performed on the partial hydrogenation of soybean oil [18-20] and the removal of dissolved oxygen from water [21].

Our work is best described as method (C) where a porous, yet highly hydrophobic polytetrafluoroethylene (PTFE) membrane was used to maintain an aqueous liquid phase on one side of the membrane while allowing hydrogen to permeate and reach ruthenium catalyst on the liquid phase surface. The surface contact method of membrane reactor function is advantageous for our aqueous phase hydrogenation system, because the separation of the gas and liquid phases allows the interfacial catalyst particles to be in simultaneous proximity with gas phase hydrogen and the liquid phase organic reactant. In contrast, the dissolution (A) and pore flow (B) methods of membrane reactor function still operate with liquid phase dissolved hydrogen. The low solubility and slower diffusion of hydrogen in the liquid phase are thought to no longer be rate limiting constraints in the surface contact (C) method of operation, thus allowing far lower

hydrogen pressures to be utilized in comparison to (A), (B), and other traditional three-phase reactors.

2.2.2. Levulinic acid hydrogenation background

The reaction studied in this work was the aqueous-phase hydrogenation of levulinic acid to gamma-valerolactone using ruthenium as a catalyst, as shown in Figure 1-5. Levulinic acid is derived from the acid-catalyzed hydrolysis of cellulose proceeding through the reaction pathway of glucose, 5-hydroxymethylfurfural (HMF), to levulinic acid (LevA) [22-25]. Levulinic acid is considered a “Top 10” biobased platform chemical and several approaches to its chemical transformation can be found in the literature [26]. Although several catalysts, supports, and solvents have been investigated for the hydrogenation of levulinic acid, many researchers agree that ruthenium is the most effective noble metal catalyst for its aqueous phase hydrogenation [27-32].

The extensive range of reaction conditions, catalyst supports, and catalyst location (heterogeneous vs. homogeneous) make a direct comparison challenging, but most literature either directly or indirectly cites mass of gamma-valerolactone produced per unit of time per mass of catalyst. This value is usually termed catalytic rate or sometimes described as catalytic ‘productivity’ and ranges from the order of one to about one thousand depending on the system. However, two of the short-comings of describing the catalytic rate in this manner include the use of catalyst mass rather than available catalyst or number of catalytic sites, and the lack of normalizing for temperature and pressure. Nevertheless, it does allow a first approximation to comparing the various catalytic systems.

To facilitate comparison of this membrane reactor work to a more traditional reactor system, the discussion section will make frequent mention and comparison to the work of

Abdelrahman, Heyden, and Bond [27]. These authors provided extensive work on reaction kinetics for the aqueous-phase hydrogenation of levulinic acid to gamma-valerolactone in a packed bed reactor (PBR) utilizing ruthenium on carbon support. The reason for making such a comparison is to highlight the benefits of the membrane reactor in terms of hydrogen delivery and availability to the catalyst, when temperature and catalyst mass are kept the same in both cases. It is noted that in the following sections any reference to PBR data or calculations is directly referring to the aforementioned work of Abdelrahman, Heyden, and Bond [27]. Another reference is available in the literature that used a packed bed reactor with Ru/C for the aqueous phase hydrogenation of levulinic acid [37]. However, less data over the temperature and pressure ranges used in our work was presented, and they actually reported slightly lower catalytic rates for GVL production than that of [27] under the same conditions. The focus of our work was to demonstrate that a phase-contacting membrane reactor can produce higher hydrogenation rates than traditional three-phase reactors in a low pressure range (0.7 to 5.6 bar) where the traditional reactors suffer from limited hydrogen availability or hydrogen starvation. This effect of hydrogen starvation actually becomes more pronounced as temperature is increased in traditional reactor systems, because the liquid phase solubility of hydrogen decreases. Whereas, conversely, the phase-contacting membrane reactor bypasses this limitation by directly supplying hydrogen from the gas phase to the catalytic sites thus offering greater benefit at higher temperatures.

2.3. Materials and methods

2.3.1. Materials

Tetratex expanded polytetrafluoroethylene (ePTFE) membrane material was purchased from Donaldson Company with 0.05 μm nominal pore size and 25 μm thickness. Matrimid 5218 powder was purchased from Huntsman Advanced Materials and used as received. All water used

was HPLC grade purchased from Fisher Scientific. Levulinic acid (98 +%), gamma-valerolactone (98 %), and RuCl₃ (anhydrous, 99 +%) were purchased from Acros Organics.

2.3.2. Catalytic membrane preparation

The ePTFE membrane was either used as received (unmodified) or modified with a thin spin-coated layer of Matrimid polyimide polymer. Solutions of Matrimid dissolved in dichloromethane (DCM) of compositions 0.20, 0.60, and 1.80 wt% were applied via spin-coating (750 rpm/s, 2500 rpm, 60 s) to one surface of respective ePTFE membranes. A 0.1 M solution of RuCl₃ in ethanol (0.2 g RuCl₃, 10 mL ethanol) was sonicated for 24 h. 100 μL of this solution was dropwise applied to the surface of a 13.8 cm² section of the unmodified or Matrimid modified ePTFE membrane. The ethanol was allowed to evaporate and the metal salt was reduced by placing the coated membrane under flowing hydrogen at 150 °C for two hours before use in the membrane reactor system. Reduction of ruthenium to a zero oxidation state was confirmed with XRD analysis.

2.3.3. TEM and SEM sample preparation and imaging

TEM imaging was performed on catalyst particles deposited on a copper grid supported Matrimid thin film. The Matrimid thin film was formed by dispensing a droplet of 0.2 wt% solution of Matrimid in DCM onto a surface of water. The thin film immediately precipitated and the copper grid was gently dipped into the water and raised underneath the film resting on the surface of the water. The deposited film was allowed to air dry for two hours and then approximately 5μL of the RuCl₃ in ethanol solution was deposited onto the film. The ethanol was allowed to evaporate and the RuCl₃ coated film/grid was placed in a flowing stream of hydrogen at 150°C for two hours. TEM was performed on a CM-100 microscope with a 100kV electron beam.

SEM samples were prepared by sputter coating the catalyst loaded ePTFE membranes with palladium. SEM imaging and EDS analysis was performed using a Hitachi S-3500N microscope equipped with an Oxford EDS detector using an electron beam in the 5 to 15kV range.

2.3.4. Reactor process

The three-phase membrane reactor process used in this study is shown below in Figure 2-1. The system is entirely comprised of stainless steel with appropriate Swagelok and NPT fittings. The liquid phase portion is 1/4" tubing with a 40 mL liquid reservoir (not shown) giving a total liquid capacity of 60 mL. The pump is a lab scale Micropump gear pump operating at about 400 mL/min. The membrane housing is a stainless steel membrane holder accommodating membranes with area = 13.8 cm² purchased from Millipore and modified to accommodate simultaneous and continuous liquid and gas cross-flows on each surface of the membrane, respectively. The gas phase stream is controlled by a low-flow metering valve allowing desired flow rate and gas pressure to be achieved. The membrane reactor system can be considered to operate under differential conditions as under our highest reported reaction rate the system achieves 0.0065 % molar conversion per pass of one reactor volume over the membrane.

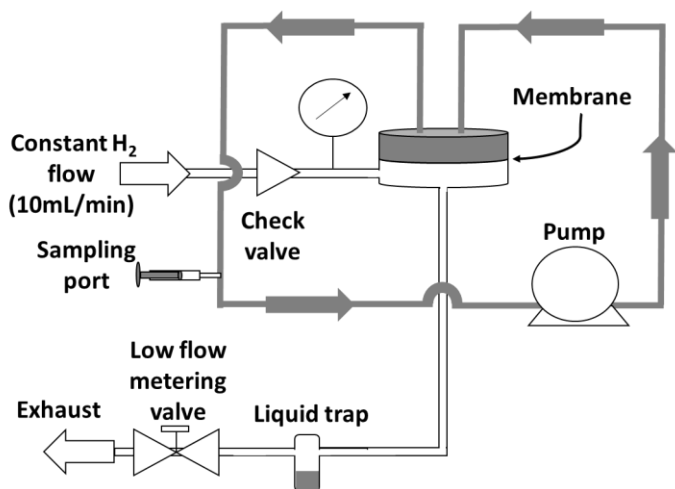


Figure 2-1 - Membrane reactor process schematic. Shaded areas indicate liquid phase while white areas indicate gas phase.

2.3.5. Levulinic acid hydrogenation

All hydrogenation experiments were performed with a 3 wt% solution of levulinic acid in water. The hydrogen reduced membrane was placed in the membrane holder and the liquid phase portion of the system was filled with 60 mL of the 3 wt% levulinic acid solution. The circulation pump was turned on and the system heated to the desired temperature. When the experimental temperature was reached a sample was taken and declared to be time $t=0$. At $t=0$ hydrogen cross-flow was initiated and set to the desired pressure.

In a typical hydrogenation experiment 0.2 mL liquid samples were taken at regular time intervals from the sampling port indicated above in Figure 2-1. Liquid samples from the ‘permeate’ gas phase cold trap were taken at regular but generally longer time intervals depending on the rate of liquid accumulation. Samples were analyzed using standard gas chromatography methods with a GC/MS (Agilent 7890A GC, Agilent 5975C VL mass spectrometer, DB-Wax column (30 m, 0.25 μm), He carrier gas, 4 min hold at 40 $^{\circ}\text{C}$, 20 $^{\circ}\text{C}/\text{min}$ temperature ramp to 240 $^{\circ}\text{C}$, 4 min hold at 240 $^{\circ}\text{C}$). Chemical identities were confirmed with mass spectra and purchased pure standards.

2.4. Results and discussion

2.4.1. Membrane characterization

2.4.1.1. Gas transport

Hydrogen and nitrogen gas permeances were measured for the unmodified ePTFE membrane, ruthenium coated, and Matrimid modified membranes in a constant pressure flux measurement apparatus, and the results are shown in Table 2-1. Not surprisingly, the unmodified porous ePTFE exhibited the highest flux. Adding successively higher amounts of Matrimid decreased the fluxes of both gases proportionally, as was also the case when adding ruthenium to

the membrane. The selectivity for hydrogen over nitrogen did not appreciably change for any of the membrane modifications and indicates a Knudsen flow regime in all cases.

Table 2-1 - Gas transport properties at 25 °C

	N₂ Permeance (GPU*)	H₂ Permeance (GPU*)	H₂/N₂ Selectivity
PTFE, unmodified	227000	754000	3.3
PTFE, Ru coated	183000	712000	3.9
0.20wt% Matrimid	200000	675000	3.4
0.60wt% Matrimid	169000	583000	3.4
1.80wt% Matrimid	41000	144000	3.5

*GPU defined as $1 \text{ GPU} = \frac{1 \times 10^{-6} \text{ cm}^3 \text{ (STP)}}{\text{cm}^2 \text{ s cmHg}}$

2.4.1.2. Water transport

The flux of liquid water from a cross-flow with zero hydrostatic pressure differential through an unmodified ePTFE membrane was measured using the reactor system shown in Figure 2-1. To better simulate reactor conditions a 1.4 bar permeate cross-flow of nitrogen at 10 mL/min was used on the gas phase side of the membrane to collect the permeating water. The 1.4 bar nitrogen stream easily penetrated the membrane and became a head pressure in the system, thus maintaining the zero hydrostatic pressure differential. The water permeate was collected over a 12 h period, and the average flux is indicated in Figure 2-2. Although not necessarily detrimental to the intended membrane reactor function, it is important to consider the loss of water from the liquid phase retentate when making calculations concerning the concentrations of reactant and products. In this work it is assumed that the permeation of hydrogen substantially increases with temperature, alongside that of water, so a high availability of hydrogen is still maintained at the catalyst interface despite the increased counter-flow of water.

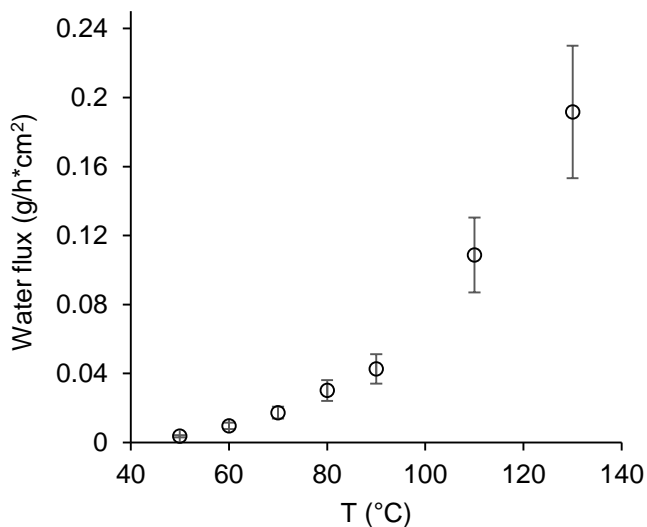


Figure 2-2 - Water flux through ePTFE membrane ($A = 13.8 \text{ cm}^2$) as a function of temperature. A 1.4 bar nitrogen cross-flow at a rate of 10 mL/min was applied to the permeate side of the membrane to facilitate permeate collection.

An attempt to increase surface area, or available area for catalyst deposition, on the liquid phase side of the membrane was made by spin-coating a dilute solution of Matrimid in DCM onto the ePTFE membrane. Matrimid polymer was chosen for this because of its thermostability, chemical inertness, and maintained mechanical rigidity in the range of reaction conditions studied. As shown in Figure 2-3, a modest decline in water flux was observed as the weight percent of the coating solution of Matrimid was increased. It is noted, though, that in the case of the 1.80 wt% Matrimid solution coating, the water flux declined by a factor of about 1.2, whereas both nitrogen and hydrogen flux decreased by a factor of about 4. There are a few possible causes for a decline in flux of both the gases and water, such as a ‘plugging’ of some of the available pores, a narrowing of the average pore diameter, or some combination of both. As described in Section 2.4.2.3, the additional polymer coating actually caused a decrease in the catalytic activity of the membrane reactor, so a thorough evaluation and discussion on the reasons for flux decline is not warranted at this time.

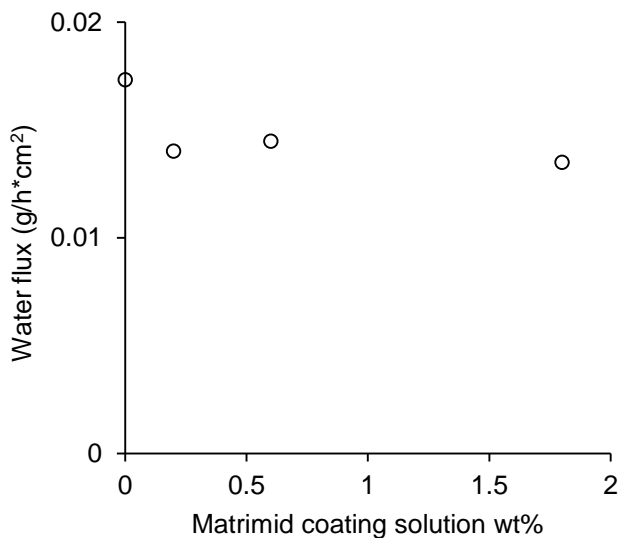


Figure 2-3 - Water flux through Matrimid modified ePTFE membrane ($A = 13.8 \text{ cm}^2$) as a function of Matrimid coating. There is a modest water flux decline as the Matrimid coating increases. All indicated fluxes were collected at $70 \text{ }^\circ\text{C}$ with a 1.3 bar gas cross-flow at 10 mL/min.

2.4.1.3. Membrane morphology and catalyst characterization

Unmodified and ruthenium coated expanded polytetrafluoroethylene (ePTFE) membranes were imaged using scanning electron microscopy and web-like fibers typical to ePTFE membranes were observed [79]. Membranes used in the reactor system were imaged and no apparent morphological changes compared to the unused membranes could be discerned. Energy dispersive x-ray spectroscopy (EDS) confirmed the presence of ruthenium on the top and bottom membrane surfaces. EDS is considered to give bulk elemental compositional information with the x-ray generation volume depending on the electron beam energy and with what elements the electrons interact [80]. EDS mapping was performed with a 15keV electron beam, and considering the carbon and fluorine composition of PTFE and the porous nature of the membrane, the x-ray generation volume is expected to be several μm in depth normal to the membrane surface. The PTFE membrane is $25 \mu\text{m}$ thick, so the EDS information is considered to represent the bulk composition. The atomic percent composition was determined to be 63.0, 36.2, and 0.82% for

carbon, fluorine, and ruthenium, respectively. This calculates to be a ruthenium loading of $64 \mu\text{g}$ per cm^2 of membrane area, or approximately $880 \mu\text{g}$ total Ru loading for the 13.8 cm^2 PTFE membrane.

Evaporating 1 mL of catalyst solution and measuring the mass with a gravimetric balance yielded 7.3 mg of Ru, which corresponds to a loading of $59 \mu\text{g}/\text{cm}^2$. Evaporating $100 \mu\text{L}$ of catalyst solution onto a quartz crystal and measuring the mass with a quartz crystal microbalance yielded a total ruthenium mass of $703 \mu\text{g}$, which corresponds to a loading of $56 \mu\text{g}/\text{cm}^2$. A membrane with an area five times that of the 13.8 cm^2 with five times the Ru coating solution was prepared to allow approximation of the Ru loading by measuring with a mass balance with 0.1 mg accuracy. This method yielded a loading of approximately $90 \mu\text{g}/\text{cm}^2$. The distribution of Ru particles throughout the membrane cross-section is expected to be uniform considering the catalyst coating method involved soaking the entire membrane in catalyst solution. The four independent methods of measuring the catalyst mass gave loadings of 64 , 59 , 56 , and $90 \mu\text{g}/\text{cm}^2$, so an average of $67 \pm 13 \mu\text{g}/\text{cm}^2$, or $930 \mu\text{g}$ total Ru for one membrane, was used for all of the rate calculations in this work for the obtained membrane reactor data and the calculated PBR rates.

TEM imaging was performed on catalyst particles deposited on a copper grid supported Matrimid thin film. The Ru particle size was determined to be $2.7 \pm 0.8 \text{ nm}$. The particle size reported in [27] was 3.6 nm for Ru/C. Considering the approximate surface areas, a particle size of 2 nm compared to 3.6 nm indicates a nearly twofold higher number of surface atoms for an equal total mass. This observation at least partially explains the 3-4 higher catalytic rates observed for the membrane reactor system compared to the PBR under equivalent reaction conditions and is more fully discussed in Section 2.4.2.1.

2.4.2. Catalytic activity

2.4.2.1. Effect of pressure

The effect of hydrogen pressure on catalytic rate was measured at 0.07, 0.175, 0.35, 0.7, 1.4, 2.8, and 5.6 bar in the ‘permeate’ gas phase stream. The 0.05 μm pore size of the ePTFE membrane allowed the hydrogen gas to easily permeate into the head space of the reactor system on the liquid phase retentate side of the membrane, thus always maintaining a zero hydrostatic pressure differential across the membrane. The vapor pressure of water did exert some additional pressure in the retentate, however at 70 °C the vapor pressure of water is about 0.3 bar. Considering the ranges of the pressure gauges used in the system and the oscillatory vibration of the circulatory pump, this pressure difference was difficult to discern. In fact, a slightly higher pressure on the retentate side of the membrane is beneficial for this system as the permeate side is mechanically supported by a stainless steel screen across the entire membrane area, whereas the retentate side is only secured at the perimeter with a Viton o-ring.

The experimental runs shown in Figure 2-4 were all conducted with the same ruthenium coated membrane (no Matrimid addition) in a continuous manner without exposing the membrane to air beginning at 0.7 bar hydrogen pressure and progressively increasing in step every approximately 24 hours to the indicated pressures. The final experiment was to return the hydrogen pressure in step to 0.7 bar. This allowed examination of catalytic activity over the course of the successive experiments. Within experimental error the first and last experiments at 0.7 bar had identical rates indicating catalyst stability.

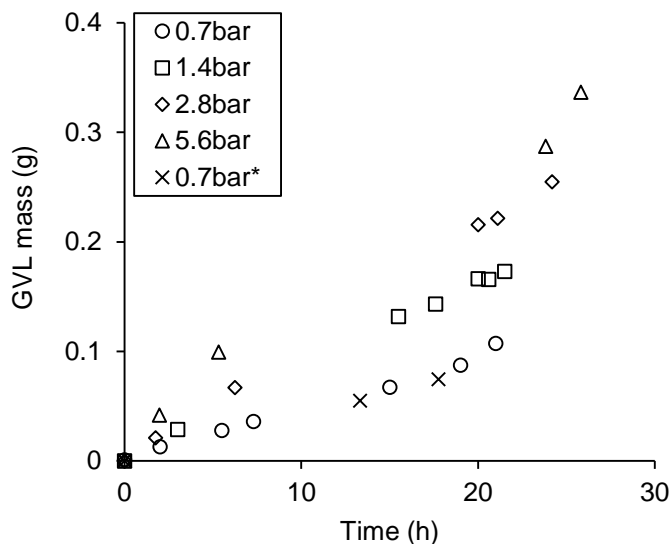


Figure 2-4 - GVL production at cross-flow hydrogen pressures ranging from 0.7 to 5.6 bar. Reaction conditions: temperature = 60 °C, 930 μ g Ru, 60 mL of 3 wt% LevA in water. One membrane was utilized for all of the above experiments and each pressure was tested in increasing succession from 0.7 to 5.6 bar and then returned to 0.7 bar for the final ~20 h of experimentation to demonstrate continued catalytic activity. The (x) data points indicate the repeated 0.7 bar experiment.

Figure 2-5 displays the calculated linear best fit rate for GVL production in the membrane reactor alongside the calculated PBR [27] rates at the same catalytic conditions (temperature, ruthenium mass). Figure 2-5 presents additional rate data for hydrogen pressures 0.07, 0.175, and 0.35 bar. These experimental runs were performed using similarly prepared membranes, but not in a continuous manner as described for the data in Figure 2-4. Hydrogen pressures of 0.07 and 0.175 bar were obtained by using a diluted stream (5 % H₂ in N₂) to obtain the desired partial pressure of H₂. It must be noted that the PBR kinetics in [27] were determined over a hydrogen pressure range from 4 to 40 bar, so the calculated PBR data shown below 4 bar is an extrapolation of the model. There is a clearly greater rate for the membrane reactor over the indicated pressure range. In [27] the authors determined the PBR reaction kinetics were established under conditions absent of mass-transfer limitations for hydrogen pressures greater than 4 bar, and using an empirically derived power-law kinetic expression ($r = k[H_2]^n$) they determined the reaction order

(n) to be 0.6 with respect to hydrogen. Assuming a similar kinetic expression for the membrane reactor, the reaction order with respect to hydrogen calculates to be 0.4 over the pressure range from 0 to 5.6 bar. The membrane reactor results are in relative agreement with the referenced PBR results and support a half-order hydrogen dependency as suggested by [27] and fractional orders reported by others investigating low temperature noble metal catalyzed liquid phase hydrogenation [81,82].

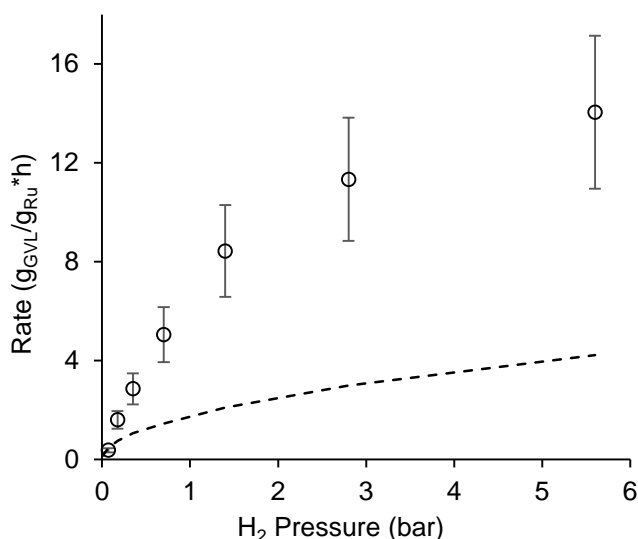


Figure 2-5 - GVL rate of production as a function of hydrogen pressure. PBR calculated rate data shown for comparison. Reaction conditions same as those in Figure 2-4. MR (○), PBR (- - -). Error bars calculated using error propagation in membrane reactor measurements.

Another method of interpreting the data presented in Figure 2-5 can be achieved by calculating the ratio of the membrane reactor rate to the PBR rate and observing how this ratio varies as a function of pressure, as shown in Figure 2-6. The PBR rate expression was strictly determined in conditions absent of mass-transfer limitations, while it is yet to be determined when hydrogen mass-transfer limitations cease in the membrane reactor system. At first approximation one may assume the mass-transfer limitations become insignificant in the membrane reactor when the rate ratio becomes constant, which appears to be above 0.7 bar. With all other reaction

conditions being equal, including catalyst mass, catalyst dispersion and temperature, a ratio of one would indicate that both reactors are operating with an equivalent resistance to hydrogen transfer. The approximate factor of 3.5 benefit that the membrane reactor displays may be due to a few reasons, improved catalyst dispersion compared to the PBR and/or the that the membrane reactor is operating not strictly in a liquid phase environment. The possibility of increased rate in the membrane reactor due to catalyst dispersion is not fully investigated in this work, but is certainly suggested by the smaller average Ru particle size determined by TEM analysis as discussed in Section 2.4.1.3. In addition, the highly hydrophobic PTFE support likely interacts with the aqueous environment differently than the carbon support in the PBR, so there may be some interaction or protection from deactivation effects caused by the aqueous solvent occurring in the membrane reactor.

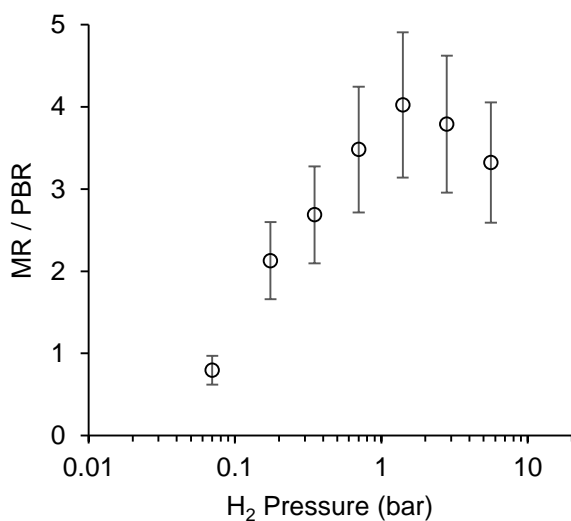


Figure 2-6 - Ratio of membrane reactor rate to calculated packed bed reactor rate, as a function of hydrogen pressure. It is evident that a maximum rate ratio is obtained above 0.7 bar of hydrogen pressure. Error bars calculated using error propagation in membrane reactor measurements.

Alternatively, or possibly in addition to the previously mentioned effects, the active catalytic sites in the membrane reactor may be present in some combination of liquid phase and

gas phase environments. This seems plausible considering the membrane reactor, which is loaded with catalyst particles throughout its entire thickness, is situated between an aqueous liquid phase and a hydrogen gas phase. A control experiment was performed with the PTFE membrane functioning like a PBR where the H₂ was dissolved in the liquid phase that flowed across the catalyst loaded membrane surface, as depicted in Figure 2-6. These results are shown in Figure 2-7. All reaction conditions were identical for the membrane reactor and control experiment. The only difference being the method of H₂ delivery into the system, liquid dissolution (control) versus permeation through the membrane (membrane reactor). The order of magnitude higher rate in the membrane reactor as compared to the control experiment supports the idea that it is not merely a benefit gained from effects related to catalyst dispersion or support composition, but rather that hydrogen delivery from membrane permeation results in a higher catalytic rate compared to the liquid dissolution and diffusion of hydrogen. However, with that said, the dissolution method of hydrogen delivery in the control experiment may have reverted to a mass-transfer limited regime, whereas the membrane permeation method of hydrogen delivery may not be mass-transfer limited under the same reaction conditions.

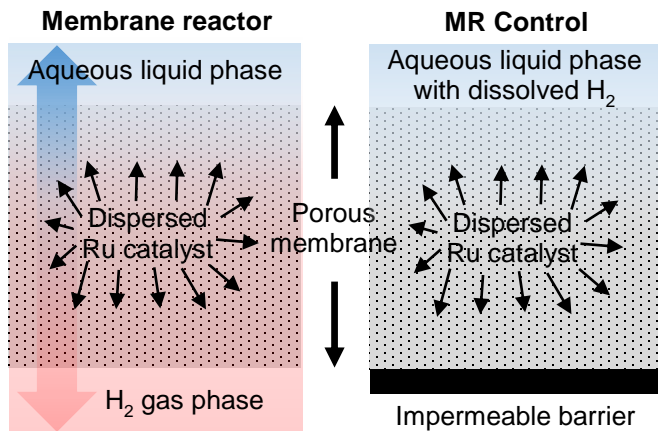


Figure 2-7 - (L) Depiction of porous membrane situated between liquid and gas phases. Shown to visualize how dispersed catalyst particles may be located in some combination of gas and liquid environments. (R) MR (membrane reactor) control experiment performed with H₂ dissolved in liquid phase and circulated over membrane, rather than delivered through the membrane as in typical experiments.

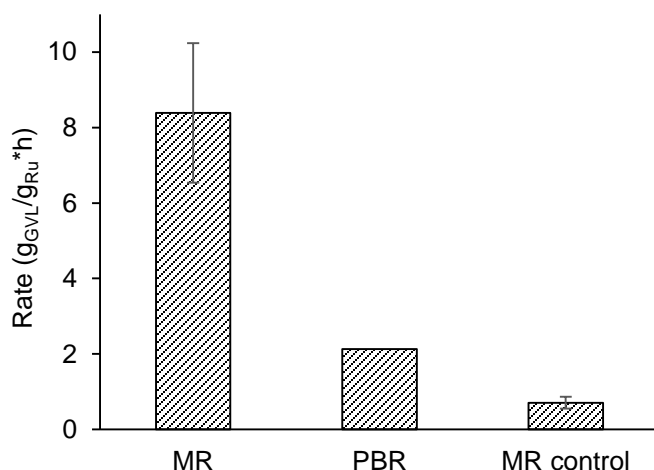


Figure 2-8 - Membrane reactor, PBR, and membrane reactor control experiment rates. Reaction conditions: temperature = 60 °C, 930 μg Ru, H₂ pressure = 1.4 bar, 60 mL of 3 wt% LevA in water. Error bars calculated using error propagation in membrane reactor measurements.

The control experiment data presented in Figure 2-8 can be used to infer the depth of aqueous phase penetration into the membrane as it flows across the surface, provided a few assumptions are made. A schematic representation of the depth of aqueous phase penetration is shown in Figure 2-9. The assumptions are: (1) the Ru particles are uniformly dispersed throughout

the thickness of the membrane, which is supported by the EDS data and the uniform visual appearance of both sides of the catalyst loaded membrane, (2) the control experiment was conducted under conditions with negligible mass-transfer limitations on reaction rate, which appeared to be the case in the membrane reactor experiment under identical reaction and flow conditions, besides that of hydrogen delivery method, and (3) the approximate factor of two higher dispersion in the membrane reactor catalyst produces a two-fold increase in reaction rate for the same catalyst mass as in the PBR. The control experiment for the membrane reactor had a rate that was 1/3 that of the calculated PBR rate, and accounting for the two-fold increase in reaction rate due to dispersion, implies that 1/6 of the total available catalyst was utilized in the membrane reactor configuration, in other words the aqueous phase only penetrated approximately 4 μm of the available 25 μm membrane thickness. This seems reasonable as only 0.01 $\text{g/h}\cdot\text{cm}^2$ of water permeates through the membrane at 60 °C. If the implication that only 1/6 of the catalyst is actually utilized for reaction is true, then all of the indicated rates in this work should be multiplied by a factor of 6. Although, the corresponding comparison to the PBR calculated rates would remain the same as the catalyst mass used in the calculation would also be decreased by a factor of 6. To avoid over-estimation of reaction rates all indicated membrane reactor and PBR rates in this work are calculated using the entire mass of ruthenium catalyst (930 μg) in the membrane. This implication may be substantiated in future work by changing the catalyst loading method, such that the catalyst particles remain only in the upper 1/6 of the membrane thickness. Alternatively, simply use identical PTFE membranes with different thicknesses and proportionally different amounts of loaded Ru catalyst and determine if the reaction rates remain the same, independent of membrane thickness.

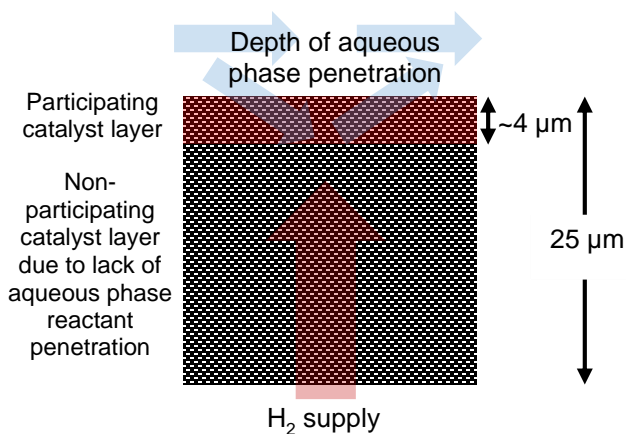


Figure 2-9 - Inferred depth of aqueous phase penetration into porous PTFE membrane reactor approximated by comparing catalytic rate of control experiment and calculated PBR [27].

2.4.2.2. Effect of temperature

The effect of temperature on the rate of GVL production in the membrane reactor was measured over the temperature range of 50 °C to 90 °C. These experiments were performed with four separate ePTFE membranes, but with the same amount of catalyst solution and deposition technique used in all cases. The data presented in Figure 2-10 show the expected trend of increased catalytic activity with increasing temperature, also giving evidence that the membrane reactor is stable over this temperature range. More specifically, the membrane is maintaining its function as a liquid/gas phase contactor without impeding the activity of the catalyst or access of hydrogen and levulinic acid to the catalyst. Often observed in polymeric systems in the presence of water or other organic species is some degree of sorption or swelling [45,56,83]. Also, it has been shown that the presence of metal nanoparticles can increase the swelling behavior of fluoropolymers when exposed to organic species [84]. Although PTFE is known for being highly inert under a variety of chemical and temperature conditions, these mentioned sorption studies at least suggest the possibility of some dynamics in the polymer phase as a function of temperature and chemical environment. These dynamics may in turn have some interaction with the metal catalyst particles.

However, in this work these effects did not appear to have any detriment to catalytic performance over the reported temperature range.

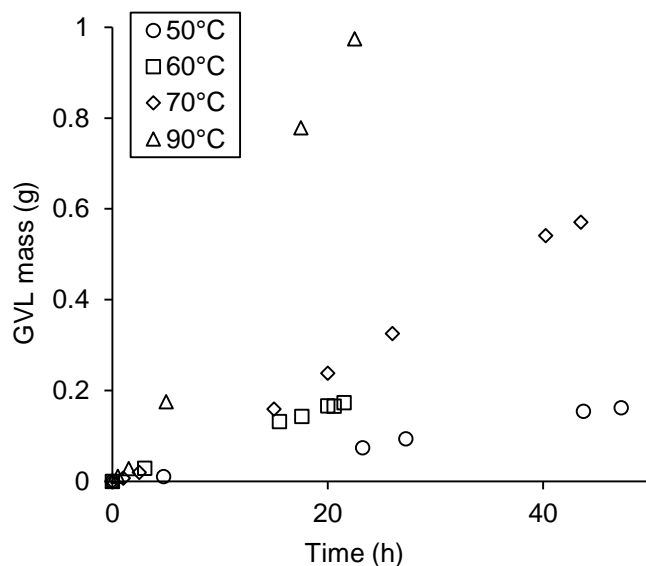


Figure 2-10 - GVL production at temperatures from 50 to 90 °C in membrane reactor. Reaction conditions: hydrogen pressure = 1.4 bar, 930 μ g Ru, 60 mL 3 wt% LevA in water.

Figure 2-11 displays the observed GVL production rates for the membrane reactor and the calculated rates for the PBR. The main cause as to why the benefit of the membrane reactor is greater at higher temperatures is related to the method of transport of hydrogen from the gas phase to the catalytic sites. As discussed in Section 2.4.1.3 the hydrogen permeates through the porous ePTFE membrane and then directly reaches catalytic sites on the membrane surface without the need for dissolution and diffusion in the liquid phase. Considering the solubility of hydrogen in water decreases with increasing temperature and the permeability of hydrogen in the membrane increases with temperature, it is not surprising to see this synergistic effect. To make this effect more apparent, Figure 2-11 displays the ratio of the membrane reactor rate to the PBR rate. There is a clear linear trend for increased catalytic benefit with increasing temperature. Recalling Figure 2-7 and the idea that the local liquid versus gas phase environment to which catalyst particles are exposed depends on their location throughout the thickness of the membrane, it seems plausible to

suggest that the number of catalyst particles experiencing a gas phase environment increases with increasing temperature. This effect may be due to a combination of greater evaporation of water near the gas/membrane interface and higher permeability of the membrane to hydrogen.

The activation energy and pre-exponential factor for this reactive system are calculated from the data shown in Figure 2-12 using the empirical rate equation $r = k[\text{H}_2]^{1/2}$ as described by [27] and an Arrhenius relation for k ($k = Ae^{-E_A/RT}$). The activation energy, E_A , is determined to be 63 kJ/mol and the pre-exponential factor, A , to be $3.8 \times 10^6 \text{ mol}^{0.5} \text{ L}^{0.5} / \text{g}_{\text{Ru}} \text{ h}$. These results are in agreement with those reported for the aqueous phase, Ru/C catalyzed hydrogenation of lactic acid ($E_A = 52 \text{ kJ/mol}$) and propionic acid ($E_A = 64 \text{ kJ/mol}$) [85].

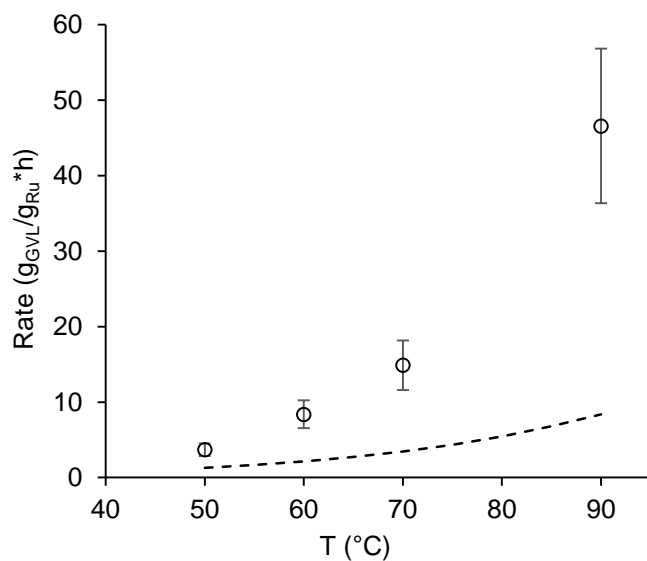


Figure 2-11 - GVL production rates as a function of temperature for membrane reactor (○) and calculated PBR (- - -). Reaction conditions same as those in Figure 2-10. Error bars calculated using error propagation in membrane reactor measurements.

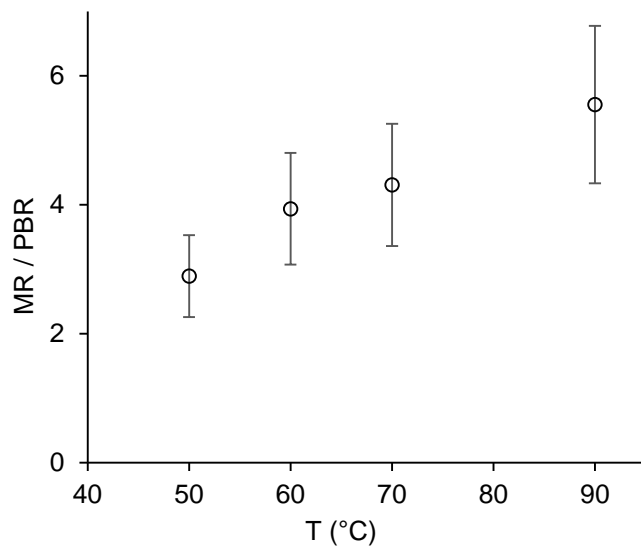


Figure 2-12 - Ratio of membrane reactor GVL hydrogenation rate to calculated packed bed reactor rate, or "catalytic benefit", as a function of temperature. Error bars calculated using error propagation in membrane reactor measurements.

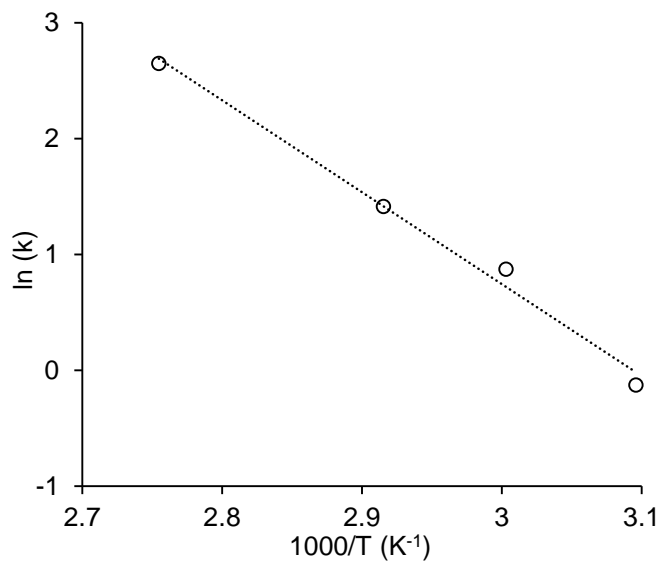


Figure 2-13 - Arrhenius plot of the natural log of the apparent rate constant, k , as a function of $1000/T$ from 50 to 90 °C. k is given in units of $\text{mol}^{0.5} \text{L}^{0.5} / \text{g}_{\text{Ru}} \text{h}$.

2.4.2.3. Additional polymer layer on PTFE membrane surface

The organophilic porous ePTFE was highly sorbing of the RuCl_3 in ethanol solution, thus leaving the ruthenium ions deep inside the membrane pores as the ethanol evaporated. This is not

the ideal location for the catalyst as little to no aqueous solution penetrates the pores to undergo reaction, but rather reacts at the catalyst located near the membrane/liquid interface. The goal was then to apply a thin, yet dispersed polymer layer at that interface to give greater superficial area for catalyst deposition. The polymer chosen for this was Matrimid, a commercially available polyimide with high thermal and chemical stability. Reactor experiments were performed with these modified ePTFE membranes and the catalytic activity is shown in Figure 2-14, and summarized catalytic rates as a function of membrane hydrogen permeances are shown in Figure 2-15. The desired effect of increased catalytic activity was not achieved and actually lessened with increased amounts of Matrimid. This suggests that the superficial Matrimid layer did not produce greater area for catalyst deposition, but actually either completely blocked a fraction of the number of pores or reduced the effective diameter of the pores. This assumedly caused less efficient hydrogen delivery to catalytic sites or impediment of the liquid phase reactants from reaching catalytic sites. It was noticed that no delamination of Matrimid from the PTFE was evident before or after use in the reactor. Although this attempt to better localize catalyst particles near the liquid/membrane interface was not effective, it seems to be a promising area for investigation to improve catalytic efficiency, because much of the catalyst mass in the membrane reactor is not actually utilized for reaction.

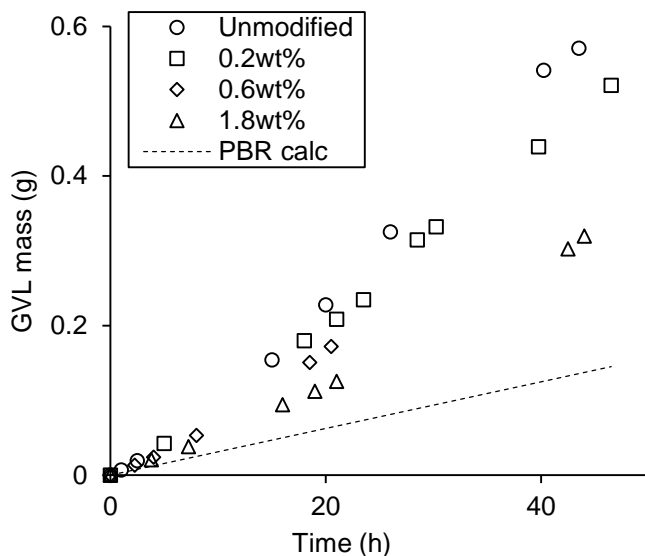


Figure 2-14 - GVL production with additional polymer layer on catalytic surface of ePTFE membrane. Reaction conditions: temperature = 70 °C, hydrogen pressure = 1.4 bar, 930 μ g Ru, 60 mL of 3 wt% LevA in water.

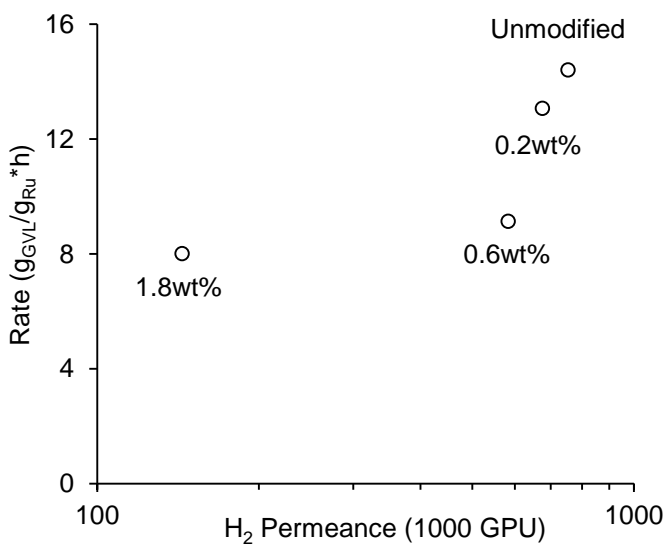


Figure 2-15 - GVL rate of production for each Matrimid modified ePTFE membrane. Data text labels indicate Matrimid coating solution wt%, and unmodified refers to an unmodified ePTFE membrane. All membranes were coated with the same amount of RuCl₃ in ethanol solution, however the depth penetration may be different for each membrane because of the Matrimid surface addition. Reaction conditions same as those in Figure 2-14.

2.4.2.4. Membrane reactor longevity

The reactor was operated for over 200 hours continuously with one membrane to demonstrate the stability and maintained catalytic activity of the membrane reactor. The reaction was conducted at the relatively low temperature of 50 °C and modest hydrogen pressure of 1.4 bar to allow continuous operation without the need for added reactant and solvent to the system. Figure 2-16 shows a constant linear production of GVL in the membrane reactor with no significant decline in rate over 200 hours of continuous operation. The instantaneous rate (dm/dt) was calculated using a second order, centered finite difference approximation with the available GVL mass data points. Further experiments at higher temperatures and hydrogen pressures are required to verify the stability of the membrane reactor over all of the reaction conditions mentioned in this study.

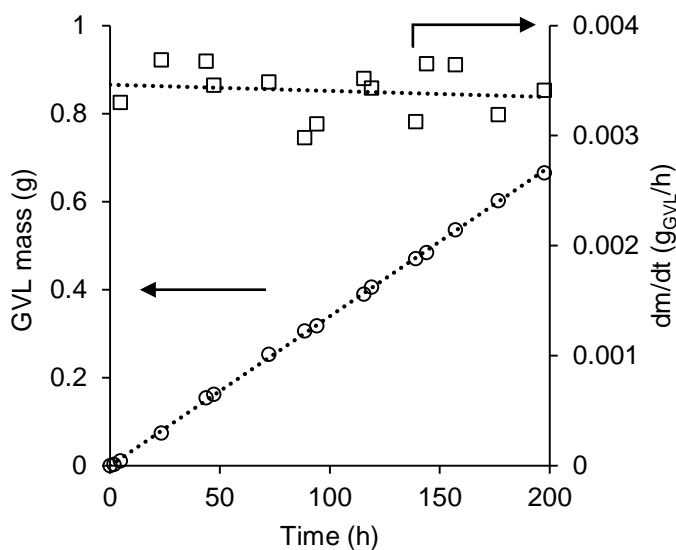


Figure 2-16 - GVL rate of production over extended time period. Reaction conditions: temperature = 50 °C, H₂ pressure = 1.4 bar, Ru mass = 930 μg, ePTFE membrane. The left y-axis shows the GVL mass production as a function of time and the right y-axis shows the calculated instantaneous rate as a function of time. This plot demonstrates the catalytic stability of the membrane reactor and suggests no loss of catalytic activity over 200 hours of continuous operation. (○) indicates GVL mass and (□) indicates the calculated instantaneous reaction rate, dm/dt .

2.4.2.5. Suggested future system improvement

The permeation of significant amounts of water vapor through the PTFE membrane at higher temperatures, as shown in Figure 2-2, limited the ability to perform membrane reactor experiments for extended periods of time at temperatures higher than 90 °C. The primary difficulty was losing significant amounts of the liquid phase retentate over a short period of time, thus prematurely ending the experiment. A proposed method to mitigate or slow the permeation of water from the retentate is to provide water saturated hydrogen gas as the permeate stream. The fully saturated permeate stream should eliminate or greatly lessen the driving force for water vapor permeation across the membrane, and thus allow the liquid phase retentate that contains levulinic acid to continue recirculating across the catalytically active membrane. This could be accomplished experimentally by passing the flowing heated hydrogen stream through a liquid bubbler and either condensing and collecting the stream to account for any levulinic acid or gamma-valerolactone permeation or simply venting the gas stream if the organic permeation is determined to be negligible.

2.5. Conclusions

This work has demonstrated the feasibility of using a porous ePTFE membrane as a gas/liquid phase contactor with integrated noble metal catalyst for the aqueous phase hydrogenation of levulinic acid. This concept could also be extended to the hydrogenation of a variety of water soluble substrates without any modification to the membrane as long as the reaction proceeds at an appreciable rate within the current temperature limits of the membrane reactor. The method of hydrogen delivery to catalytic sites in the membrane reactor is fundamentally different than traditional three-phase reactors in the sense that it is not necessary for the hydrogen to dissolve and diffuse in the liquid phase to reach the catalyst. Instead, the

hydrogen easily permeates through the pores of the membrane reaching the catalyst located at the liquid/membrane interface. The membrane reactor is shown to be more catalytically efficient than a packed bed reactor using published kinetics available for the same metal catalyst on carbon support [27]. Membrane reactor catalytic rates as a function of hydrogen pressure over the range 0.07 to 5.6 bar are presented and shown to be higher than those of a PBR under similar reaction conditions with no mass-transfer limitations. Increasingly greater catalytic benefits can be obtained by operating at higher temperatures, considering the membrane becomes more permeable to hydrogen and avoids the decreasing solubility of hydrogen in water with increasing temperature. The membrane reactor was shown to be stable with no decrease in catalytic activity over 200 h of operation. Future work is to include better utilization of catalyst mass in the membrane by improving localization of catalyst near the liquid/membrane interface rather than dispersed in the entire porous structure of the membrane.

Chapter 3 - Ruthenium Integrated Matrimid Membrane Reactor for the Aqueous Phase Hydrogenation of Levulinic Acid

3.1. Abstract

Membrane reactors offer an alternative approach for conducting three-phase heterogeneous chemical reactions. The membrane acts as a liquid/gas phase contactor, while also serving as the support for a solid catalyst. In our study we utilize an integrally-skinned asymmetric polyimide membrane with ruthenium catalyst coated on the dense surface. A benefit from this approach is circumvention of gas phase dissolution and diffusion in the liquid phase to reach catalytic sites. This method of gas phase mass transfer allows a significant reduction in operating pressure compared to traditional three-phase reactors that often require higher gas pressures due to low gas solubility and diffusivity in the liquid phase. The reaction studied is the aqueous phase hydrogenation of levulinic acid to produce γ -valerolactone. Our work demonstrates the feasibility of applying a polymeric membrane reactor for an aqueous phase hydrogenation reaction and focuses on the impact that membrane hydrogen permeance and catalyst loading have on catalytic activity. In all membrane reactor experiments performed the membrane delivered H_2 produced 3 to 10 times higher reaction rates than a control experiment with H_2 provided only through bulk liquid phase dissolution. We also examine the effect of reversing the membrane configuration, which places the catalyst at the interface of the gaseous hydrogen phase where the membrane then acts as a selective deliverer of the aqueous phase organic substrate to the catalytic sites. Finally, based on our findings we offer potential membrane reactor design improvements and comment on what catalytic rates are achievable.

3.2. Introduction

3.2.1. Polymeric membrane reactors

Catalytic membrane reactors offer an alternative and potentially more efficient method for performing three-phase heterogeneous chemical reactions. The membrane serves as a gas-liquid phase contactor allowing selective transport of the gas into the liquid phase. If a solid catalyst is integrated onto the membrane surface at this interface, the membrane may allow rapid and controllable delivery of the gaseous reactant to the catalytic sites. Traditional three-phase reactors often present mass transfer limitations, namely relatively large diffusional distances to reach catalytic sites exacerbated by low gas solubility in the liquid phase [86]. In three-phase hydrogenation reactions hydrogen availability at the catalytic sites is often the rate limiting step [6]. Membrane reactors can alleviate the inherent mass transfer limitations by directly and abundantly supplying gas to the catalytic sites located on the membrane surface, thus lessening or even bypassing liquid phase dissolution and diffusion [11].

The catalyst phase of the membrane reactor may be integrated onto the surface or distributed/impregnated throughout the entire membrane. The choice of catalyst location depends on the permeability of the membrane to the liquid and gaseous substrates. One may envision a membrane with relatively high permeability to both substrates having the catalyst integrated throughout the thickness of the membrane, and conversely, if only certain substrates are relatively permeable, then the most benefit will be gained by positioning the catalyst at the interface where the impermeable substrate comes into contact with the membrane. This work suggests that this distinction is not absolute depending on reaction conditions (temperature and feed pressure), which impact the relative permeation of reaction solvent, reactant and product.

Examples of hydrogenation reactions performed using membrane reactors can be found in the literature, but there are notable differences in membrane function and catalyst location. In [14,15] the membrane functioned as a catalyst support where the authors sought to control the reaction zone and contact time by dispersing palladium nanoparticles throughout the dense membrane and permeating the gaseous substrate and hydrogen through the membrane. In [16,17,87] the membranes were porous with catalyst coated inside the pores. Hydrogen was dissolved in the liquid phase containing the substrate and the liquid passed through the membrane pores. However, this method of membrane reactor function still required dissolution of hydrogen in the liquid phase. Examples of the membrane distinctly separating the gas and liquid phases where the gas selectively permeates the membrane to reach the catalyst are shown in [18-21,88,89].

In this work we investigate the aqueous phase hydrogenation of levulinic acid to produce γ -valerolactone using an integrally-skinned asymmetric polyimide membrane with integrated ruthenium catalyst on the dense surface of the membrane. Figure 3-1 schematically depicts the configuration and function of the asymmetric membrane acting as the catalyst support and phase-contacter allowing transport of hydrogen directly from the gas phase to catalytic sites. The functionality of our membrane reactor relies on hydrogen gas permeating through the dense layer of the membrane to reach catalytic sites, so our first hypothesis is that increasing the hydrogen permeance of the membrane allows higher reaction rates to be achieved by allowing a more rapid replacement of hydrogen consumed by the reaction. Secondly, it is thought that catalyst loading density ($\mu\text{g}/\text{cm}^2$) should have a significant impact on catalytic activity as not only does it affect the number of active catalytic sites, but also changes the dispersion and proximity of the active sites to the membrane surface. We present catalytic rate data as a function of membrane hydrogen

permeance, as tested with pure hydrogen before use in the reaction, and as a function ruthenium mass loading on the membrane dense surface per unit of membrane area.

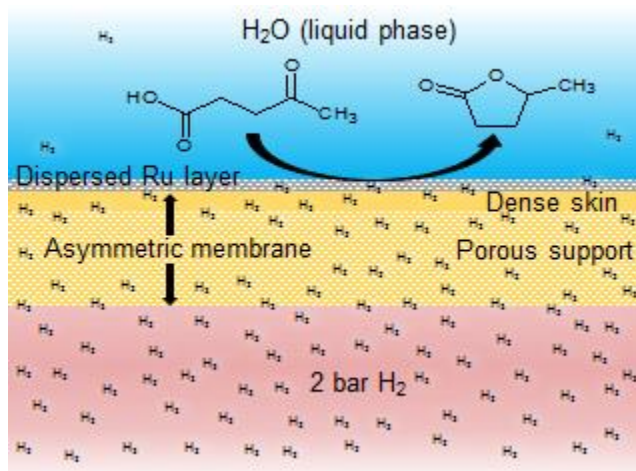


Figure 3-1 - Schematic representation of asymmetric polymeric membrane with dispersed Ru coating on the dense surface used for the aqueous phase hydrogenation of levulinic acid (LevA) to gamma-valerolactone (GVL).

3.2.2. Levulinic acid hydrogenation

The reaction studied in this work was the aqueous-phase hydrogenation of levulinic acid using ruthenium as a catalyst, as shown in Figure 1-5. Levulinic acid is derived from the acid-catalyzed hydrolysis of cellulose proceeding through the reaction pathway of glucose, 5-hydroxymethylfurfural (HMF), to levulinic acid (LevA) [22-25]. We consider the aqueous phase hydrogenation of levulinic acid to γ -valerolactone to be a model reaction for study in our application as reaction rates are appreciable under reaction conditions suitable for the polymeric membrane to maintain stability, namely, water as a reaction solvent, reaction temperatures well below the T_g of Matrimid (320 °C) [90], and >99 % selectivity of the reaction for γ -valerolactone. Although water is documented to have some plasticizing effects in Matrimid [91], our early investigations with alternative organic solvents proved to be far more challenging in terms of maintaining membrane stability. Membrane treatments such as chemical cross-linking and

thermal annealing can be used to improve stability in a wider variety of reaction solvents [73,92,93], but a detailed study of these methods in specific relation to our membrane reactor application is left as future work. Indeed though, we did employ a sub- T_g thermal treatment of the membrane before use in the reaction and are currently investigating the applicability of other liquid solvents for use with a Matrimid based membrane reactor.

3.3. Materials and Methods

3.3.1. Materials

Matrimid 5218 powder was purchased from Huntsman Advanced Materials and used as received. Levulinic acid (LevA) (98+ %), gamma-valerolactone (GVL) (98 %), gamma-butyrolactone (GBL), tetrahydrofuran (THF), and RuCl_3 (anhydrous, 99+ %) were purchased from Acros Organics. HPLC grade water and *n*-butanol were purchased from Fisher Scientific. Ultrahigh purity hydrogen and nitrogen were purchased from Matheson Gas.

3.3.2. Catalytic membrane preparation

Integrally-skinned asymmetric Matrimid membranes were prepared via the phase-inversion method. A 16 wt% solution of Matrimid in THF (38 wt%), GBL (38 wt%), and *n*-butanol (8 wt%) was prepared and allowed to stir overnight. Membranes were cast on a Teflon surface and placed in a water coagulation bath and left overnight. The membranes were then removed and allowed to air dry for 24 h and then placed in a vacuum oven at 60 °C for 24 h. A sub- T_g thermal annealing treatment was performed by situating the membrane sheets in between glass plates and placing them in a vacuum oven at 200 °C for two hours.

Integrating the ruthenium catalyst onto the membrane surface was accomplished using spin-coating techniques. Solutions of RuCl_3 in ethanol were prepared with molarities of 0.025, 0.05, 0.10, and 0.20 M in efforts to produce different catalyst mass loadings on the membranes.

The catalyst solutions were sonicated for 24 h and then 0.20 μm filtered to remove any undissolved large aggregates. A membrane sample was then cut and placed on a small glass sheet with the dense surface facing up and sealed on all edges to prevent catalyst solution intrusion into the porous side of the membrane. The prepared membrane was then spun at 1500 rpm and 100 μL of the catalyst solution was dispensed onto the spinning membrane from 1 cm above the surface. To obtain the most uniform dispersion of the catalyst solution it was crucially important to completely seal the membrane so only the dense surface was exposed and to have a completely smooth and flat dense surface. Any wave or slight elevation in a portion of the membrane would disrupt the centrifugal motion of the coating solution and lead to coalescence of catalyst particles into large and visible aggregates as shown in Figure 3-2. Any membranes with greater than approximately 20 % of their surface exhibiting poor dispersion were not used for reactor experiments. Satisfactorily RuCl_3 coated membranes were reduced in flowing hydrogen at 200 $^\circ\text{C}$ for 2 h. Reduction of ruthenium to a zero oxidation state was confirmed with XRD analysis.

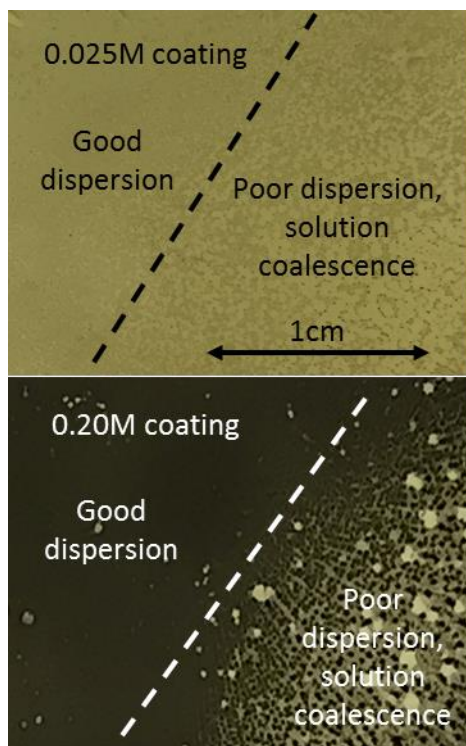


Figure 3-2 - RuCl₃ in ethanol spin-coated Matrimid membranes. Low loading (0.025 M) and high loading (0.20 M) hydrogen reduced membranes are shown with indicated regions of good and poor catalyst dispersion.

3.3.3. Reactor process

Refer to Section 3.4.2 for a detailed description of the reactor process and a schematic representing the system operation given in Figure 2-1.

3.3.4. Levulinic acid hydrogenation

All hydrogenation experiments were performed with a 3 wt% solution of levulinic acid in water. The hydrogen reduced membrane was placed in the membrane holder and the liquid phase portion of the system was filled with 60 mL of the 3 wt% levulinic acid solution. The circulation pump was turned on and the system heated to 120 °C. When the experimental temperature was reached a sample was taken and declared to be time $t=0$. At $t=0$ hydrogen cross-flow was initiated and set to the desired pressure.

See Section 2.3.5 for a detailed description of the sampling procedure and chemical analysis methods used to identify and quantify the chemical species in the reactive system.

3.3.5. SEM and TEM sample preparation and imaging

SEM imaging was performed on Ru coated membrane cross-sections and dense surfaces. Cross-sectional view samples were prepared by immersing membranes in liquid nitrogen and subsequently fracturing. Surface view samples were obtained by simply cutting representative sections from Ru coated membranes. SEM imaging was performed using an FEI Versa 3D Dual Beam microscope.

See Section 2.3.3 for the details regarding TEM sample preparation and imaging. It is noted that the TEM samples were catalyst coated using a drop-coating process as opposed to the spin-coating method used for coating the membranes with catalyst solution. Although it was not possible to replicate the spin-coating process for the Matrimid coated TEM grids, the smallest particle size should be similar in both cases as the low velocity spin-coating should not induce any decrease in particle size.

3.4. Results and Discussion

3.4.1. Membrane and catalyst characterization

3.4.1.1. Membrane morphology and gas transport properties

The morphology of the asymmetric Matrimid membranes used in our membrane reactor application are very similar to those used in more traditional gas separation processes. Figure 3-3 shows the asymmetric structure of the membrane common to those produced using the phase-inversion process where most of the thickness consists of a porous support that transitions to a thin dense layer on one surface of the membrane. In efforts to demonstrate the effect of hydrogen permeance on reaction rate a range of dense layer thickness was sought for the membranes used

in reactor experiments. Figure 3-4 displays the hydrogen permeance for each membrane used and its corresponding selectivity for hydrogen over nitrogen as tested at 35 °C. This data represents a range of dense layer effective thickness of approximately 1.5 to 20 μm assuming a hydrogen permeability of 16 Barrer [94]. The average H_2/N_2 selectivity of membranes used for reactor experiments was 58 with an arbitrary lower cut-off of 35. At 35 °C the ideal H_2/N_2 selectivity is 97 [95], therefore we can reasonably state that the membranes used were close to ‘defect free’ in nature.

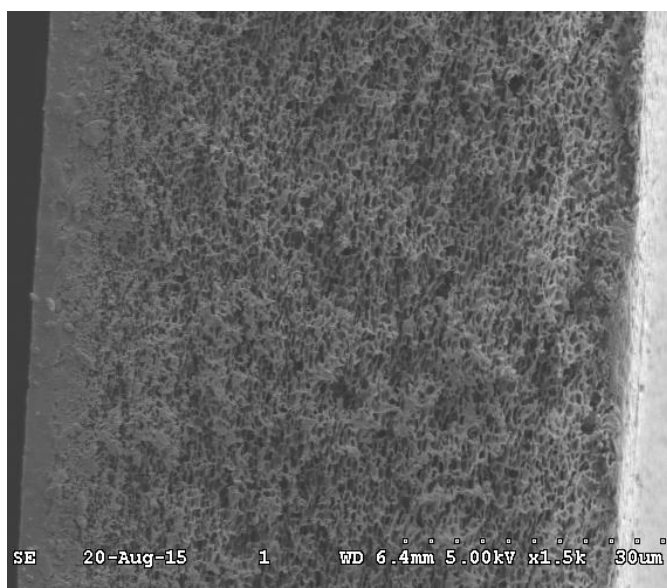


Figure 3-3 - SEM image of asymmetric Matrimid membrane showing a porous support layer approximately 60 μm thick on the right of the image transitioning to a completely dense layer on the left of the image. Not evident is the dispersed Ru layer located on the exterior of the membrane dense surface and calculated to be on the order of 10 nm.

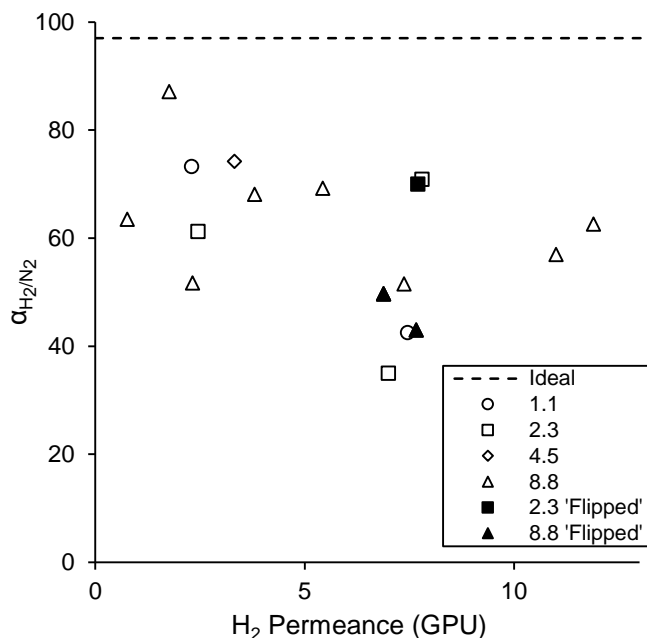


Figure 3-4 - Hydrogen permeance of Ru coated membranes used in hydrogenation reaction experiments. Hydrogen and nitrogen permeances measured at 35 °C. Dashed line indicates ideal selectivity of Matrimid for hydrogen over nitrogen at 35 °C [95]. The legend values refer to the Ru loading in $\mu\text{g}/\text{cm}^2$ and 'Flipped' refers to the flipped configuration experiments described in Section 3.4.2.3.

3.4.1.2. Catalyst loading

Varying catalyst loadings were accomplished by using different concentrations of Ru in ethanol solutions for the spin-coating process, as detailed in Section 3.3.2. The mass loading as a function of molarity produced a very linear relationship with good reproducibility, as shown in Figure 3-5. The measurements for Figure 3-5 were obtained by spin-coating the Ru solution onto a quartz crystal with a thin, adhered Matrimid film layer, so the surface was ideal in terms of flatness (long-range surface height fluctuations) and lack of roughness (short-range surface height fluctuations). The Matrimid membranes in general had the same lack of roughness as the thin film on quartz crystal, but the flatness was not as easily controlled, especially after the membrane began to sorb the ethanol from the catalyst solution during spin-coating. A visual screening process using

the images in Figure 3-6 as reference was used to decide the acceptability of the membranes for further use in reactor experiments.

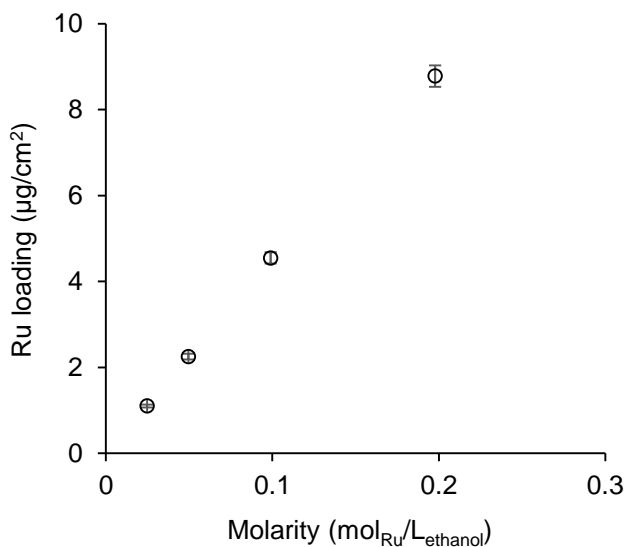


Figure 3-5 - Ru loading as a function of the coating solution molarity measured by quartz crystal microbalance (QCM) using Matrimid coated quartz crystals. Error bar indicates one standard deviation for five independent measurements for each coating solution molarity.

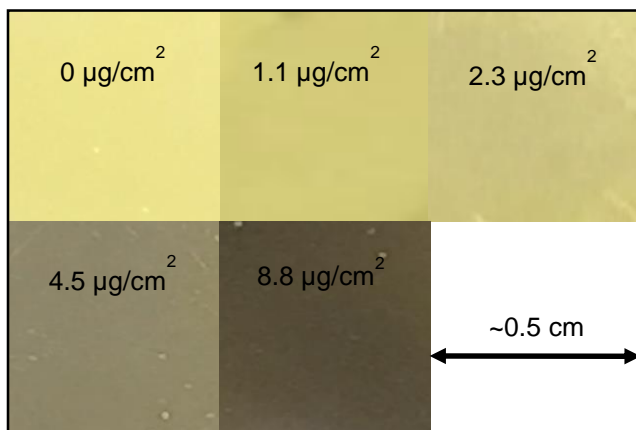


Figure 3-6 - Photographs of Ru (reduced) coated Matrimid membrane surfaces for each loading density. A clear visual difference in the amount of catalyst loaded is apparent. Loading amounts are those determined from QCM analysis.

Figure 3-7 gives Ru loading as determined by energy dispersive x-ray spectroscopy analysis of the spin-coated membrane surfaces. The amount of Ru present on the surface was

determined by taking the ratio of Ru to C and O detected for each sample. At least two sites were analyzed for each loading. The absolute amount of Ru present is not reported for this method due to lack of a precise calibration, therefore the results are normalized to the highest loading amount. The trend is in good agreement with that obtained from the QCM analysis of mass loading on the surface presented in Figure 3-5.

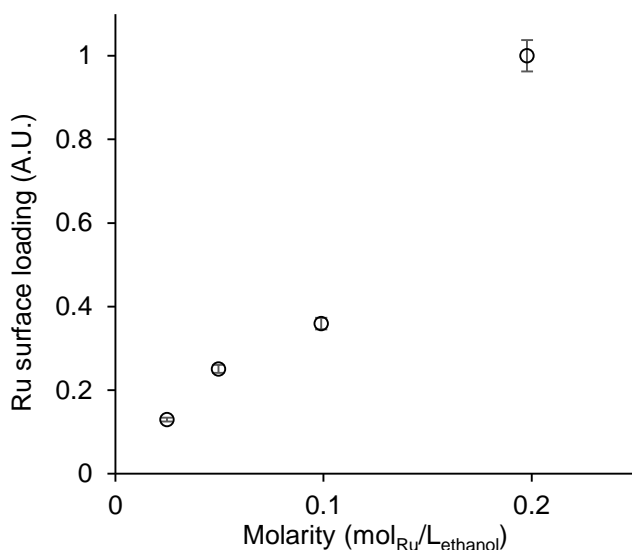


Figure 3-7 - Ru surface loading as determined by energy dispersive x-ray spectroscopy of coated membrane surfaces. The Ru loading was determined from the ratio of Ru to C and O atoms and is therefore given in arbitrary units. Error bars indicate one standard deviation of four independent measurements of the 0.2 mol/L coated surface.

Figure 3-8 displays information about the roughness of the ruthenium coated membrane surfaces. The y-axis indicates the root mean square of the surface height variation as measured by atomic force microscopy. It is evident that the lower ruthenium loadings (1.1, 2.3, and 4.5 $\mu\text{g}/\text{cm}^2$) have a relatively higher roughness of approximate similar magnitude suggesting dispersion of individual catalyst particles or clusters. The roughness for the 8.8 $\mu\text{g}/\text{cm}^2$ loading drops significantly suggesting the formation of a smoother and more continuous catalyst layer, which is also supported by the SEM images in Figure 3-9. It is important to note that the 8.8 $\mu\text{g}/\text{cm}^2$ loading does not produce a completely dense layer of metal, as evidenced by statistically identical

hydrogen and nitrogen gas flux measurements before and after coating. Considering the roughness of the unmodified Matrimid surface is approximately 1 nm and the roughness of the lower ruthenium loadings is approximately 20 nm, one may reason that the ruthenium catalyst particles/aggregates deposited on the surface of the membrane are on the order of 20 nm in size. This is in good agreement with literature results for the preparation of ruthenium nanoparticles by sonication of RuCl_3 in solution, where the authors determined ruthenium particle sizes in the range of 10 to 20 nm [96,97].

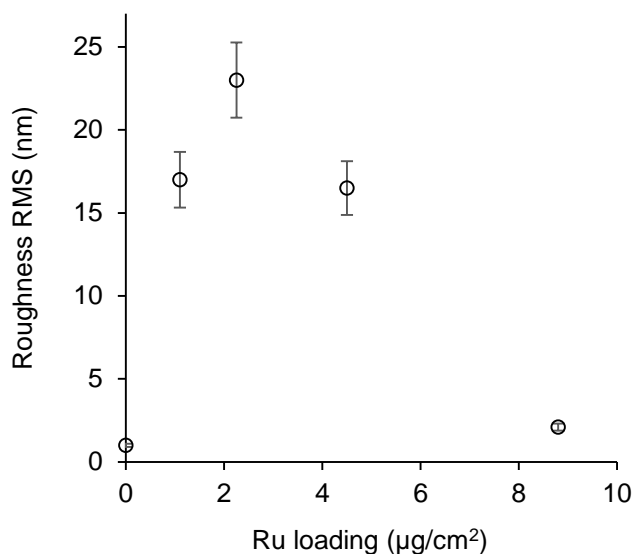


Figure 3-8 - Roughness (RMS) of Ru (reduced) coated Matrimid membrane surface as a function of Ru loading determined by AFM measurements. Error bars represent one standard deviation for seven independent measurements of one sample.

Figure 3-9 shows SEM images of the 4.5 and 8.8 $\mu\text{g}/\text{cm}^2$ loaded membrane surfaces. It is apparent that the 8.8 $\mu\text{g}/\text{cm}^2$ surface is more dense or continuous in comparison to the discontinuous ‘island-like’ features of the 4.5 $\mu\text{g}/\text{cm}^2$ surface, which is in agreement with the AFM determined surface roughness measurement presented in Figure 3-8. Figure 3-10 displays TEM images of Ru coated Matrimid thin films, which exhibit a small particle (~2-3 nm) base layer and larger (10-100 nm) aggregates of particles. The size of the small particles in the base layer is

2.7±0.8 nm. Although the larger particles may contribute to the overall observed catalytic rate, their contribution is expected to be minimal due to a low surface area to volume ratio. With that in mind, if the coating of these larger particles or agglomeration of smaller particles is eliminated, the catalyst mass normalized reaction rates should improve beyond those reported in this chapter. It is also important to note that the TEM samples were prepared by a dip or drop-coating process as opposed to the spin-coating method used for coating the SEM samples and membranes actually used in reactor experiments. Therefore particle agglomeration may be different for each of those coating methods, although it is expected that the small particle base layer is present in both methods as the catalyst solution was the same.

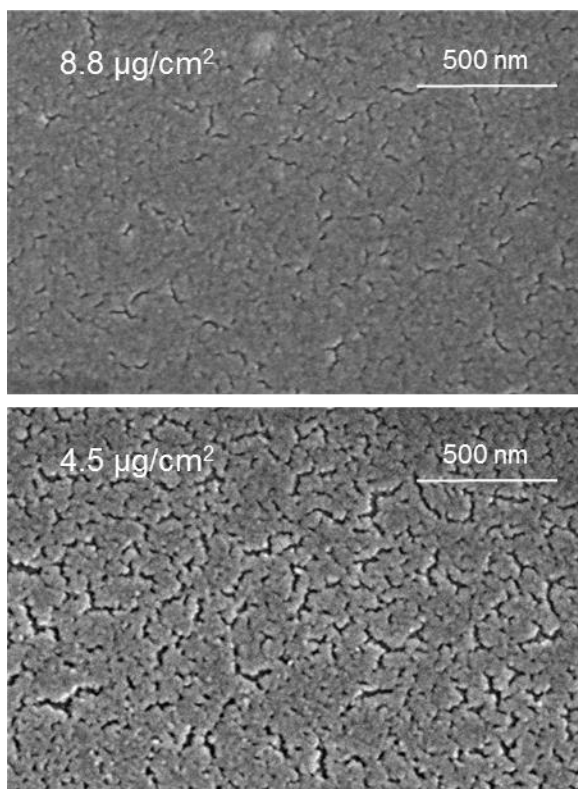


Figure 3-9 - SEM images of 8.8 and 4.5 µg/cm² Ru loaded membrane surfaces. The higher loaded surface displays a more continuous layer of catalyst whereas the lesser loaded surface is more fractured or 'island-like'.

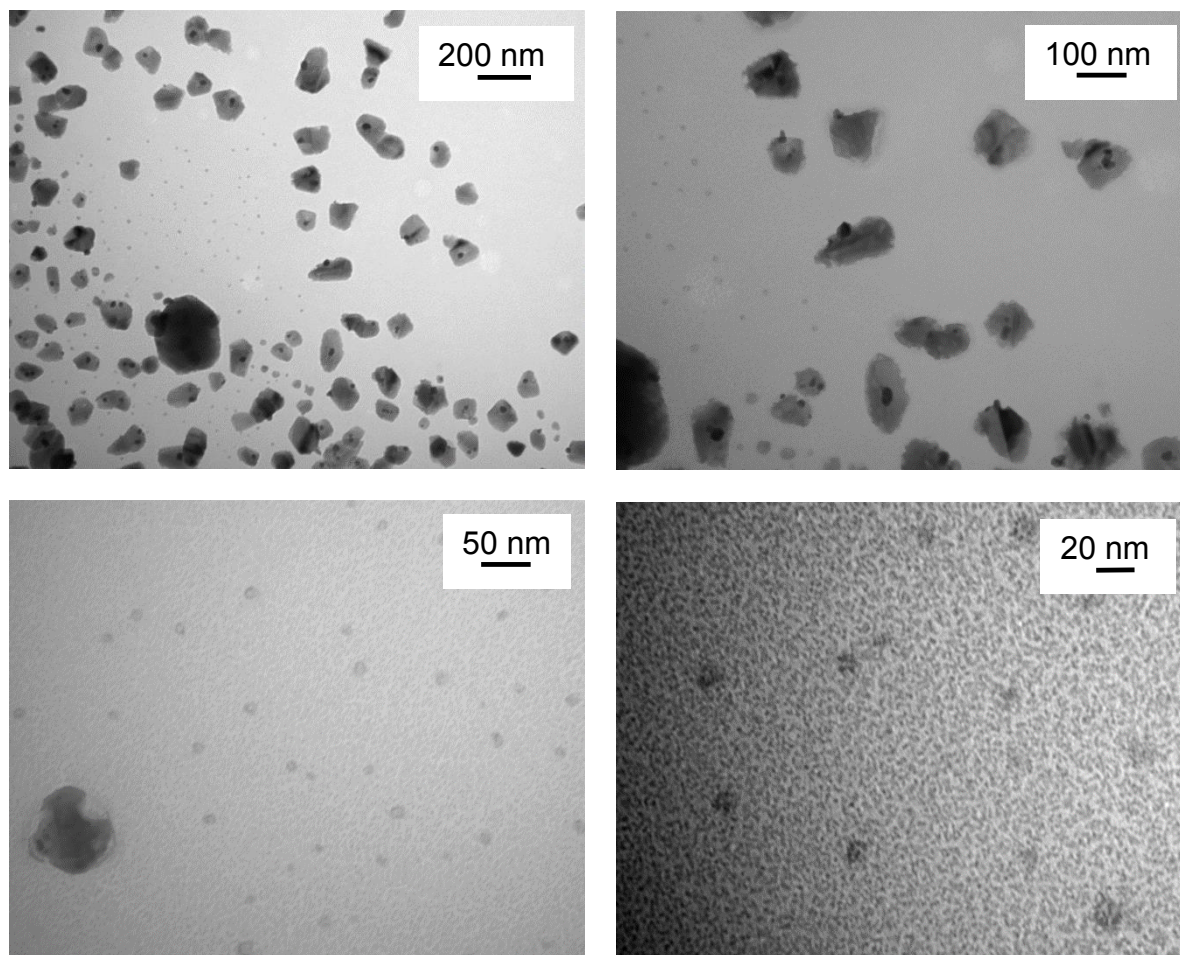


Figure 3-10 - TEM images of Ru coated Matrimid surface. It is apparent that there is a 'base' layer of 2.7 ± 0.8 nm Ru particles with intermediate and larger agglomerates of Ru (10-100 nm) dispersed on the membrane surface.

3.4.2. Reaction results

3.4.2.1. Effect of membrane properties

The fundamental hypothesis of this work is that using a polymeric membrane as an interface between a hydrogen gas phase and a catalyst results in a higher effective concentration of hydrogen at the catalyst surface than compared to a catalyst located in the liquid phase with bulk phase dissolved hydrogen, assuming the same overall pressure in both cases. The primary means in our work of providing evidence for this hypothesis is by measuring the hydrogenation reaction rate. The aqueous phase hydrogenation of levulinic acid to produce gamma-valerolactone

can be considered a model reaction for this study as both species are completely soluble in water and the reaction is greater than 99 % selective for GVL, therefore a higher rate of GVL formation can be considered indicative of greater hydrogen availability at the catalyst, with all other reaction parameters being equal.

Figure 3-11 gives results for the reaction rate as a function of membrane H₂ permeance for each membrane and its corresponding catalyst loading density. In all cases the membrane delivered H₂ exceeded the reaction rate of the control experiment as indicated with a dashed line in Figure 3-11. The control was performed the same as the other experiments except the membrane delivered H₂ was replaced with a N₂ stream as depicted in Figure 3-12. There was still an observable reaction rate, because in all experiments, including the control, the water phase side of the membrane reactor had a headspace that was pressurized with H₂. This was done to eliminate the need for repeated purging of H₂ from the headspace due to permeation through the membrane, the rate of which would have been different for each membrane and consequently influenced the reaction rate differently for each experiment. However, the control experiment did require repeated re-pressurizing of the headspace with H₂ due to its loss through permeation of the membrane. Pressurizing the headspace also helped ensure that a slightly higher overall pressure was maintained on the liquid phase side (due to additional water vapor pressure) assisting in mechanical stability of the membrane during operation.

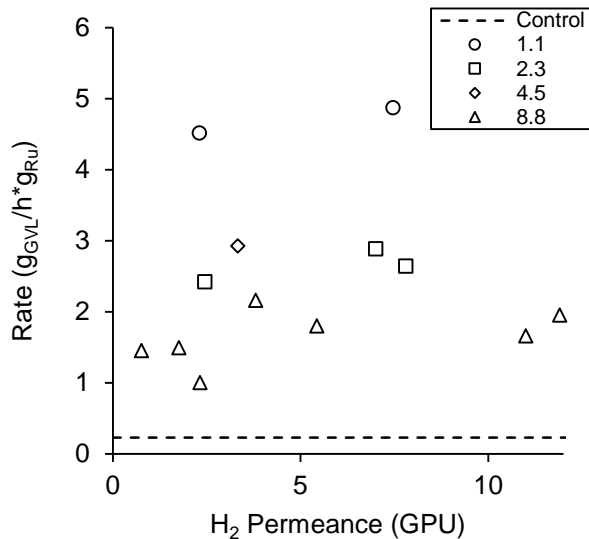


Figure 3-11 - Reaction rate as a function of membrane hydrogen permeance as tested with pure hydrogen at 35 °C before use in the reaction. The legend values refer to the Ru loading for each membrane in μg/cm². Reaction conditions: T = 120 °C and H₂ pressure = 2 bar.

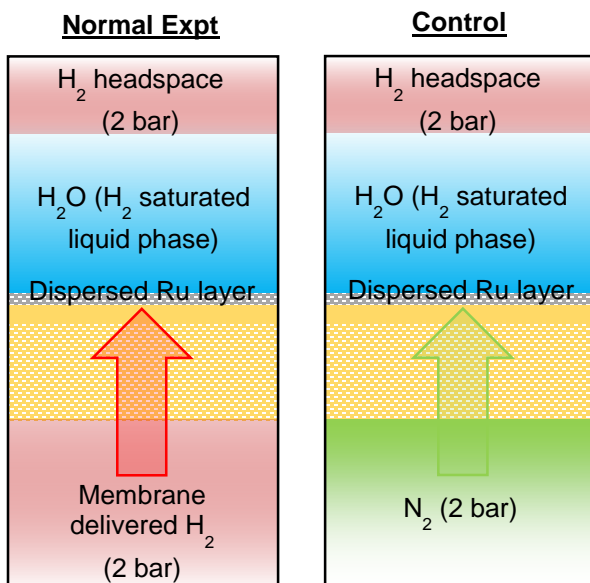


Figure 3-12 - Schematic representation of normal and control experiments. The gas phase permeate stream is N₂ for the control experiment instead of H₂.

The scatter in the data for each catalyst mass loading presented in Figure 3-11 is attributed to each experiment having been conducted with a different membrane and thus different H₂/N₂ selectivity and catalyst coating. Although there is some sample-to-sample variability, clear

patterns are present. First, increasing hydrogen permeance increases reaction rate. Second, decreasing the catalyst loading increases the reaction rate dependency on hydrogen permeance for each catalyst loading, which is presented in Figure 3-13. Third, the reaction rate normalized by catalyst mass was shown to have a clear inverse dependency on Ru catalyst loading, as shown in Figure 3-14. For example, the $1.1 \mu\text{g}/\text{cm}^2$ loading exhibited approximately a factor of 4 higher catalyst mass normalized reaction rate than the $8.8 \mu\text{g}/\text{cm}^2$ loading.

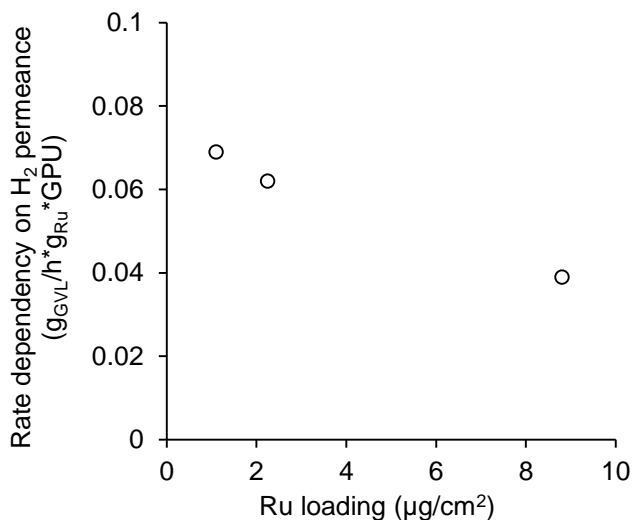


Figure 3-13 - Reaction rate dependency on membrane hydrogen permeance as a function of Ru mass loading. The lower the Ru mass loading, the more efficient the membrane reactor utilizes hydrogen that permeates through the membrane.

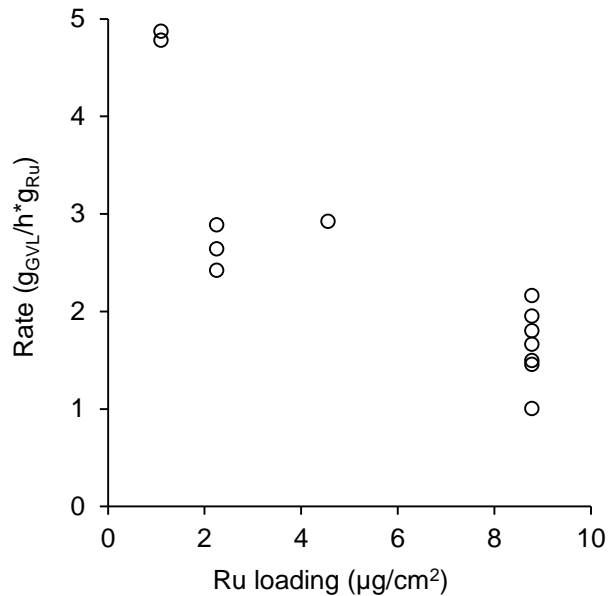


Figure 3-14 - Reaction rate as a function of Ru mass loading on the dense surface layer of the membrane. Although the higher catalyst loading produces more overall GVL, normalizing the reaction rate by the catalyst mass present reveals that lessening the loading improves the efficiency of the system in terms of catalytic rate per unit catalyst mass. Reaction conditions: $T = 120\text{ }^\circ\text{C}$ and H_2 pressure = 2 bar.

There are a few explanations for these observations. First, the lesser catalyst loadings likely have a higher active catalyst site to total catalyst mass ratio arising from better dispersion and lack of forming larger catalyst agglomerates. Second, the membranes with lower loading have a lower active sites to membrane area ratio. Thus more H_2 is delivered per catalyst site. Unfortunately, direct measurement of the catalytic sites using H_2 chemisorption is not possible, because the polymeric membrane support absorbs approximately 100 times the H_2 that would be expected to adsorb on the catalyst surface (see Appendix B for H_2 sorption calculations).

3.4.2.2. Permeate analysis

Matrimid is permeable to all of the chemical species present in our membrane reactor system, namely, water, H_2 , LevA, and GVL, so for one to begin to consider a mass balance, or even carbon balance, the permeate flux and composition should be determined. The mass of water permeating through the membrane is in relative agreement with the permeability of Matrimid for

water vapor at 120 °C reported as approximately 1700 Barrer [94]. The water flux scales accordingly with membrane H₂ permeance, as one would expect. Water flux through each Ru coated Matrimid membrane during operation in the reactor system is given in Appendix B. Under reaction conditions the amount of LevA that permeates relative to the total amount available in the retentate stream that recirculates across the membrane is quite small, *e.g.* approximately 0.01 g over 10 h of operation relative to the 2 g available in the retentate. Even though the flux of LevA is relatively small, the values scale with membrane H₂ permeance and are shown in Figure 3-15. Since the LevA fluxes are quite small, increasing the temperature of the reactor beyond 120 °C is not expected to cause substantial loss of the reactant through permeation.

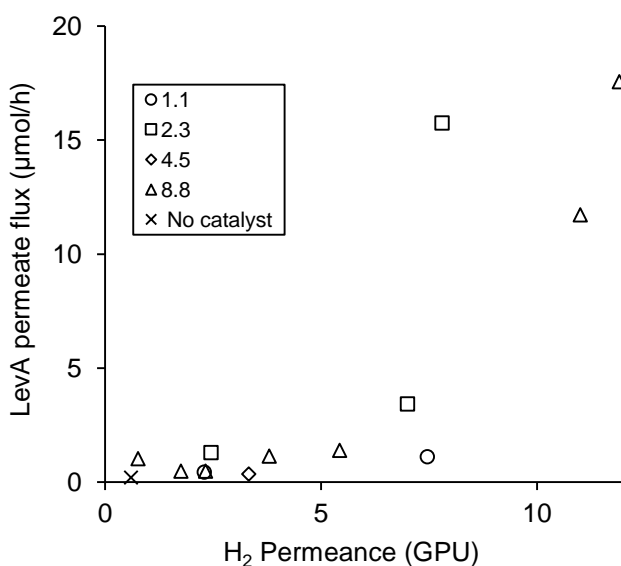


Figure 3-15 - LevA permeate molar flux as a function of membrane H₂ permeance under reaction conditions. The “No catalyst” data point was obtained using a feed concentration of 1 wt% LevA and 0.1 wt% GVL in water with an uncoated dense film with an H₂ permeance of 0.6 GPU.

Gamma-valerolactone permeate flux values are given in Figure 3-16, and also generally scale with membrane H₂ permeance. However, GVL flux through the membrane is substantially higher than that expected if only the bulk liquid phase concentration of GVL in the retentate was considered. The data points indicated with an ‘x’ in Figures 16 and 17 were obtained using an

uncoated thin Matrimid dense film and providing a feed solution consisting of 1 wt% LevA and 0.1 wt% GVL in water. This is approximately two orders of magnitude higher GVL in the retentate than that produced after 10 hours of operation with the most productive membrane reactor experiment given in this study (0.002 wt% GVL). Even with the significantly higher feed composition, the GVL permeate flux is still two orders of magnitude lower compared to the membrane with similar H₂ permeance but coated with catalyst. This evidence suggests that with catalyst present at the membrane surface, GVL formation produces a local concentration that is substantially higher than that in the bulk liquid phase. Thus the observation of relatively higher GVL permeate fluxes for the reactive membranes compared to the uncoated membrane.

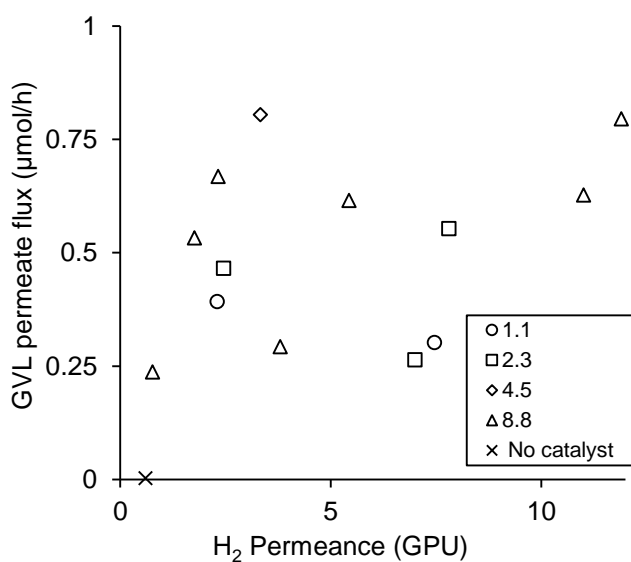


Figure 3-16 - GVL permeate molar flux as a function of membrane H₂ permeance under reaction conditions. The “No catalyst” data point was obtained using a feed concentration of 1 wt% LevA and 0.1 wt% GVL in water with an uncoated dense film with an H₂ permeance of 0.6 GPU.

3.4.2.3. Effect of catalyst location

The selectivity of Matrimid for the reactant (LevA) over the product (GVL) motivated investigation of reversing the role of the membrane as a selective deliverer of H₂ to selective deliverer of LevA. This was accomplished by merely flipping the configuration of the membrane

so that the dense layer with coated catalyst was positioned facing the H₂ gas phase (permeate) and the porous side of the membrane was facing the liquid phase (retentate). Now the catalyst is provided an excess of hydrogen and the reaction rate is clearly limited by the permeation rate of LevA through the membrane. In the ‘flipped’ configuration the reactor is functioning in a single pass mode as compared to the normal configuration where the liquid reactant solution was recirculated across the catalytic surface. Important benefits of this approach include the ability to use even lower hydrogen pressures considering the catalyst is located in the gas phase, and GVL is now only found in the permeate stream, assuming any amount that diffuses through the membrane into the liquid phase is relatively negligible. In an optimized reactor one may even envision a permeate stream that is entirely reacted as it passes by the catalyst layer producing only GVL, thus eliminating any extra separation steps besides that from water.

Figure 3-17 gives reaction rate as a function of gas phase H₂ pressure for the indicated catalyst loadings. Although these experiments are more preliminary and limited in number than the normal membrane configuration experiments, the notable finding was that for both the 0.35 and 2 bar H₂ experiments the reaction rates were nearly identical. This supports the idea that in this configuration the reaction rate is limited by the availability of LevA rather than H₂. Perhaps the simplest remedy for this is to increase LevA permeation by increasing the system temperature. This would also serve to improve the reaction kinetics while still maintaining high H₂ availability due to the catalyst being located in the gas phase. Figure 3-18 shows a comparison of the normal and flipped membrane reactor configurations. Although the results are conflicting for the presented catalyst loadings, it is notable that reaction rates obtained for the flipped configuration were of similar magnitude to the normal configuration rates. This observation serves as motivation

to improve the reactor parameters for the flipped configuration in efforts to work with even lower H₂ pressures while still obtaining favorable reaction rates.

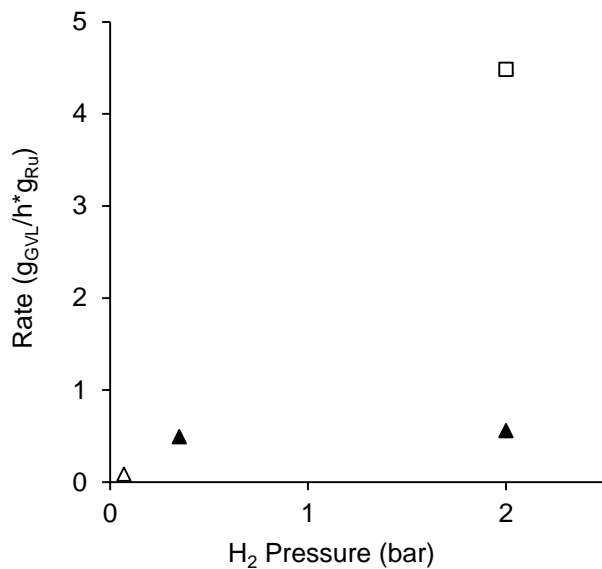


Figure 3-17 - Reaction rate as a function of H₂ pressure for the 'flipped' membrane reactor configuration. Δ indicates a catalyst loading of 8.8 μg/cm² and □ indicates 2.3 μg/cm². The filled symbol ▲ indicates that the same membrane was used for both experiments run in succession for 24 hours each without exposing the membrane to air. The membranes used in this plot had an H₂ permeance of 7 GPU. Reaction temperature was 120 °C.

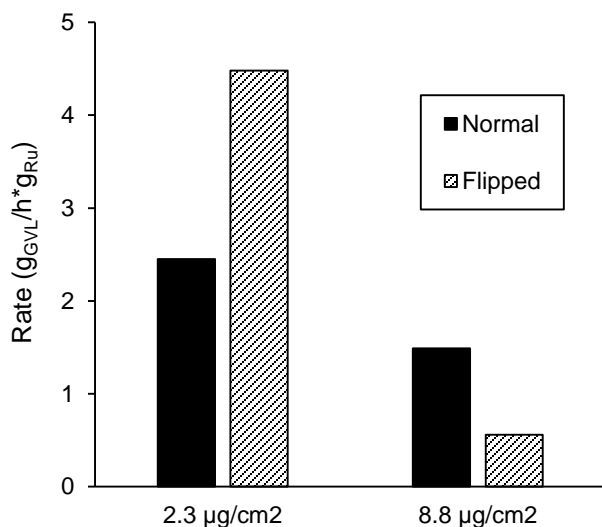


Figure 3-18 - Reaction rate comparison of 'normal' and 'flipped' membrane reactor configurations for low and high catalyst loadings. Experimental conditions: T = 120°C and H₂ pressure = 2 bar.

3.4.2.4. Catalytic improvement and scale-up

The trends reported in Section 3.4.2.1 for the dependency of the reaction rate on membrane H₂ permeance and catalyst loading can be extrapolated to evaluate what potential an optimized membrane reactor may yield in terms of product formation. The ranges of H₂ permeance and catalyst loading investigated spanned only one order of magnitude, respectively. The highest H₂ permeance used was 12 GPU which corresponds to an effective dense layer thickness of 1.5 µm. It is routinely possible to obtain dense layer thicknesses of asymmetric Matrimid membranes about an order of magnitude less [72,98,99], so it seems reasonable to extrapolate the H₂ permeance trend by about an order of magnitude higher. Figure 3-19 displays predicted reaction rates given as g_{GVL}/h for the membrane reactor system as a function of membrane H₂ permeance and Ru loading. It is apparent that increasing the catalyst mass has limiting returns at higher loadings. For all of the catalyst loadings investigated in this work there was no significant impact on the membrane H₂ permeance, but one may assume that at some point the additional catalyst loading

will start to decrease the H₂ permeance of the membrane. It is not yet clear what that loading is, so it seems the more predictable parameter to extrapolate is the H₂ permeance. According to Figure 3-19 one may generalize to say that increasing the H₂ permeance of the membrane by an order of magnitude may give a 2 to 3 factor increase in overall GVL production rate, and increasing the catalyst loading from 1 to 10 μg/cm² may give a 2 to 4 factor increase in GVL production rate depending also on the H₂ permeance.

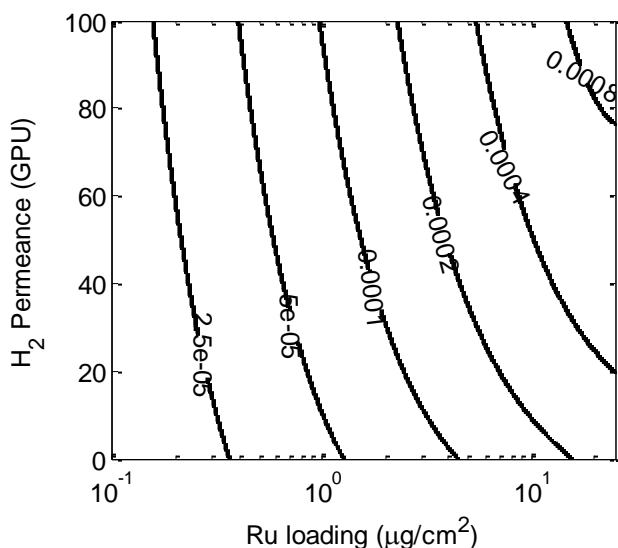


Figure 3-19 - This plot is an extrapolation of observed catalytic trends in terms of membrane H₂ permeance and Ru loading. The trends were determined over experimental ranges of 1 to 12 GPU for H₂ permeance and 1.1 to 8.8 μg/cm² for Ru loading. The contour lines represent GVL production rates in units of g_{GVL}/h.

If one looks at catalyst mass normalized reaction rates as Figure 3-19 displays, one sees that decreasing catalyst loading yields improved reactor efficiency in terms of catalyst mass. The size of catalyst particles has a finite lower limit, and the optimum distribution of catalyst particles must have an upper limit in terms of membrane area utilization. Finding these boundaries is left as future work, however, if it is possible to extrapolate one order of magnitude lower, this gives a hypothetical 2 to 3 factor improvement in normalized rate. Simultaneously increasing the H₂

permeance an order of magnitude would produce an overall 4 to 6 factor improvement in normalized rate. To achieve a higher total GVL mass production with a lower catalyst mass system, one would need only to scale up the membrane area. If a $20 \text{ g}_{\text{GVL}}/\text{h} \cdot \text{g}_{\text{Ru}}$ rate is achievable with a $0.1 \mu\text{g}/\text{cm}^2$ Ru loading, a spiral wound module with 3 m^2 membrane area would require 3 mg Ru and produce 1.5 g GVL per day. A hollow fiber module with 75 m^2 membrane area would require 75 mg Ru and produce 36 g GVL per day [3]. Increasing the Ru loading by a factor of 10 to $1.0 \mu\text{g}/\text{cm}^2$ would give 7.5 and 180 g GVL per day for the spiral wound and hollow fiber modules, respectively.

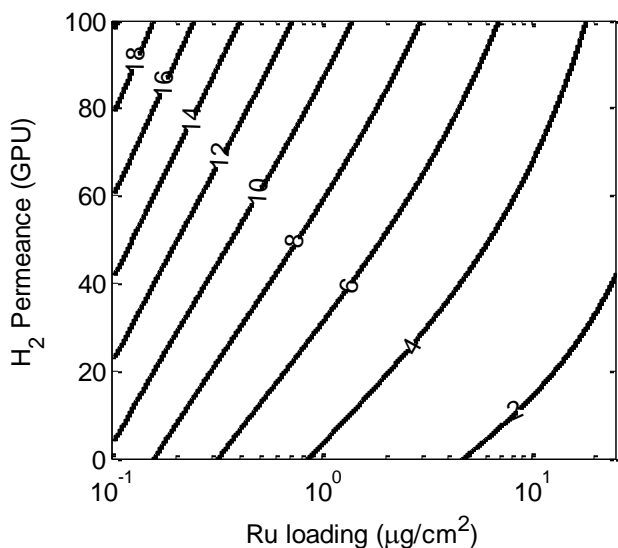


Figure 3-20 - This plot presents the same extrapolated catalytic trends as those shown in Figure 3-19, but here the contour lines represent catalyst mass normalized rates given in units of $\text{g}_{\text{GVL}}/\text{h} \cdot \text{g}_{\text{Ru}}$.

3.5. Conclusions

This work has demonstrated the feasibility of using an asymmetric polymeric membrane with a dispersed layer of ruthenium catalyst on the dense surface of the membrane for the aqueous phase hydrogenation of levulinic acid to gamma-valerolactone. The motivation for using a polymeric membrane as a gas/liquid phase contactor was to allow rapid delivery of H_2 to catalytic

sites located at the liquid/membrane interface. We have shown that membrane delivered H₂ achieves a higher reaction rate than an identical catalytic system under the same reaction conditions (120 °C, 2 bar H₂) but with liquid phase dissolved H₂. The parameters investigated were membrane H₂ permeance ranging from 0.7 to 12 GPU and Ru catalyst loading ranging from 1.1 to 8.8 μg/cm². The impact of membrane H₂ permeance on reaction rate was found to be higher for lower catalyst loadings and over the range of loadings averaged to be an approximate 2% gain in reaction rate per 1 GPU increase in membrane H₂ permeance. Lessening the catalyst loading per membrane area produced a higher catalyst mass normalized reaction rate. An alternative reactor configuration was investigated where the membrane was flipped so the catalyst coated dense membrane layer was exposed to the H₂ phase (permeate) and the porous side of the membrane was exposed to the liquid phase (retentate). This configuration utilized the membrane as a selective deliverer of levulinic acid to catalyst sites as opposed to the original function as a selective deliverer of H₂. This method produced comparable reaction rates to the normal configuration and offered the possibility of using even lower gas phase H₂ pressure. Finally, extrapolations based on observed trends in dependencies on membrane H₂ permeance and Ru catalyst loading suggest catalyst normalized reaction rates 4 to 6 times higher are achievable by increasing H₂ permeance an order of magnitude to 100 GPU and decreasing catalyst loading an order of magnitude to 0.1 μg/cm².

Chapter 4 - Kinetic and Equilibrium Sorption of Organic Liquids and Vapors in Matrimid*

4.1. Abstract

This work examines the kinetic and equilibrium sorption characteristics of a variety of chemical penetrants in the polyimide polymer Matrimid. Liquid equilibrium sorption for dense films with thicknesses of 50 μm for a large variety of organic species including alkanes, alcohols, acetates, furans, and ionic liquids is presented. Vapor equilibrium sorption isotherms and kinetic sorption behavior for water and C1-C6 alcohols as a function of chemical activity from 0 to 0.9 were measured using a quartz crystal microbalance with films ranging in thickness from 0.07 to 2.0 μm . Diffusion coefficients and relaxation parameters were calculated according to the diffusion-relaxation model for penetrants in glassy polymers. Diffusion coefficients at infinite dilution for water and C1-C6 alcohols are given as a function of van der Waals molar volume and a clear dependency is shown ranging from $2\text{E-}11$ to $6.5\text{E-}13$ cm^2/s for water and hexanol, respectively, for 0.26 μm thick films. Diffusion coefficients for all studied vapor penetrants displayed a marked dependence on thickness spanning approximately two orders of magnitude for each respective vapor penetrant over the range 0.1 to 1.0 μm . Penetrant-induced relaxation behavior accounts for the majority of mass sorption at chemical activities of 0.2 and above for the C1-C6 alcohol vapors.

*This chapter has been submitted to the *Journal of Membrane Science* and accepted for publication. doi: 10.1016/j.memsci.2016.03.054

4.2. Introduction

4.2.1. Background

As novel applications for high performance polymers and membrane separation processes are developed an understanding of the sorptive capacity and diffusion properties of the chemical species in which they are in contact must be further investigated. Examples of such novel applications include solvent resistant nanofiltration [74,75,100] and polymeric membrane reactors [10,18-20]. In these applications the polymeric membranes encounter chemical environments not often seen in more traditional gas separation processes, including exposure to highly plasticizing and swelling agents such as alcohols, furans, aromatics, and related hydrocarbons [74,76,101]. Gas, liquid, and vapor sorption and diffusion in polymers has been an active area of research for several decades with a large variety of penetrant sorption, diffusion, and polymer behaviors observed [45-51]. Experimental techniques for exploring these phenomena include standard gravimetry, magnetic suspension balance [49], quartz spring microbalance (QSM) [52], FTIR-ATR [48], quartz crystal microbalance (QCM) [53,54], NMR [55], time-lag permeation [56], and pressure decay (PD) [57].

This work investigates the equilibrium sorption of several solvents and the kinetic transport of water and short-chain alcohols in Matrimid 5218 using gravimetry and quartz crystal microbalance techniques. Quartz crystal microbalance is an excellent technique for measuring masses down to the order of nanograms and has been explored and applied for a variety of mass-sensitive uses including high pressure gas sorption [53,54,64], vapor sorption [48,65,66], chemical sensor applications [67,68], and ligand binding [69,70]. QCM was chosen for this work for its ability to examine films with thicknesses in the range of 0.05 to 5 μm , which encompasses the range of thicknesses often observed in the dense layer of asymmetric polymeric membranes

[3,5,71,72]. QCM also possesses the potential for high-throughput experimentation considering the use of inexpensive quartz crystals and the immediate availability for data collection assuming the chemical and temperature environments are appropriately controlled. Matrimid is a commercially available amorphous polyimide with a glass transition temperature of 320 °C, whose chemical structure is shown in Figure 4-1 [102]. Sorption of condensable vapors in glassy materials is often accompanied by swelling or volume dilation of the material [45,46]. In this work the diffusion-relaxation model developed by Berens and Hopfenberg is used to describe the kinetic transport of the studied vapors in Matrimid [45]. Diffusion coefficients and relaxation parameters for the penetrants in Matrimid are calculated using the diffusion-relaxation mathematical framework.

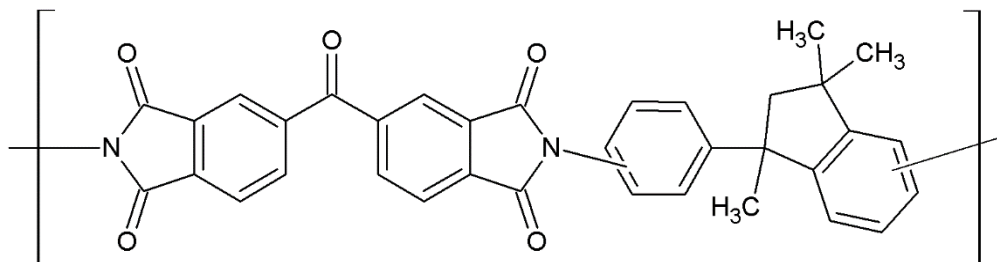


Figure 4-1 - Repeat unit of Matrimid 5218 polyimide.

4.2.2. Quartz crystal microbalance (QCM) measurement, calculation, and error

The technique of utilizing the piezoelectric property of appropriately cut quartz crystal to measure thin film deposition thickness was originally described and developed by Günter Sauerbrey [63]. The essence of the technique relies on applying an alternating electric field to electrodes on the faces of the cut crystal, which induces a directional mechanical deformation, or shear oscillation, in the crystal matrix [62]. Although the frequency of oscillation in the crystal depends on crystal cut and thickness, each individual crystal has a unique fundamental frequency. When a thin film is deposited onto the electrodes of the crystal and is mechanically adhered, the

frequency decreases in direct proportion to the deposited mass. This mathematical relation is known as the Sauerbrey equation:

$$\Delta f = \frac{2\Delta m f_0^2}{A(\mu_q \rho_q)^{1/2}} \quad (4-1)$$

where Δf is the frequency change, Δm is the mass change, f_0 is the fundamental frequency of the uncoated crystal, A is the active area of one face of the crystal, μ_q is the shear modulus of quartz (29.47 GPa), and ρ_q is the density of quartz (2.648 g/cm³).

QCM is a highly sensitive technique and is often described as having sub-nanogram mass resolution. There is an upper limit on QCM mass detection and it depends largely on the type of material adhered to the crystal and its viscoelastic properties. Other experiments in the literature investigating polymers using QCM generally work with film thickness less than 5 μm in efforts to avoid significant error induced from viscoelastic effects [53,103]. However, one source suggests that when measuring sorption in polymers, only thicknesses up to 0.2 μm may be considered absent of apparent mass uptake errors due to viscoelastic effects [62]. Although the work of [62] raises caution on the acceptable polymer film thickness, it does not exhaustively rule out the acceptability of using modestly thicker polymeric films. The work of Davis, *et al.* [66], investigated water vapor sorption in polylactide using QCM on a 7 μm film and obtained good agreement with measurements using quartz spring microbalance and ATR-FTIR. Other sources have discussed errors induced from imperfectly smooth quartz crystals, pressure, and temperature effects [54,64]. In this work all QCM measurements were taken at 30 °C and all polymer coated crystals were exposed to the same thermal history in regards to preparation and drying. Also, all QCM measurements can be considered to be conducted at atmospheric pressure, therefore temperature and pressure induced anomalies should be minimized. Our work focuses on the range of

approximately 0.1 to 2 μm , and all relevant figures except Figure 4-14, present data collected in the 0.2 to 0.3 μm range. Therefore, until a more exhaustive examination of polymer thickness induced errors for QCM vapor sorption analysis is reported, we will assume our results for polymer thicknesses 2.0 μm and lower are considered valid.

4.3. Experimental

4.3.1. Materials

AT-cut 5 MHz quartz crystals (1 inch diameter) were purchased from Inficon. Matrimid 5218 was purchased from Huntsman Advanced Materials and used as received. Dichloromethane (certified ACS, purity $\geq 99.9\%$) and all liquid penetrants (certified ACS, purity $\geq 99.9\%$) were purchased from Fisher Scientific or Acros Organics and used as received. A Maxtek Research Quartz Crystal Microbalance was used to perform all vapor sorption QCM experiments. Omega mass flow controllers (FMA5504 0-20SCCM) and ultrahigh purity nitrogen (Matheson Gas) were used for controlling gas phase compositions.

4.3.2. Equilibrium liquid sorption

Films were prepared from a 2 wt% solution of Matrimid powder dissolved in dichloromethane (DCM). The solution was allowed to dissolve for 48 hours and was 0.45 μm filtered before use. The solution was poured into casting rings with a diameter of 8 cm situated on glass plates where the solvent was allowed to evaporate overnight producing dense films with thicknesses on the order of 30-50 μm . The films were washed with DI water and placed in a vacuum oven at 70 $^{\circ}\text{C}$ for 24 hours. The films were submerged in the liquids of interest for 6 weeks and were then weighed weekly to determine the relative mass uptake. The films submerged in the liquids of interest at the specified temperature were removed, rapidly and carefully blotted dry within 10-15 seconds, and were placed on a balance for mass measurement. This ‘blot and

dry' technique is seen in several literature examples that examined liquid sorption in polymer films [46,104,105]. It is generally assumed that the mass of penetrant that diffuses and evaporates from the polymer surface is negligible compared to the total equilibrium amount sorbed. After the sixth week measurement, when the subsequent weekly measurements of relative mass uptake (mass sorbed penetrant / mass polymer) varied by less than $\pm 5\%$ compared to the previous two weeks of measurements, the film was considered to have reached equilibrium with the liquid phase.

4.3.3. Kinetic vapor sorption

Vapor sorption experiments were performed with Matrimid spin-coated AT-cut quartz crystals. Matrimid in DCM solutions of 0.5 to 3 wt% were 0.45 μm filtered and about 1.5 mL of the desired solution was placed onto one surface of the crystal situated on the spin-coater. The acceleration of the spin-coating was 750 rpm/sec with a final velocity of 2500 rpm for a total spinning time of 60 seconds. The 0.5 to 3 wt% solutions produced thicknesses ranging from 0.05 to 2.0 μm , respectively, as calculated by the Sauerbrey equation [63]. The coated crystals were placed in a vacuum oven at 60 $^{\circ}\text{C}$ for 24 hours to ensure complete removal of solvent. After drying the coated crystals were placed in the QCM crystal holders under 10 mL/min flowing nitrogen at 30 $^{\circ}\text{C}$ for 6 hours to ensure thermal stabilization of the system. The crystal holders, gas lines, and liquid penetrant reservoir were all positioned inside an isothermal water bath.

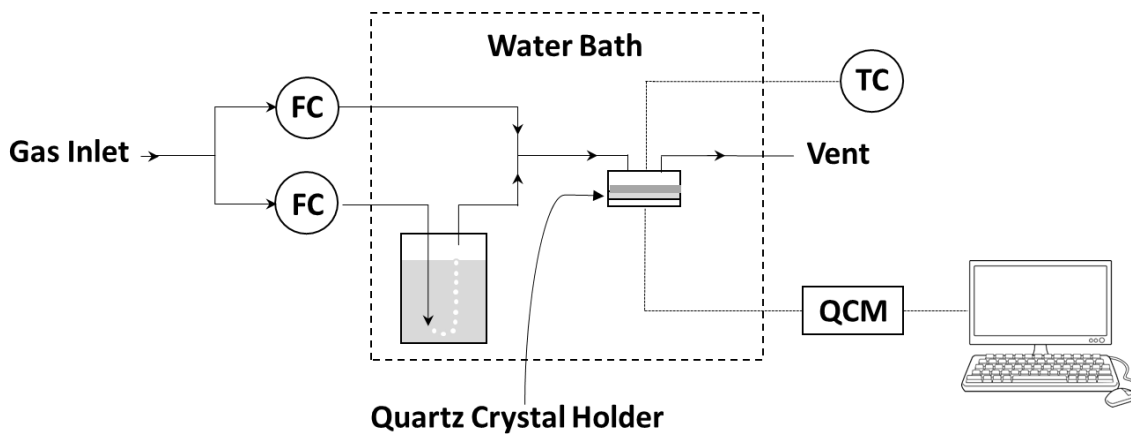


Figure 4-2 - QCM Vapor Sorption Setup – FC denotes ‘flow controller’ and quartz crystal holder contains polymer coated crystal in an o-ring sealed cell with appropriate electrodes for QCM control. Dashed line indicates components were submerged in temperature controlled (± 0.05 °C) water bath.

The vapor sorption experimental setup is shown in Figure 4-2. Two streams of nitrogen were proportioned and combined to provide a continuous total flow of 10 mL/min. One of the streams bubbles through a reservoir of the desired liquid penetrant to produce saturated vapor. In this way the chemical activity of the penetrant (P/P^{sat}) to which the polymer is exposed is controlled (± 1.5 % based on the accuracy of the flow controllers). The chemical activity was increased in 0.1 (0.2 for 48 h sorption interval experiments) step changes every 12 hours (or 48 hours for long term comparison experiments) across the activity range 0 to 0.9 for all penetrants studied. Nitrogen is considered an acceptable choice as the vapor phase carrier gas, because under experimental conditions (30 °C, atmospheric pressure) nitrogen sorption is approximately $88 \mu\text{g}/\text{cm}^3$ in comparison to the range of sorbed vapor penetrants being 0 to $2.7\text{E}5 \mu\text{g}/\text{cm}^3$ [72,106]. Frequency measurements were recorded at 1 sample/sec.

4.3.4. Calculations

Equilibrium liquid sorption values were calculated as the mass of solute or penetrant sorbed per mass of dry polymer, as shown in Equation (4-2).

$$m_{equil. sorption} = \frac{m_{pol+sol} - m_{dry polymer}}{m_{dry polymer}} \quad (4-2)$$

Equilibrium vapor sorption was calculated in a similar manner for each 0.1 chemical activity interval. The diffusion and relaxation model developed by Berens and Hopfenberg was used to describe the kinetic behavior of the polymer/penetrant systems and is shown in Equation (4-3).

$$m_{total} = m_F \left(1 - \frac{4}{\pi} \sum_{n=0}^{\infty} \frac{(-1)^n}{(2n+1)^2} \exp \left[\frac{-D(2n+1)^2 \pi^2 t}{4L^2} \right] \right) + m_R (1 - \exp(-k_R t)) \quad (4-3)$$

The meanings of the terms in Equation (4-3) are shown in Table 4-1. This model separates the total amount of penetrant sorbed into sorption due to relatively rapid Fickian diffusion and sorption due to much slower polymer chain relaxations, $m_{total} = m_{diffusive} + m_{relaxation}$. Figure 4-3 exemplifies the separation of the diffusion and relaxation sorption processes and indicates what the model parameters represent. The relaxation portion is actually represented by an infinite sum of relaxation processes or stages, but for many polymer/penetrant systems only one relaxation term is needed to capture the behavior [45,48,49,107,108]. The assumption with applying this model is that the time constant for the diffusive sorption is sufficiently greater than that for the relaxation sorption, or more specifically that the Deborah number [109], shown in Equation (4-4), is much greater than unity. Data analysis and model parameter calculations were performed using non-linear regression in MATLAB software.

$$De = \frac{D/L^2}{k} \gg 1 \quad (4-4)$$

Table 4-1 – Diffusion-relaxation model terms.

Term	Description
m_{total}	Total mass of penetrant sorbed due to diffusion and relaxation
m_F	Mass of penetrant sorbed due to Fickian diffusion

m_R	Mass of penetrant sorbed due to 1st polymer chain relaxation stage
D	Diffusion coefficient of penetrant in polymer (cm^2/s)
L	Polymer film thickness (cm)
k_R	Relaxation constant (s^{-1})
t	Time (s)

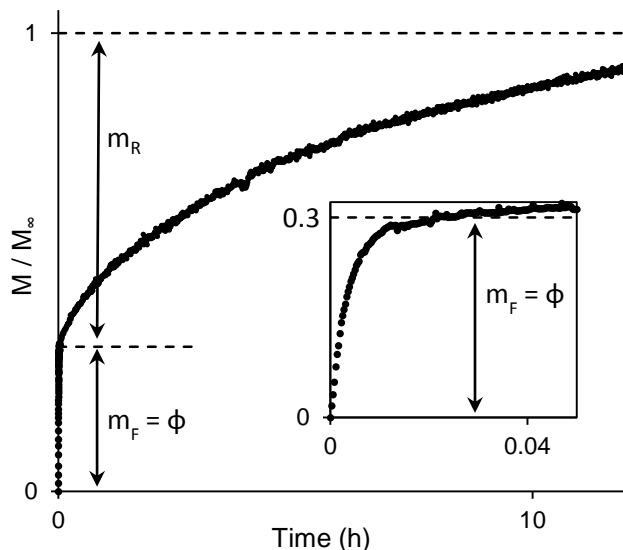


Figure 4-3 - Ethanol sorption in Matrimid for an activity step change from 0.1 to 0.2 at $t = 0$ over a 12 h time period displayed to exemplify model parameter definitions and the associated approximate time intervals used.

4.4. Results and discussion

4.4.1. Equilibrium liquid sorption

The equilibrium liquid sorption of several chemical species in Matrimid was determined at 30 °C unless otherwise indicated, and the results are displayed in Figure 4-4. The chemical species are approximately organized into three groups based on chemical identity and amount sorbed, namely, (1) alkanes, (2) alcohols, and (3) other organics, including furans, acetates, aromatics, and a few other highly sorbing species. All of the shown alcohols are of the normal isomeric form unless otherwise indicated. The highest sorbing chemicals in Figure 4-4 are on the apparent verge

of acting as solvents for Matrimid, and one would anticipate that upon slightly elevating the temperature they would become solvents for Matrimid. The chemicals shown in Table 4-2 completely dissolved Matrimid at the indicated temperature. If one compares the chemical structures of the highest sorbing chemicals in Figure 4-4 to the listed solvents in Table 4-2, it is not surprising the relatively high observed amounts of sorption considering their similarity in chemical structure. A somewhat eclectic collection of solvents was tested for sorption in Matrimid, ranging from alkanes to ionic liquids. Rather than exhaustively testing a certain class of chemicals a variety was sought to guide choices for applicable non-solvents for future application development with Matrimid membranes in organic liquid/vapor systems.

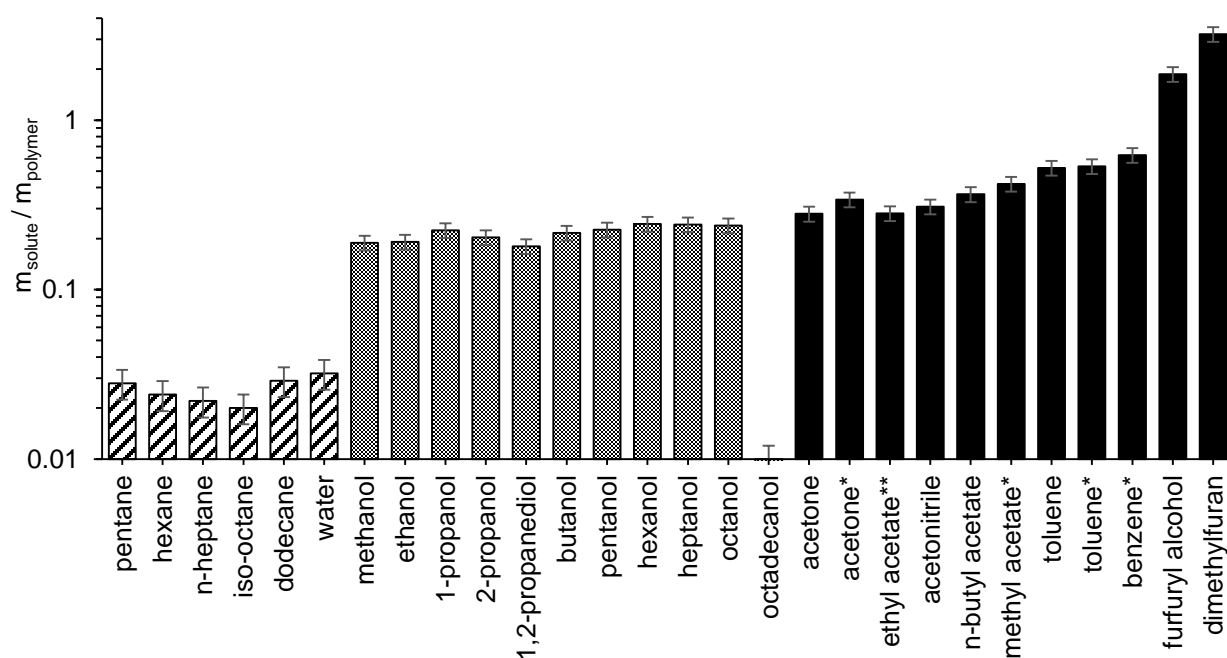





Figure 4-4 - Equilibrium liquid sorption of indicated chemical species in Matrimid at 30 °C. * and ** indicate values taken from literature references at 35 °C and 25 °C, respectively [91,105]. Note that the y-axis ranges over 2 orders of magnitude for the chemical species listed. Species are approximately organized into three groups: alkanes , alcohols , and other organics . Exact values of mass of solute sorbed per mass of polymer can be found in Supporting Information Table A1.

Table 4-2 - Solvents for Matrimid. These listed chemicals dissolved films of Matrimid at the indicated temperature.

Chemical	Temperature (°C)
Tetrahydrofuran (THF)	25
Ethylbenzoate	25
Gamma-butyrolactone (GBL)	25
Gamma-valerolactone (GVL)	25
1-Ethyl-3-methylimidazolium chloride [EMIM]Cl	25
1-Ethyl-3-methylimidazolium acetate [EMIM]OAc	60

4.4.2. Equilibrium vapor sorption

The sorption of alcohol vapors (C1-C6) and water in the activity range 0 to 0.9 was measured using QCM and is shown in Figure 4-5 and Figure 4-6, for 12 h and 48 h intervals, respectively, for each activity step, represented as mass of solute per mass of Matrimid polymer. C3-C6 alcohols were all of the normal isomeric form. The 12 h sorption interval data presented in Figure 4-5 is not considered to have reached true equilibrium at each activity level, and by comparing to the equivalent data in Figure 4-6 for 48 h sorption intervals one sees that the lower activity range (0 to ~0.5) was further from equilibrium than the latter half of the range. The data points for sorption at an activity of one in both Figure 4-5 and Figure 4-6 were independent measurements of Matrimid films immersed in the respective liquid penetrant for approximately eight weeks, so more certainty can be placed on the upper bound of all of the presented isotherms. There is a high level of coincidence for the alcohol vapor data, which is not surprising considering the chemical similarity of the C1-C6 alcohols and their similar equilibrium liquid sorption values presented in Figure 4-4. The longer chain alcohols display a slightly higher sorption amount for each activity level, which is consistent with their relatively higher liquid equilibrium sorption amounts and expected greater condensability in the polymer. An inverse sigmoidal shape is seen

for the C1-C6 alcohol isotherms, which is consistent with other literature observations for the sorption of plasticizing penetrants in glassy polymers [91,107,110,111].

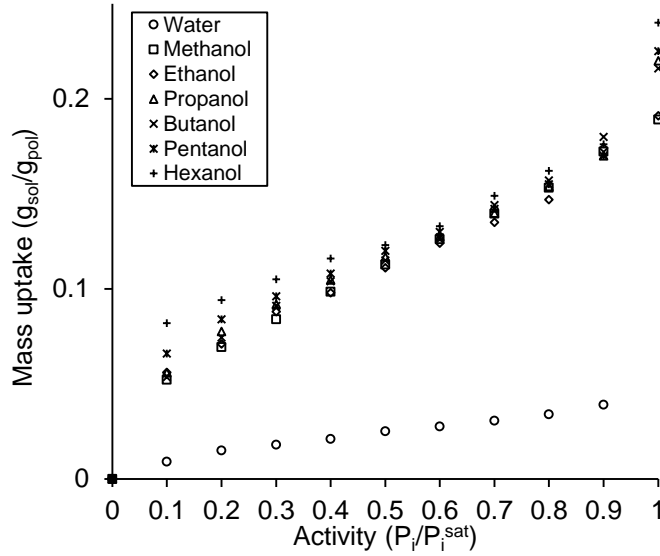


Figure 4-5 - Vapor sorption for 12 h intervals in Matrimid at 30 °C for 0.1 chemical activity step changes. Values listed at an activity of 1 are taken from equilibrium liquid sorption of dense Matrimid films. All film thicknesses were 0.26 μm ($\pm 0.015 \mu\text{m}$). Error bars omitted for clarity. The standard deviation of six independent measurements of methanol isotherms was at most 5 % of the average value for each 0.1 activity increment.

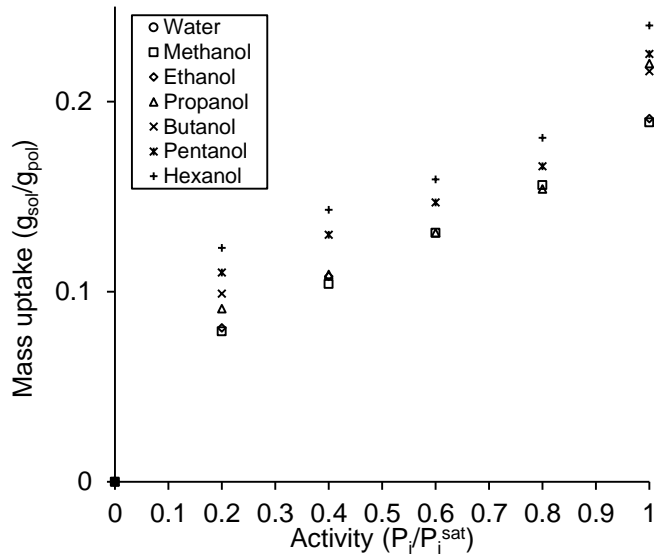


Figure 4-6 - Vapor sorption for 48 h intervals in Matrimid at 30 °C for 0.2 chemical activity step changes. Values listed at an activity of 1 are taken from equilibrium liquid sorption of dense Matrimid films. Film thicknesses ranged from 0.26 to 0.40 μm . See Figure 5 caption for error discussion.

4.4.3. Penetrant-induced T_g depression

One implication of sorbing species into the polymer matrix is depression of the glass transition temperature of the polymer-penetrant system ($T_{g,mixture}$) in relation to the pure polymer T_g . This phenomenon is well-described in the literature [112-114] and has alternatively been discussed as a penetrant-induced glass transition (P_g) [115]. We offer an estimation of this effect in Figure 4-7 as calculated by Chow's model [116] and the Fox equation, respectively, using the sorption isotherm data presented in Figure 4-6. These calculations are in modest agreement for the alcohols, however must still be viewed as only an estimate, as Chow's model requires the use of the difference in heat capacity of the polymer below and above its glass transition, ΔC_p . The ΔC_p for Matrimid was not directly available in the literature, so an estimate of 0.1 J/gK was used, as determined from a correlation presented by [117] between ΔC_p and CO_2 diffusivity for a series of polyimides (using $D_{\text{CO}_2/\text{Matrimid}} = 3\text{E-}8 \text{ cm}^2/\text{s}$ [118]). Despite Figure 4-7 being treated as estimates, the general conclusion to infer is that even under low alcohol penetrant activity

conditions (0 to 0.2), the $T_{g,mixture}$ may be depressed substantially more than 100 °C for all of the alcohol penetrants. This observation has importance as we seek to employ Matrimid and related polymers in membrane applications requiring elevated temperatures and organic liquid/vapor environments.

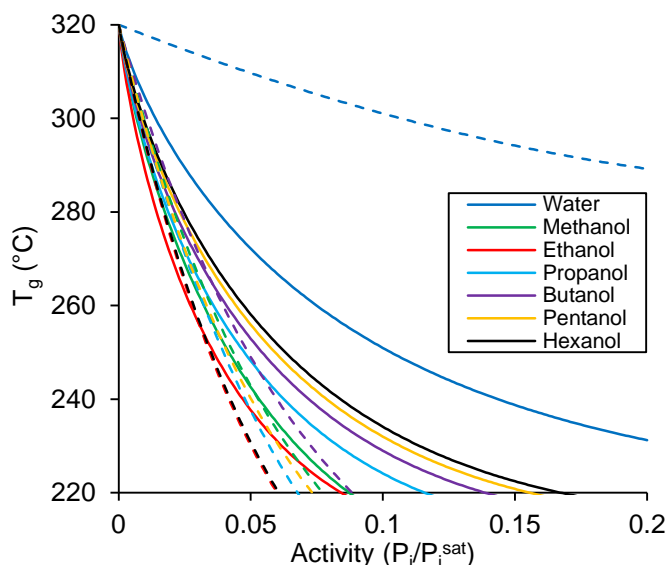


Figure 4-7 - T_g depression as calculated by Chow's model (—) and Fox equation (- -) using sorption isotherm data. It is stressed that these calculations are estimates.

4.4.4. Kinetic vapor sorption

4.4.4.1. Diffusion

Thermodynamically corrected diffusion coefficients for water and C1-C6 alcohols as a function of chemical activity are presented in Figure 4-8. The transport, or uncorrected, diffusion coefficients can be found in the Supporting Information. The thermodynamic correction factor arises from the nonlinearity in the sorption isotherm, as seen in Figures 5 and 6 where there is significantly higher extents of sorption at very low and high chemical activities. The correction factor is described in detail in [119] and has been applied by others investigating diffusion in non-solvent/polymer systems [120]. The form of the correction factor is given in Equation (4-5).

$$D = D_{TC} \frac{d \ln p}{d \ln q} \quad (4-5)$$

where p is the partial pressure of the penetrant, q is the concentration or loading of penetrant in the polymer, and D_{TC} is the thermodynamically corrected diffusivity.

The diffusion coefficients are plotted at the midpoint value of the chemical activity step. For example, the diffusion coefficient for the activity step from 0.1 to 0.2 is plotted at an activity of 0.15. The first general observation is the clear trend that the longer the alkyl chain, the smaller the diffusion coefficient. The diffusional behavior of water is in contrast to the alcohols in that the diffusion coefficient slightly decreases as a function of activity. This is attributed to the clustering behavior that water undergoes at higher activities where water moves in multi-molecular clusters rather than single molecules. More in depth characterization of this behavior is described by others looking strictly at water diffusion in their glassy polymer of interest [48,121,122].

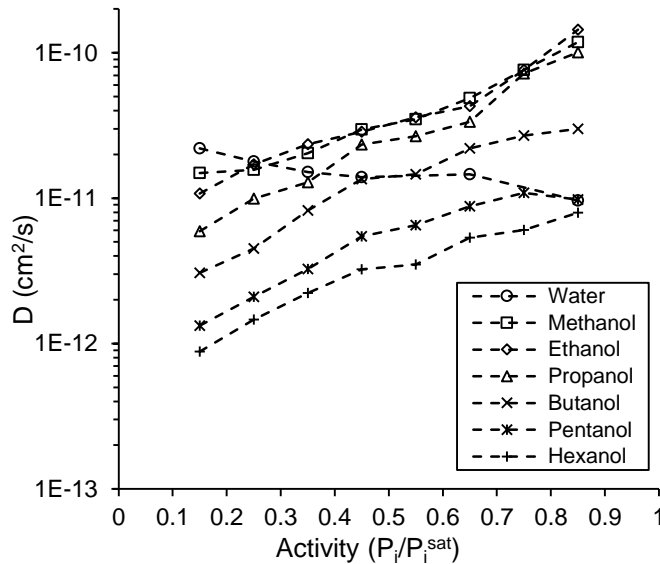


Figure 4-8 - Thermodynamically corrected vapor diffusion coefficients in Matrimid at 30 °C as a function of chemical activity. All initial film thicknesses were 0.26 μm ($\pm 0.015 \mu m$). Error bars omitted for clarity. See Appendix C for error analysis, which places approximately $\pm 25\%$ error on the diffusion coefficient values reported. Lines added for visual aid.

Figure 4-9 presents diffusion coefficients at infinite dilution for water and the C1-C6 alcohols in Matrimid as a function of van der Waals molar volume. Infinite dilution was estimated by fitting an exponential curve to the data in Figure 4-8 and extrapolating to an activity of 0. The clear trend of decreasing diffusion coefficient with increasing molecular volume is commonly seen in penetrant/glassy polymer systems [3,123].

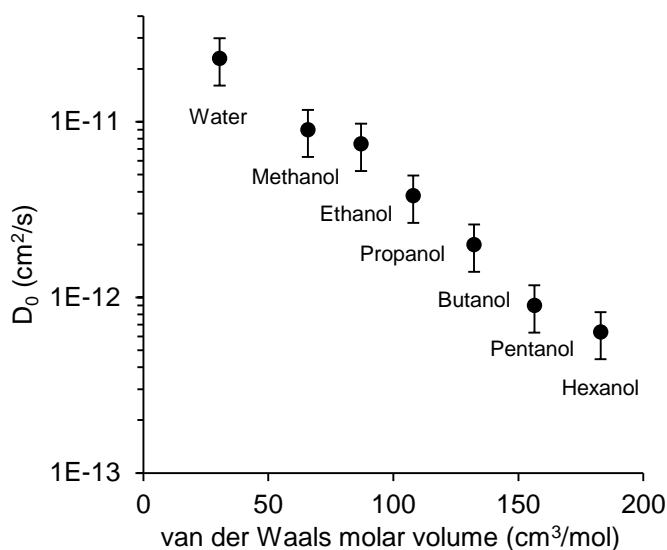


Figure 4-9 - Diffusion coefficients at infinite dilution for the indicated chemical species in Matrimid at 30 °C as a function of van der Waals molar volume. All film thicknesses were 0.26 μm ($\pm 0.015 \mu\text{m}$). Error bars represent one standard deviation for 15 independent samples for methanol sorption. See Supporting Information for expanded error discussion.

Figure 4-10 displays the ethanol sorption profile for 0.1 activity steps every 12 hours. The diffusive portions of each interval are easily identified and are displayed in Figure 4-11. The general appearance of the sorption profile and respective diffusive portions for each activity interval displayed in Figures 10 and 11 are representative of the other alcohol penetrants studied, C1 and C3-C6, and corresponding sorption profiles can be found in the Supporting Information. Figure 4-12 gives the sorption profile for propanol using 0.2 activity steps over 48 hour intervals and is included here for comparison to Figure 4-10 to show the extent of continued relaxation induced sorption over the extended time period.

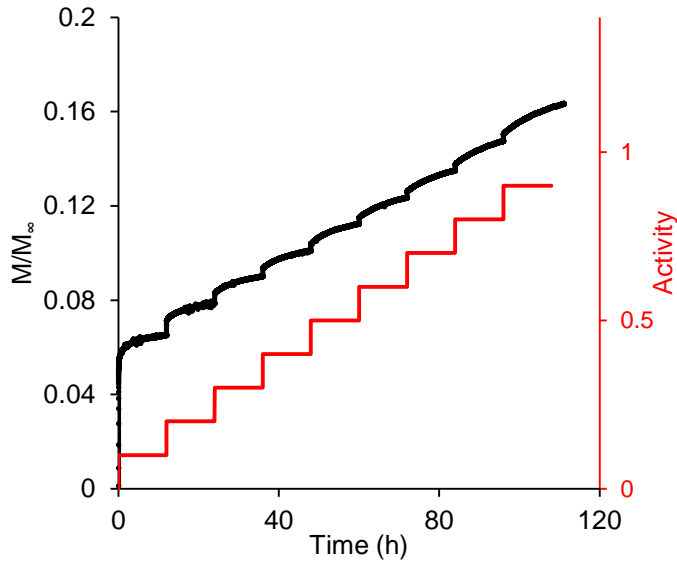


Figure 4-10 - Ethanol sorption profile for 0.1 chemical activity steps every 12 h at 30 °C. Film thickness = 0.278 μm .

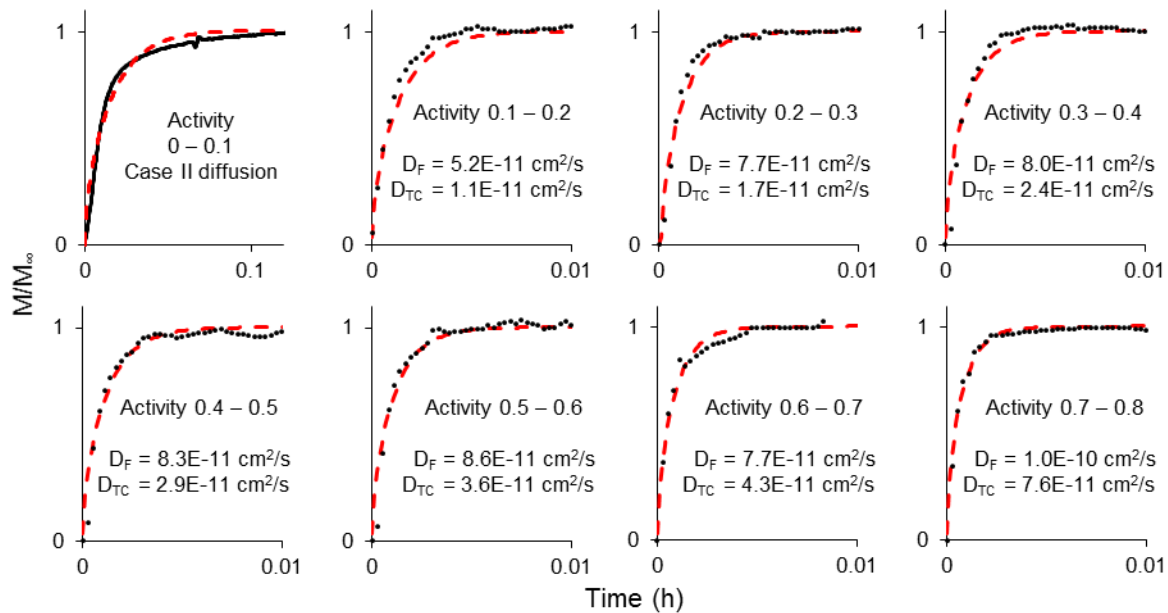


Figure 4-11 - Initial short-time interval for each 0.1 activity step change for ethanol sorption. $\Delta t = 1$ second. (- - -) represents fit BH equation. D_F signifies the Fickian or transport diffusion coefficient. D_{TC} signifies the thermodynamically corrected diffusion coefficient. It was determined that the sorption data for activity change 0 to 0.1 exhibited Case II diffusion, so coefficients are not reported for that interval.

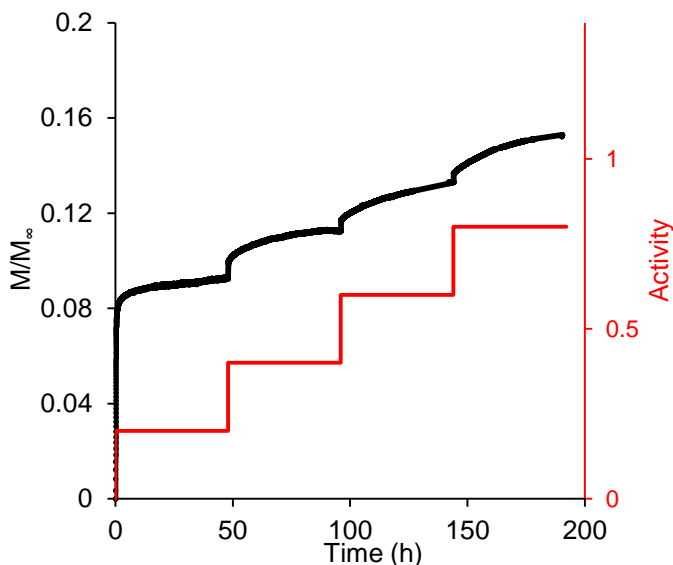


Figure 4-12 - Propanol sorption profile for 0.2 chemical activity steps every 48 h at 30 °C.

One consideration with extracting diffusion coefficients from sorption data is what diffusion regime the sorption data exhibits, *i.e.* Case I, anomalous, or Case II diffusion. A method for classifying which regime is present is by fitting the initial portion of the sorption curve with the equation $M/M_{\infty} = kt^n$ over the respective time interval for $M/M_{\infty} < 0.5$. A value of $n = 0.5$ suggests purely Fickian diffusion, $0.5 < n < 1.0$ indicates anomalous diffusion, and $n = 1$ indicates Case II diffusion. Case I and anomalous diffusion behavior are considered appropriate for determining regressed diffusion coefficients in Fickian and Berens-Hopfenberg frameworks, respectively. Case II sorption data is generally not considered appropriate for Fickian or Berens-Hopfenberg analysis due to conflation of penetrant diffusion and the moving front velocity of the penetrant within the polymer [120,124,125]. A sorption case analysis for each penetrant is provided in the Supporting Information. In general it was found that the first activity step from 0 to 0.1 nominally exhibited Case II diffusion, however, that initial step also included the actuation of the penetrant stream flow valve producing a non-instantaneous activity change, which influences the first few seconds of sorption. Regardless of the physical reason, the value of n for

that step for all penetrants and film thicknesses was approximately 1, therefore the extracted coefficients for an activity step from 0 to 0.1 are not included in any relevant figures. All subsequent 0.1 activity steps from 0.1 to 0.9 for all penetrants and film thicknesses (~0.07 to 1.5 μm) had n values in the range 0.5 to approximately 0.9.

A notable challenge in determining accurate diffusion coefficients was estimating the film thickness increase as a function of activity. No experimental dilatometric values for C1-C6 alcohols in Matrimid could be found in the literature, however detailed swelling measurements for CO_2 sorption in Matrimid are given in [118]. At 30 bar of CO_2 pressure, the solubility in Matrimid was reported as approximately $65 \text{ cm}^3(\text{STP})/\text{cm}^3$ and film thickness increase given on the order of 4-5 %. Another source provides regressed values for swelling parameters used when applying the non-equilibrium lattice fluid model to Matrimid-methanol and Matrimid-acetone systems [91]. One may then use those parameters to calculate polymer/penetrant system density as a function of penetrant activity, and assuming isotropic film expansion, make some estimate regarding film thickness. Calculations show that the thicknesses at an activity of 1 and temperature of 30 $^\circ\text{C}$ increase by 5 and 16 % for methanol and acetone, respectively. In the absence of experimentally determined thicknesses, it seems reasonable based on [118] and [108] to estimate a thickness increase on the order of 5-10 % at an activity of 1 for the alcohol vapor/Matrimid systems. Therefore, diffusion calculations were performed assuming a 5 % increase in film thickness for C1-C3 alcohols, 10 % increase for C4-C6 alcohols, and no increase for water at a chemical activity of 1. The larger increase for C4-C6 was decided based on the higher sorption amounts for the longer alkyl-chain alcohols, as shown in Figure 4-5 and Figure 4-6, and conversely no increase due to water sorption considering its significantly lower sorption amount by comparison. Figure 4-8 assumes a linear increase in thickness over the entire activity range, although sources do

indicate that increases in volume are greater at higher activities [108]. It is noted, though, that increasing the film thickness by 10 % in the calculation only increases the diffusion coefficient value by approximately 20%, which is still within the margin of error given for our reported diffusion coefficients. Refer to Appendix C for expanded error analysis and discussion.

4.4.4.2. Polymer relaxation

Penetrant-induced polymer relaxation is a well-documented phenomenon observed in glassy polymers for a wide variety of penetrants, including noble gases [49], CO₂ [54], water vapor and liquid [52], and organic vapors and liquids [45,120,123]. It is often classified as non-Fickian diffusion or sorption behavior and is usually observed on several orders of magnitude longer time scales than Fickian diffusion processes for glassy polymer/penetrant systems. When the initial observed Fickian diffusion process occurs on a time scale comparable to the penetrant-induced polymer relaxation and consequent sorption, it is difficult or even impossible to isolate the two processes and only the superposed sorption behavior is empirically visible. To separate the two phenomena, the Deborah number, which is the ratio of the time constants for the Fickian sorption process and the penetrant-induced relaxation sorption process, must be significantly greater than unity ($De \gg 1$). In the case that the system seems to present strictly Fickian behavior, relaxation may also still be occurring, but its contribution to overall sorption is either insignificant or negligible over the time scale of observation.

The parameters associated with the relaxation portion of sorption are $\phi = m_F$, which is the fraction of total mass uptake for an activity interval that is attributed to the initial Fickian sorption process (conversely, $1 - \phi$ represents the fraction of sorption that is attributed to the penetrant induced relaxation process), and k , the relaxation parameter. These values can be found in Appendix C.

Deborah numbers were calculated for all chemical species using the associated diffusion coefficient values and k values for each 0.1 activity interval (excluding 0 to 0.1 for reasons described in Section 3.4.1) and the initial film thickness. All calculated Deborah numbers were greater than two orders of magnitude above unity, except those for the C4-C6 alcohols at activity less than 0.3, as shown in Figure 4-13. This observation supports the ease of separating the initial diffusive sorption from the relaxation sorption stages. It is not surprising that the trend of the Deborah numbers for all of the penetrants is quite similar to the diffusion coefficient trend, as the relaxation parameter for all penetrants only varied by approximately a factor of 4 across the entire activity range. Relaxation parameter values for the studied vapor penetrants for 0.26 μm films are shown in Appendix C.

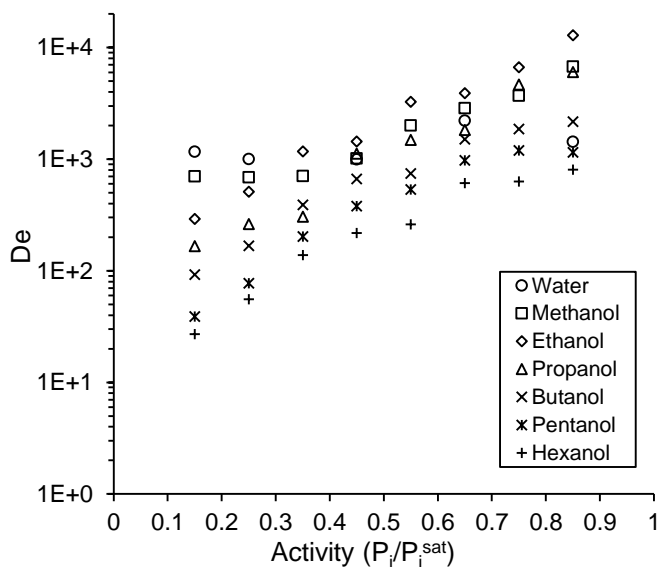


Figure 4-13 - Deborah number as a function of chemical activity calculated using regressed diffusion coefficients and relaxation parameters. All film thicknesses were 0.26 μm ($\pm 0.015 \mu\text{m}$).

4.4.5. Thickness dependence on diffusion and relaxation

Figure 4-14 displays thermodynamically corrected diffusion coefficients at infinite dilution for water and C1-C6 alcohols over a film thickness range of 0.07 to 2 μm . Values at infinite

dilution were determined by extrapolating an exponential curve fit to thermodynamically corrected diffusion coefficients over an activity range of 0.1 to 0.4 to an activity of 0. There is a clear trend of decreasing diffusion coefficient values as film thickness decreases. This phenomenon has been shown to occur for a variety of penetrant/polymer systems, not only for diffusion [121,126,127] but for other physical phenomena, including changes in glass transition temperature [128], polymer dynamics [129], and permeability [130-132]. Thickness-dependent phenomena in glassy polymer systems are often correlated to the accelerated effects of physical ageing and loss of fractional free volume (FFV) with decreasing thickness [133,134]. There are also discussions related to the increasing dependence on the environment at the interface of the polymer film surface and the media with which it is in contact, for example free-standing films versus supported films [135-137].

It is notable that the water and methanol diffusion coefficients span over two orders of magnitude for only a single order of magnitude in thickness over the range 0.1 to 1.0 μm . This observation becomes extremely important if one considers the submicron effective thicknesses of polymers used in applications such as membrane separations, coatings, and drug delivery. Extrapolating measurements of thick films or bulk systems where the properties are measured on samples with thicknesses greater than 1 μm may lead to incorrect predictions for the transport behavior of the systems. Figure 4-14 gives additional data for water diffusion coefficients in Matrimid at infinite dilution from [121] for comparison to values obtained for thick films (regressed from film permeation data at 35 °C). Another noteworthy observation is that the water diffusion coefficient values in [121] are also given as a function of activity spanning an activity range 0 to 1 and decreased by a factor of approximately three over that range. This is nearly identical to the trend for water diffusion coefficients reported here, as shown in Figure 4-8. No

dependence of the relaxation parameter, k , on film thickness could be discerned over the thickness range studied in this work, approximately 0.1 to 2 μm .

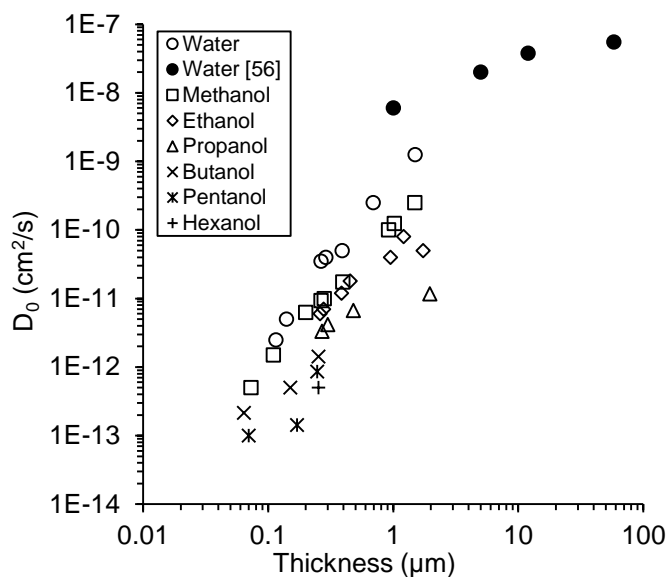


Figure 4-14 - Diffusion coefficients at infinite dilution for the indicated chemical species at 30 °C as a function of film thickness. The filled symbols (●) represent diffusion coefficients for water in Matrimid at 35 °C taken from [121] for comparison to thick film values. An expanded view of this plot is found in Appendix C.

4.5. Conclusions

This work has presented the equilibrium sorption of a large variety of liquid penetrants in Matrimid. Also presented was the kinetic and equilibrium sorption of water and C1-C6 alcohol vapors in Matrimid at 30 °C. Isotherms for these species over the chemical activity range 0 to 1 are given. Significant polymer relaxation behavior was observed over the entire activity range for all penetrants. Vapor sorption, diffusion, and polymer relaxation were measured using a quartz crystal microbalance. Diffusion coefficients and relaxation parameters were regressed from the data by applying the diffusion-relaxation model developed by Berens and Hopfenberg, which appropriately captured the behavior of the studied penetrant/polymer systems. Analysis of the Deborah number for all of studied systems indicated clear separation of diffusional and relaxation sorption processes. Film thicknesses studied ranged from 0.07 to 2.0 μm and an approximate two

to one order of magnitude dependence of diffusion coefficients on film thickness was determined for all penetrants.

Chapter 5 - Effect of Vapor Phase Ethylenediamine Cross-linking of Matrimid on Alcohol Vapor Sorption and Diffusion

5.1. Abstract

This work examines the sorption, diffusion, and polymer relaxation behavior for water and C1-C7 alcohol vapors in ethylenediamine vapor-phase cross-linked Matrimid at 30 °C. Ethylenediamine is sufficiently volatile at room temperature that cross-linking can occur by exposing the polymeric film to saturated vapor. This is in contrast to more conventional means of dissolving the cross-linker in a solvent, *e.g.* methanol, and immersing the polymeric film in the solution. The vapor-phase exposure method avoids the use of additional solvent and the undesirable swelling that the solvent induces in the polymer. Cross-linking kinetics over five hours of vapor exposure at 20, 25 and 30 °C are given in terms of mass of ethylenediamine reacted per mass of Matrimid for thin films in the range 0.25-0.7 μm . Equilibrium sorption isotherms for water and C1-C7 alcohol vapors are provided for 0.2 chemical activity steps over the range 0 to 0.8 for unmodified and cross-linked Matrimid. Equilibrium sorption for water and C1-C5 alcohols did not appreciably differ for unmodified and cross-linked Matrimid, however an approximate 90% reduction in equilibrium sorption was determined for hexanol and heptanol. Cross-linking Matrimid had only a minor impact on alcohol diffusion coefficients for water and C1-C3 alcohols, while those of butanol and pentanol were reduced over an order of magnitude. Relaxation kinetics were similarly unchanged for water and C1-C3 alcohols, while being significantly reduced for butanol and higher alcohols. The Berens-Hopfenberg model for sorption of swelling-inducing penetrants in glassy polymers was applied for describing the diffusion and penetrant-induced relaxation behavior for the mentioned penetrants in unmodified and EDA cross-linked Matrimid.

5.2. Introduction

5.2.1. Polymeric membranes and cross-linking

Chemically cross-linking polymer chains is one method to enhance the chemical stability of polymeric membranes in the presence of harsh chemical environments. This strategy is often employed in membrane based gas separation applications where one or more of the gases cause significant plasticization, as in the removal of CO₂ from natural gas [92,138,139], and in the area of solvent-resistant nanofiltration where the separation of harsh liquid organic solvents is often encountered [73-75,101]. A growing application for membranes that also potentially encounters harsh gas and liquid chemical environments is the use of the membrane in a chemically reactive system, or membrane reactor. Membrane reactors offer a unique approach combining reaction and separation of desirable products or selectively delivering reactants into catalytic systems at controlled rates and location. The use of polymeric membranes in contrast to ceramic and metal based membranes for this application is advantageous considering the high fluxes that are possible and the ease and relatively low cost in manufacturing. However, a notable challenge is the compatibility of the polymer with the solvent in the reactive system.

This study is motivated by our previous work on applying asymmetric Matrimid membranes for membrane reactor applications in three-phase hydrogenation reactions. In efforts to expand the reaction conditions and the solvents used in the membrane reactor, this work examines the use of ethylenediamine (EDA) vapor as the cross-linking agent for the Matrimid membrane. Specifically, we seek to understand the impact that EDA cross-linking has on the sorption, diffusion, and penetrant-induced polymer swelling behavior of water and C1-C7 alcohols in Matrimid. The use of diamines as cross-linking agents for polyimide membranes is a popular choice, but most cross-linking techniques involve dissolving the diamine in a solvent and then

exposing the membrane to the liquid solution [76,92,140]. This can result in undesired change in the membrane due to swelling effects. To circumvent the use of an additional solvent our work simply exposes the polymeric film to an EDA saturated vapor environment, much like the work in [141] where 50 μm films of 6FDA-durene were immersed in the saturated vapor. Our work utilizes a similar method, but for the cross-linking of Matrimid films with two orders of magnitude less thickness (0.25 to 0.7 μm) and for cross-linking times ranging from 15 min to 5 h. The thin Matrimid films were obtained by spin-coating quartz crystals. The polymer film coated crystals were subsequently cross-linked and used for experiments examining the sorption of water and C1-C7 alcohol vapors in Matrimid as a function of chemical activity ranging from 0 to 0.8. Figure 5-1 displays Matrimid monomers with amide groups forming the cross-link with ethylenediamine.

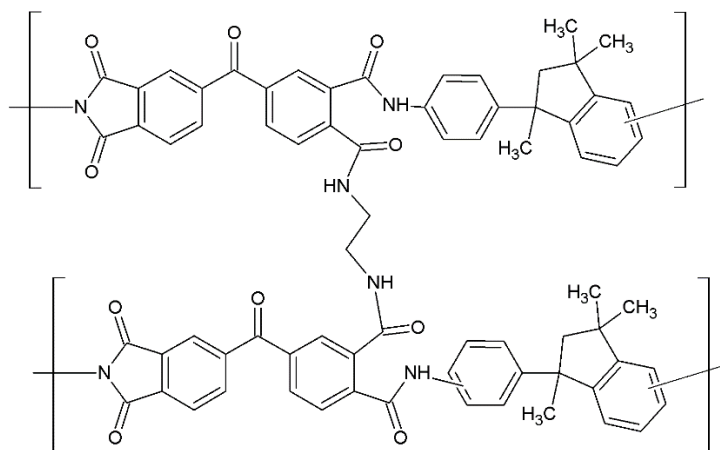


Figure 5-1 - Matrimid monomeric units cross-linked showing formation of amide groups linking the chains with ethylenediamine.

The extent of the EDA cross-linking reaction and, separately, the mass-uptake associated with penetrant sorption were measured using a quartz crystal microbalance. Quartz crystal microbalance is an excellent technique for measuring masses down to the order of nanograms and has been explored and applied for a variety of mass-sensitive uses including high pressure gas sorption [53,54,64], vapor sorption [48,65,66], chemical sensor applications [67,68], and ligand binding [69,70]. QCM was chosen for this work for its ability to examine films with thicknesses

in the range of 0.05 to 5 μm , which encompasses the range of thicknesses often observed in the dense layer of asymmetric polymeric membranes [3,5,71,72]. The diffusion-relaxation model developed by Berens and Hopfenberg is used to describe the kinetic transport of the studied vapors in cross-linked Matrimid [45]. Diffusion coefficients and relaxation parameters for the penetrants in cross-linked Matrimid are calculated using the diffusion-relaxation mathematical framework. Refer to section 4.2.2 for a detailed description of using quartz crystal microbalance as a mass measurement device, the calculations used to determine film thickness and mass uptake, and the associated potential errors in measurement using this technique.

5.3. Experimental

5.3.1. Materials

Refer to Section 4.3.1 for materials descriptions and procurement. Ethylenediamine was purchased from Acros Organics and used as received.

5.3.2. Quartz crystal film coating

A Matrimid in DCM solution of 1 wt% was 0.45 μm filtered and about 1.5 mL of the solution was placed onto one surface of the quartz crystal situated on the spin-coater. The acceleration of the spin-coating was 750 rpm/sec with a final velocity of 2500 rpm for a total spinning time of 60 seconds. The 1 wt% solution produced thicknesses ranging from 0.35 to 0.40 μm , as calculated by the Sauerbrey equation [63]. The coated crystals were placed in a vacuum oven at 60 $^{\circ}\text{C}$ for 24 hours to ensure complete removal of solvent. After drying, the coated crystals were placed in the QCM crystal holders under 10 mL/min flowing nitrogen at 30 $^{\circ}\text{C}$ for 6 hours to ensure thermal stabilization of the system. After obtaining a stable measurement of the polymer coated crystal, the crystals were removed for the cross-linking step detailed in Section 5.3.3 and then returned to the holders for thermal stabilization and consequent sorption experiment. The

crystal holders, gas lines, and liquid penetrant reservoir were all positioned inside an isothermal water bath.

5.3.3. Ethylenediamine (EDA) vapor-phase cross-linking

Varied extents of Matrimid cross-linking with ethylenediamine (EDA) were accomplished by exposing the Matrimid coated quartz crystals to an EDA saturated vapor environment for specified amounts of time. Approximately 5 mL of EDA was placed in a closed one liter container and after one hour the Matrimid coated crystals were placed in the closed container. After the desired amount of EDA exposure time was reached, the crystals were removed and gently immersed in a bath of DI water to rinse off any residual unreacted EDA. The crystals were then placed in a vacuum oven at 60 °C for 24 hours to remove any sorbed water and remaining unreacted EDA.

5.3.4. Kinetic vapor sorption and calculations

Sorption experiments were performed with Matrimid spin-coated AT-cut quartz crystals. The vapor sorption experimental setup is shown in Figure 4-2. Refer to Section 4.3.4 for a detailed description of the experimental set-up and how the vapor phase chemical activity was controlled. Refer to Section 4.3.5 for a detailed description of the relevant kinetic and equilibrium mass sorption calculations.

5.4. Results and Discussion

5.4.1. Ethylenediamine (EDA) cross-linking kinetics

The extent of ethylenediamine (EDA) cross-linking over approximately five hours at 20, 25 and 30 °C was measured using a quartz crystal microbalance and is represented in Figure 5-2 as mass of EDA per mass Matrimid as a function of time. The actual process involves EDA diffusion into the polymer film and then reaction with available imide groups, however considering

the film thicknesses were in the range 0.25 to 0.7 μm , it is assumed that diffusion of EDA was not a significant limitation over the studied time range. EDA is a relatively volatile substance, which is key in achieving significant cross-linking reaction in a short amount of time. The vapor pressures of EDA and water for comparison are given in Figure 5-3.

There are two available imide groups per monomer of Matrimid as shown in Figure 5-1, however reaction of one EDA with one imide group does not necessarily assume a cross-linking has occurred with a proximal Matrimid polymer chain. The second reaction of an attached EDA molecule with a proximal imide group will not lead to a mass change for the system, and is therefore undetectable using quartz crystal microbalance alone. For this reason we are hesitant to formally report on cross-linking reaction kinetics, however it is clear that significant amounts of EDA react with the polymer over the range of 0 to 5 hours at 20, 25 and 30 $^{\circ}\text{C}$. In further investigations, one may also consider the relative mobility of polymer chains as a function of temperature and the possible use of an additional vapor penetrant (*i.e.* one of the alcohols extensively studied in this work and in Chapter 4) to allow enhanced polymer chain motion and potentially greater degree of actual cross-linking as opposed to simple EDA addition.

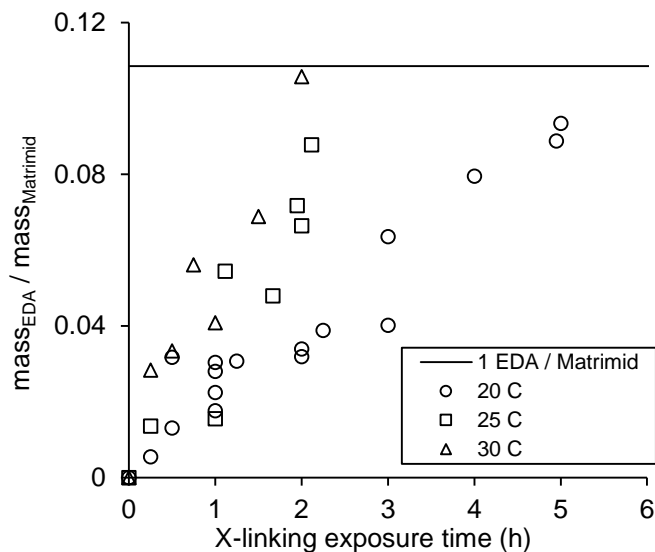


Figure 5-2 - Mass of EDA per mass of Matrimid polymer as a function of cross-linking agent (EDA vapor) exposure time at 20, 25 and 30 °C as measured with QCM. The solid line indicates the calculated ratio of the molecular weights of one molecule of EDA per one monomer of Matrimid.

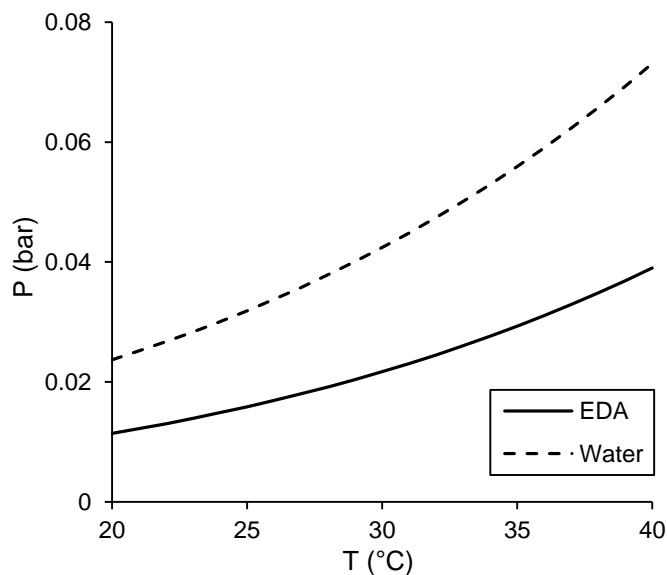


Figure 5-3 - Vapor pressures of ethylenediamine (EDA) [142] and water for comparison.

5.4.2. Equilibrium vapor sorption

The equilibrium sorption of water and alcohol vapors (C1-C7) in the activity range 0 to 0.8 was measured using QCM and is shown in Figure 5-4, represented as mass of solute per mass of

Matrimid polymer. C3-C7 alcohols were all of the normal isomeric form. An inverse sigmoidal shape is seen for the C2-C7 alcohol isotherms, which is consistent with other literature observations for the sorption of plasticizing penetrants in glassy polymers [91,107,110,111]. The standard deviation of six independent measurements of methanol isotherms was at most $\pm 5\%$ of the average value for each 0.1 activity increment.

Figure 5-4 displays the sorption isotherms for each penetrant in unmodified and EDA cross-linked (2 h vapor exposure) Matrimid thin films at 30 °C. One can see there is little effect on vapor sorption of water and C1-C4 alcohols. Figure 5-5 shows sorption isotherms of ethanol in cross-linked Matrimid films of varying extents of EDA vapor exposure ranging 0 to 300 min. Increasing the extent of EDA cross-linking has a marginal impact ($\sim 10\text{-}15\%$) on reducing ethanol sorption and it is assumed this trend continues with propanol and butanol. It seems there is some initial depression in the pentanol cross-linked isotherm, however inspection of the 0.2 and 0.4 activity level sorption curves reveals that the system had not reached equilibrium in those 48 h time intervals. There is substantial depression in the hexanol and heptanol sorption cross-linked isotherms, which did appear to have reached equilibrium for every 48 h interval for each 0.2 activity level. The drastic difference between pentanol and hexanol sorption in the cross-linked Matrimid is attributed to the polymer-EDA-polymer linkage creating an effective size-exclusion effect for hexanol and larger molecules.

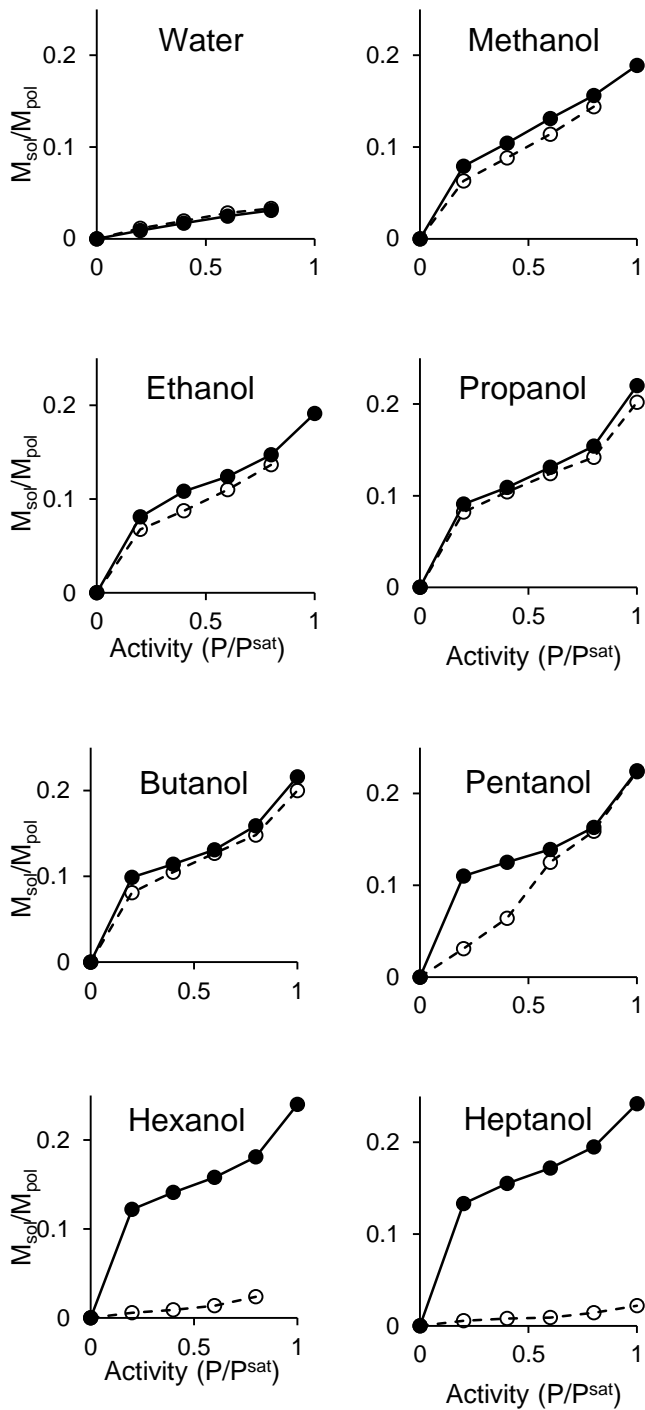


Figure 5-4 - Vapor sorption isotherms for 0.2 chemical activity steps with 48 hours at each activity at 30 °C. (—) indicates unmodified Matrimid film and (- - -) indicates EDA cross-linked (2 h EDA vapor exposure) Matrimid film.

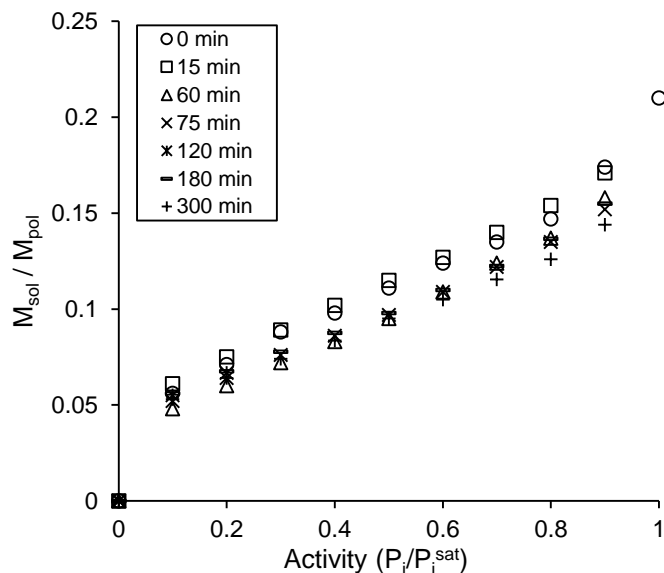


Figure 5-5 - Ethanol sorption in EDA cross-linked Matrimid films with thickness $0.30 \pm 0.03 \mu\text{m}$ at 30°C for films with varying durations of 20°C EDA vapor exposure.

As an aside, this effect could be exploited in a polymeric membrane reactor scenario where the reactant, take levulinic acid (Chapters 2 and 3) for example, is a linear 5-carbon chain molecule that upon hydrogenation forms a 5-carbon cyclic product, gamma-valerolactone. The cyclic product may then have substantially greater permeability through the membrane than the linear reactant because of the size-exclusion taking significant effect over a narrow range of molecular size. Ideally, one would take a reaction of interest, and consequently ‘tune’ the cross-linked membrane’s size-exclusion effect by choice of cross-linker and extent of cross-linking to create a membrane reactor that acts to selectively remove the product, possibly in addition to still being a selective gas deliverer.

5.4.3. Kinetic vapor sorption

5.4.3.1. Diffusion case analysis

When extracting diffusion coefficients from sorption data it is important to ensure the data are not representing a situation where significant non-Fickian behavior is occurring. Diffusion of penetrants in polymers is often classified as either Case I (Fickian), anomalous, or Case II (non-

Fickian) diffusion. One method for determining the diffusion case is by fitting the equation $M/M_{\infty} = kt^n$ over the respective time interval for $M/M_{\infty} < 0.5$. A value of $n = 0.5$ suggests purely Fickian diffusion, $0.5 < n < 1.0$ indicates anomalous diffusion, and $n = 1$ indicates Case II diffusion. Case I and anomalous diffusion allow use of Fickian and Berens-Hopfenberg analysis, whereas Case II sorption data is generally not considered appropriate for such analysis due to conflation of penetrant diffusion and the moving front velocity of the penetrant within the polymer [120,124,125]. An n value < 1 was established for the C1-C6 alcohols in Matrimid for chemical activities above 0.1 in Chapter 4. This also appeared to be the case for heptanol sorption in unmodified Matrimid above an activity of 0.2 and for all of the alcohol penetrants in the EDA cross-linked Matrimid (2 h EDA vapor exposure). Examples of this type of analysis for hexanol sorption in unmodified and cross-linked Matrimid are shown in Figure 5-6 and Figure 5-7, respectively, with n values of 0.85 and 0.5 determined. Considering n values for sorption of all of the penetrants for 0 to 0.1 and 0 to 0.2 activity steps were approximately one, no diffusion coefficients are reported for those intervals in any relevant figures.

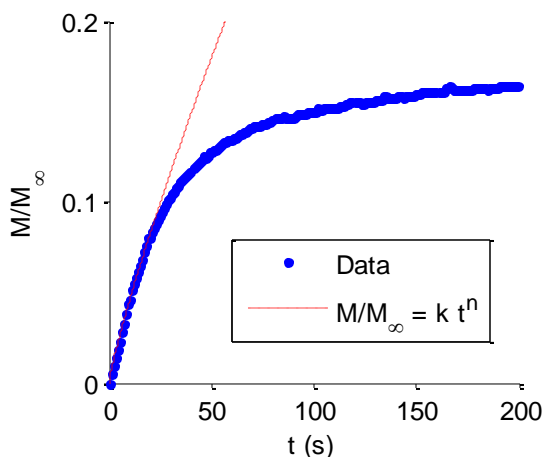


Figure 5-6 - Hexanol sorption for 0.2 to 0.4 activity step change in unmodified Matrimid. The value of the parameter $n = 0.85$, which is indicative of anomalous diffusion. It is noted that the y-axis is only 0.2 for this interval indicating the rest of the sorption for this activity step change was due to penetrant induced polymer relaxation.

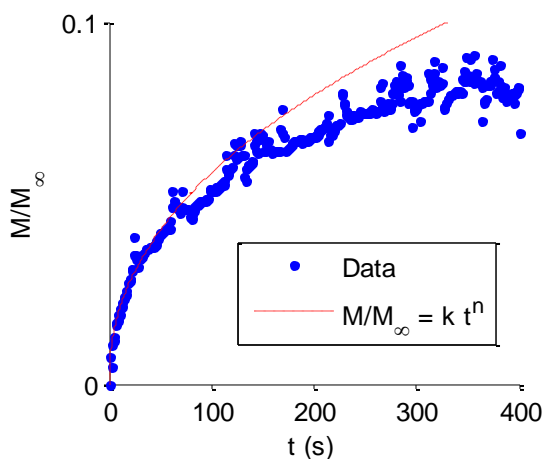


Figure 5-7 - Hexanol sorption for 0.2 to 0.4 activity step change in EDA cross-linked Matrimid (2 h vapor exposure). The value of the parameter $n = 0.5$, which is indicative of Fickian diffusion. It is noted that the y-axis is only 0.1 for this interval indicating the rest of the sorption for this activity step change was due to penetrant induced polymer relaxation.

5.4.3.2. Diffusion

Thermodynamically corrected diffusion coefficients for water and C1-C7 alcohols in unmodified Matrimid and cross-linked Matrimid (2 h EDA vapor exposure) as a function of chemical activity are presented in Figure 5-8 and Figure 5-9, respectively. The diffusion coefficients are plotted at the midpoint value of the chemical activity step. For example, the

diffusion coefficient for the activity step from 0.2 to 0.4 is plotted at an activity of 0.3. The correction factor is described in detail in [119] and has been applied by others investigating diffusion in non-solvent/polymer systems [120]. The form of the correction factor is given in Equation (5-1).

$$D = D_{TC} \frac{d \ln p}{d \ln q} \quad (5-1)$$

where p is the partial pressure of the penetrant, q is the concentration or loading of penetrant in the polymer, and D_{TC} is the thermodynamically corrected diffusivity. The use of the correction factor arises from the non-linearity in the sorption isotherms. All presented diffusion coefficients in this work have been thermodynamically corrected, which in general amounted to dividing the originally calculated diffusion coefficient by a factor of approximately 3 to 4 in the low activity range and by 1 to 2 in the higher activity range, depending on the chemical species.

The diffusion coefficients for C1-C7 alcohols in unmodified Matrimid display a clear trend of decreasing value with increasing alkyl chain length and an approximate exponential dependence on chemical activity. Water is the exception, which decreases as a function of chemical activity due to multi-molecular clustering behavior at higher activities, as referenced in Chapter 4. These trends are also present in the cross-linked Matrimid films for water and C1-C4 alcohols, as shown in Figure 5-9, although propanol and butanol are about an order of magnitude lower than in the unmodified polymer. The pattern drastically changes for C5 and higher alcohols, seemingly exhibiting substantially higher diffusivities. This observation is more apparent in Figure 5-10, which compares the infinite dilution diffusion coefficients for the penetrants in unmodified and cross-linked Matrimid. Although the sorption curve for each activity step change for C5 and higher alcohols appears to be Fickian, it is not clear that the penetrant is truly entering and diffusing throughout the polymer matrix. The relatively very low equilibrium sorption amounts for hexanol

and heptanol in cross-linked Matrimid also arouse skepticism in applying a Fickian or Berens-Hopfenberg type diffusion analysis. Although included here for completeness, the diffusion coefficients for C5 and higher alcohols in cross-linked Matrimid determined in this work should probably be discarded until further work ascertains whether the penetrant is truly entering and diffusing in the film.

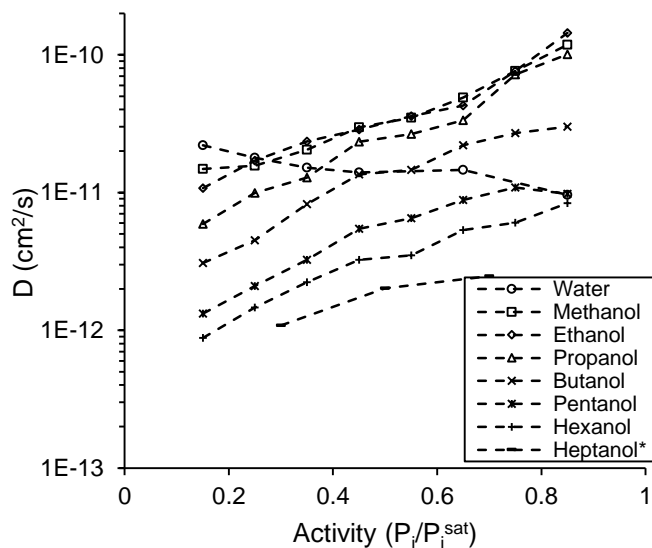


Figure 5-8 - Thermodynamically corrected diffusion coefficients for indicated species in Matrimid as a function of chemical activity at 30 °C. All film thicknesses were $0.26 \pm 0.015 \mu m$, except heptanol, which is marked with an * indicating a film thickness of $0.46 \mu m$. The heptanol calculated diffusion coefficients were multiplied by 0.5 as suggested by the thickness dependence on diffusion coefficients presented in Chapter 4 for the difference between 0.26 and $0.46 \mu m$.

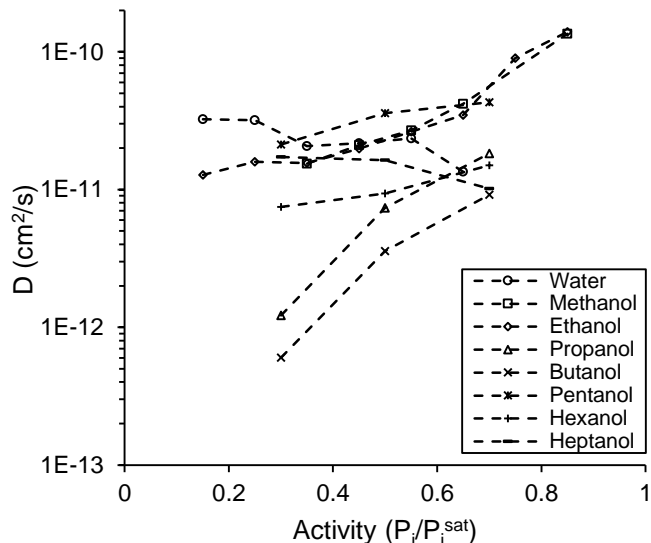


Figure 5-9 - Thermodynamically corrected diffusion coefficients for the indicated species in EDA cross-linked (2 h vapor exposure) Matrimid films of thickness $0.45 \pm 0.05 \mu\text{m}$ at 30°C .

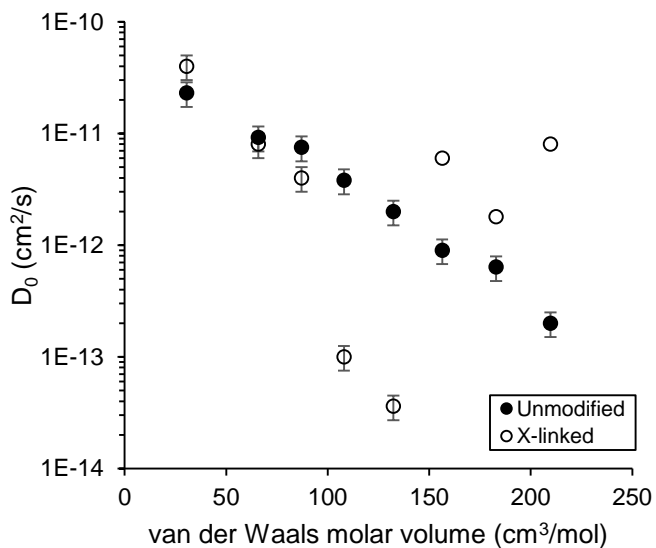


Figure 5-10 - Diffusion coefficients at infinite dilution for water and C1-C7 alcohols plotted at their respective van der Waals molar volumes for unmodified (●) and EDA cross-linked (○) Matrimid films at 30°C . The unmodified films were $0.26 \pm 0.015 \mu\text{m}$ and the cross-linked films were $0.45 \pm 0.05 \mu\text{m}$ in thickness. This difference in thickness was accounted for by multiplying the originally calculated cross-linked diffusion coefficients by 0.5 as suggested by the thickness dependence trend presented in Chapter 4. Error bars determined by varying thickness and time by expected uncertainties when performing the diffusion calculation, which produced a larger error than the standard deviation of three independent experiments and consequently determined diffusion coefficients.

5.4.3.3. Polymer relaxation

Penetrant-induced polymer relaxation is a well-documented phenomenon observed in glassy polymers for a wide variety of penetrants, including noble gases [49], CO₂ [54], water vapor and liquid [52], and organic vapors and liquids [45,123]. It is often classified as non-Fickian diffusion or sorption behavior and is usually observed on orders of magnitude longer time scales than Fickian diffusion processes. The proportion of mass sorption due to penetrant-induced polymer relaxation for an activity step change interval is given as the variable m_R in Equation (4-3) and the associated kinetic parameter describing the relaxation time for that interval is k_R . The calculated relaxation parameters and their exponential extension to infinite dilution are given in Figure 5-11 and Figure 5-12, respectively. It is apparent that water and C1-C3 alcohols in unmodified and cross-linked Matrimid are similar, with significant reduction in value occurring for butanol and higher alcohols. This trend is expected as the existence of cross-linking between polymer chains should lessen and slow the polymer chains' ability to undergo motion. For hexanol and larger penetrants in cross-linked Matrimid where the sorption isotherm is significantly reduced it begins to become trivial to discuss polymer chain relaxation as there is not enough relaxation associated sorption occurring to reliably assign parameters. Nevertheless, the Deborah number calculated to be greater than 100 for all of the penetrants in cross-linked Matrimid for each sorption experiment's respective film thickness above a chemical activity of 0.1. It is suggested that some threshold be established indicating a certain amount of strictly relaxation based sorption in proportion to the diffusive sorption or to the overall total sorption has occurred to allow reliable assignment of relaxation parameters. At this time it is therefore urged to only qualitatively compare the unmodified and cross-linked polymer systems, concluding that penetrants smaller than the chemical cross-linker do not significantly impact the penetrant-induced relaxation

process, while penetrants approximately the size of the cross-linker and larger do lessen and slow the penetrant-induced polymer chain relaxations.

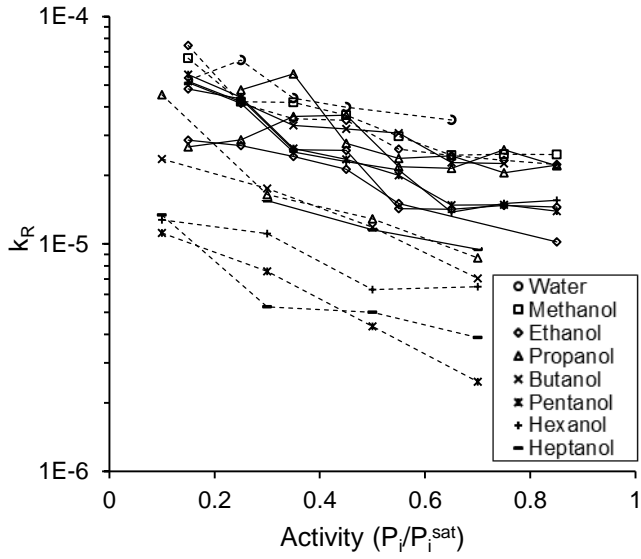


Figure 5-11 - Relaxation parameter, k_R , as a function of chemical activity for unmodified (—) and EDA cross-linked (- - -) Matrimid films at 30 °C.

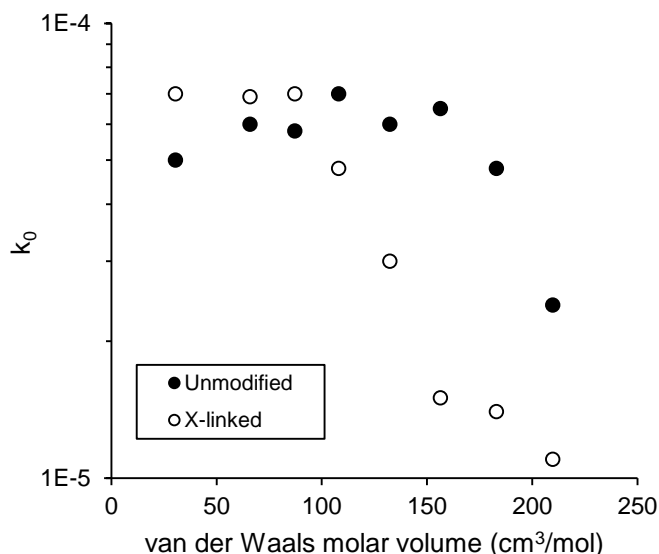


Figure 5-12 - Relaxation parameter, k_R , at infinite dilution of water and C1-C7 alcohols plotted at their respective van der Waals molar volume for unmodified (●) and EDA cross-linked (○) Matrimid films at 30 °C.

5.5. Conclusions

This work has explored the use of ethylenediamine (EDA) as a vapor phase cross-linking agent for Matrimid films in the range 0.25 to 0.7 μm under ambient conditions. The extent of cross-linking was measured using a quartz crystal microbalance to determine the mass of EDA chemically attached to Matrimid polymer chains. The impact of EDA cross-linking on reducing and mitigating the extent of swelling and penetrant-induced relaxation was investigated using water and C1-C7 alcohols as vapor phase penetrants. Sorption isotherms and diffusion coefficients were reported over the chemical activity range 0.2 to 0.8 for the water and alcohol penetrants. It was determined that the sorption, diffusion and penetrant-induced relaxation behavior for water and C1-C3 alcohols was only marginally different for unmodified and cross-linked Matrimid films. Butanol and pentanol alcohols exhibited little change in their respective sorption isotherms, however diffusion coefficients were reduced from $3.8E-12$ and $2E-12$ cm^2/s to $1E-13$ and $3.6E-14$ cm^2/s , respectively. The sorption isotherms for hexanol and heptanol were approximately 90%

reduced in cross-linked versus unmodified Matrimid, which consequently did not allow reliable calculation of diffusion coefficients for the cross-linked films.

Chapter 6 - Future Work

6.1. Introduction

The following five research proposals represent further development and extension of the membrane reactor work conducted for this dissertation. Membrane reactors are still a niche area for heterogeneous catalysis and have in general only been applied to a limited number of mostly model catalytic systems. There is certain possibility for expansion of membrane reactors into new catalytic applications where having control of the delivery rate and location of reactants may offer benefits in terms of lower pressures, concentrations, and/or improved reaction selectivity. Although not the focus of this work, membrane reactors can also be used for selective removal of the formed product in a reactive system thus accomplishing a process intensification combining reaction and separation into one reactor or module. This avenue of research is beneficial for applications where space may be a high priority or the separation step may be enhanced by taking advantage of high concentrations of formed product at the membrane surface. A related use for membrane reactors is utilizing the membrane to selectively remove product from a thermodynamically limited reaction, however this type of application is generally applied to homogeneous catalysis where the membrane is not also functioning as the catalyst support.

6.2. Mixed matrix Matrimid membrane surface hydrophobization for aqueous phase membrane reactor applications

The objective of this first proposed future work is to utilize the favorable aspects of the Ru integrated PTFE membrane reactor and Ru surface coated asymmetric Matrimid membrane reactor, as described in Chapters 2 and 3, respectively, for aqueous phase hydrogenation reactions. A major advantage of the PTFE membrane was its highly hydrophobic character. However, the success of this system at higher temperatures was limited because of its porous nature, which

allowed significant water permeation when a pressure differential was created due to the increasing vapor pressure of water. The porous nature also meant that isolating the Ru catalyst only near the surface in contact with the aqueous phase was not very effective, leaving much of the catalyst mass in the system not actually utilized for reaction. The asymmetric Matrimid membrane partially addressed the limitations of the PTFE membrane reactor considering the dense layer of the Matrimid membrane allowed a pressure differential to be maintained. It also provided a dense surface for Ru coating isolating the Ru at the membrane/aqueous phase interface, thus requiring an order of magnitude less catalyst per membrane area than the PTFE membrane reactor system. Matrimid is, however, inherently highly permeable to water, notably having a water permeability of approximately 1800 Barrer at 150 °C, compared to 150 Barrer for hydrogen [94]. This factor made operating at modestly higher temperatures (> 120 °C) increasingly challenging. Especially considering that the liquid phase organic reactants permeated alongside the water and assumedly had much higher permeabilities when dissolved in water than in their pure state.

The proposed solution to the described challenges for both membrane reactor systems is to fabricate a composite membrane with a porous Matrimid layer and a dense surface layer consisting of a mixed matrix of titania, alumina, or silica nanoparticles in Matrimid. The inorganic nanoparticles can be surface functionalized by attaching highly hydrophobic molecules, namely perfluorinated octyltrichlorosilane (FOTS), as shown in Figure 6-1 [89].

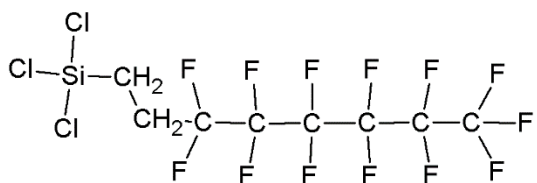


Figure 6-1 - Perfluorinated octyltrichlorosilane (FOTS) used for attachment to titania, alumina, or silica nanoparticles in dense layer of membrane to increase hydrophobicity.

One may wonder, why not use the PTFE material as the porous substrate for the dense mixed matrix Matrimid layer? Indeed, this was attempted several times in the laboratory, but to attain a defect-free dense layer of Matrimid on the PTFE substrate required dense layer thicknesses too large for practical membrane reactor applications. Utilizing a porous Matrimid substrate with a subsequently added dense layer of Matrimid avoids the issue of material compatibility and allows the inorganic nanoparticles to be isolated in the dense surface layer of Matrimid. The dense layer may be integrated onto the porous support by spin-coating, dip-coating, or evaporative coating. An important step to allow deposition of a Matrimid solution onto a Matrimid support is to chemically cross-link the Matrimid support before integrating the dense layer. This would ensure that the solvent used for the Matrimid dense layer would also not dissolve the support layer as it comes into contact. Chapter 5 describes substantial work on cross-linking Matrimid films with ethylenediamine and could easily be extended to porous Matrimid membranes.

Synthesizing titania, alumina, or silica nanoparticles on the order of 20-40 nm seems reasonable according to literature [143,144]. A 0.2 μm dense layer of Matrimid gives a hydrogen permeance of 85 GPU at 35 °C, which is an order of magnitude higher permeance than the Matrimid membranes described in Chapter 3. These dimensions suggest that a high enough loading of nanoparticles in the Matrimid dense layer would allow significant portions of the nanoparticles to be exposed on the membrane surface. This idea allows for investigating performing the hydrophobization of the nanoparticles before or after integration in the dense Matrimid layer. Figure 6-2 shows a schematic of the envisioned dense layer composition with exposed hydrophobized nanoparticles. Depositing the Ru catalyst layer onto the dense Matrimid layer could be accomplished by spin-coating techniques as described in Chapter 4 or by sputter-coating techniques described elsewhere [18-20]. The final membrane reactor should offer

relatively high hydrogen permeance on the order of 100 GPU (as tested at 35 °C), while having reduced water permeation compared to that described in Chapter 3 for the asymmetric Matrimid membranes. These characteristics should allow operation of the membrane reactor at temperatures approaching 200 °C, thus taking advantage of even higher hydrogen permeances and hydrogenation reaction kinetics.

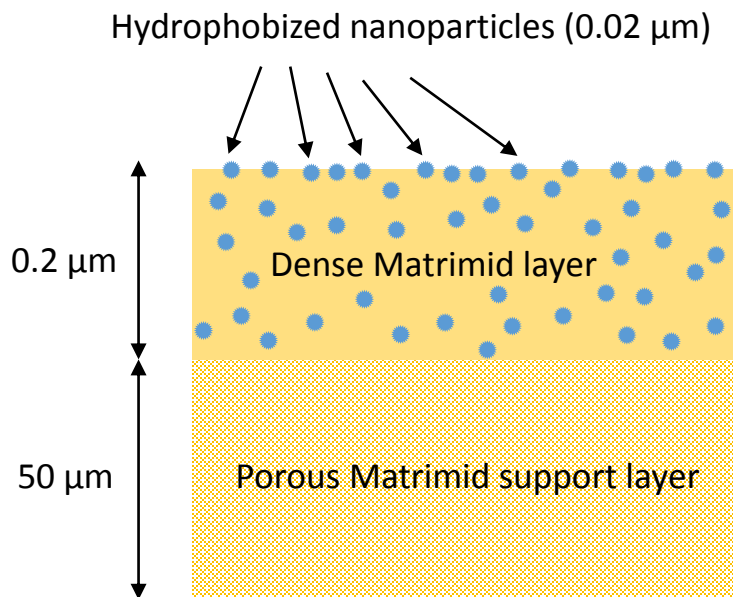


Figure 6-2 - Schematic representation of membrane consisting of a porous Matrimid layer with a hydrophobized nanoparticle loaded dense layer of Matrimid.

6.3. Complexation-induced phase separation formed composite membrane

with dense skin layer loaded with catalyst ions for membrane reactor

application

The proof of concept for the catalyst integrated membrane of this proposed work is described in a recently published work by Klaus-Victor Peinemann, *et al.* [145]. In this work the authors fabricated a composite membrane with a metal loaded dense layer approximately 0.2 μm in thickness using three main steps. First, a polymer dissolved in DMSO was cast as a flat sheet, which ultimately became the porous support layer. The sheet was then dipped into a solution of

DMSO containing the desired metal ion for a short amount of time, on the order of seconds. The polymers used were specifically chosen for their known complexation or chelating behavior when in contact with the metal ions, which induced formation of the thin dense layer. Finally, the composite membrane was immersed in a non-solvent bath to induce phase separation in the polymer support layer. The polymers used were polythiosemicarbazide and polythiourea, both chosen because their chains contain sulfur moieties that strongly interact with the metal ions inducing complexation, or skin formation. It is not clear at this point if these polymers would be a suitable choice for membrane reactor conditions, but surely the idea can be explored for a variety of other polymer/metal ion combinations. Two great advantages of this composite membrane are the high metal loading densities possible in the skin layer (~30 wt%) and the thinness of dense layers achievable and tunable by controlling the exposure time to the metal ion solution, *e.g.* 5 s exposure formed a 200 nm layer. Another benefit is the location of the metal inside the dense layer, which should greatly decrease any leaching that may occur when used in the liquid environments of the membrane reactor. Figure 6-3 and Figure 6-4 show SEM images and schematics of the CIPS formed asymmetric membranes with metal loaded dense layer.

Recalling Chapter 3, when one considers the permeation of the organic reactant, levulinic acid, to be significant, and desirable in the case of the ‘flipped’ membrane configuration, integrating the catalyst inside of the dense layer rather than on the surface does not seem to pose any detriment to the potential catalytic activity of the system. Even when suitable polymers are found for our membrane reactor applications, I certainly do not underestimate the challenges for fabricating defect-free dense layers with substantial hydrogen permeance. My first recommendation for polymer investigation is polybenzimidazole (PBI), as it is relatively chemically inert and thermally stable and our research group has some experience in fabricating

asymmetric membranes with the polymer [146]. As indicated in [146], it was challenging to obtain defect-free asymmetric membranes using the phase-inversion process, so if complexation with a suitable metal ion is achieved, this might offer an alternative route for obtaining defect-free and metal integrated asymmetric PBI membranes for membrane reactor applications. Also, if it is not possible to induce complexation of PBI with a desirable metal ion, there are methods available for adding chemical functional groups to the PBI backbone to achieve the desired polymer properties [147,148]. One notable limitation for applying this system to membrane reactor applications is the location of the metal inside the dense layer of polymer, necessitating permeation of the reactant through the membrane. This implies this membrane is not applicable to systems where no liquid permeation through the membrane occurs, as in the vegetable oil hydrogenation described in [18-20], but rather is applicable to systems where significant permeation of reactant and product through the membrane does occur, as in the aqueous phase hydrogenation of levulinic acid to gamma-valerolactone.

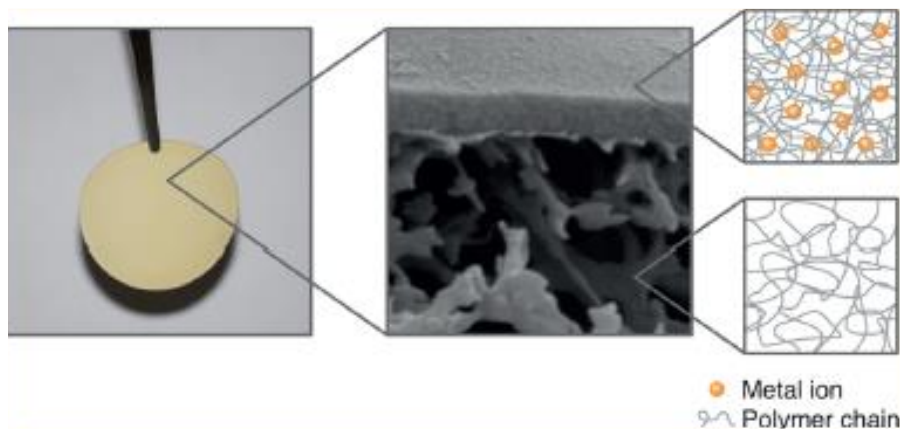


Figure 6-3 - Complexation-induced phase separation composite membrane image and schematic. Image taken from [145].

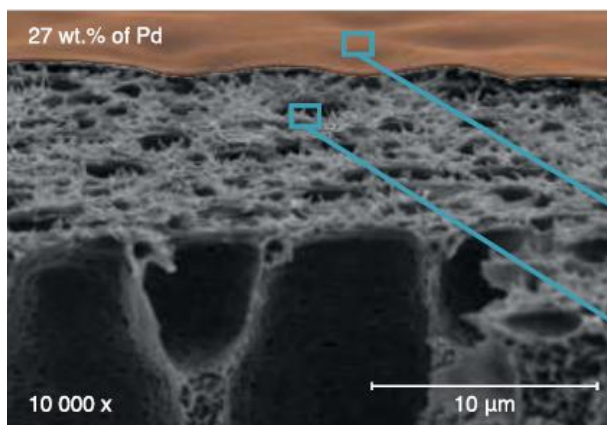


Figure 6-4 - Metal loaded dense layer of CIPS composite membrane. Image taken from [145].

6.4. Conversion of fructose to desirable hydrogenated products using ionic liquid solvents in membrane reactor

The depolymerization and conversion of cellulose to higher valued chemical species having lower oxygen content is usually performed as multiple reaction steps. A popular route is to acid treat the cellulose to depolymerize to glucose monomers. The glucose can be further acid treated to isomerize to fructose and then convert to the platform chemical 5-hydroxymethylfurfural (HMF) [22,23,149-152]. There are then multiple catalytic routes available for converting HMF to other products. If the HMF is acid treated, the primary product is levulinic acid, which is also considered a platform chemical for a variety of other conversions [24,25,30]. One catalytic route for converting HMF that is particularly challenging is its aqueous phase hydrogenation, as HMF tends to polymerize and form insoluble humins in aqueous phase hydrogenation conditions. Consequently, many approaches employ a biphasic reactor system utilizing an organic solvent to prevent HMF polymerization [22,149,150].

An area for biomass conversion that has recently gained a lot of attention is the use of ionic liquids as reaction solvents and catalysts. Certain ionic liquids can replace the function of the acid

catalyst in the depolymerization of cellulose to glucose and can further act as reaction solvent for the conversion of glucose to fructose and fructose to HMF, levulinic acid, and other desirable products, if the appropriate additional catalyst is used [153-159].

Early investigations in my work looked at the aqueous phase hydrogenation of HMF using a ruthenium catalyst coated membrane reactor, but it too suffered from humin formation and rapid catalyst deactivation due to deposited insoluble species, as shown in Figure 6-5.

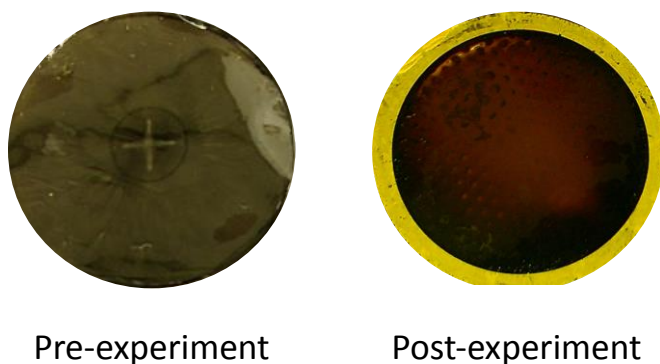


Figure 6-5 - Ruthenium coated membrane before and after use in aqueous phase hydrogenation of HMF reaction.

To remedy the challenge of humin formation, I explored reaction solvents other than water that might also be compatible with Matrimid, the membrane material. As described in Chapter 4, many organic solvents have a high solubility in Matrimid at 30 °C that is exacerbated at higher temperatures. Hence, the progression to exploring the potential use of ionic liquids for the membrane reactor application. There is a niche area in the field of membranes that investigates the use of supported ionic liquid membranes (SILM) in efforts to take advantage of the ionic liquid's potentially superior separation properties. Wickramanayake, *et al.* [160] investigated the use of Matrimid hollow fibers as support for the ionic liquid [HMIM][Tf2N]. Hydrogen and carbon dioxide gas transport properties in the ionic liquid loaded hollow fibers were measured at temperatures up to 150 °C. Marais, *et al.* used the ionic liquids [BMIM]PF₆, [BMIM]BF₄, and

[HMIM]PF₆ in porous Matrimid supports where they investigated the permeation of water, ethanol, and cyclohexane in the SILMs at 25 °C [161]. Santos, *et al.* used [EMIM]OAc and [BMIM]OAc in porous polyvinylidene fluoride membranes for gas separations up to 60 °C [162].

There may be concern that the thermophysical properties of the ionic liquid are not suitable for the membrane reactor application, including viscosity and thermal degradation. Table 6-1 shows viscosity data at 25 and 90 °C, unless otherwise indicated. Several studies that use [EMIM]OAc and [BMIM]OAc also report on the thermal degradation of the ionic liquids based on TGA data. Greater than 5 wt% mass loss does not begin in [EMIM]OAc until 220 °C and in [BMIM]OAc until 285°C [163].

Table 6-1 - Viscosity of select ionic liquids and other liquids for comparison.

Ionic Liquid Symbol	Chemical Name	Viscosity, 25 °C (cP)	Viscosity, 90 °C (cP)
[EMIM]OAc	1-Ethyl-3-methylimidazolium acetate	143.6	10.95
[BMIM]OAc	1-Butyl-3-methylimidazolium acetate	297	15
[BMIM]BF ₄	1-Butyl-3-methylimidazolium tetrafluoroborate	94.9	9.36
[HMIM]PF ₆	1-Hexyl-3-methylimidazolium phosphohexafluorate	411	18
[BMIM]Cl	1-Butyl-3-methylimidazolium chloride	solid at room temp	
[EMIM]EtSO ₄	1-Ethyl-3-methylimidazolium ethyl sulfate	122.4	14.3 (80 °C)
[HMIM][Tf ₂ N]	1-Hexyl-3-methylimidazolium bis(trifluoromethylsulfonyl)imide		10.95
[BMIM]PF ₆	1-butyl-3-methylimidazolium hexafluorophosphate	109 (313 K) [164]	24 (80 °C)
Water		0.89	
Glycerol		1200	
n-Octanol		7.39	4.53 (40 °C)

References: [163-165]

Despite some researchers' reported success with using [EMIM]OAc in combination with Matrimid at elevated temperatures (150 °C), the reactor experiments I performed with [EMIM]OAc as the reaction solvent at 90 °C led to membrane failure and dissolution in a matter of hours, as shown in Figure 6-6.

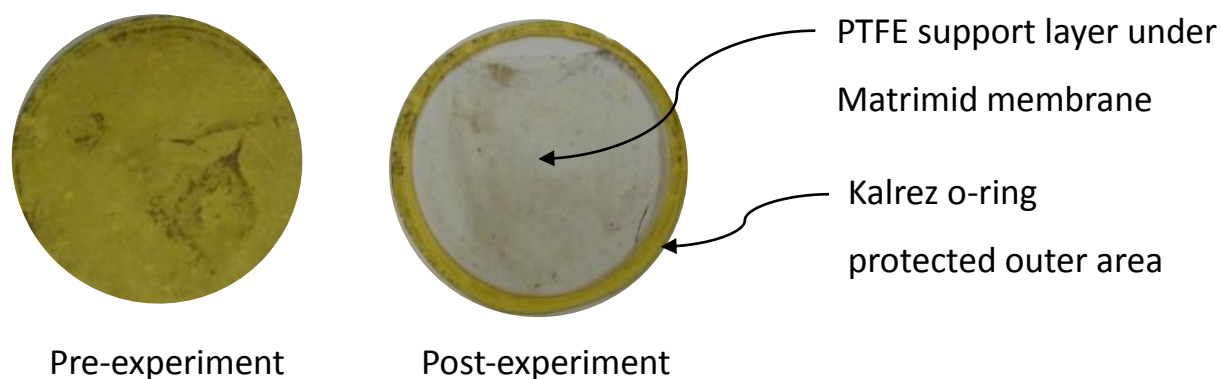


Figure 6-6 - Membrane used in membrane reactor with [EMIM]OAc as solvent. Matrimid dissolved in the ionic liquid at 90 °C.

I have three specific proposals for future work related to using ionic liquids in membrane reactor applications. First, I propose the investigation of the compatibility of [HMIM][Tf2N] with Matrimid at elevated temperatures and its potential use as a reaction solvent for the membrane reactor three-phase hydrogenation of HMF or levulinic acid. The higher molecular weights of the [HMIM] and [Tf2N] ions as compared to [EMIM] and OAc, respectively, initially suggest they may be less likely to solubilize Matrimid. Also, applying the ethylenediamine cross-linking techniques described in Chapter 5 should greatly enhance the chemical stability of the Matrimid membranes.

Second, as shown in Figure 6-6, the porous PTFE membrane was entirely intact after use with [EMIM]OAc at 90 °C. With the notable success of the PTFE membrane reactor described in Chapter 2, it seems possible to use the Ru coated PTFE membrane reactor for three-phase hydrogenation reactions with an ionic liquid as solvent for HMF and levulinic acid hydrogenation.

If the heterogeneous reaction of hydrogenating HMF or levulinic acid is successful, it seems natural to extend the reaction pathway to begin with fructose, for which there is much documented success at converting fructose to HMF using ionic liquids. The ionic liquid would act as the solvent and homogeneous catalyst for the conversion of fructose to HMF. Subsequently the HMF could undergo further homogeneous conversion to levulinic acid or be immediately hydrogenated by the ruthenium catalyst located at the membrane surface where hydrogen is available from permeation through the membrane.

Third, one may also use a ceramic membrane reactor with ionic liquid as solvent. The ceramic should be very chemically and thermally stable in the presence of a variety of ionic liquids, with the only foreseeable complication arising from the porous nature of the ceramic membrane. I have used composite ceramic membranes consisting of a porous alumina support layer with a thin titania layer with pore size of approximately 20 nm (1 kDa molecular weight cut-off). These ceramic membranes were 0.5 cm thick and purchased from Sterlitech. The pores are not quite small enough to prevent intrusion of [HMIM][Tf2N], however, surface functionalizing the titania layer with FOTS, as described above, should narrow the pores. The FOTS addition will also provide substantial hydrophobic character to the membrane surface, which should enhance the barrier to ionic liquid intrusion much like the PTFE membrane shown in Figure 6-6. Integrating a metal catalyst to the ceramic membrane surface may be achieved with a variety of catalyst coating techniques and should offer better coating and adhesion characteristics as compared to the polymeric membrane surface [166,167].

6.5. Kinetic and equilibrium sorption of liquid and vapor penetrants in P84, PBI, and blended polymers using QCM

Extension of the sorption work on Matrimid described in Chapters 4 and 5 to other polymer/penetrant systems should be relatively straightforward, with perhaps the only challenge being forming and attaching thin films of the other polymers to the QCM crystals. Matrimid has the advantage of being soluble in dichloromethane, a highly volatile solvent, which makes spin-coating the crystals relatively simple. P84 and PBI are not soluble in any volatile solvents, so other coating methods must be used, with the only requirement being that the thin film be less than 5 μm and mechanically adhere to the crystal surface. This should be possible by dissolving P84 or PBI in an appropriate non-volatile solvent, coating the crystal with thin layer of polymer solution, and using vacuum oven drying to remove the solvent, leaving a thin, dense film on the crystal surface. This will require determining what concentration of polymer solution to use and the appropriate temperature for the vacuum oven drying, but certainly seems possible if these parameters are optimized.

This proposed work benefits from having the entire sorption experimental set-up currently designed and functioning appropriately, in addition to having all of the mathematical data analysis already programmed in MATLAB software. MATLAB is a very appropriate choice for analyzing this data as it has many options for applying non-linear regression methods on the sorption data to obtain diffusion coefficients, relaxation parameters, and other parameters depending on the sorption model applied. It is also very well suited to handle the massive amount of data collected by the QCM, which is on the order of one million data points per one penetrant/polymer sorption experiment assuming data sampling at 1 sample/second. The high sampling rate is needed to capture the relatively fast diffusion processes, which occur over approximately 10 to 1000 seconds

depending on the film thickness, but the sampling must continue for 12-48 hours per 0.1 activity step change to capture the longer penetrant-induced polymer relaxation sorption behavior.

6.6. Controlling polymer swelling and cross-linking initiation to produce membranes with different molecular weight cut-offs

As shown in Chapter 4 the relaxation or swelling kinetics for exposing Matrimid to vapor phase penetrants occurs over an approximate 48 h range. Chapter 5 gave kinetic data for the ethylenediamine vapor phase cross-linking of Matrimid, which occurs over the range of approximately 4 hours. This order of magnitude difference in times for these processes implies that one could initiate the cross-linking reaction in various states of swollen polymer. Having this control suggests that one could obtain different membrane permeation properties depending on how swollen the polymer was at the time of cross-linking. Essentially what one would be doing is controlling the pores or expanded volume elements within the polymer that become ‘locked’ in place when the polymer chains become cross-linked. Various degrees of swelling could be obtained by initiating the cross-linking reaction at a specified time during the swelling process or by using different penetrants to induce different swelling behaviors. In principle this technique could occur in either liquid or vapor phase swelling and cross-linking, however to avoid mass-transfer issues I would suggest inducing the swelling using vapor phase penetrants, as described in Chapter 4, and using vapor phase ethylenediamine cross-linking, as described in Chapter 5.

It seems this technique would be more efficacious for liquid separations where there exists a much larger range of kinetic diameters of penetrating species and where controlling precision in the molecular weight cut-off is often desired. Figure 6-7 shows a schematic representation of swelling the polymer matrix to different extents and then ‘locking’ in the expanded volume elements with the vapor phase cross-linking agent.

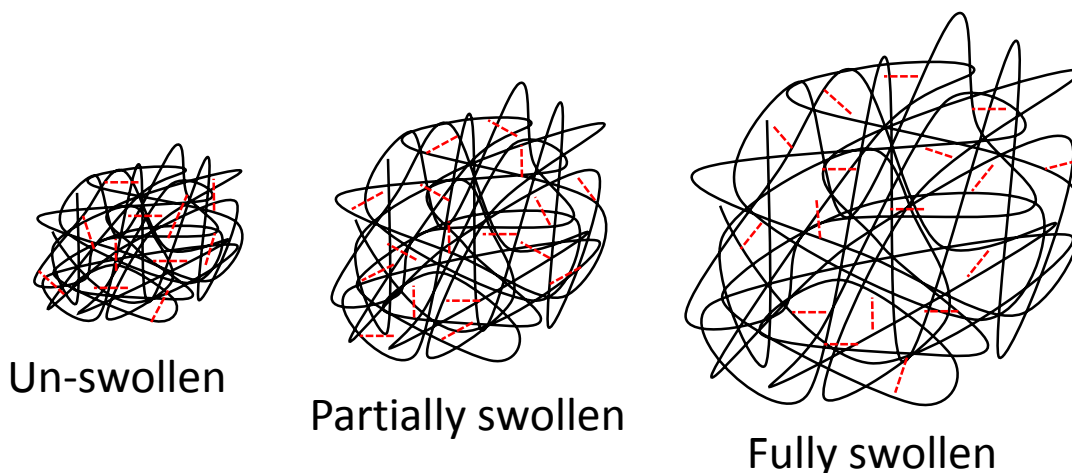


Figure 6-7 – Schematic of polymer matrix swollen to different extents and cross-linked in the swollen state effectively ‘locking’ in the relative expanded volume elements within the matrix. (—) are the polymer chains and (- - -) indicates cross-linking.

6.7. Effect of pH on catalytic activity and membrane permeability

The role of solution pH on the activity of the ruthenium catalyst integrated in the PTFE membrane and Matrimid membrane was not examined in the membrane reactor work presented in Chapters 2 and 3. In both chapters the experimental conditions involved using a relatively dilute solution of levulinic acid in water (2-3 wt%), so the solution pH was not expected to change considerably over the course of the reactions. Levulinic acid has a pKa value of 4.6, so it is expected to be in anionic form in the unbuffered aqueous solution. Literature sources are available that have examined the effect of pH on reaction kinetics for the hydrogenation of levulinic acid [27] using Ru/C, the hydrogenation of HMF using Ru on a variety of supports (CeO_x, C, γ -alumina, Mg-Zr, and silica) [168], and the hydrogenation of benzylidene acetone using a ruthenium complex [169]. Similar investigations could certainly be extended to examining varying the solution pH and its effect on the kinetics of levulinic acid hydrogenation using ruthenium on membrane support, however a related question may be how the solution pH and thus the ionic form of levulinic acid changes the permeability of levulinic acid and gamma-valerolactone in the

membrane material, whether it is PTFE or Matrimid. Recalling the ‘flipped’ configuration of the membrane reactor presented in Section 3.4.2.3 where it was desirable to have levulinic acid permeation through the membrane to reach the catalyst in the gas phase location, one may propose using an anion exchange membrane (fixed positive charges) to enhance the transport of deprotonated levulinic acid through the membrane [170]. The proposal for this future work project is to identify a suitable anion exchange membrane to allow significant transport of levulinic acid while also not being too permeable to the reaction solvent (water in the case of Chapters 2 and 3). The next question would be characterize the transport properties of all the species present for this reactive system, *e.g.* water, LevA, GVL, H₂, in the membrane and determine its suitability for deposition of ruthenium catalyst. Varying the pH of the feed solution would dictate the ionic form of levulinic acid and change its relative permeation properties.

Chapter 7 - Conclusions

Membrane reactors offer a novel approach for performing three-phase hydrogenation reactions utilizing a thin, yet dense gas/liquid separating layer that also functions as the solid catalyst support. Appropriately selecting and tailoring the membrane material allows abundant and selective transport of the hydrogen through the membrane to reach catalytic sites at the membrane/liquid interface. The reaction studied in this work was the hydrogenation of levulinic acid in aqueous solution to produce gamma-valerolactone using the noble metal ruthenium as the catalyst. Two very different polymeric membranes, porous polytetrafluoroethylene and asymmetric integrally-skinned Matrimid membranes, were studied for this reaction application, yet the fundamental function of both was similar. Both membranes functioned as aqueous phase barriers, while allowing hydrogen to selectively permeate to reach catalytic sites integrated in the membrane. Both membrane reactors were successful at converting levulinic acid to gamma-valerolactone, although the PTFE membrane reactor exhibited reaction rates nearly 50-fold greater and at a lower temperature, 90 versus 120 °C. This difference in reaction rate is attributed to the several orders of magnitude greater hydrogen permeance of the porous PTFE compared to the asymmetric Matrimid membrane. However, the Matrimid membrane system is more robust in terms of having control over the hydrogen permeance, isolating the catalyst specifically at the liquid/membrane interface, and the potential for use of other reaction solvents than water and operation in temperatures upwards of 200 °C.

Concurrent studies to the membrane reactor work focused on characterizing the effect and extent of a range of liquid and vapor sorbing chemical species in Matrimid. The goal of this work was to identify liquid chemicals other than water appropriate for use as reaction solvents in the Matrimid membrane reactor system and to quantitatively describe the solvent/polymer sorption

and transport thermodynamics. Equilibrium liquid sorption in Matrimid was measured for approximately 20 different liquid chemicals and equilibrium and kinetic vapor sorption over the entire activity range was measured for C1-C6 alcohols. Diffusion coefficients, sorption coefficients, and relaxation parameters were regressed from the sorption data. A quartz crystal microbalance was the primary measuring device for vapor sorption in submicron-scale thin Matrimid dense films. A final study was performed examining how chemically cross-linking Matrimid polymer chains with ethylenediamine impacts the sorption behavior of C1-C6 alcohols. Cross-linking Matrimid with ethylenediamine had the greatest impact on larger chain alcohol sorption (C4 and higher) and appears to be a promising technique for improving the Matrimid membrane reactor system and extending its applicability to more reaction solvents.

References

- [1] NIH, Kidney Disease Statistics for the United States, 2015.
- [2] DOE, Annual Energy Outlook, Natural Gas, 2015.
- [3] R.W. Baker, Membrane Technology and Applications, West Sussex, England, John Wiley & Sons, Ltd, 2004.
- [4] J. Wijmans, R.W. Baker. The solution-diffusion model: a review. *J.Membr.Sci.*, 107 (1995) 1.
- [5] W.J. Koros, G.K. Fleming. Membrane-based gas separation. *J. Membr. Sci.*, 83 (1993) 1.
- [6] P.N. Rylander, Catalytic Hydrogenation in Organic Syntheses, New York, New York, Academic Press, Inc., 1979.
- [7] L.B. Datsevich, Conventional Three-Phase Fixed-Bed Technologies, New York, Springer, 2012.
- [8] M.P. Dudukovic. Multiphase catalytic reactors: A perspective on current knowledge and future trends. *Catalysis reviews.Science and engineering*, 44 (2002) 123.
- [9] M.P. Dudukovic, F. Larachi, and P.L. Mills. Multiphase reactors – revisited. *Chemical engineering science*, 54 (1999) 1975.
- [10] I. Vankelecom, Polymeric Membranes in Catalytic Reactors, *Chem. Rev.*, (2002) 3779.
- [11] J. Vital, J.M. Sousa, Polymeric membranes for membrane reactors, in A. Basile (Ed.), *Handbook of Membrane Reactors*, Cambridge, UK, Woodhead Publishing Limited, 2013, pp. 3-41.
- [12] R. Dittmeyer. A Review of Catalytic Membrane Layers for Gas/Liquid Reactions. *Topics in catalysis*, 29 (2004) 3.
- [13] V. Gryaznov. Reactors with metal and metal-containing membranes. *Chemical industries*, 110 (2006) 579.
- [14] L. Brandão, D. Fritsch, A.M. Mendes, and L.M. Madeira, Propylene Hydrogenation in a Continuous Polymeric Catalytic Membrane Reactor, *Ind. Eng. Chem. Res.*, (2007) 5278.
- [15] L. Brandão, L.M. Madeira, and A.M. Mendes. Propyne hydrogenation in a continuous polymeric catalytic membrane reactor. *Chemical Engineering Science*, 62 (2007) 6768.
- [16] A. Schmidt, R. Haidar, and R. Schomäcker. Selectivity of partial hydrogenation reactions performed in a pore-through-flow catalytic membrane reactor. *Catalysis Today*, 104 (2005) 305.

- [17] D. Fritsch, G. Bengtson. Catalytic polymer membranes for high temperature hydrogenation of viscous liquids. *Advanced engineering materials*, 8 (2006) 386.
- [18] D. Singh, M.E. Rezac, and P.H. Pfromm, Partial Hydrogenation of Soybean Oil with Minimal Trans Fat Production Using a Pt-Decorated Polymeric Membrane Reactor, *Journal of the American Oil Chemists' Society*, (2009) 93.
- [19] D. Singh, M.E. Rezac, and P.H. Pfromm. Overcoming mass-transfer limitations in partial hydrogenation of soybean oil using metal-decorated polymeric membranes. *AIChE J.*, 57 (2010) 2450.
- [20] D. Singh, M.E. Rezac, and P.H. Pfromm. Partial hydrogenation of soybean oil using metal-decorated integral-asymmetric polymer membranes: Effects of morphology and membrane properties. *J. Membr. Sci.*, 348 (2010) 99.
- [21] V.V. Volkov, I.V. Petrova, V.I. Lebedeva, V.I. Roldughin, and G.F. Tereschenko, *Palladium-loaded polymeric membranes for hydrogenation in catalytic membrane reactors*, Wiley, 2011.
- [22] A.A. Rosatella, S.P. Simeonov, R.F. Frade, and C.A. Afonso, 5-Hydroxymethylfurfural (HMF) as a building block platform: Biological properties, synthesis and synthetic applications. *Green Chemistry*, (2011) 754.
- [23] R. van Putten, van der Waal, Jan C, E. de Jong, C. Rasrendra, H. Heeres, and J. de Vries. Hydroxymethylfurfural, A Versatile Platform Chemical Made from Renewable Resources. *Chem.Rev.*, 113 (2013) 1499.
- [24] D.M. Alonso, S.G. Wettstein, and J.A. Dumesic. Gamma-valerolactone, a sustainable platform molecule derived from lignocellulosic biomass. *Green Chem.*, 15 (2013) 584.
- [25] B. Girisuta, Girisuta, L. P. B. M., H.J. Janssen, and Heeres. A kinetic study on the decomposition of 5-hydroxymethylfurfural into levulinic acid. *Green Chem.*, 8 (2006) 701.
- [26] J. Bozell, G. Petersen. Technology development for the production of biobased products from biorefinery carbohydrates—the US Department of Energy’s “Top 10” revisited. *Green Chem.*, 12 (2010) 539.
- [27] O.A. Abdelrahman, A. Heyden, and J.Q. Bond. Analysis of Kinetics and Reaction Pathways in the Aqueous-Phase Hydrogenation of Levulinic Acid To Form γ -Valerolactone over Ru/C. *ACS catalysis*, 4 (2014) 1171.

- [28] O.A. Abdelrahman, H.Y. Luo, A. Heyden, Y. Román-Leshkov, and J.Q. Bond. Toward rational design of stable, supported metal catalysts for aqueous-phase processing: Insights from the hydrogenation of levulinic acid. *Journal of catalysis*, 329 (2015) 10.
- [29] M. Chalid, A.A. Broekhuis, and H.J. Heeres. Experimental and kinetic modeling studies on the biphasic hydrogenation of levulinic acid to γ -valerolactone using a homogeneous water-soluble Ru-(TPPTS) catalyst. *Journal of molecular catalysis.A, Chemical*, 341 (2011) 14.
- [30] L. Corbel-Demilly, B. Ly, D. Minh, B. Tapin, C. Especel, F. Epron, et al. Heterogeneous Catalytic Hydrogenation of Biobased Levulinic and Succinic Acids in Aqueous Solutions. *ChemSusChem*, 6 (2013) 2388.
- [31] Y. Yao, Z. Wang, S. Zhao, Z. Wu, and M. Zhang. A stable and effective Ru/polyethersulfone catalyst for levulinic acid hydrogenation to γ -valerolactone in aqueous solution. *Catalysis today*, 234 (2014) 245.
- [32] W. Luo, U. Deka, A.M. Beale, E.R.H. van Eck, P.C.A. Bruijninx, and B.M. Weckhuysen. Ruthenium-catalyzed hydrogenation of levulinic acid: Influence of the support and solvent on catalyst selectivity and stability. *Journal of catalysis*, 301 (2013) 175.
- [33] P.P. Upare, J. Lee, D. Hwang, S.B. Halligudi, Y. Hwang, and J. Chang, Selective hydrogenation of levulinic acid to γ -valerolactone over carbon-supported noble metal catalysts, *Journal of industrial and engineering chemistry*, 17 (2011) 287.
- [34] V. Swarna Jaya, M. Sudhakar, S. Naveen Kumar, and A. Venugopal, Selective hydrogenation of levulinic acid to γ -valerolactone over a Ru/Mg-LaO catalyst, *RSC Advances*, 5 (2015) 9044.
- [35] C. Ortiz-Cervantes, J.J. Garcia, Hydrogenation of levulinic acid to γ -valerolactone using ruthenium nanoparticles, *Inorganica chimica acta*, 397 (2013) 124.
- [36] M. Sudhakar, M. Lakshmi Kantam, V. Swarna Jaya, R. Kishore, K.V. Ramanujachary, and A. Venugopal, Hydroxyapatite as a novel support for Ru in the hydrogenation of levulinic acid to γ -valerolactone, *Catalysis communications*, 50 (2014) 101.
- [37] J.M. Tukacs, R.V. Jones, F. Darvas, G. Dibó, G. Lezsák, and L.T. Mika. Synthesis of γ -valerolactone using a continuous-flow reactor. *RSC Advances*, 3 (2013) 16283.
- [38] M. Selva, M. Gottardo, and A. Perosa. Upgrade of Biomass-Derived Levulinic Acid via Ru/C-Catalyzed Hydrogenation to $\hat{\text{I}}^{\beta}$ -Valerolactone in Aqueous Organic-Ionic Liquids Multiphase Systems. *ACS Sustainable Chem.Eng.*, 1 (2013) 180.

- [39] L. Corbel-Demaiilly, B. Ly, D. Minh, B. Tapin, C. Especel, F. Epron, et al. Heterogeneous Catalytic Hydrogenation of Biobased Levulinic and Succinic Acids in Aqueous Solutions. *ChemSusChem*, 6 (2013) 2388.
- [40] J. Tan, J. Cui, T. Deng, X. Cui, G. Ding, Y. Zhu, et al, Water-Promoted Hydrogenation of Levulinic Acid to γ -Valerolactone on Supported Ruthenium Catalyst, *ChemCatChem*, 7 (2015) 508.
- [41] Y. Yang, C. Sun, Y. Ren, S. Hao, and D. Jiang. New route toward building active ruthenium nanoparticles on ordered mesoporous carbons with extremely high stability. *Scientific Reports*, 4 (2014) 4540.
- [42] C. Delhomme, L. Schaper, M. Zhang-Pressé, G. Raudaschl-Sieber, D. Weuster-Botz, and F.E. Kuehn, Catalytic hydrogenation of levulinic acid in aqueous phase, *Journal of organometallic chemistry.*, 724 (2013) 297.
- [43] A. Ruppert, A.M. Ruppert, M. Grams, J. Jędrzejczyk, N. Matras-Michalska, K. Keller, et al. Titania-Supported Catalysts for Levulinic Acid Hydrogenation: Influence of Support and its Impact on γ -Valerolactone Yield. *ChemSusChem*, 8 (2015) 1538.
- [44] H. Mehdi, V. Fabos, R. Tuba, A. Bodor, L.T. Mika, and I.T. Horvath. Integration of homogeneous and heterogeneous catalytic processes for a multi-step conversion of biomass: from sucrose to levulinic acid, β -valerolactone, 1,4-pentanediol, 2-methyl-tetrahydrofuran, and alkanes. *Top.Catal.*, 48 (2008) 49.
- [45] A.R. Berens, H.B. Hopfenberg. Diffusion and relaxation in glassy polymer powders: 2. Separation of diffusion and relaxation parameters. *Polymer*, 19 (1978) 489.
- [46] L. Hesse, S. Naem, and G. Sadowski. VOC sorption in glassy polyimides—Measurements and modeling. *J. Membr. Sci.*, 415 (2012) 596.
- [47] F. Doghieri, M. De Angelis, M. Baschetti, and G. Sarti. Solubility of gases and vapors in glassy polymers modelled through non-equilibrium PHSC theory. *Fluid Phase Equilib.*, 241 (2006) 300.
- [48] E.M. Davis, M. Minelli, B. Giacinti Marco, and Y.A. Elabd. Non-Fickian Diffusion of Water in Polylactide. *Ind Eng Chem Res*, 52 (2013) 8664.
- [49] T. Visser, M. Wessling. When Do Sorption-Induced Relaxations in Glassy Polymers Set In? *Macromolecules*, 40 (2007) 4992.

- [50] J. Crank, G.S. Park, Diffusion in Polymers, London, Great Britian, Academic Press Inc., 1968.
- [51] R. Barrer. Diffusion and permeation in heterogeneous media. Diffus. Polym., (1968) 165.
- [52] S. Burgess, D. Mikkilineni, D. Yu, D. Kim, C. Mubarak, R. Kriegel, et al. Water sorption in poly(ethylene furanoate) compared to poly(ethylene terephthalate). Part 1: Equilibrium sorption. Polymer, 55 (2014) 6861.
- [53] C. Zhang, B.P. Cappleman, M. Defibaugh-Chavez, and D.H. Weinkauf. Glassy polymer-sorption phenomena measured with a quartz crystal microbalance technique. Journal of Polymer Science: Part B, Polymer Physics, 41 (2003) 2109.
- [54] X. Li, G. Cao, L. Chen, R. Zhang, H. Liu, and Y. Shi. Study of the Anomalous Sorption Behavior of CO₂ into Poly(methyl methacrylate) Films in the Vicinity of the Critical Pressure and Temperature Using a Quartz Crystal Microbalance (QCM). Langmuir, 29 (2013) 14089.
- [55] R. Mueller, S. Zhang, C. Zhang, R. Lively, and S. Vasenkov. Relationship between long-range diffusion and diffusion in the ZIF-8 and polymer phases of a mixed-matrix membrane by High field NMR diffusometry. J.Membr.Sci., (2014).
- [56] J. Jansen, K. Friess, and E. Drioli. Organic vapour transport in glassy perfluoropolymer membranes: A simple semi-quantitative approach to analyze clustering phenomena by time lag measurements. J. Membr. Sci., 367 (2011) 141.
- [57] S. Burgess, O. Karvan, J.R. Johnson, R. Kriegel, and W. Koros. Oxygen sorption and transport in amorphous poly(ethylene furanoate). Polymer, 55 (2014) 4748.
- [58] R.M. Barrer, J.A. Barrie, and J. Slater, Sorption and diffusion in ethyl cellulose. III. Comparison between ethyl cellulose and rubber, Journal of polymer science, 27 (1958) 177.
- [59] W.J. Koros, Model for sorption of mixed gases in glassy polymers, Journal of polymer science., 18 (1980) 981.
- [60] F. Doghieri, G.C. Sarti, Nonequilibrium Lattice Fluids: A Predictive Model for the Solubility in Glassy Polymers, Macromolecules, (1996) 7885.
- [61] I.C. Sanchez, R.H. Lacombe. Statistical thermodynamics of polymer solutions. American Chemical Society, 11 (1978) 1145.
- [62] L. Banda, M. Alcoutlabi, and G.B. McKenna. Errors induced in quartz crystal mass uptake measurements by nongravimetric effects: Considerations beyond the EerNisse caution. Journal of polymer science.Part B, Polymer physics, 44 (2006) 801.

- [63] G. Sauerbrey. Verwendung von Schwingquarzen zur Wagung dünner Schichten und zur Mikrowagung. *European physical journal.A, Hadrons and nuclei*, 155 (1959) 206.
- [64] P. Hesketh, S. Nair, K. McCarley, M. Navaei, K. Bagnall, and A. Venkatasubramanian, High-pressure quartz crystal microbalance, , Google Patents, US8718956 B2, 2014.
- [65] G.C. Abuin, M. Cecilia Fuertes, and H.R. Corti. Substrate effect on the swelling and water sorption of Nafion nanomembranes. *J. Membr. Sci.*, 428 (2013) 507.
- [66] E.M. Davis, M. Minelli, M.G. Baschetti, G.C. Sarti, and Y.A. Elabd. Nonequilibrium Sorption of Water in Polylactide. *Macromolecules*, 45 (2012) 7486.
- [67] P. Palmas, J. Palmas, B. Klingenfus, E. Vedeau, P. Girard, L. Montmeat, et al. A simple thermodynamic approach to predict responses from polymer-coated quartz crystal microbalance sensors exposed to organic vapors. *Talanta*, 115 (2013) 616.
- [68] B. Pejicic, E. Crooke, L. Boyd, C. Doherty, A. Hill, M. Myers, et al. Using plasticizers to control the hydrocarbon selectivity of a poly(methyl methacrylate)-coated quartz crystal microbalance sensor. *Anal. Chem.*, 84 (2012) 8564.
- [69] J. Michael, L. Schönzart, I. Israel, D. Scharnweber, H. Worch, U. Hempel, et al. Oligonucleotide-RGD Peptide Conjugates for Surface Modification of Titanium Implants and Improvement of Osteoblast Adhesion. *Bioconjug.Chem.*, 20 (2009) 710.
- [70] K.A. Marx. Quartz Crystal Microbalance: A Useful Tool for Studying Thin Polymer Films and Complex Biomolecular Systems at the Solution-Surface Interface. *Biomacromolecules*, 4 (2003) 1099.
- [71] G. Chen, C. Scholes, C. Doherty, A. Hill, G. Qiao, and S. Kentish. The thickness dependence of Matrimid films in water vapor permeation. *Chem.Eng.J.*, 209 (2012) 301.
- [72] S. Shishatskiy, C. Nistor, M. Popa, S.P. Nunes, and K.V. Peinemann. Polyimide asymmetric membranes for hydrogen separation: influence of formation conditions on gas transport properties. *Advanced engineering materials*, 8 (2006) 390.
- [73] K. Vanherck, G. Koeckelberghs, and I.F. Vankelecom. Crosslinking polyimides for membrane applications: A review. *Progress in polymer science*, (2012).
- [74] K. Vanherck, P. Vandezande, S.O. Aldea, and I.F. Vankelecom. Cross-linked polyimide membranes for solvent resistant nanofiltration in aprotic solvents. *J. Membr. Sci.*, 320 (2008) 468.

- [75] I. Valtcheva, S. Kumbharkar, J. Kim, Y. Bhole, and A. Livingston. Beyond polyimide: Crosslinked polybenzimidazole membranes for organic solvent nanofiltration (OSN) in harsh environments. *J. Membr. Sci.*, 457 (2014) 62.
- [76] K. Hendrix, K. Vanherck, and I.F.J. Vankelecom. Optimization of solvent resistant nanofiltration membranes prepared by the in-situ diamine crosslinking method. *J. Membr. Sci.*, 421-422 (2012) 15.
- [77] J. da Silva Burgal, L.G. Peeva, S. Kumbharkar, and A. Livingston. Organic solvent resistant poly(ether-ether-ketone) nanofiltration membranes. *Journal of membrane science*, 479 (2015) 105.
- [78] J.F. Kim, G. Székely, I.B. Valtcheva, and A.G. Livingston, Increasing the sustainability of membrane processes through cascade approach and solvent recovery-pharmaceutical purification case study. *Green Chem.*, (2013) 133.
- [79] M. Wikol. Expanded polytetrafluoroethylene membranes and their applications. *Drugs Pharm.Sci.*, 174 (2008) 619.
- [80] J. Goldstein, D. Newbury, D. Joy, C. Lyman, P. Echline, E. Lifshin, et al, Generation of X-Rays in the SEM Specimen, in Anonymous , *Scanning Electron Microscopy and X-Ray Microanalysis*, New York, NY, Springer, 2003, pp. 286.
- [81] Z. Zhang, J.E. Jackson, and D.J. Miller. Kinetics of Aqueous-Phase Hydrogenation of Lactic Acid to Propylene Glycol. *Ind Eng Chem Res*, 41 (2002) 691.
- [82] U.K. Singh, Vannice, and M. Albert. Kinetics of liquid-phase hydrogenation reactions over supported metal catalysts — a review. *Applied catalysis.A, General*, 213 (2001) 1.
- [83] A. Tokarev, K. Friess, J. Machkova, M. Šipek, and Y. Yampolskii. Sorption and diffusion of organic vapors in amorphous Teflon AF2400. *Journal of Polymer Science: Part B, Polymer Physics*, 44 (2006) 832.
- [84] N. Cioffi, L. Torsi, I. Farella, D. Altamura, A. Valentini, M. Quinto, et al. The swelling of vapor-sensitive fluoropolymers modified with metal nanoparticles: interpretation of the material–vapor interaction mechanism. *Sensors and actuators.B, Chemical*, 100 (2004) 9.
- [85] Y. Chen, D.J. Miller, and J.E. Jackson, Kinetics of Aqueous-Phase Hydrogenation of Organic Acids and Their Mixtures over Carbon Supported Ruthenium Catalyst, *Ind. Eng. Chem. Res.*, (2007) 3334.

- [86] U.K. Singh, M.A. Vannice, Kinetics of liquid-phase hydrogenation reactions over supported metal catalysts - a review, *Applied catalysis A: General*, 213 (2001) 1.
- [87] O.M. Ilinitch, P.A. Simonov, and F.P. Cuperus. Nanosize palladium loaded catalytic membrane: preparation and cis-trans selectivity in hydrogenation of sunflower oil. *Studies in Surface Science and Catalysis*, 118 (1998) 55.
- [88] V.V. Volkov, V.I. Lebedeva, I.V. Petrova, A.V. Bobyl, S.G. Konnikov, V.I. Roldughin, et al, Adlayers of palladium particles and their aggregates on porous polypropylene hollow fiber membranes as hydrogenization contractors/reactors, *Advances in colloid and interface science*, 164 (2011) 144.
- [89] H. Aran, H.C. Aran, R. Chinthaginjala, T. Groote, L. Roelofs, M. Lefferts, et al. Porous ceramic mesoreactors: A new approach for gas-liquid contacting in multiphase microreaction technology. *Chem.Eng.J.*, 169 (2011) 239.
- [90] A.C. Comer, D.S. Kalika, B.W. Rowe, B.D. Freeman, and D.R. Paul. Dynamic relaxation characteristics of Matrimid polyimide. *Polymer*, 50 (2009) 891.
- [91] M. Minelli, G. Cocchi, L. Ansaloni, M.G. Baschetti, M.G. De Angelis, and F. Doghieri, Vapor and Liquid Sorption in Matrimid Polyimide: Experimental Characterization and Modeling, *Ind. Eng. Chem. Res.*, (2013) 8936.
- [92] P.S. Tin, T.S. Chung, Y. Liu, R. Wang, S.L. Liu, and K.P. Pramoda. Effects of cross-linking modification on gas separation performance of Matrimid membranes. *J. Membr. Sci.*, 225 (2003) 77.
- [93] W. Qiu, C. Chen, L. Xu, L. Cui, D. Paul, and W. Koros. Sub-Tg Cross-Linking of a Polyimide Membrane for Enhanced CO₂ Plasticization Resistance for Natural Gas Separation. *Macromolecules*, 44 (2011) 6046.
- [94] J.R. Klaehn, C.J. Orme, F.F. Stewart, and E.S. Peterson. Humidified Gas Stream Separations at High Temperatures Using Matrimid 5218. *Sep. Sci. Technol.*, 47 (2012) 2186.
- [95] S.S. Hosseini, M.M. Teoh, and T.S. Chung, Hydrogen separation and purification in membranes of miscible polymer blends with interpenetration networks, *Polymer*, 49 (2008) 1594.
- [96] Y. He, K. Vinodgopal, M. Ashokkumar, and F. Grieser. Sonochemical synthesis of ruthenium nanoparticles. *Research on Chemical Intermediates*, 32 (2006) 709.

- [97] Y. He, K. Vinodgopal, M. Ashokkumar, and F. Grieser, Sonochemically Prepared Platinum–Ruthenium Bimetallic Nanoparticles, *J. Phys. Chem. B*, (2006) 849.
- [98] J. Peter, K. Peinemann, Multilayer composite membranes for gas separation based on crosslinked PTMSP gutter layer and partially crosslinked Matrimid 5218 selective layer, *J. Membr. Sci.*, 340 (2009) 62.
- [99] T. Visser, N. Masetto, and M. Wessling. Materials dependence of mixed gas plasticization behavior in asymmetric membranes. *J. Membr. Sci.*, 306 (2007) 16.
- [100] Y.H. See Toh, F.W. Lim, A.G. Livingston, and Y. Toh. Polymeric membranes for nanofiltration in polar aprotic solvents. *J. Membr. Sci.*, 301 (2007) 3.
- [101] P. Marchetti, M.F. Jimenez Solomon, G. Szekely, and A.G. Livingston. Molecular Separation with Organic Solvent Nanofiltration: A Critical Review. *Chem. Rev.*, 114 (2014) 10735.
- [102] G.C. Kapantaidakis, G.H. Koops. High flux polyethersulfone–polyimide blend hollow fiber membranes for gas separation. *J. Membr. Sci.*, 204 (2002) 153.
- [103] J. Hossenlopp, L. Jiang, R. Cernosek, and F. Josse. Characterization of epoxy resin (SU-8) film using thickness-shear mode (TSM) resonator under various conditions. *Journal of polymer science. Part B, Polymer physics*, 42 (2004) 2373.
- [104] M. Emamikia, M. Barikani, and G. Bakhshandeh. Relationship between structure and aromatic solvent permeability of crosslinked polyurethanes based on hyperbranched polyesters. *Polym. Int.*, 64 (2015) 1142.
- [105] C. Ribeiro, Separation of aromatic/aliphatic mixtures by pervaporation using ortho-functionalized polyimide membranes, in I.C. Escobar and B. Van der Bruggen (Ed.), *Modern Applications in Membrane Science and Technology*, Washington D.C., American Chemical Society, 2011, pp. 81.
- [106] C. Scholes, W.X. Tao, G.W. Stevens, and S.E. Kentish. Sorption of Methane, Nitrogen, Carbon Dioxide, and Water in Matrimid 5218. *J Appl Polym Sci*, 117 (2010) 2284.
- [107] A. Berens. Transport of Plasticizing Penetrants in Glassy Polymers. *ACS Symp. Ser.*, 423 (1990) 92.
- [108] M. Böhning, J. Springer. Sorptive dilation and relaxational processes in glassy polymer/gas systems—I. Poly(sulfone) and poly(ether sulfone). *Polymer*, 39 (1998) 5183.

- [109] J.S. Vrentas, C.M. Jarzebski, and J.L. Duda. A Deborah number for diffusion in polymer-solvent systems. *AIChE J.*, 21 (1975) 894.
- [110] H. Feng. Modeling of vapor sorption in glassy polymers using a new dual mode sorption model based on multilayer sorption theory. *Polymer*, 48 (2007) 2988.
- [111] P. Chandra, W.J. Koros. Sorption and transport of methanol in poly(ethylene terephthalate). *Polymer*, 50 (2009) 236.
- [112] A.F. Ismail, W. Lorna, Penetrant-induced plasticization phenomenon in glassy polymers for gas separation membrane, *Separation and purification technology*, 27 (2002) 173.
- [113] J.S. Vrentas, C.M. Vrentas. Sorption in glassy polymers. *Macromolecules*, 24 (1991) 2404.
- [114] S. Boyer A., J.P. Grolier, Modification of the glass transitions of polymers by high-pressure gas solubility. *Pure Appl. Chem.*, 77 (2005) 593.
- [115] W. Ogieglo, M. Wessling, and N.E. Benes, Polymer Relaxations in Thin Films in the Vicinity of a Penetrant- or Temperature-Induced Glass Transition, *Macromolecules*, (2014) 3654.
- [116] T.S. Chow. Molecular interpretation of glass transition temperature of polymer-diluent systems. *Macromolecules*, 13 (1980) 362.
- [117] I. Blume, E. Smit, M. Wessling, and C.A. Smolders. Diffusion through rubbery and glassy polymer membranes. *Makromol. Chem., Macromol. Symp.*, 45 (1991) 237.
- [118] N.R. Horn, D.R. Paul. Carbon Dioxide Sorption and Plasticization of Thin Glassy Polymer Films Tracked by Optical Methods. *Macromolecules*, 45 (2012) 2820.
- [119] J. Karger, D.M. Ruthven, and D.N. Theodorou, *Diffusion in Nanoporous Materials*, Weinheim, Germany, Wiley-VCH, 2012.
- [120] M.L. Jue, C.S. McKay, B.A. McCool, M.G. Finn, and R.P. Lively. Effect of Nonsolvent Treatments on the Microstructure of PIM-1. *Macromolecules*, 48 (2015) 5780.
- [121] G.Q. Chen, C.A. Scholes, C.M. Doherty, A.J. Hill, G.G. Qiao, and S.E. Kentish. The thickness dependence of Matrimid films in water vapor permeation. *Chem.Eng.J.*, 209 (2012) 301.
- [122] S.R. Thrasher, M.E. Rezac. Transport of water and methanol vapors in alkyl substituted poly(norbornene). *Polymer*, 45 (2004) 2641.
- [123] A.R. Berens, H.B. Hopfenberg. Diffusion of organic vapors at low concentrations in glassy PVC, polystyrene, and PMMA. *J.Membr.Sci.*, 10 (1982) 283.

- [124] H.L. Frisch, Sorption and Transport in Glassy Polymers - A Review, *Polymer engineering and science*, 20 (1980) 2.
- [125] R.C. Lasky, E.J. Kramer, The initial stages of Case II diffusion at low penetrant activities, *Polymer*, 29 (1988) 673.
- [126] D.B. Hall, J.M. Torkelson, Small Molecule Probe Diffusion in Thin and Ultrathin Supported Polymer Films, *Macromolecules*, (1998) 8817.
- [127] L. Singh, P.J. Ludovice, and C.L. Henderson. Effect of thin film confinement on the transport properties of ultra-thin polymer films. *Materials Research Society symposia proceedings*, 790 (2004) 203.
- [128] S. Kim, S.A. Hewlett, C.B. Roth, and J.M. Torkelson. Confinement effects on glass transition temperature, transition breadth, and expansivity: Comparison of ellipsometry and fluorescence measurements on polystyrene films. *European Physical Journal E -- Soft Matter*, 30 (2009) 83.
- [129] K. Chrissopoulou, S.H. Anastasiadis. Effects of nanoscopic-confinement on polymer dynamics. *Soft matter*, 11 (2015) 3746.
- [130] J. Xia, T. Chung, and D.R. Paul. Physical aging and carbon dioxide plasticization of thin polyimide films in mixed gas permeation. *J. Membr. Sci.*, 450 (2014) 457.
- [131] Y. Huang, D.R. Paul, Effect of Film Thickness on the Gas-Permeation Characteristics of Glassy Polymer Membranes, *Ind. Eng. Chem. Res.*, (2007) 2342.
- [132] A. Shishatskii, Y. Yampolskii, and K. Peinemann. Effects of film thickness on density and gas permeation parameters of glassy polymers. *J. Membr. Sci.*, 112 (1996) 275.
- [133] P.H. Pfromm, W.J. Koros. Accelerated Physical Aging of Thin Glassy Polymer-Films - Evidence from Gas-Transport Measurements. *Polymer*, 36 (1995) 2379.
- [134] Y. Huang, X. Wang, and D.R. Paul. Physical aging of thin glassy polymer films: Free volume interpretation. *J. Membr. Sci.*, 277 (2006) 219.
- [135] M.E. Rezac, P.H. Pfromm, L.M. Costello, and W.J. Koros. Aging of thin polyimide-ceramic and polycarbonate-ceramic composite membranes. *Ind Eng Chem Res*, 32 (1993) 1921.
- [136] R.D. Priestley. Physical aging of confined glasses. *Soft matter*, 5 (2009) 919.
- [137] J.S. Sharp, J.H. Teichroeb, and J.A. Forrest. The properties of free polymer surfaces and their influence on the glass transition temperature of thin polystyrene films. *European Physical Journal E -- Soft Matter*, 15 (2004) 473.

- [138] Shao, L Chung, TS Goh, SH Pramoda, KP. Polyimide modification by a linear aliphatic diamine to enhance transport performance and plasticization resistance. *J.Membr.Sci.*, 256 (2005) 46.
- [139] J. Wind, W. Koros. Natural gas permeation in polyimide membranes. *J.Membr.Sci.*, 228 (2004) 227.
- [140] H.-. Zhao. Effects of cross-linkers with different molecular weights in cross-linked Matrimid 5218 and test temperature on gas transport properties. *J.Membr.Sci.*, 323 (2008) 176.
- [141] Shao, Lu Lau, Cher-Hon Chung, Tai-Shung. A novel strategy for surface modification of polyimide membranes by vapor-phase ethylenediamine (EDA) for hydrogen purification. *Int J Hydrogen Energy*, 34 (2009) 8716.
- [142] W. Hieber, A. Woerner, Thermochemical measurements of complex-forming amines and alcohols, *Z. Elektrochem. Angew. Phys. Chem.*, 40 (1934) 252.
- [143] A. Razmjou, E. Arifin, G. Dong, J. Mansouri, and V. Chen, Superhydrophobic modification of TiO₂ nanocomposite PVDF membranes for applications in membrane distillation, *Journal of membrane science*, 415-416 (2012) 850.
- [144] G. Sawyer, K.D. Freudenberg, P. Bhimaraj, and L.S. Schadler, A study on the friction and wear behavior of PTFE filled with alumina nanoparticles, *Wear*, 254 (2003) 573.
- [145] L.F. Villalobos, M. Karunakaran, and K. Peinemann, Complexation-Induced Phase Separation: Preparation of Composite Membranes with a Nanometer-Thin Dense Skin Loaded with Metal Ions, *Nano Lett.*, (2015) 3166.
- [146] L. Schulte, Blending high performance polymers for improved stability in integrally skinned asymmetric gas separation membranes, (2015).
- [147] J.R. Klaehn, T.A. Luther, C.J. Orme, M.G. Jones, A.K. Wertsching, and E.S. Peterson, Soluble N-Substituted Organosilane Polybenzimidazoles, *Macromolecules*, (2007) 7487.
- [148] Q. Li, D. Aili, J. Yang, H.C. Rudbeck, J.O. Jensen, and N.J. Bjerrum, Polybenzimidazoles: synthesis, characterizations and applications in form of membranes, *Adv.Mater.Sci.Res.*, 14 (2012) 1.
- [149] T. Okano. Dehydration of fructose to 5-hydroxymethylfurfural (HMF) in an aqueous acetonitrile biphasic system in the presence of acidic ionic liquids. *Applied catalysis.A, General*, 451 (2013) 1.

- [150] Y. Roman-Leshkov. Production of dimethylfuran for liquid fuels from biomass-derived carbohydrates. *Nature*, 447 (2007) 982.
- [151] V. Schiavo. Catalytic hydrogenation of 5-(hydroxymethyl)furfural in aqueous medium. *Bulletin de la Société chimique de France*, (1991) 704.
- [152] X. Tong. Biomass into chemicals: Conversion of sugars to furan derivatives by catalytic processes. *Applied catalysis.A, General*, 385 (2010) 1.
- [153] N. Sun, M. Rahman, Y. Qin, M. Maxim, H. Rodriguez, H. Rodríguez, et al. Complete dissolution and partial delignification of wood in the ionic liquid 1-ethyl-3-methylimidazolium acetate. *Green Chem.*, 11 (2009) 646.
- [154] H.I. Kilpelainen. Dissolution of wood in ionic liquids. *J.Agric.Food Chem.*, 55 (2007) 9142.
- [155] M. Zavrel, D. Bross, M. Funke, J. Buechs, A. Spiess, and J. Büchs. High-throughput screening for ionic liquids dissolving (ligno-)cellulose. *Bioresour. Technol.*, 100 (2009) 2580.
- [156] A. Jadhav, A. Chinnappan, R. Patil, S. Kostjuk, and H. Kim. Green chemical conversion of fructose into 5-hydroxymethylfurfural (HMF) using unsymmetrical dicationic ionic liquids under mild reaction condition. *Chem.Eng.J.*, 243 (2014) 92.
- [157] W. Liu, J. Holladay. Catalytic conversion of sugar into hydroxymethylfurfural in ionic liquids. *Catalysis today*, 200 (2013) 106.
- [158] J.B. Binder, R.T. Raines, Simple Chemical Transformation of Lignocellulosic Biomass into Furans for Fuels and Chemicals, *J. Am. Chem. Soc.*, (2008) 1979.
- [159] M. Chidambaram, A. Bell. A two-step approach for the catalytic conversion of glucose to 2,5-dimethylfuran in ionic liquids. *Green Chem.*, 12 (2010) 1253.
- [160] S. Wickramanayake, D. Hopkinson, C. Myers, L. Sui, and D. Luebke. Investigation of transport and mechanical properties of hollow fiber membranes containing ionic liquids for pre-combustion carbon dioxide capture. *J. Membr. Sci.*, 439 (2013) 58.
- [161] A. Dahi, K. Fatyeyeva, D. Langevin, C. Chappey, S. Rogalsky, O. Tarasyuk, et al. Supported ionic liquid membranes for water and volatile organic compounds separation: Sorption and permeation properties. *J.Membr.Sci.*, 458 (2014) 164.
- [162] E. Santos, J. Albo, and A. Irabien, Acetate based Supported Ionic Liquid Membranes (SILMs) for CO₂ separation: Influence of the temperature, *Journal of membrane science*, 452 (2014) 277.

- [163] F. Wendler, L. Todi, and F. Meister. Thermostability of imidazolium ionic liquids as direct solvents for cellulose. *Thermochimica acta*, 528 (2012) 76.
- [164] Y. Qiao, F. Yan, S. Xia, S. Yin, and P. Ma. Densities and Viscosities of [Bmim][PF₆] and Binary Systems [Bmim][PF₆] + Ethanol, [Bmim][PF₆] + Benzene at Several Temperatures and Pressures: Determined by the Falling-Ball Method. *Journal of chemical & engineering data*, 56 (2011) 2379.
- [165] J. Safarov, R. Hamidova, S. Zepik, H. Schmidt, I. Kul, A. Shahverdiyev, et al. Thermophysical properties of 1-hexyl-3-methylimidazolium bis(trifluoromethylsulfonyl)imide at high temperatures and pressures. *Journal of molecular liquids*, 187 (2013) 137.
- [166] B.M. Dooos, I.F. Vankelecom, and P.A. Jacobs. Aspects of Immobilisation of Catalysts on Polymeric Supports. *Advanced synthesis & catalysis*, 348 (2006) 1413.
- [167] A. Bottino, G. Capannelli, A. Comite, A. Del Borghi, and R. Di Felice. Catalytic ceramic membrane in a three-phase reactor for the competitive hydrogenation–isomerisation of methylenecyclohexane. *Separation and purification technology*, 34 (2004) 239.
- [168] R. Alamillo, The selective hydrogenation of biomass-derived 5-hydroxymethylfurfural using heterogeneous catalysts. *Green Chemistry*, (2012) 1413.
- [169] C.A. Mebi, B.J. Frost. Effect of pH on the Biphase Catalytic Hydrogenation of Benzylidene Acetone Using CpRu(PTA)₂H. *Organometallics*, 24 (2005) 2339.
- [170] P. Jannasch, E.A. Weiber, Configuring Anion-Exchange Membranes for High Conductivity and Alkaline Stability by Using Cationic Polymers with Tailored Side Chains, *Macromolecular chemistry and physics*, (2016).
- [171] Z.P. Smith, R.R. Tiwari, T.M. Murphy, D.F. Sanders, K.L. Gleason, D.R. Paul, et al. Hydrogen sorption in polymers for membrane applications. *Polymer*, 54 (2013) 3026.
- [172] J. Okal, M. Okal, L. Zawadzki, L. Kępiński, W. Krajczyk, and Tylus. The use of hydrogen chemisorption for the determination of Ru dispersion in Ru/γ-alumina catalysts. *Applied catalysis.A, General*, 319 (2007) 202.
- [173] L. Lomba, B. Giner, I. Bandres, C. Lafuente, and M.R. Pino, Physicochemical properties of green solvents derived from biomass, *Green chemistry*, 13 (2011) 2062.
- [174] V.N. Emel'yanenko, S.A. Kozlova, S.P. Verevkin, and G.N. Roganov, Vapour pressures and enthalpies of vapourization of a series of the gamma-lactones, *The journal of chemical thermodynamics*, 40 (2008) 911.

Appendix A - Additional Information for Chapter 2

Figures A1-A3 are example images of Ru loaded ePTFE membranes used in the aqueous phase hydrogenation experiments.



Figure A-1 - Ru loaded ePTFE membrane example 1 (top view).

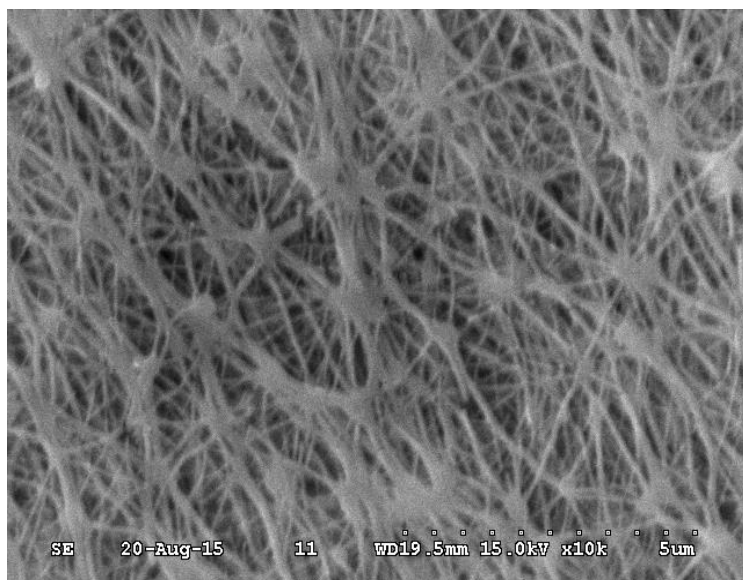


Figure A-2 - Ru loaded ePTFE membrane example 2 (top view).

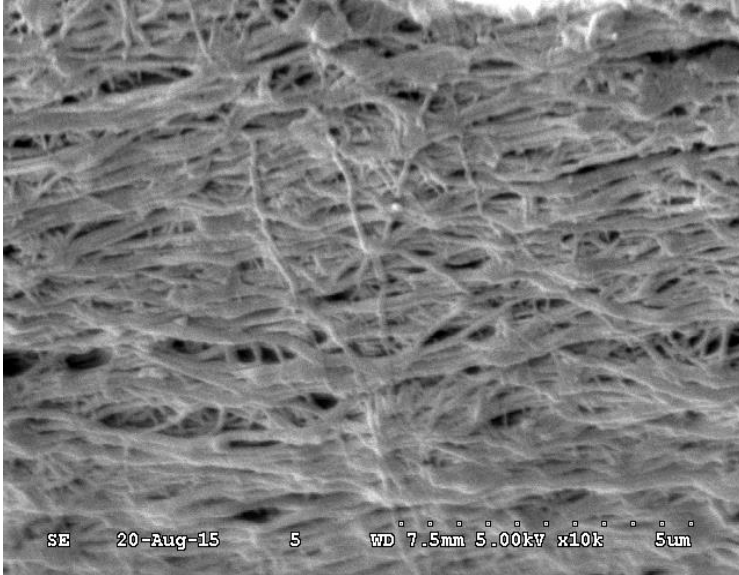


Figure A-3 - Ru loaded ePTFE membrane (cross-sectional view).

The following page is a summary report produced by the Oxford EDS software giving the carbon, fluorine, and ruthenium composition of the ePTFE membrane. This compositional information was one of four methods used to determine the ruthenium mass loading of the membrane and is discussed in detail in Section 2.4.1.3 "Membrane morphology and catalyst characterization".

Spectrum processing :

No peaks omitted

Processing option : All elements analyzed

Number of iterations = 2

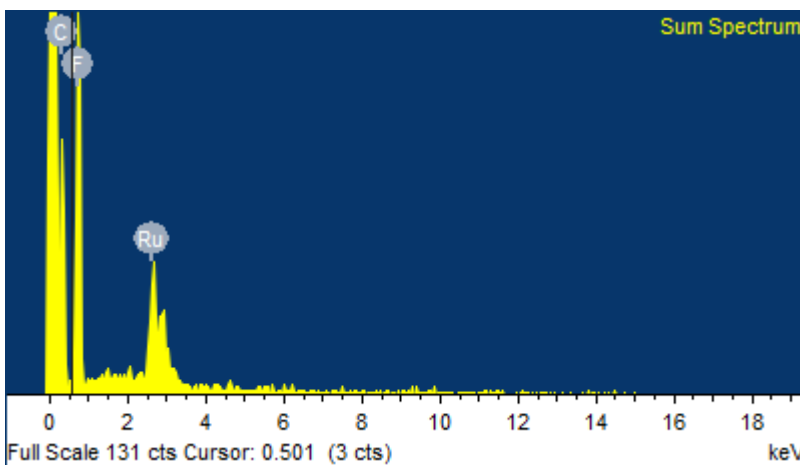
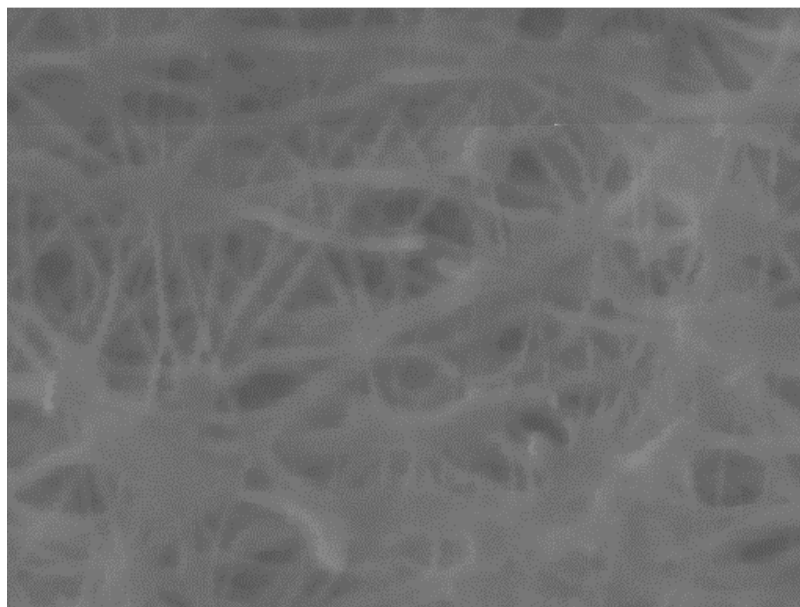
Standard :

C CaCO3 1-Jun-1999 12:00 AM

F MgF2 1-Jun-1999 12:00 AM

Ru Ru 1-Jun-1999 12:00 AM

Element	Weight%	Atomic%
C K	0.63	63.03
F K	0.57	36.16
Ru L	0.07	0.82
Totals	1.28	



Appendix B - Additional Information for Chapter 3

H₂ Sorption Calculations

One may argue that the catalyst loading scenarios discussed in Section 3.2.1. of the paper would be better understood if the active sites were determined by H₂ chemisorption methods. The largest problem with using H₂ chemisorption on the catalyst loaded polymeric membrane is the polymer itself and its relatively high solubility for H₂, which would completely overshadow the potential amount of H₂ sorbed on ruthenium sites. For example, in the highest ruthenium loading case, 8.8 μg/cm², there is about 100 μg, or approximately 1E-6 mol Ru on the entire surface of one membrane. For one membrane sample there is approximately 0.01 g Matrimid. The solubility of H₂ in Matrimid at 20 °C and 20 bar applied H₂ pressure is 1.75 cm³ (STP) / cm³_{polymer} [171] or approximately 1E-6 mol H₂ per one membrane sample. Clearly every atom of loaded ruthenium is not an active site, so using values that others have obtained for the number of active sites per total mass of Ru in Ru/γ-alumina [172] and Ru/C [27] catalytic systems, there would equivalently be 1E-9 or 1E-8 mol active sites, respectively, per 8.8 μg/cm² loaded membrane. This represents a two to three order of magnitude higher amount of H₂ sorbed into the polymer compared to H₂ chemisorbed on Ru active sites, hence the foreseen difficulty in using this method for determining the number of active Ru sites in our catalyst loaded membrane.

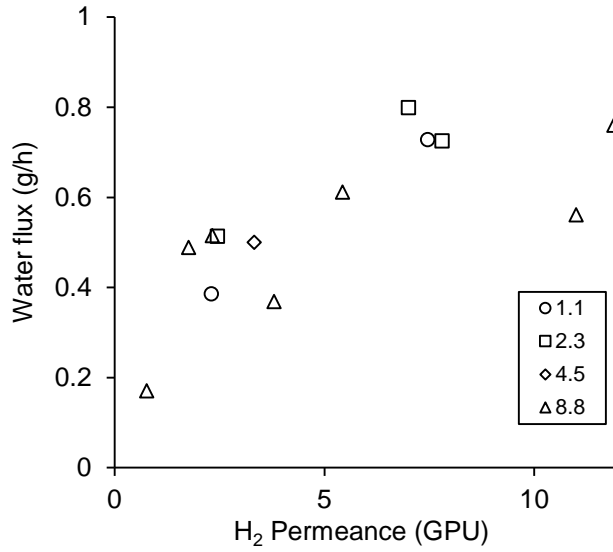


Figure B-1 - Water flux through Ru coated membrane as a function of membrane hydrogen permeance collected during use in reactor. The legend values refer to the Ru loading for each membrane in µg/cm². Membrane area = 13.8 cm².

Appendix C - Vapor Pressures of Levulinic Acid and γ -valerolactone

The vapor pressures of levulinic acid and gamma-valerolactone were calculated using variants of the Antoine equation and are shown in Figure C-1 over the temperature range 0 to 200 °C. The form of the Antoine equation used for levulinic acid is $\log p = A - \frac{B}{C+T}$ [173], where T is temperature in degrees C, p is vapor pressure in kPa, and the values of the constants are: A = 8.665, B = 3585.420, C = 293.474. The equation for gamma-valerolactone is $R \ln p_i^{sat} = a + \frac{b}{T} + \Delta_l^g C_p \ln\left(\frac{T}{T_0}\right)$ [174], where T is temperature in degrees K, p is vapor pressure in Pa, and the values of the constants are: a = 268.3, b = -70575.5, $\Delta_l^g C_p = -56.0$.

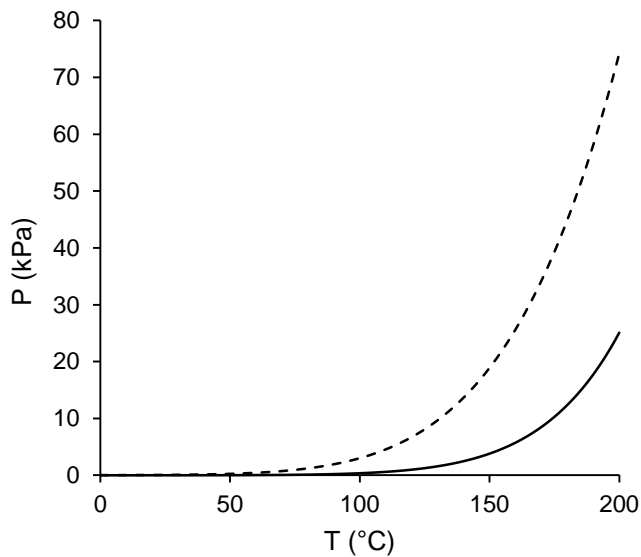


Figure C-1 - Vapor pressures of levulinic acid (—) and gamma-valerolactone (- - -).

Appendix D - Additional Information for Chapter 4

Table D-1 - Equilibrium liquid sorption in Matrimid at 30 °C.

Chemical	Mass sorbed (g _{sol} /g _{polymer})
pentane	0.028
hexane	0.024
n-heptane	0.022
iso-octane	0.020
dodecane	0.029
water	0.032
<hr style="border-top: 1px dashed black;"/>	
methanol	0.189
ethanol	0.191
1-propanol	0.224
2-propanol	0.203
1,2-propanediol	0.180
butanol	0.216
pentanol	0.226
hexanol	0.244
heptanol	0.242
octanol	0.239
octadecanol	0.002
<hr style="border-top: 1px dashed black;"/>	
acetone	0.280
acetone*	0.340
ethyl acetate**	0.282
acetonitrile	0.309
<i>n</i> -butyl acetate	0.365
methyl acetate*	0.420
toluene	0.522
toluene*	0.533
benzene*	0.622
<hr style="border-top: 1px dashed black;"/>	
furfuryl alcohol	1.87
dimethylfuran	3.22
tetrahydrofuran	Dissolved
gamma-butyrolactone (GBL)	Dissolved
gamma-valerolactone (GVL)	Dissolved
1-Ethyl-3-methylimidazolium chloride [EMIM]Cl	Dissolved
1-Ethyl-3-methylimidazolium acetate [EMIM]OAc	Dissolved

---- indicates arbitrary chemical groups approximately separated by amount sorbed

* and ** indicate values taken from literature references at 35 °C and 25 °C, respectively.[91,105]

Kinetic parameters

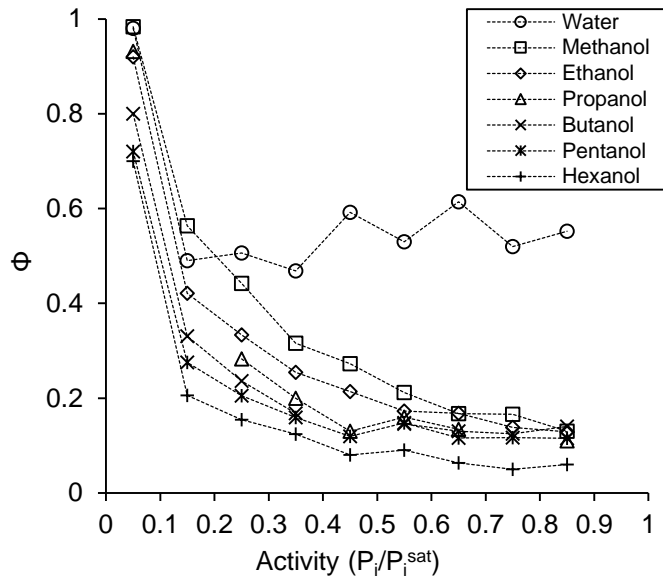


Figure D-1 - Φ represents the proportion of total equilibrium sorption that is nominally diffusive for each 0.1 chemical activity level. Total sorption for each activity level is normalized and a visual determination is made to decide where diffusive sorption is separated from relaxation sorption, which occurred sometime in the first 40-400 s of the total 12 h sorption interval for each activity level. This parameter must therefore be used only as an approximation. All film thicknesses were $0.26 \mu\text{m}$ ($\pm 0.015 \mu\text{m}$). Lines are added for visual aid only.

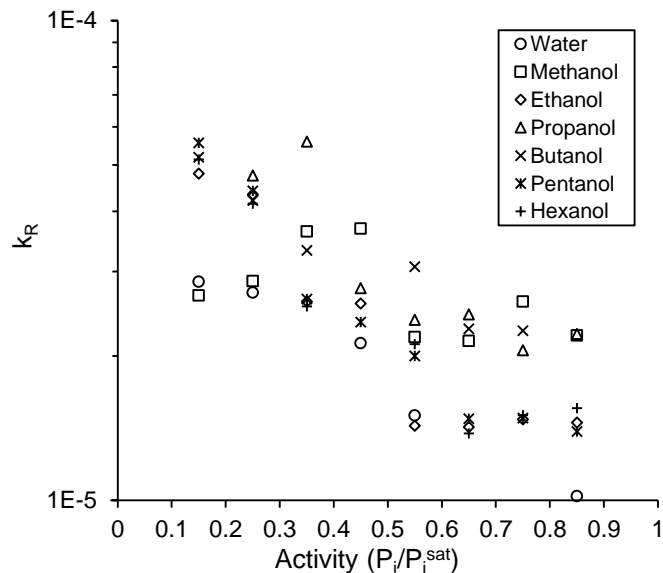


Figure D-2 - Relaxation parameter, k , as a function of chemical activity. All film thicknesses were $0.26 \mu\text{m}$ ($\pm 0.015 \mu\text{m}$).

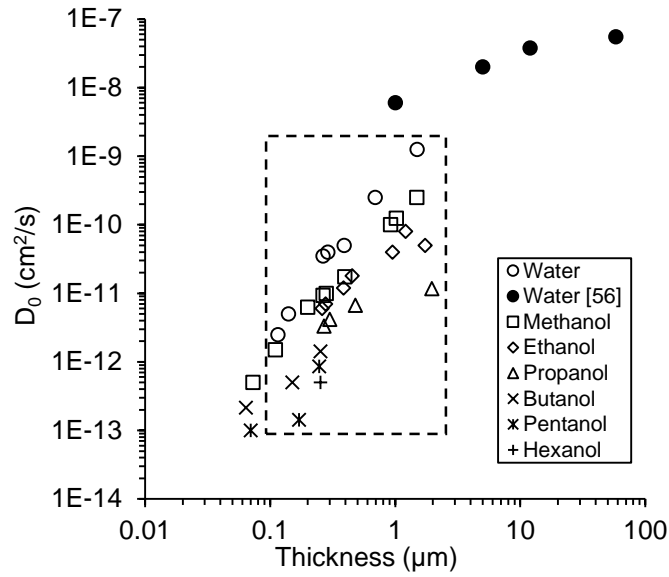


Figure D-3 - Figure 4-14 from main document displaying infinite dilution diffusion coefficients for indicated species in Matrimid at 30 °C. Boxed region is expanded below in Figure D-4.

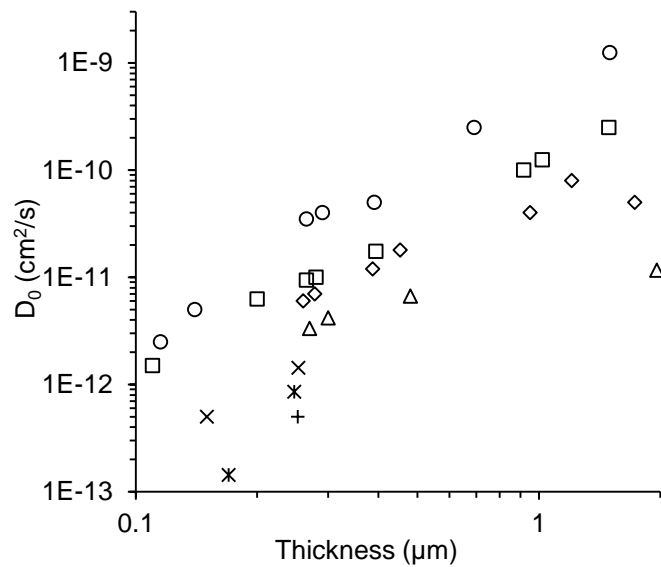


Figure D-4 - Expanded region from Figure D-3.

Error analysis

The error associated with the diffusion coefficient measurements and calculations was determined using three different methods. The first method looked at the variance in D_0 values for methanol in Matrimid taking into consideration the thickness dependence of the film. This data is given in Figure D-5. The black dotted line indicates a linear fit to the data and the red dashed lines indicate ± 1 standard deviation from that line. One standard deviation represents approximately $\pm 22\%$ error for the diffusion coefficient value.

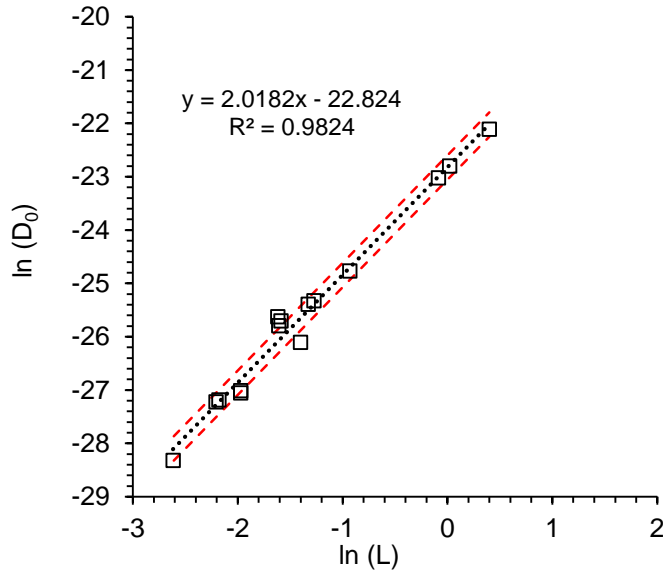


Figure D-5 - The natural log of infinite dilution diffusion coefficients for methanol as a function of the natural log of film thickness. The black dotted line represents a linear best fit for those values and the red dashed lines indicate ± 1 standard deviation from that line. It was determined that 1 standard deviation is approximately an error of $\pm 22\%$ of the diffusion coefficient value.

The second method for determining the possible error for the reported diffusion coefficients was to vary the initial time placement for the diffusion data, *i.e.* use ± 1 and ± 2 seconds from when the chemical activity step occurred and determining its impact on the calculated diffusion coefficient. A similar approach was done for varying the thickness in the diffusion calculation by $\pm 10\%$ of the determined film thickness. These parametric variations produced nothing larger than a 29% change in the originally calculated diffusion coefficient value.

The third method for estimating the error was simply taking the standard deviation of D_0 values for two groups of three separate samples with similar thickness for methanol in Matrimid sorption. As shown below the error associated with each group was 19.4 and 7.3 %.

L (μm)	D_0 (cm^2/s)	L (μm)	D_0 (cm^2/s)
0.246	2.04E-11	0.139	8.25E-12
0.205	3.05E-11	0.139	7.90E-12
0.198	3.29E-11	0.113	6.93E-12
Mean	2.79E-11		7.69E-12

Standard deviation	5.42E-12		5.58E-13
% from mean	19.4 %		7.26 %

Based on these three methods it was determined that placing an approximate error of $\pm 25\%$ on the reported diffusion coefficient values was reasonable.

Diffusion case analysis (Case I, Anomalous, Case II diffusion)

The following tables present the sorption isotherms of water and C1-C6 alcohols collected and analyzed in this work. Individual 0.1 activity step changes are partitioned and labeled according to the interval activity step change, *e.g.* activity = 0.4 to 0.5. The diffusion case analysis was performed by fitting the early time of each sorption interval with $M/M_\infty = k t^n$ and regressing values for k and n . $n = 0.5$ indicates Case I, or Fickian diffusion, $0.5 < n < 1$ indicates anomalous diffusion (appropriate for Berens-Hopfenberg model), and $n = 1$ indicates Case II diffusion (not appropriate for traditional Fickian or BH diffusion analysis). In higher activity intervals much of the total mass sorbed is attributed to relaxation sorption leaving the initial Fickian portion only representing a fraction of the total sorption for a given activity step interval. Therefore, the early time interval used is considered to be $M/M_\infty < 0.5$ of the *Fickian* diffusion portion of the total sorption in efforts to allow reasonable fitting of $M/M_\infty = k t^n$, *i.e.* not $M/M_\infty < 0.5$ of the total sorption interval (Fickian diffusion + polymer relaxation induced sorption).

Notes:

- (1) The sorption steps presented below for varying film thicknesses for methanol sorption are either activity = 0 to 0.1 or 0.1 to 0.2. The 0.1 to 0.2 intervals are shown instead of 0 to 0.1 due to the 0 to 0.1 interval clearly exhibiting Case II diffusion ($n \approx 1$). As shown in the following diffusion case analysis for different penetrants (water, C1-C6 alcohols), the 0 to 0.1 interval for each penetrant in every case, except hexanol, can be classified as Case II diffusion, while all subsequent higher activity intervals (0.2 to 0.9) exhibit anomalous diffusion.
- (2) If one ever notices an uncanny resemblance between two different sorption curves for samples of different thicknesses, it is because the experimental setup allows two samples to run in series with the same vapor phase penetrant flow. Thus, both samples experience the same flow stream giving rise to the same minor fluctuations or noise in the sorption curves due to very small fluctuations with the mass flow controllers.
- (3) All M/M_∞ curves for each sorption interval are normalized to 1 using the final sorption amount (mass of sorption due to Fickian diffusion + mass of sorption due to relaxation) as the normalizing value. The curves below present only an initial small fraction of the sorption curve to highlight the Fickian diffusion portion for $M/M_\infty = k t^n$ curve fitting for $M/M_\infty < 0.5$ of the nominally Fickian diffusive portion, which is not equivalent to using $M/M_\infty = 0.5$ on the corresponding full interval plots below. This normalization does not impact the value of n , but does change the value of k if one were to isolate the Fickian diffusion portion of the curve and normalize to its maximum.
- (4) All 0.1 activity sorption intervals were 12 h in length, which does not guarantee that the system has reached equilibrium, *i.e.* $M/M_\infty = 1$. Based on this observation the plots below show the sorption data normalized to an estimated equilibrium sorption based on the trend of the sorption curve at $t = 12$ h. This was done to avoid the confusion of incorrectly presenting sorption data at $M/M_\infty = 1$ that clearly had not reached equilibrium. 48 h sorption interval experiments confirmed that this normalization does not impact the values of the fitted BH sorption parameters D and k_R , as expected.
- (5) The following outlines the sorption data presented below.

- 1) Thickness variation for methanol sorption
 - a) $L = 0.07 \mu\text{m}$, activity = 0 to 0.1
 - b) $L = 0.20 \mu\text{m}$, activity = 0 to 0.1
 - c) $L = 0.26 \mu\text{m}$, activity = 0.1 to 0.2
 - d) $L = 0.39 \mu\text{m}$, activity = 0.1 to 0.2
 - e) $L = 0.92 \mu\text{m}$, activity = 0.1 to 0.2
 - f) $L = 1.01 \mu\text{m}$, activity = 0 to 0.1
 - g) $L = 1.49 \mu\text{m}$, activity = 0 to 0.1
 - h) $L = 1.49 \mu\text{m}$, activity = 0.1 to 0.2
- 2) Water sorption, $L = 0.27 \mu\text{m}$, all 0.1 activity intervals from 0 to 0.7
- 3) Methanol sorption, $L = 0.275 \mu\text{m}$, all 0.1 activity intervals from 0 to 0.9
- 4) Ethanol sorption, $L = 0.39 \mu\text{m}$, all 0.1 activity intervals from 0 to 0.9
- 5) Ethanol sorption, $L = 0.275 \mu\text{m}$, all 0.1 activity intervals from 0 to 0.9
- 6) Propanol sorption, $L = 0.27 \mu\text{m}$, sorption curve and summarized n values
- 7) Butanol sorption, $L = 0.255 \mu\text{m}$, sorption curve and summarized n values
- 8) Pentanol sorption, $L = 0.26 \mu\text{m}$, sorption curve and summarized n values

Methanol sorption for varying film thicknesses (0.073 to 1.49 μm)

Thickness = 0.073 μm

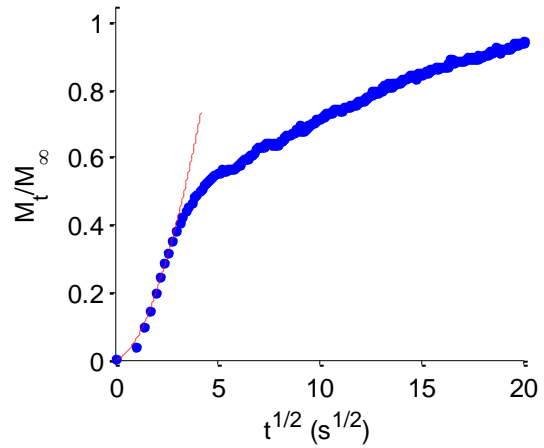
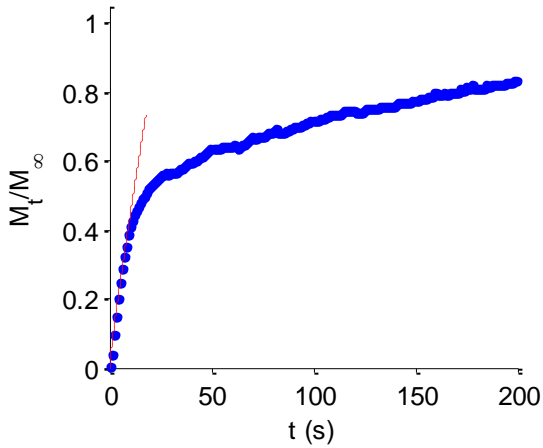
Sorption activity step: 0 to 0.1

$$M_t/M_\infty = k t^n \text{ (---)}$$

k = 0.0558

n = 0.8918

Anomalous diffusion



Thickness = 0.073 μm

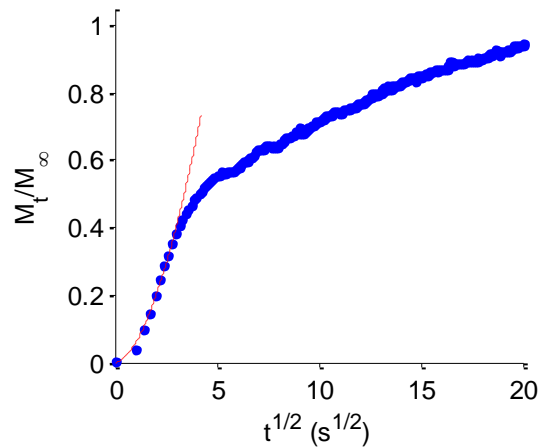
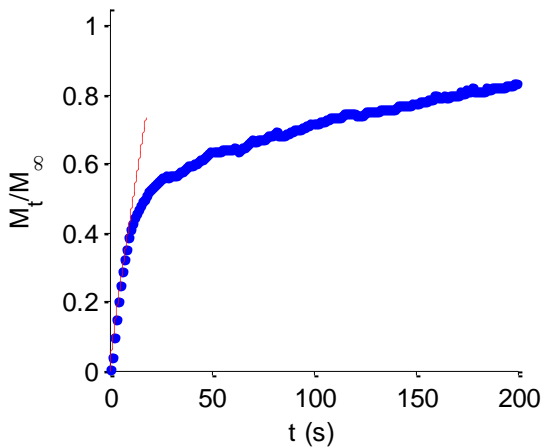
Sorption activity step: 0 to 0.1

$$M_t/M_\infty = k t^n \text{ (---)}$$

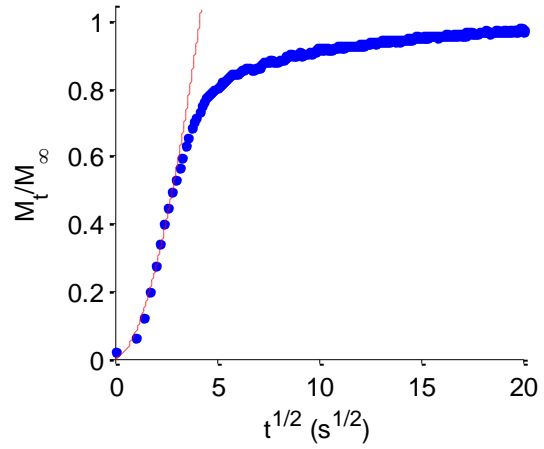
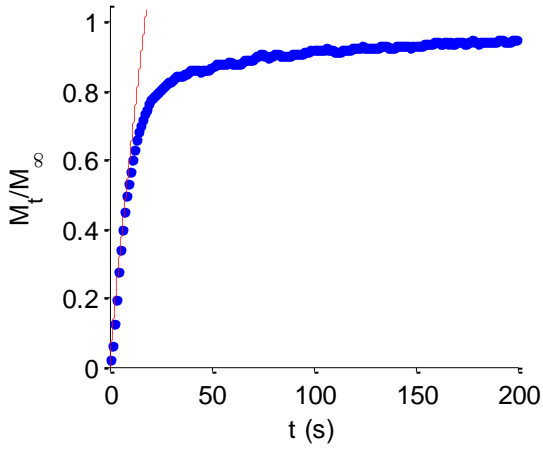
k = 0.0558

n = 0.8918

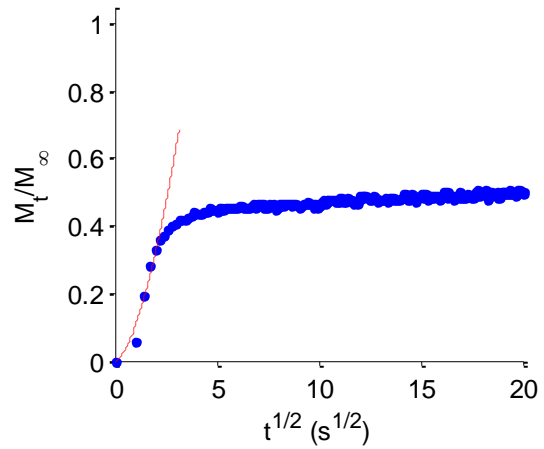
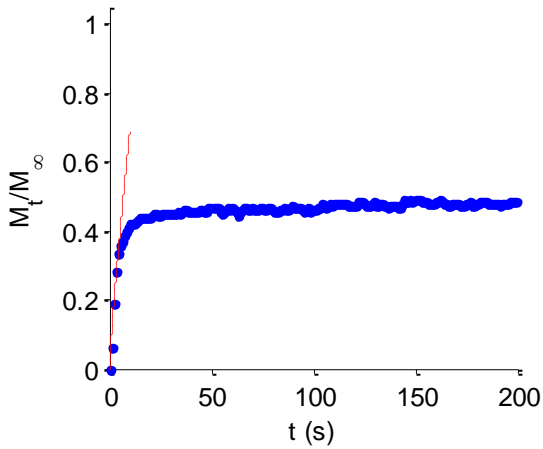
Anomalous diffusion



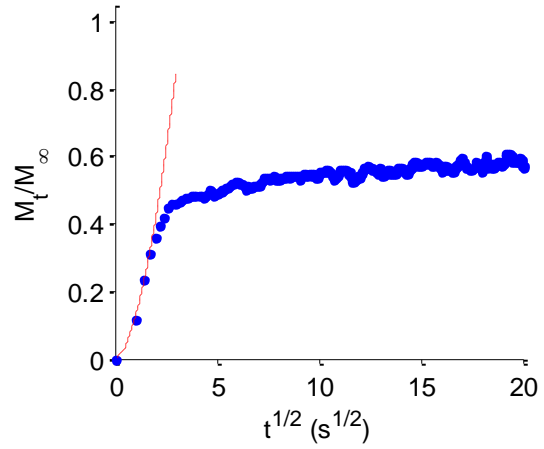
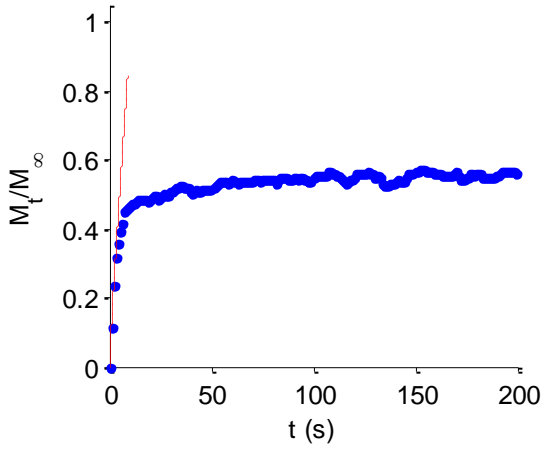
Thickness = 0.20 μm
Sorption activity step: 0 to 0.1
 $M_t/M_\infty = k t^n$ (---)
 $k = 0.0760$
 $n = 0.905$
Anomalous diffusion



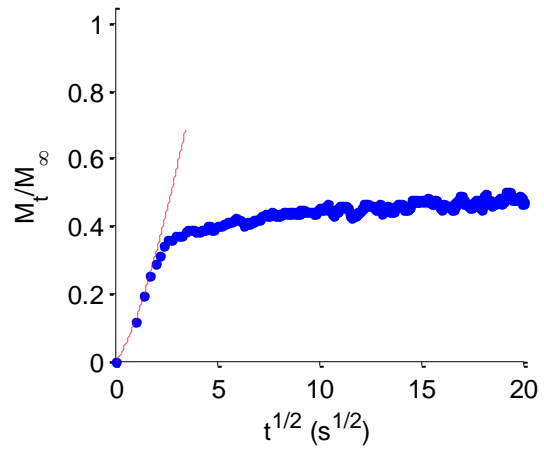
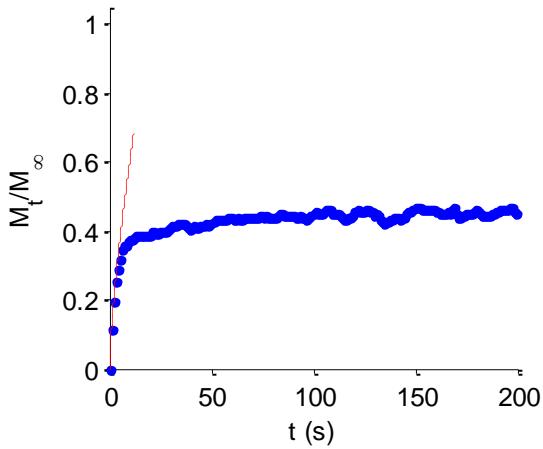
Thickness = 0.26 μm
Sorption activity step: 0.1 to 0.2
 $M_t/M_\infty = k t^n$ (---)
 $k = 0.113$
 $n = 0.759$
Anomalous diffusion



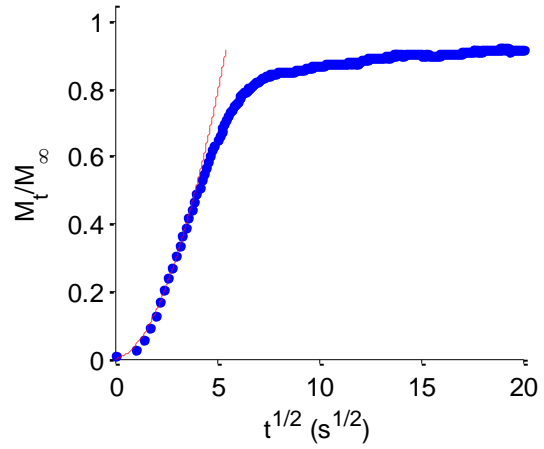
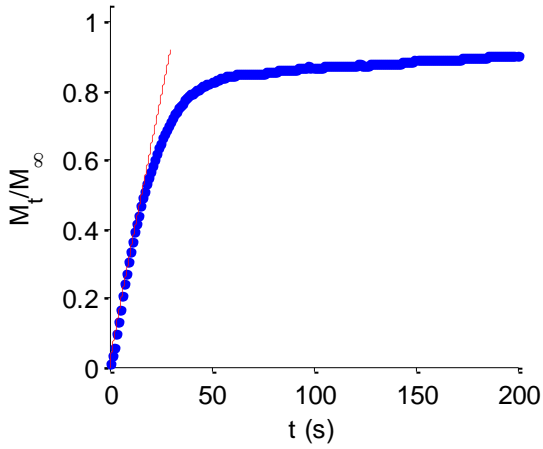
Thickness = 0.39 μm
Sorption activity step: 0.1 to 0.2
 $M_t/M_\infty = k t^n$ (---)
 $k = 0.120$
 $n = 0.888$
Anomalous diffusion



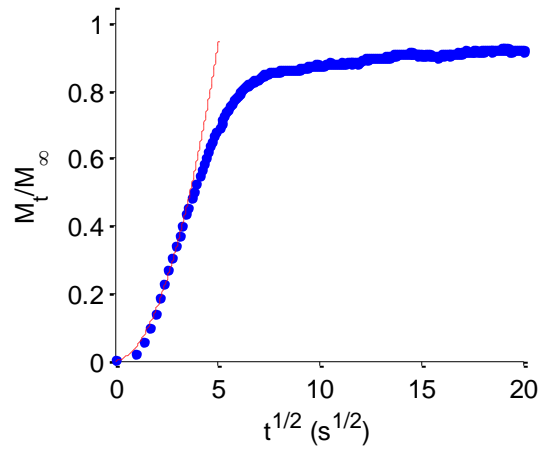
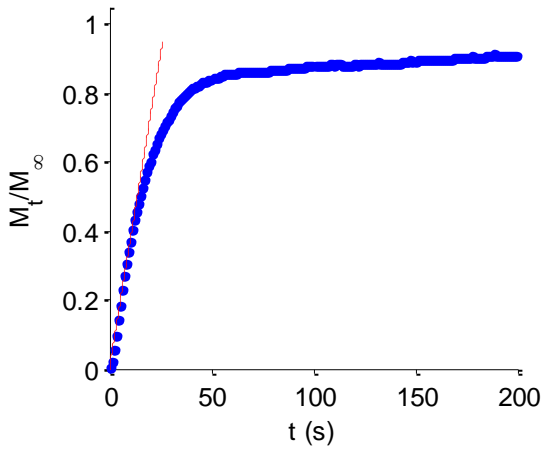
Thickness = 0.92 μm
Sorption activity step: 0.1 to 0.2
 $M_t/M_\infty = k t^n$ (---)
 $k = 0.116$
 $n = 0.712$
Anomalous diffusion



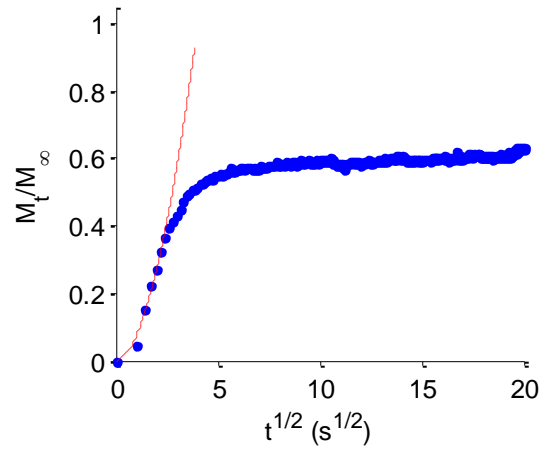
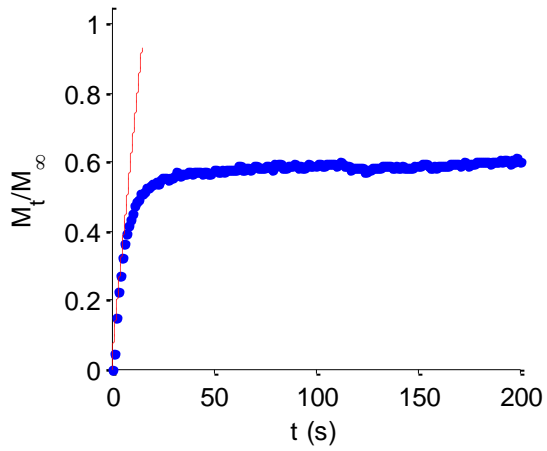
Thickness = 1.01 μm
Sorption activity step: 0 to 0.1
 $M_t/M_\infty = k t^n$ (---)
 $k = 0.0371$
 $n = 0.944$
Anomalous diffusion



Thickness = 1.49 μm
Sorption activity step: 0 to 0.1
 $M_t/M_\infty = k t^n$ (---)
 $k = 0.0370$
 $n = 0.995$
Case II

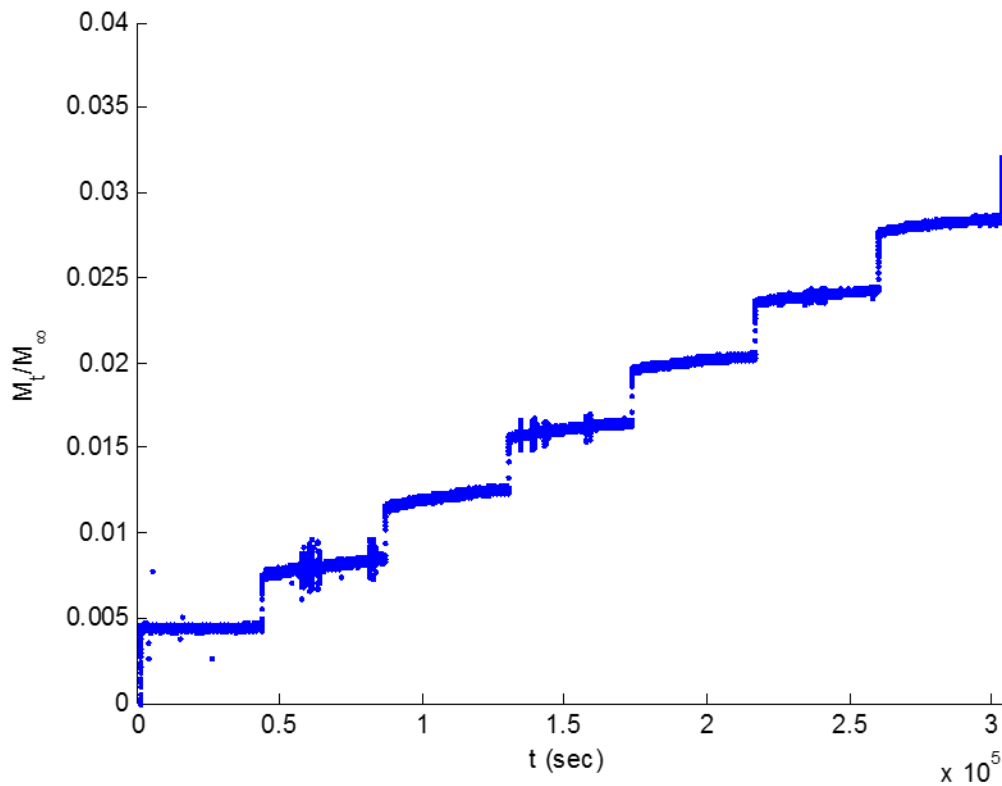


Thickness = 1.49 μm
Sorption activity step: 0.1 to 0.2
 $M_t/M_\infty = k t^n$ (---)
 $k = 0.0726$
 $n = 0.9411$
Anomalous diffusion



Water

(0.1 activity 12 h step intervals up to activity = 0.8), Film thickness = 0.27 μm



The below short time intervals are used for determination of the type of diffusion classification for each sorption step, *i.e.* Case I (Fickian, $n = 0.50$), Anomalous ($0.5 < n < 1.0$), or Case II ($n = 1.0$).

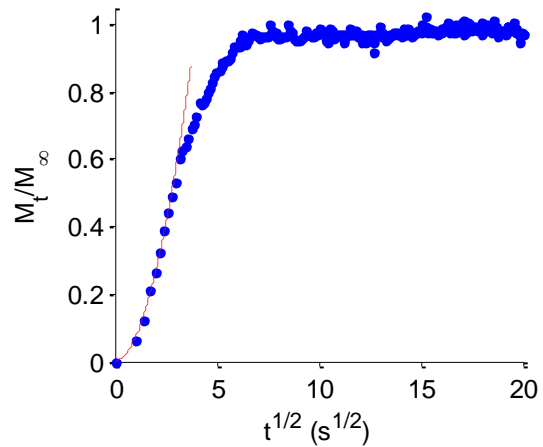
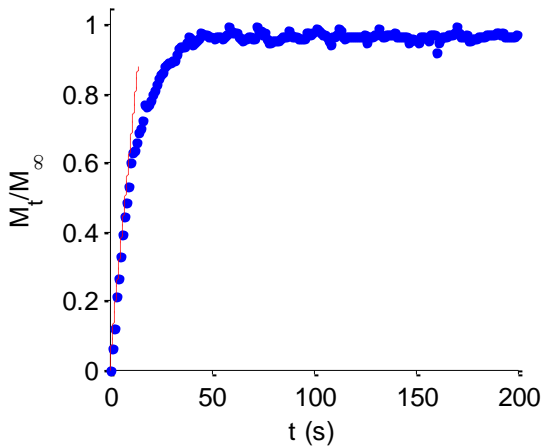
Sorption activity step: **0 to 0.1**

$$M_t/M_\infty = k t^n \text{ (---)}$$

$$k = 0.069$$

$$n = 0.964$$

Case II or anomalous



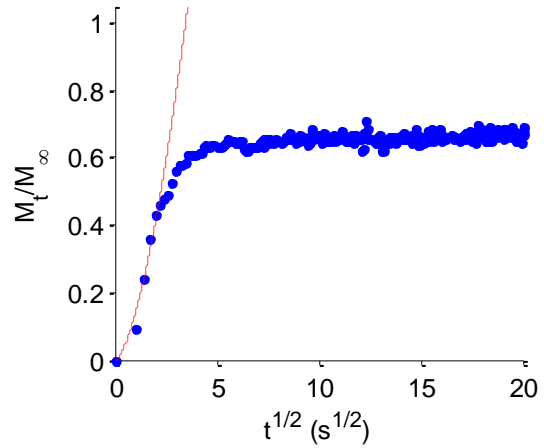
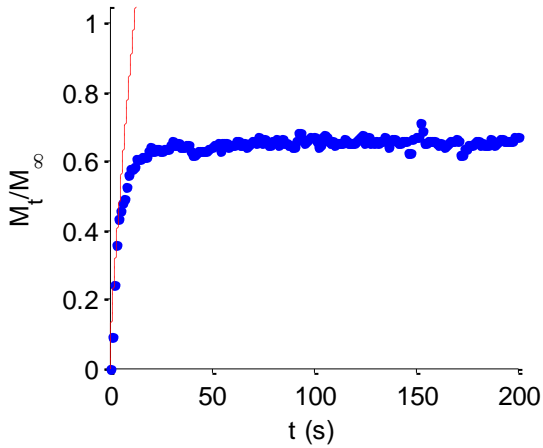
Sorption activity step: **0.1 to 0.2**

$$M_t/M_\infty = k t^n \text{ (---)}$$

$$k = 0.134$$

$$n = 0.806$$

Anomalous diffusion



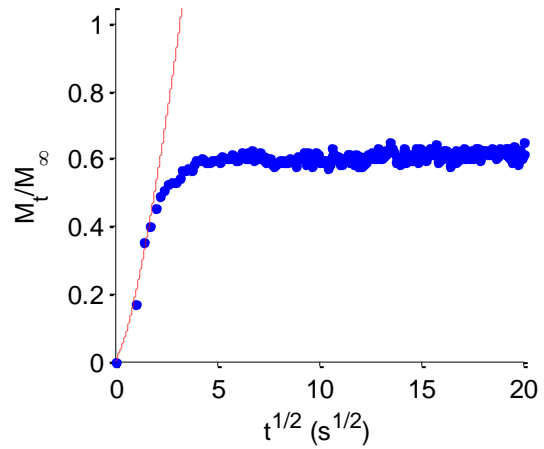
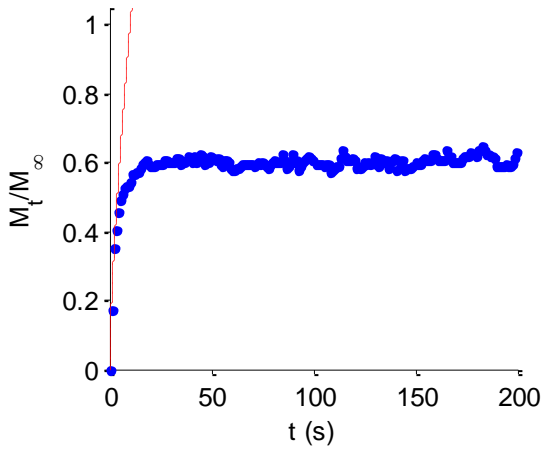
Sorption activity step: **0.2 to 0.3**

$$M_t/M_\infty = k t^n \text{ (---)}$$

$$k = 0.192$$

$$n = 0.711$$

Anomalous diffusion



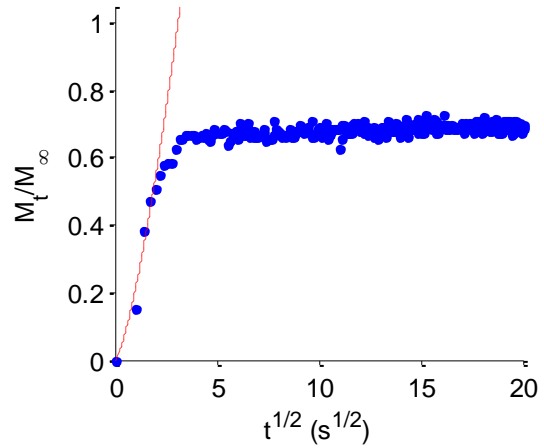
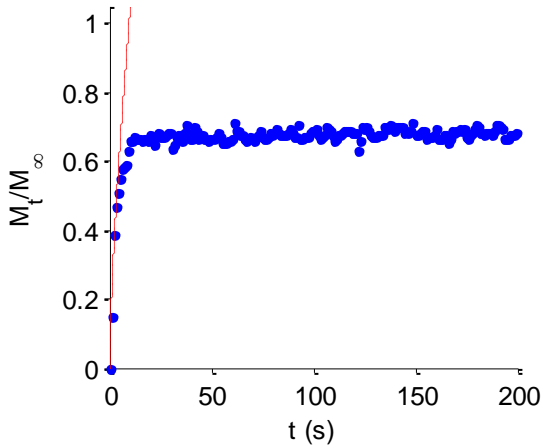
Sorption activity step: **0.3 to 0.4**

$$M_t/M_\infty = k t^n \text{ (---)}$$

$$k = 0.205$$

$$n = 0.700$$

Anomalous diffusion



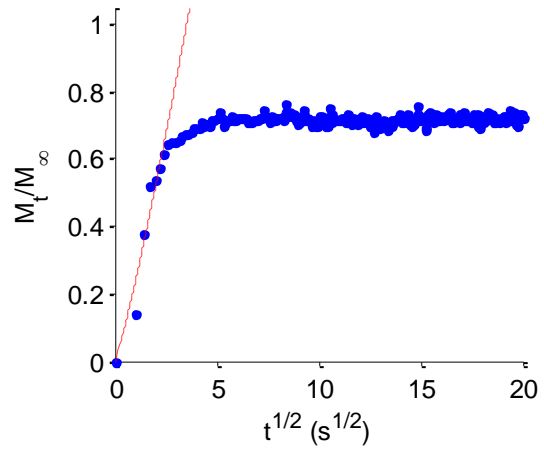
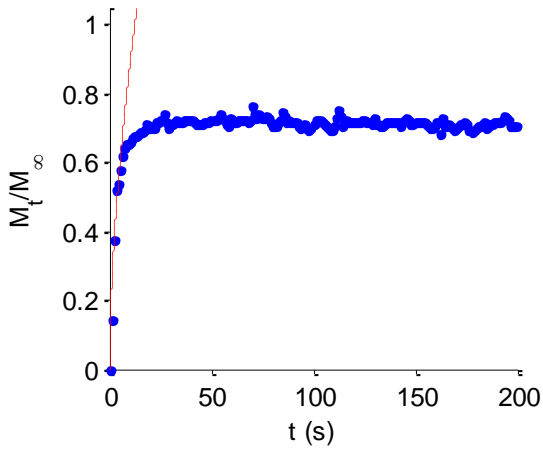
Sorption activity step: **0.4 to 0.5**

$$M_t/M_\infty = k t^n \text{ (---)}$$

$$k = 0.232$$

$$n = 0.579$$

Anomalous diffusion



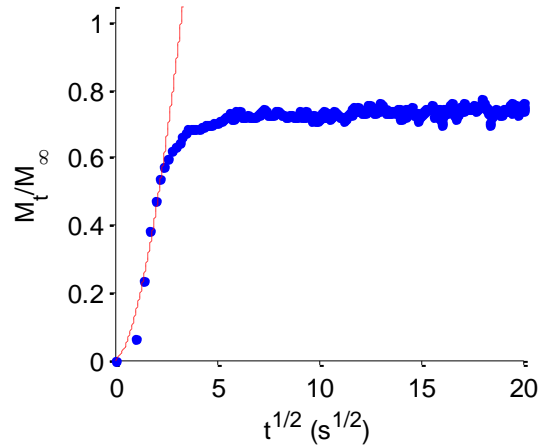
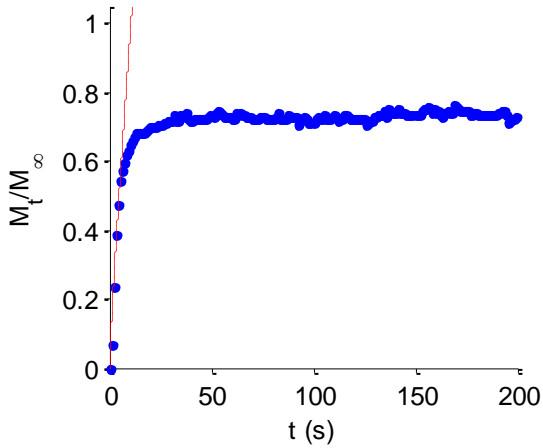
Sorption activity step: **0.5 to 0.6**

$$M_t/M_\infty = k t^n \text{ (---)}$$

$$k = 0.133$$

$$n = 0.857$$

Anomalous diffusion



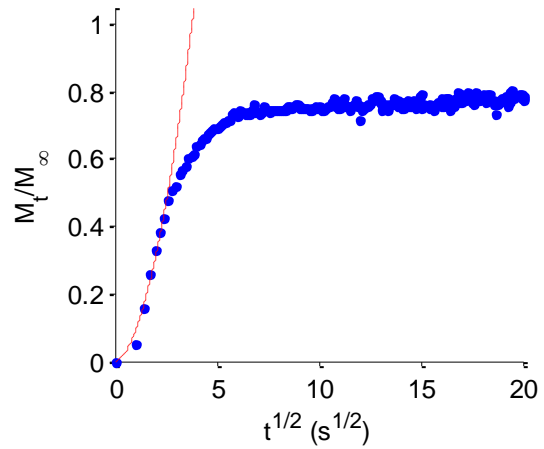
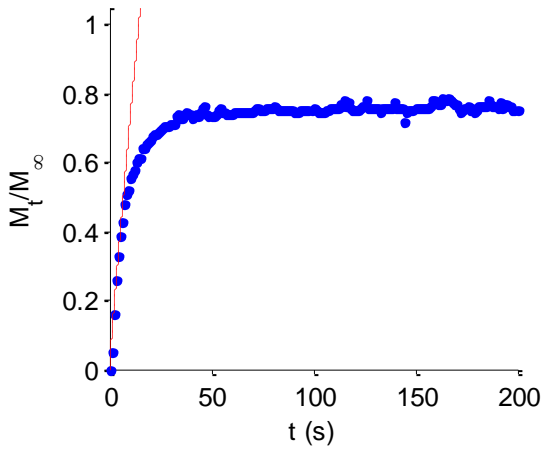
Sorption activity step: **0.6 to 0.7**

$$M_t/M_\infty = k t^n \text{ (---)}$$

$$k = 0.086$$

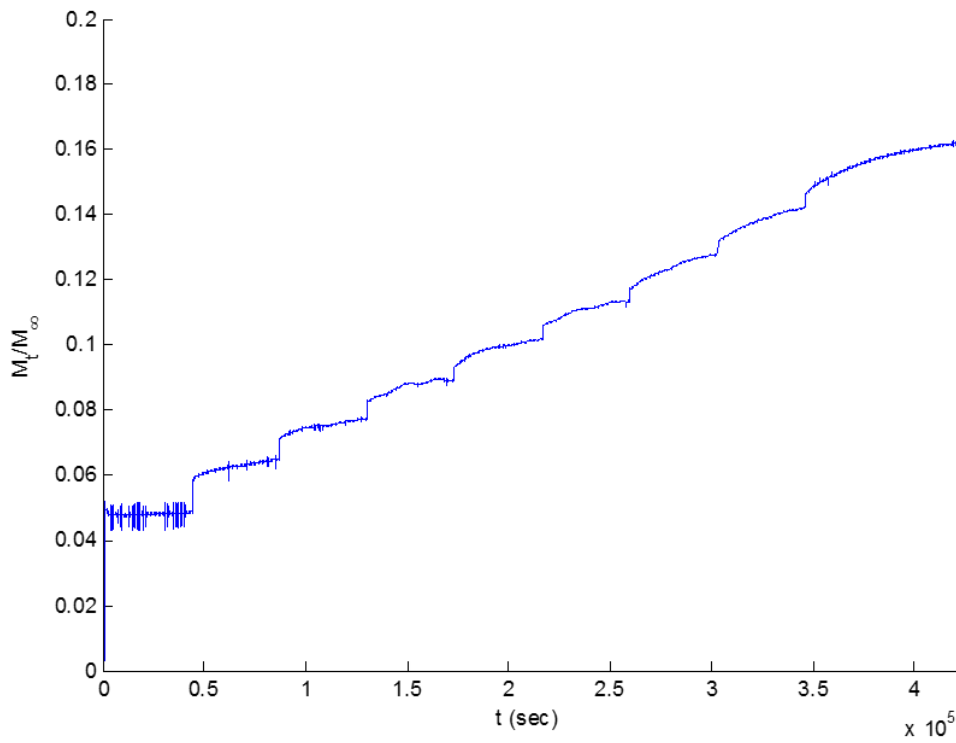
$$n = 0.921$$

Anomalous diffusion



Methanol

0.1 activity 12 h step intervals up to activity = 0.9, Film thickness = 0.275 μm



The below short time intervals are used for determination of the type of diffusion classification for each sorption step, *i.e.* Case I (Fickian, $n = 0.50$), Anomalous ($0.5 < n < 1.0$), or Case II ($n = 1.0$). One can see as the chemical activity increases, the 'Fickian' diffusive portion of each sorption interval shrinks in sorption amount and length of time, therefore the fit values for k and n must be viewed with caution.

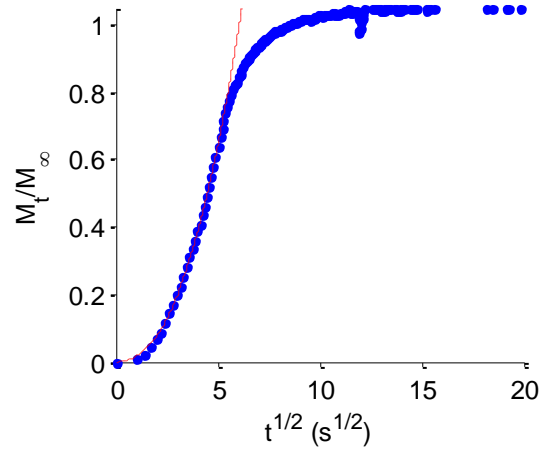
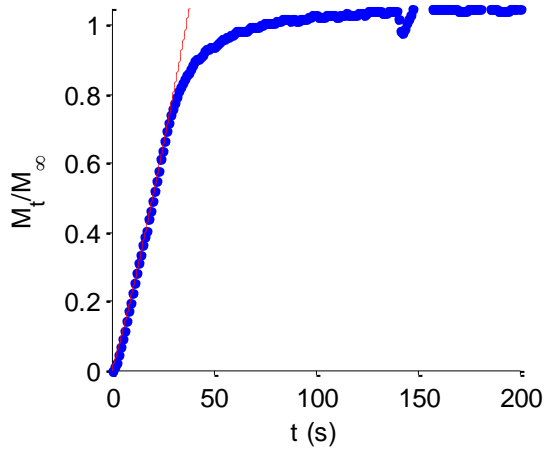
Sorption activity step: **0 to 0.1**

$$M_t/M_\infty = k t^n \text{ (---)}$$

$$k = 0.0152$$

$$n = 1.162$$

Case II



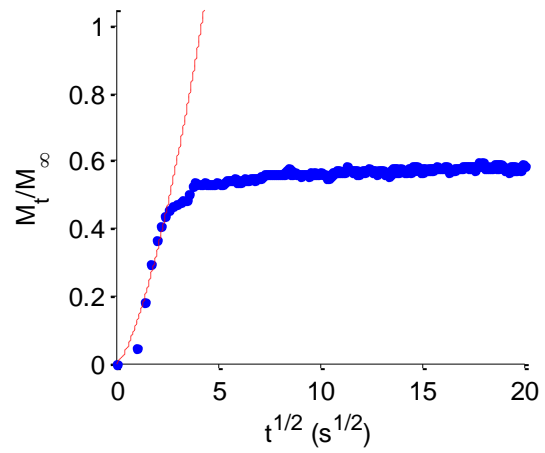
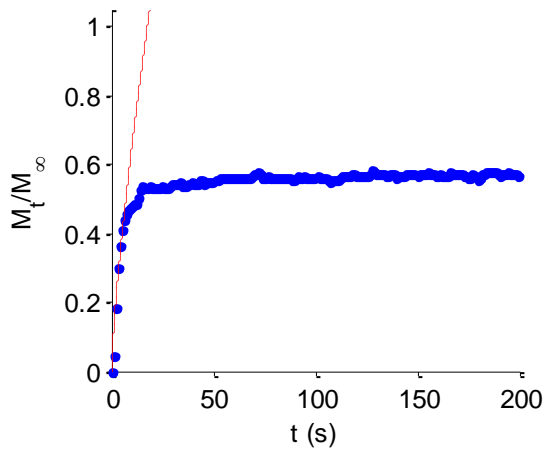
Sorption activity step: **0.1 to 0.2**

$$M_t/M_\infty = k t^n \text{ (---)}$$

$$k = 0.113$$

$$n = 0.759$$

Anomalous diffusion



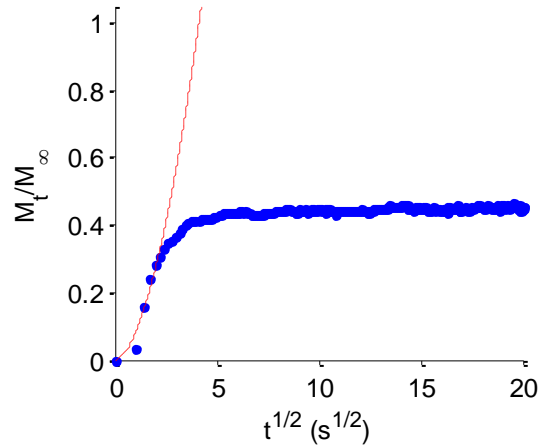
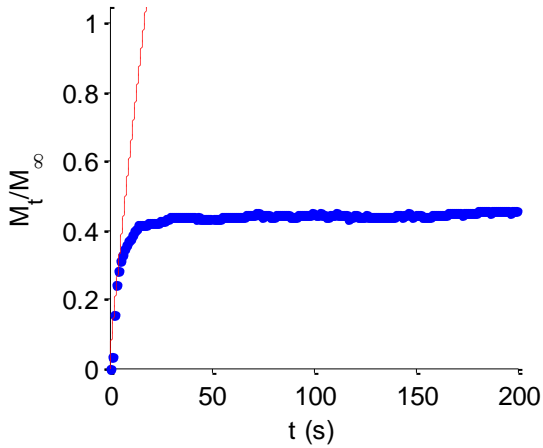
Sorption activity step: **0.2 to 0.3**

$$M_t/M_\infty = k t^n \text{ (---)}$$

$$k = 0.0776$$

$$n = 0.901$$

Anomalous diffusion



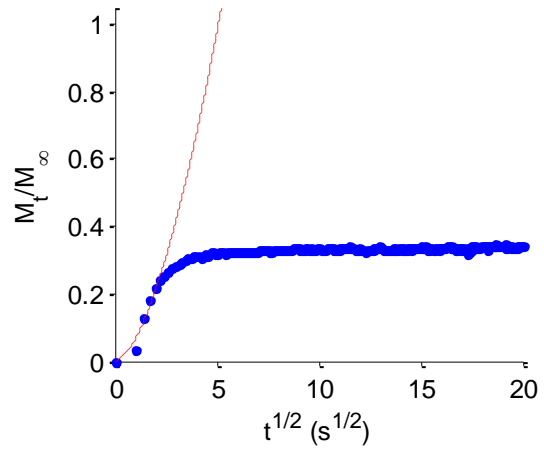
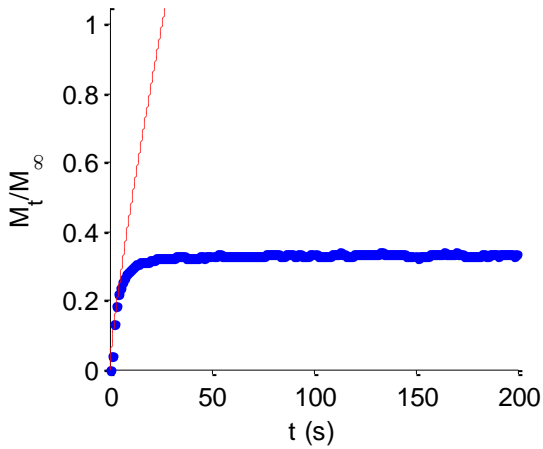
Sorption activity step: **0.3 to 0.4**

$$M_t/M_\infty = k t^n \text{ (---)}$$

$$k = 0.0659$$

$$n = 0.837$$

Anomalous diffusion



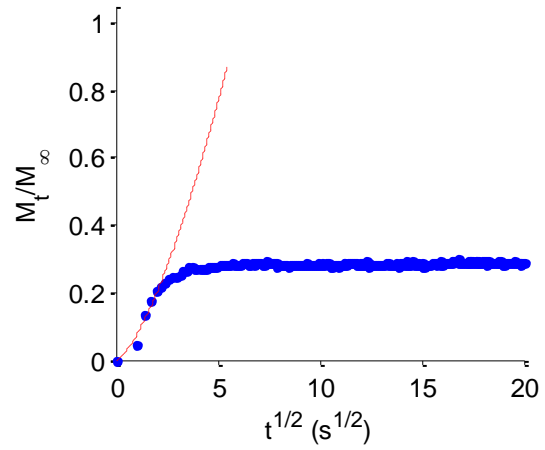
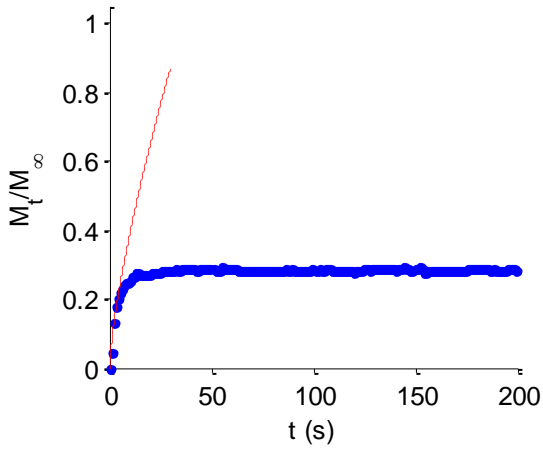
Sorption activity step: **0.4 to 0.5**

$$M_t/M_\infty = k t^n \text{ (---)}$$

$$k = 0.0713$$

$$n = 0.735$$

Anomalous diffusion



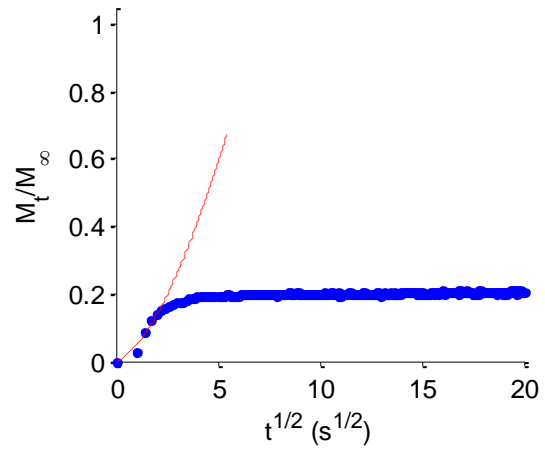
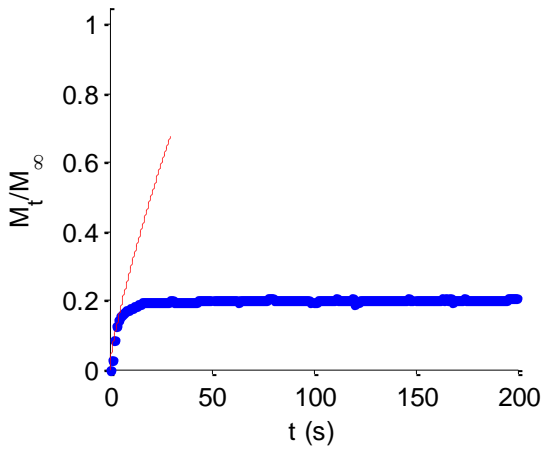
Sorption activity step: **0.5 to 0.6**

$$M_t/M_\infty = k t^n \text{ (---)}$$

$$k = 0.0451$$

$$n = 0.796$$

Anomalous diffusion



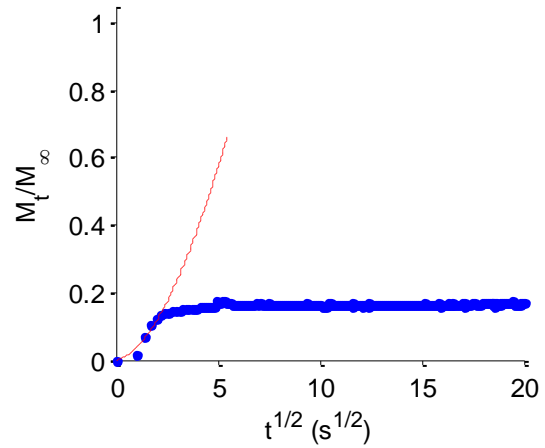
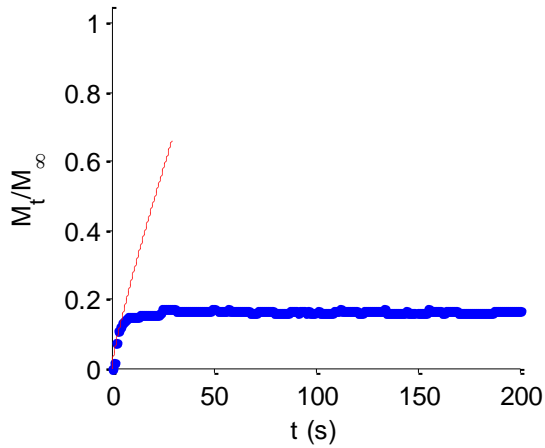
Sorption activity step: **0.6 to 0.7**

$$M_t/M_\infty = k t^n \text{ (---)}$$

$$k = 0.0353$$

$$n = 0.862$$

Anomalous diffusion



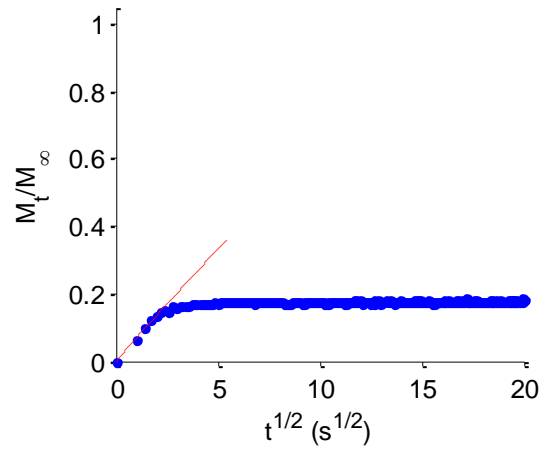
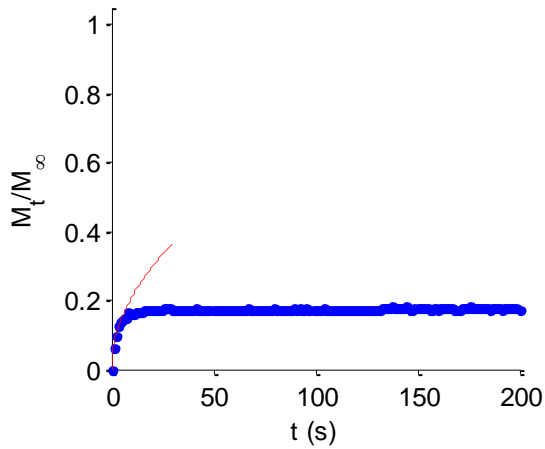
Sorption activity step: **0.7 to 0.8**

$$M_t/M_\infty = k t^n \text{ (---)}$$

$$k = 0.0670$$

$$n = 0.495$$

Anomalous diffusion



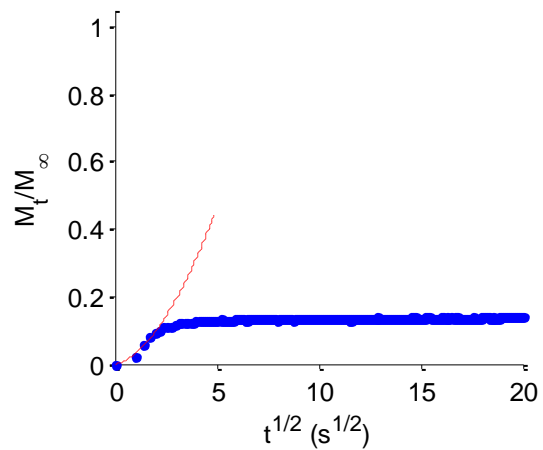
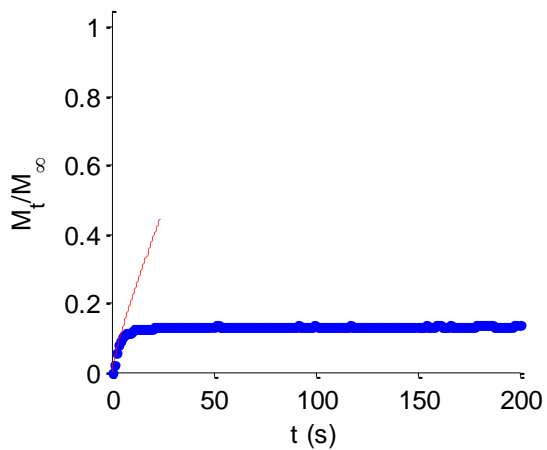
Sorption activity step: **0.8 to 0.9**

$$M_t/M_\infty = k t^n \text{ (---)}$$

$$k = 0.0290$$

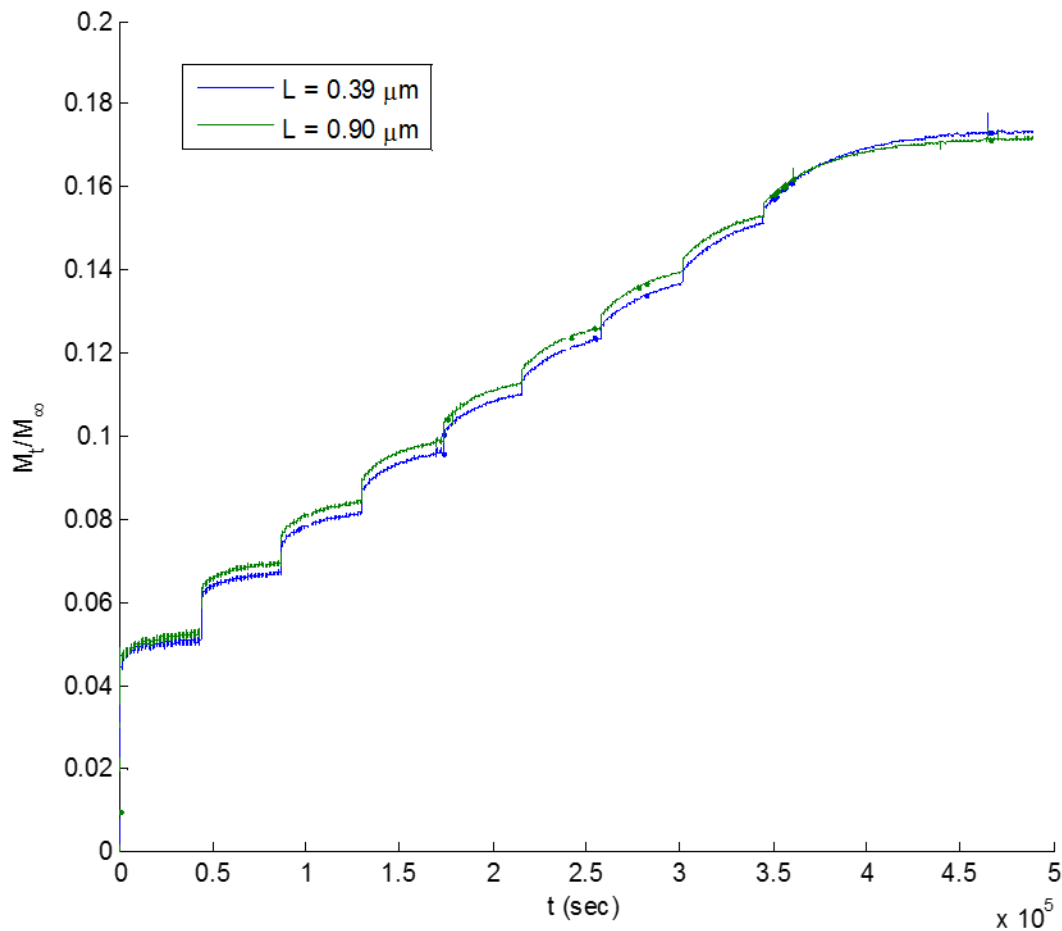
$$n = 0.859$$

Anomalous diffusion



Ethanol

0.1 activity 12 h step intervals up to activity = 0.9, film thickness = 0.39 μm



The below short time intervals are used for determination of the type of diffusion classification for each sorption step, *i.e.* Case I (Fickian, $n = 0.50$), Anomalous ($0.5 < n < 1.0$), or Case II ($n = 1.0$). One can see as the chemical activity increases, the 'Fickian' diffusive portion of each sorption interval decreases in amount, therefore the fit values for k and n must be viewed with caution.

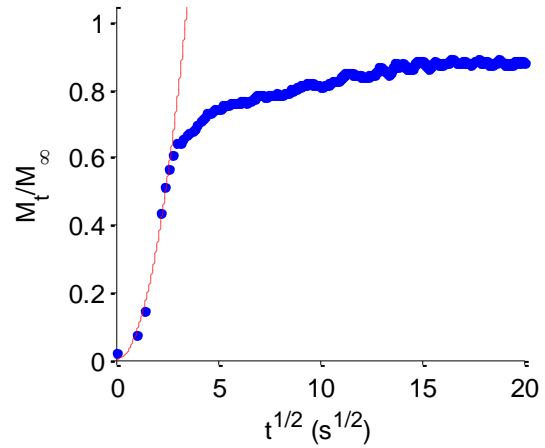
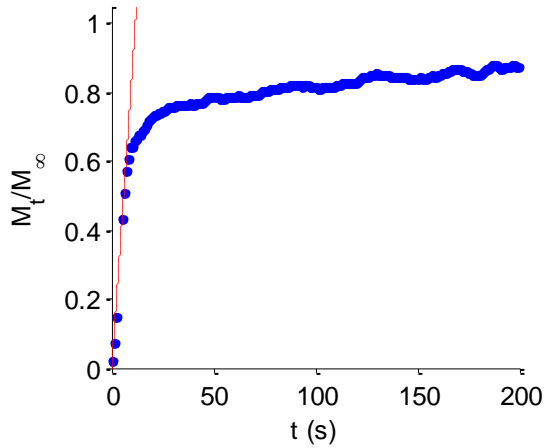
Sorption activity step: **0 to 0.1**

$$M_t/M_\infty = k t^n \text{ (---)}$$

$$k = 0.0785$$

$$n = 1.034$$

Case II or anomalous



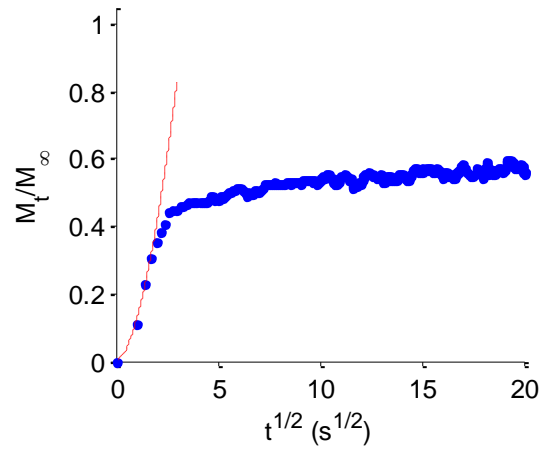
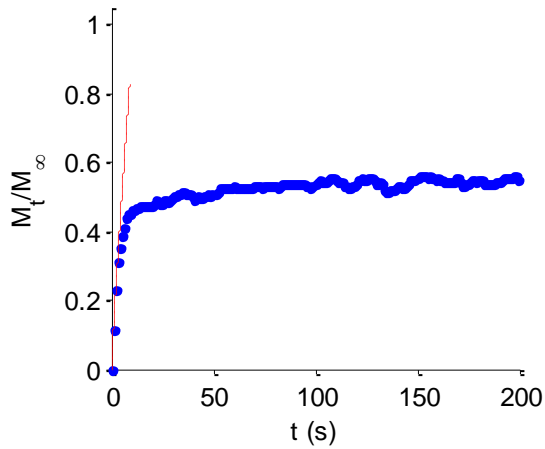
Sorption activity step: **0.1 to 0.2**

$$M_t/M_\infty = k t^n \text{ (---)}$$

$$k = 0.118$$

$$n = 0.888$$

Anomalous diffusion



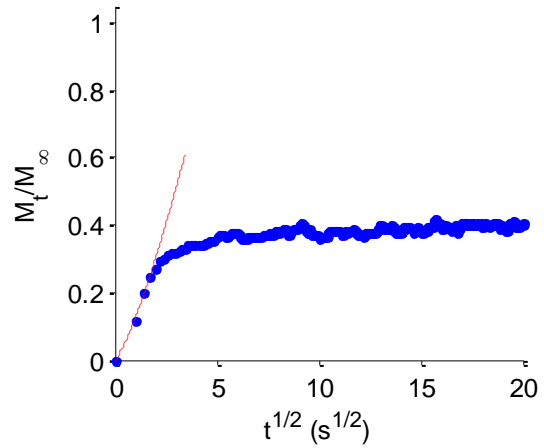
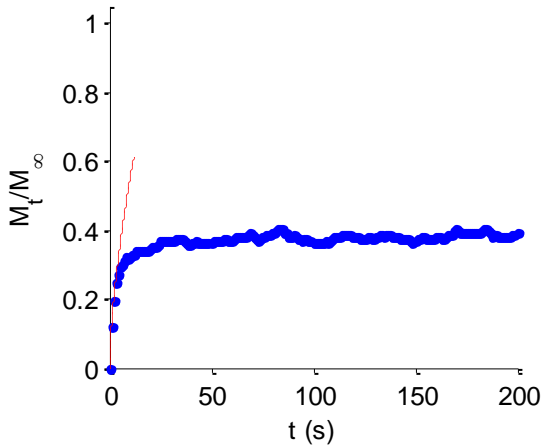
Sorption activity step: **0.2 to 0.3**

$$M_t/M_\infty = k t^n \text{ (---)}$$

$$k = 0.124$$

$$n = 0.650$$

Anomalous diffusion



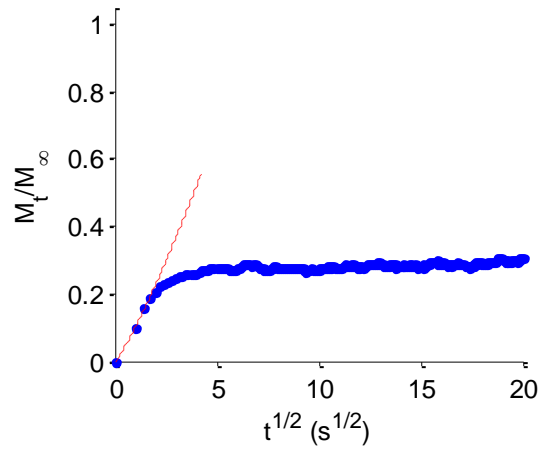
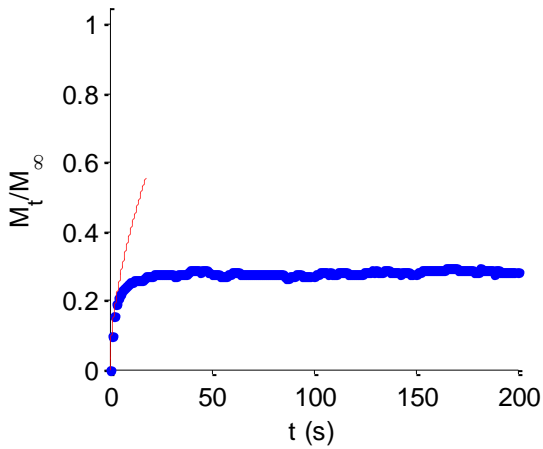
Sorption activity step: **0.3 to 0.4**

$$M_t/M_\infty = k t^n \text{ (---)}$$

$$k = 0.0989$$

$$n = 0.597$$

Anomalous diffusion



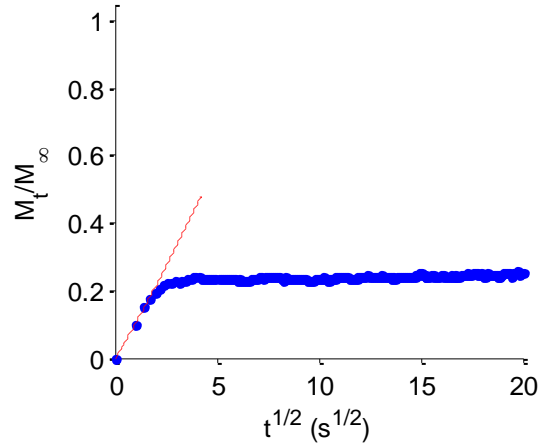
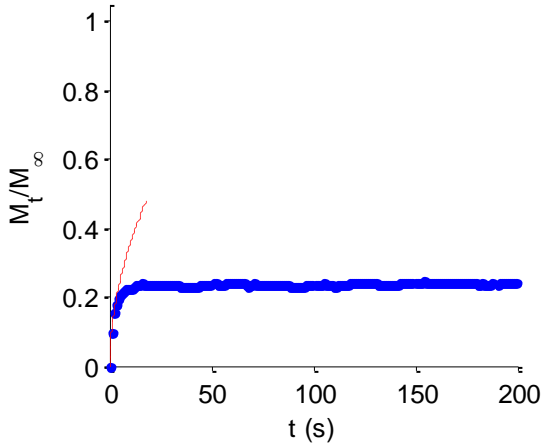
Sorption activity step: **0.4 to 0.5**

$$M_t/M_\infty = k t^n \text{ (---)}$$

$$k = 0.100$$

$$n = 0.540$$

Anomalous diffusion



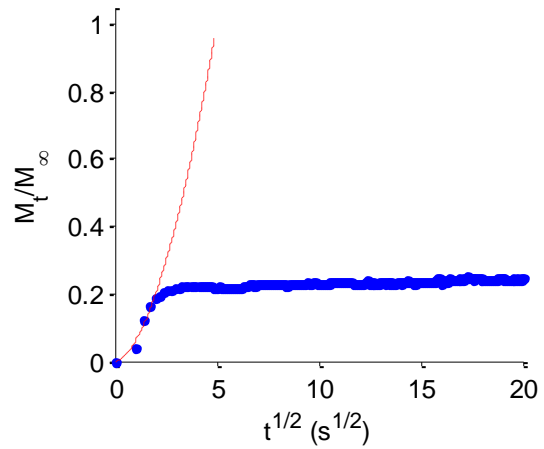
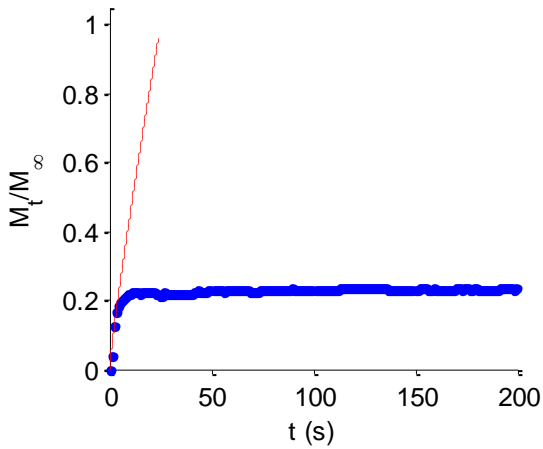
Sorption activity step: **0.5 to 0.6**

$$M_t/M_\infty = k t^n \text{ (---)}$$

$$k = 0.0578$$

$$n = 0.885$$

Anomalous diffusion



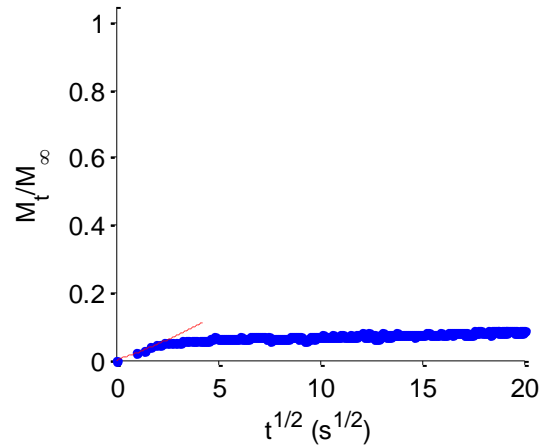
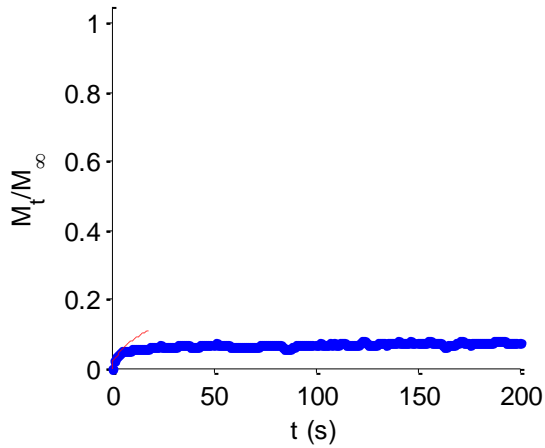
Sorption activity step: **0.6 to 0.7**

$$M_t/M_\infty = k t^n \text{ (---)}$$

$$k = 0.0195$$

$$n = 0.596$$

Anomalous diffusion



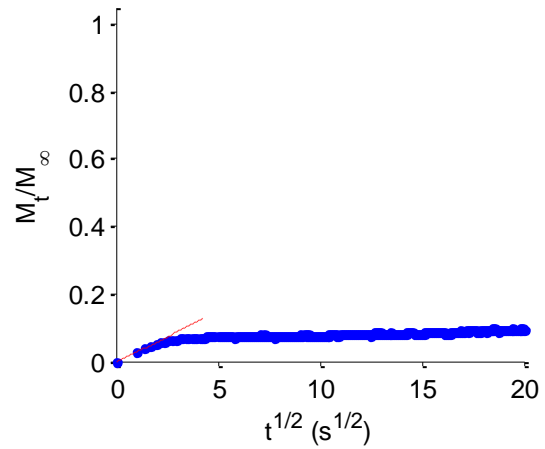
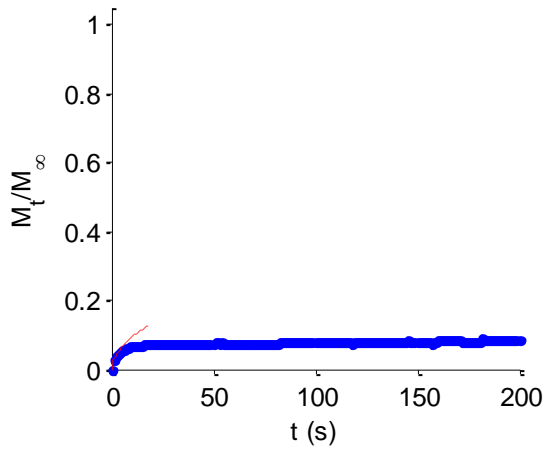
Sorption activity step: **0.7 to 0.8**

$$M_t/M_\infty = k t^n \text{ (---)}$$

$$k = 0.0251$$

$$n = 0.555$$

Anomalous diffusion



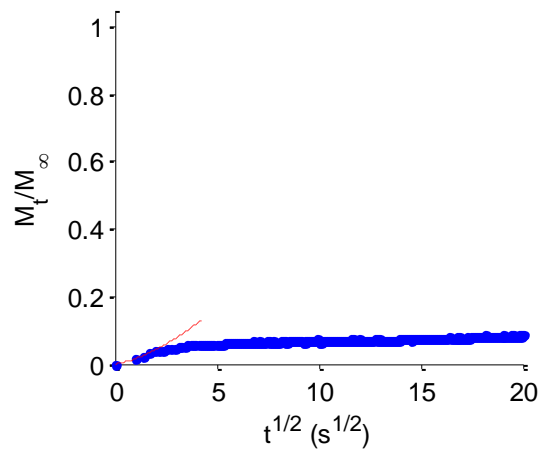
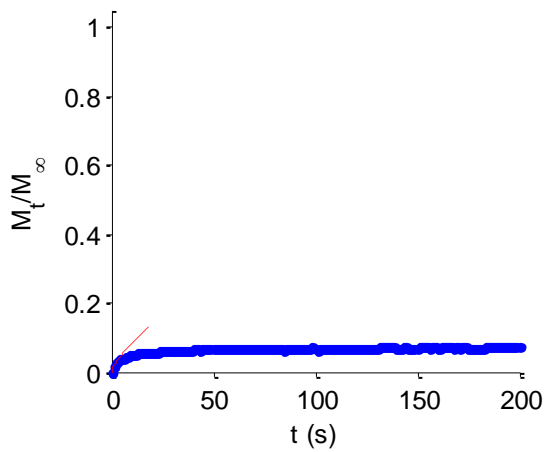
Sorption activity step: **0.8 to 0.9**

$$M_t/M_\infty = k t^n \text{ (---)}$$

$$k = 0.0142$$

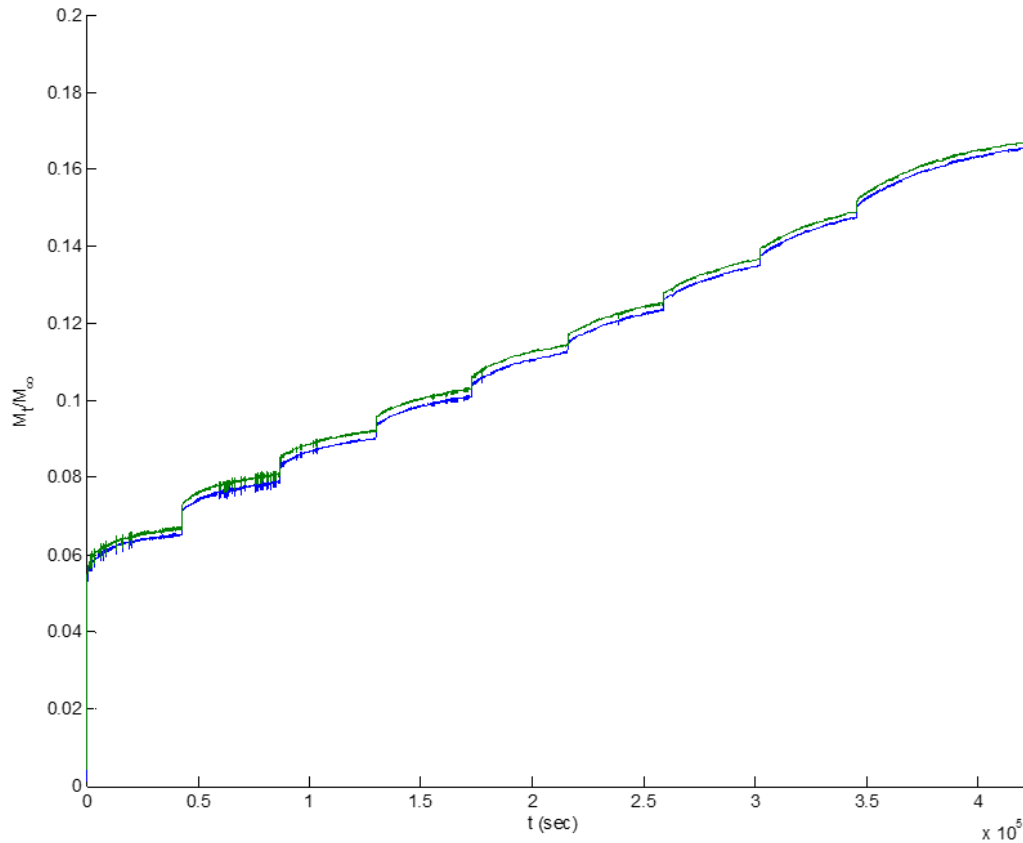
$$n = 0.760$$

Anomalous diffusion



Ethanol

0.1 activity 12 h step intervals up to activity = 0.9, Film thickness = 0.275 μm (blue), 0.28 μm (green)



The below short time intervals are used for determination of the type of diffusion classification for each sorption step, *i.e.* Case I (Fickian, $n = 0.50$), Anomalous ($0.5 < n < 1.0$), or Case II ($n = 1.0$). One can see as the chemical activity increases, the 'Fickian' diffusive portion of each sorption interval decreases in amount, therefore the fit values for k and n must be viewed with caution.

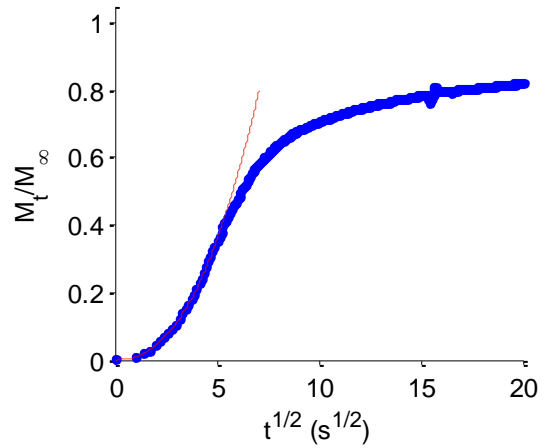
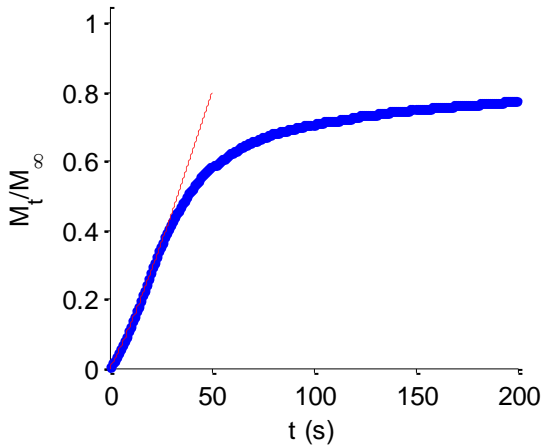
Sorption activity step: **0 to 0.1**

$$M_t/M_\infty = k t^n \text{ (---)}$$

$$k = 0.0121$$

$$n = 1.053$$

Case II



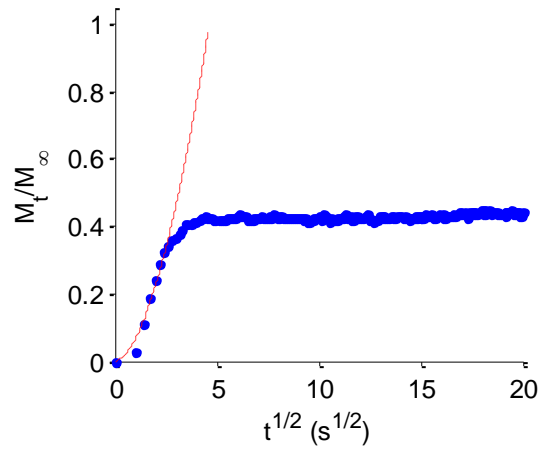
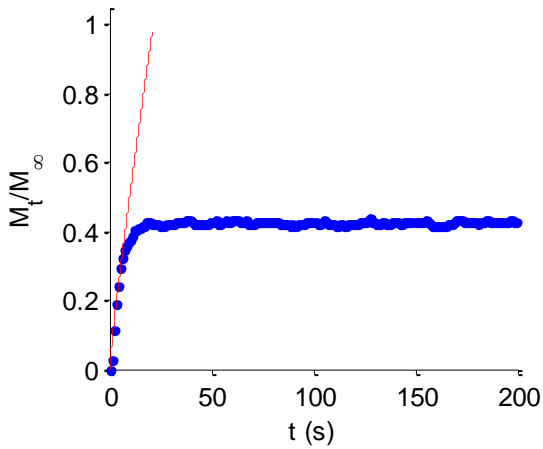
Sorption activity step: **0.1 to 0.2**

$$M_t/M_\infty = k t^n \text{ (---)}$$

$$k = 0.0661$$

$$n = 0.891$$

Anomalous diffusion



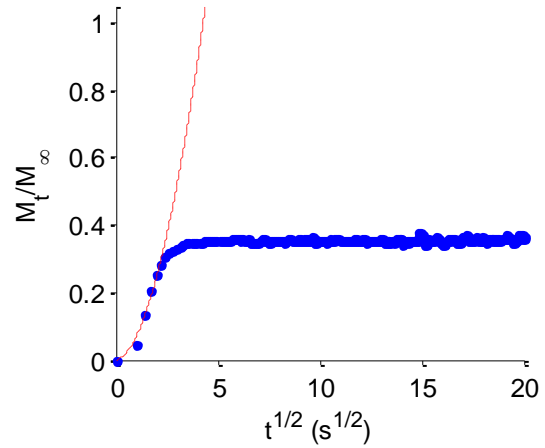
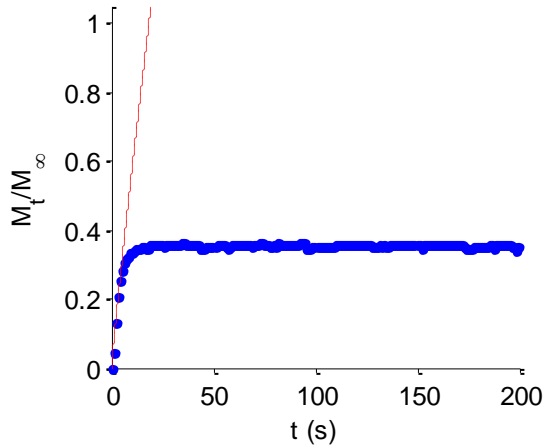
Sorption activity step: **0.2 to 0.3**

$$M_t/M_\infty = k t^n \text{ (---)}$$

$$k = 0.0636$$

$$n = 0.925$$

Anomalous diffusion



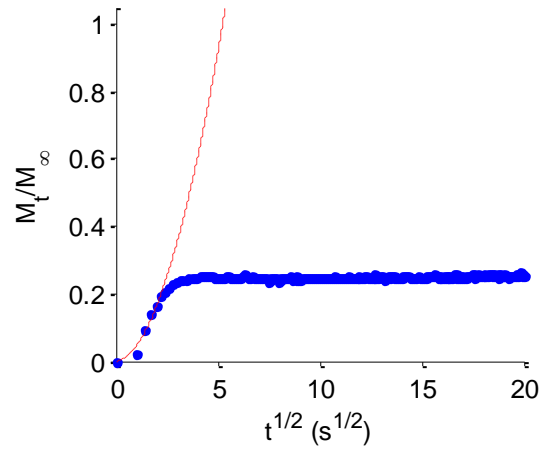
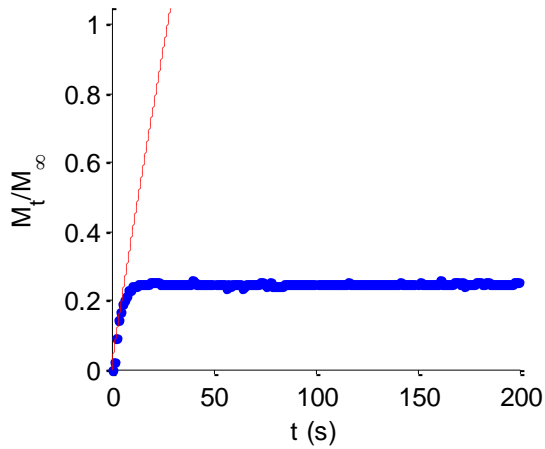
Sorption activity step: **0.3 to 0.4**

$$M_t/M_\infty = k t^n \text{ (---)}$$

$$k = 0.0460$$

$$n = 0.940$$

Anomalous diffusion



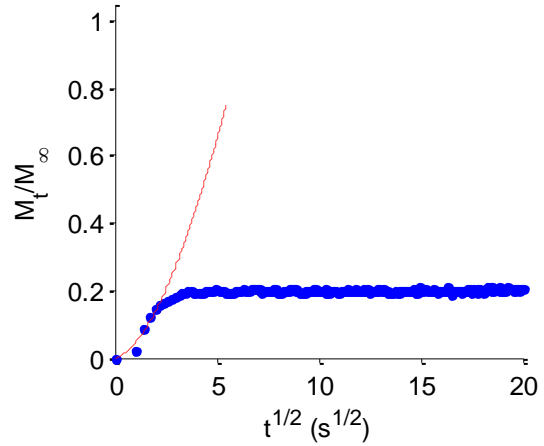
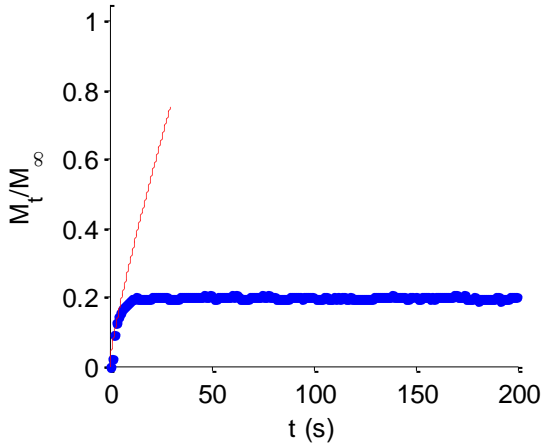
Sorption activity step: **0.4 to 0.5**

$$M_t/M_\infty = k t^n \text{ (---)}$$

$$k = 0.0467$$

$$n = 0.838$$

Anomalous diffusion



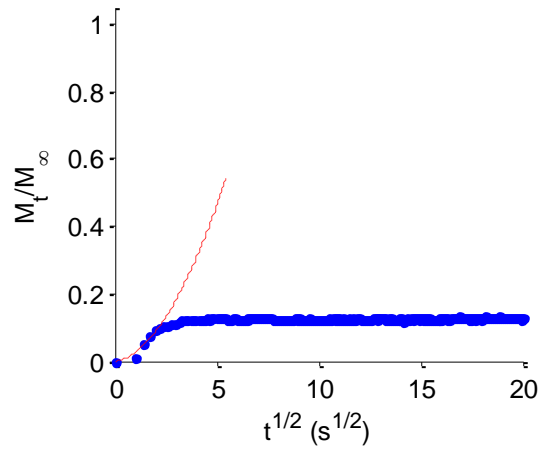
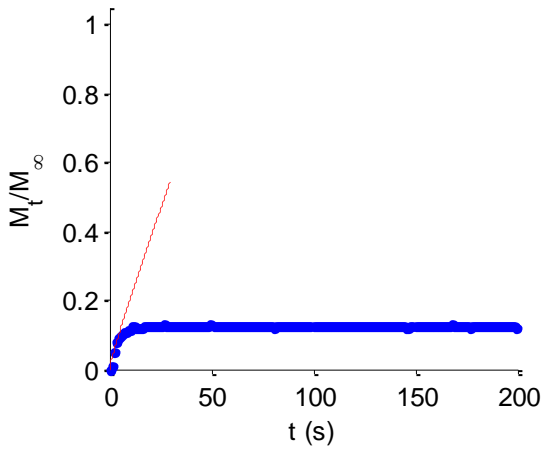
Sorption activity step: **0.5 to 0.6**

$$M_t/M_\infty = k t^n \text{ (---)}$$

$$k = 0.0298$$

$$n = 0.914$$

Anomalous diffusion



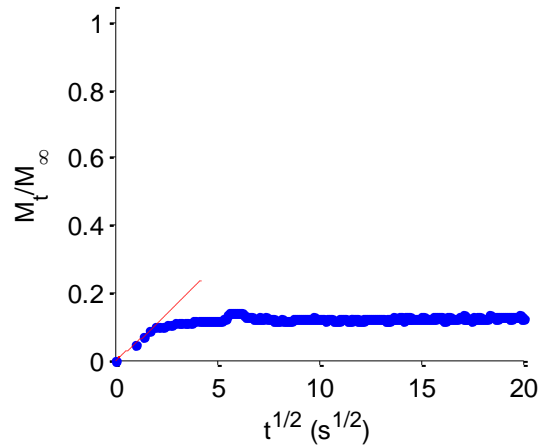
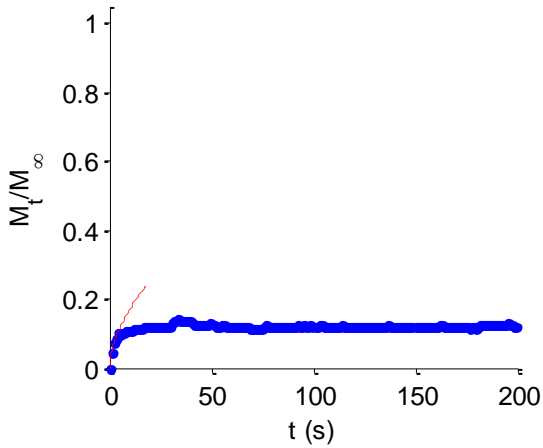
Sorption activity step: **0.6 to 0.7**

$$M_t/M_\infty = k t^n \text{ (---)}$$

$$k = 0.0512$$

$$n = 0.573$$

Anomalous diffusion



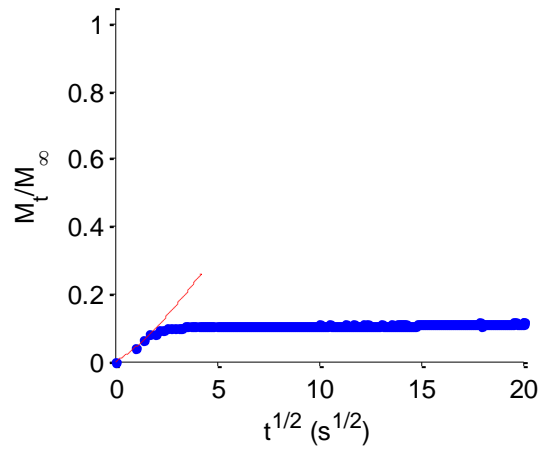
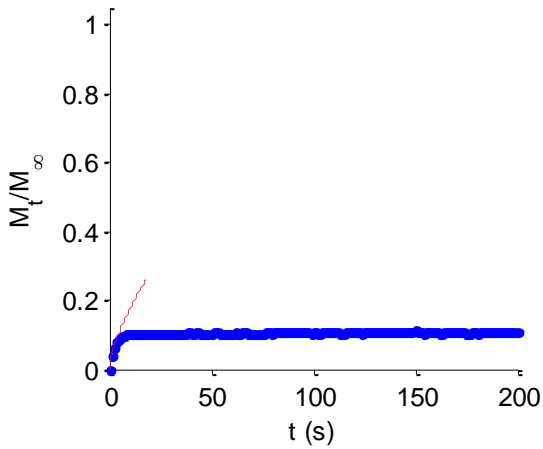
Sorption activity step: **0.7 to 0.8**

$$M_t/M_\infty = k t^n \text{ (---)}$$

$$k = 0.0437$$

$$n = 0.664$$

Anomalous diffusion



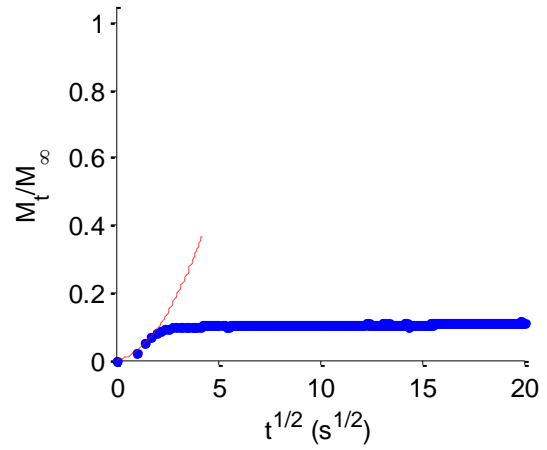
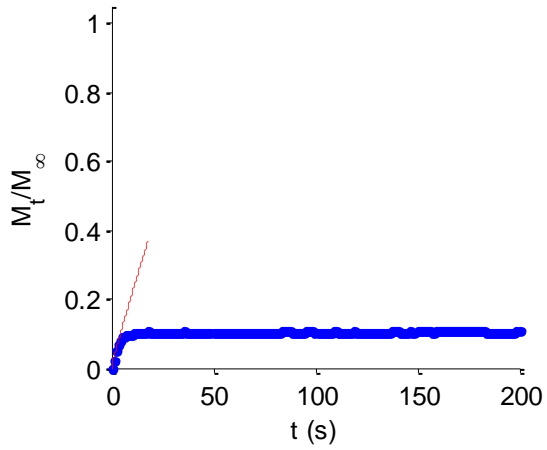
Sorption activity step: **0.8 to 0.9**

$$M_t/M_\infty = k t^n \text{ (---)}$$

$$k = 0.0294$$

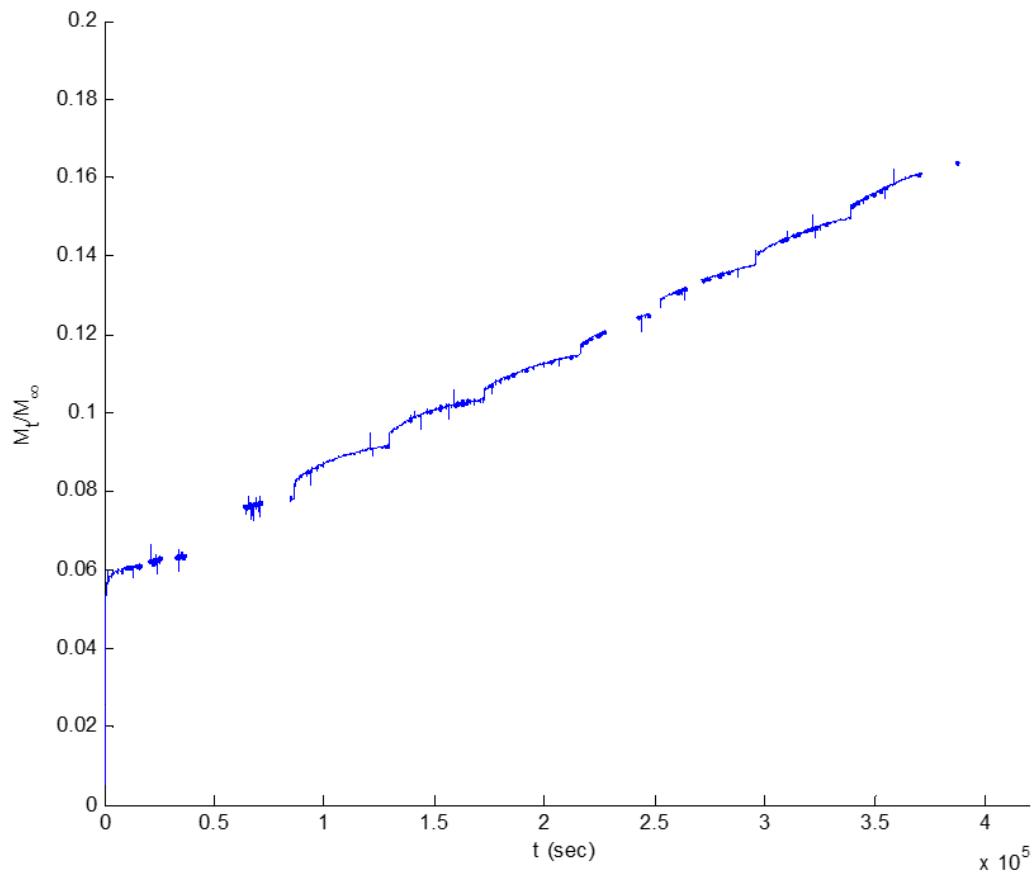
$$n = 0.849$$

Anomalous diffusion



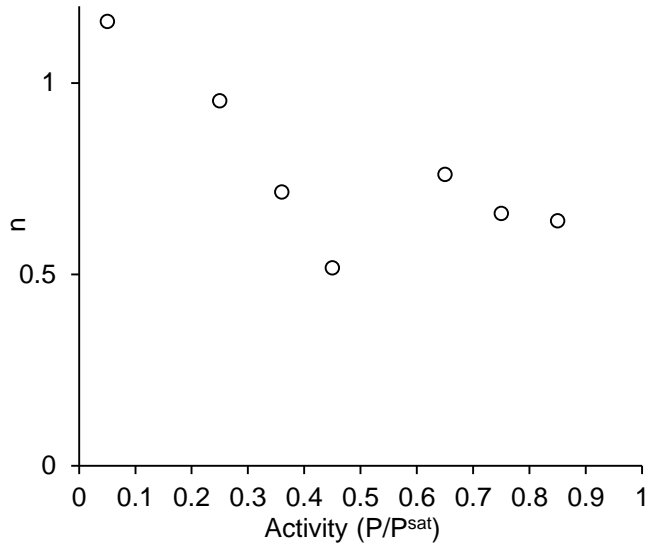
Propanol

0.1 activity 12 h step intervals up to activity = 0.9, Film thickness = 0.270 μm



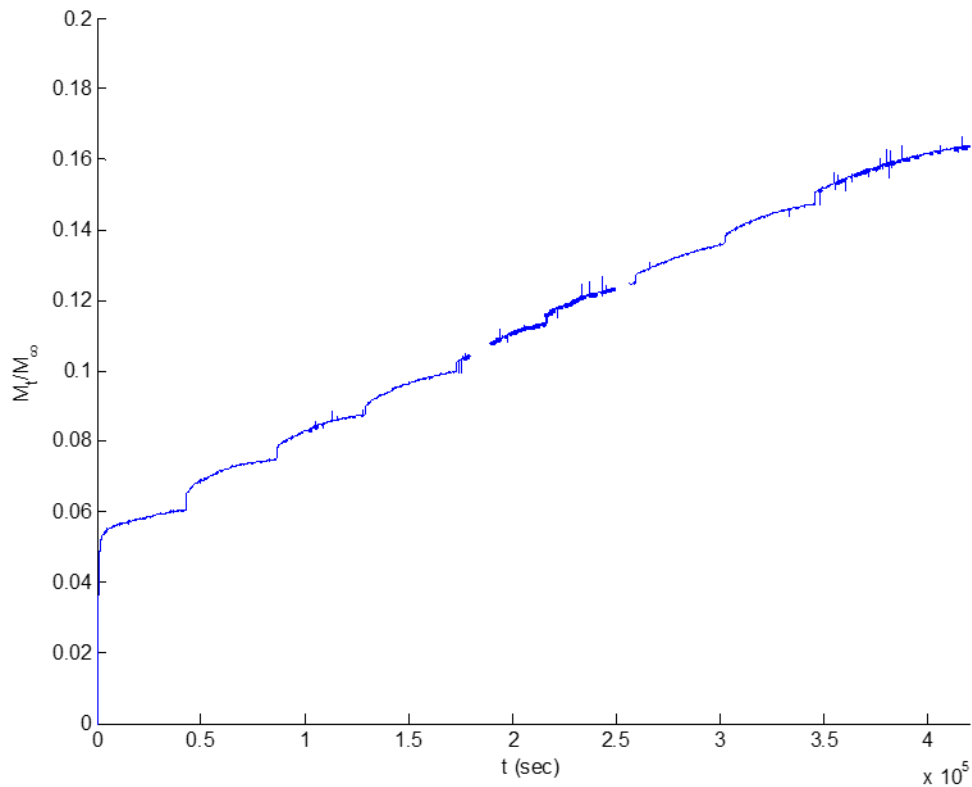
*The missing gaps of data in the above sorption curve were due to difficulties with the recording device. Partial sorption runs were performed separately when needed to allow calculation of the relevant parameters. This separate additional data is not shown. The 0.1 activity step sorption intervals are still easy to identify and isolate, because each interval is run for 12 h regardless of dropped sample recording.

Short time intervals were used for determination of the type of diffusion classification for each sorption step, *i.e.* Case I (Fickian, $n = 0.50$), Anomalous ($0.5 < n < 1.0$), or Case II ($n = 1.0$). The following is a summary of calculated n values for $M/M_{\infty} = k t^n$ for each 0.1 activity sorption interval.



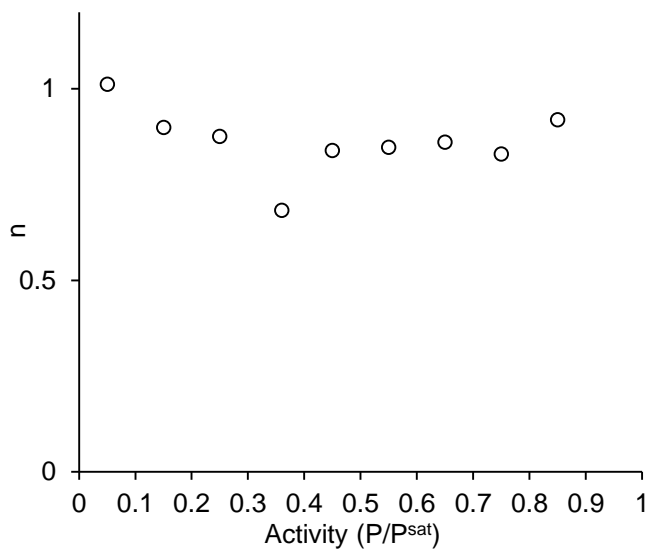
Butanol

0.1 activity 12 h step intervals up to activity = 0.9, Film thickness = 0.255 μm



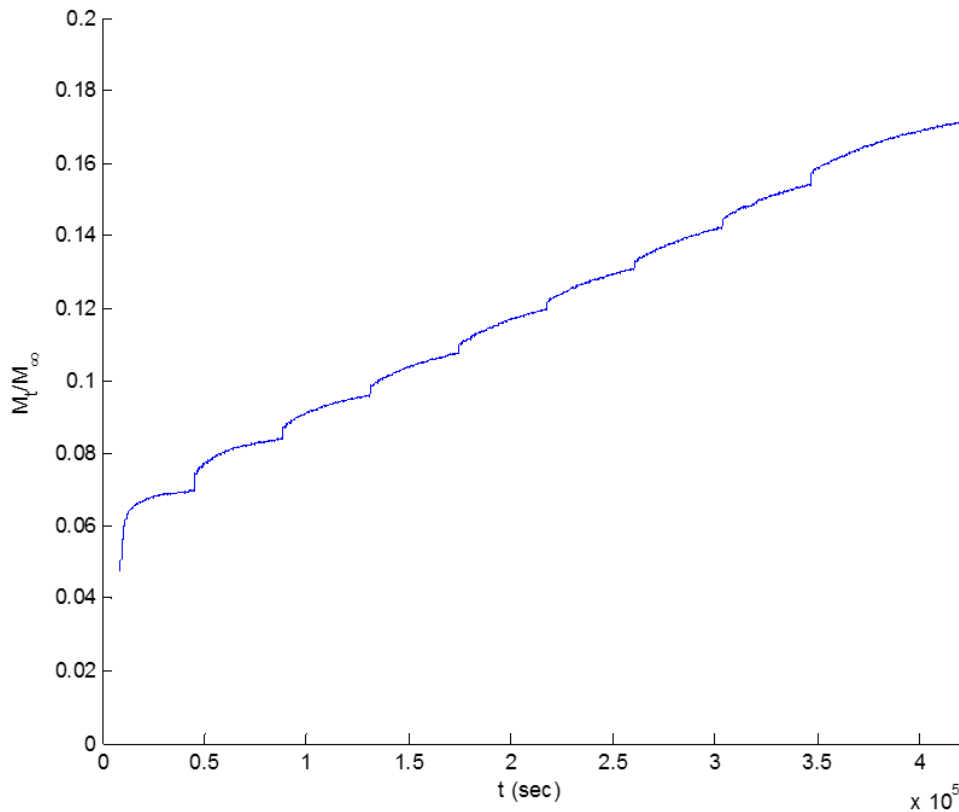
Short time intervals were used for determination of the type of diffusion classification for each sorption step, *i.e.* Case I (Fickian, $n = 0.50$), Anomalous ($0.5 < n < 1.0$), or Case II ($n = 1.0$).

The following is a summary of calculated n values for $M/M_\infty = k t^n$ for each 0.1 activity sorption interval.

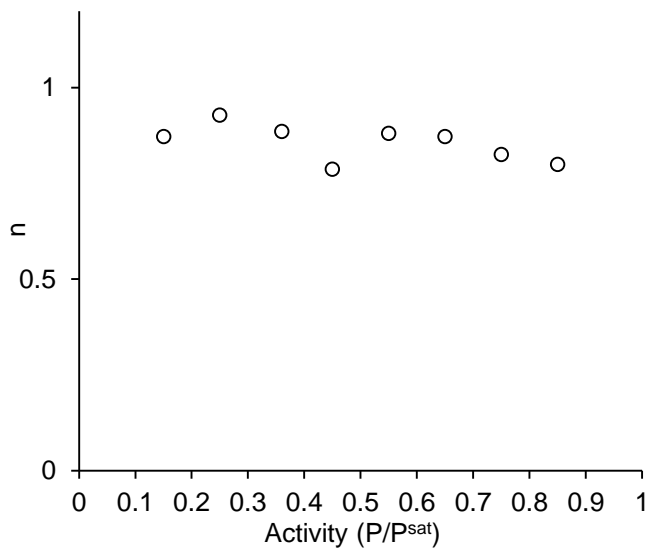


Pentanol

0.1 activity 12 h step intervals up to activity = 0.9, Film thickness = 0.260 μm

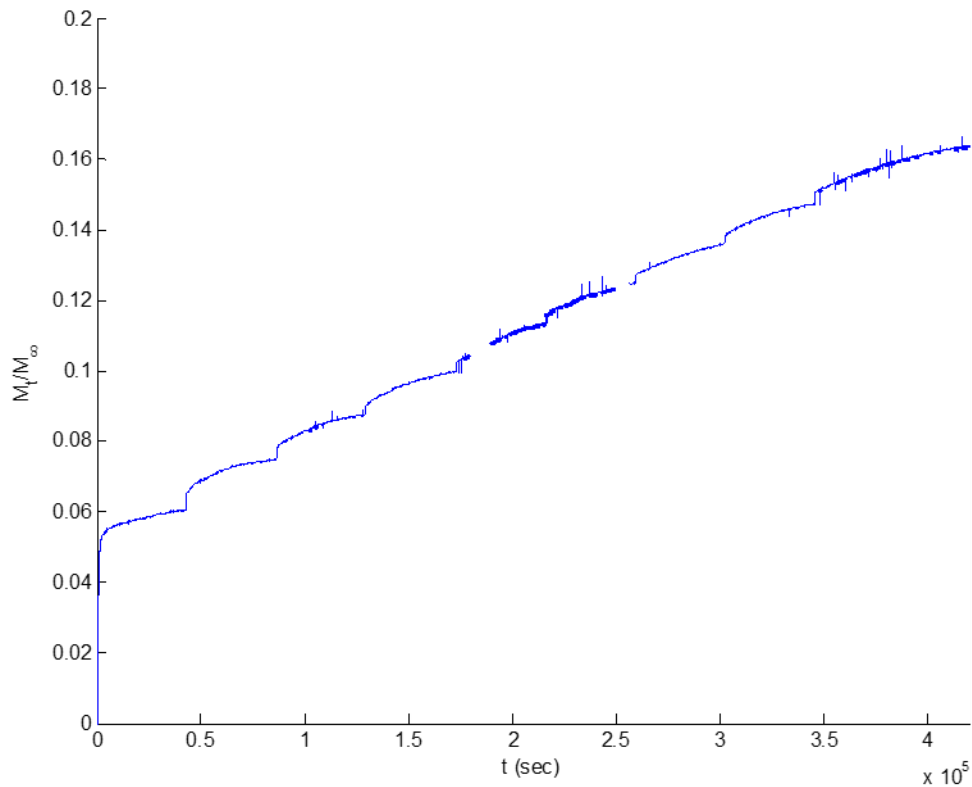


Short time intervals were used for determination of the type of diffusion classification for each sorption step, *i.e.* Case I (Fickian, $n = 0.50$), Anomalous ($0.5 < n < 1.0$), or Case II ($n = 1.0$). The following is a summary of calculated n values for $M_t/M_\infty = k t^n$ for each 0.1 activity sorption interval.



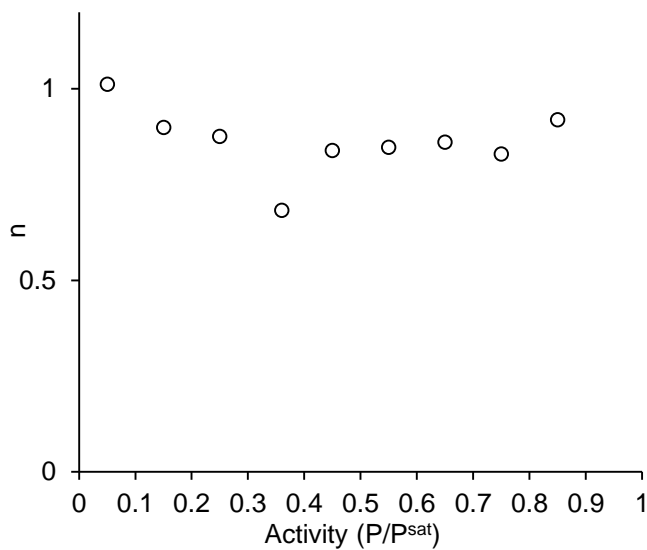
Butanol

0.1 activity 12 h step intervals up to activity = 0.9, Film thickness = 0.255 μm



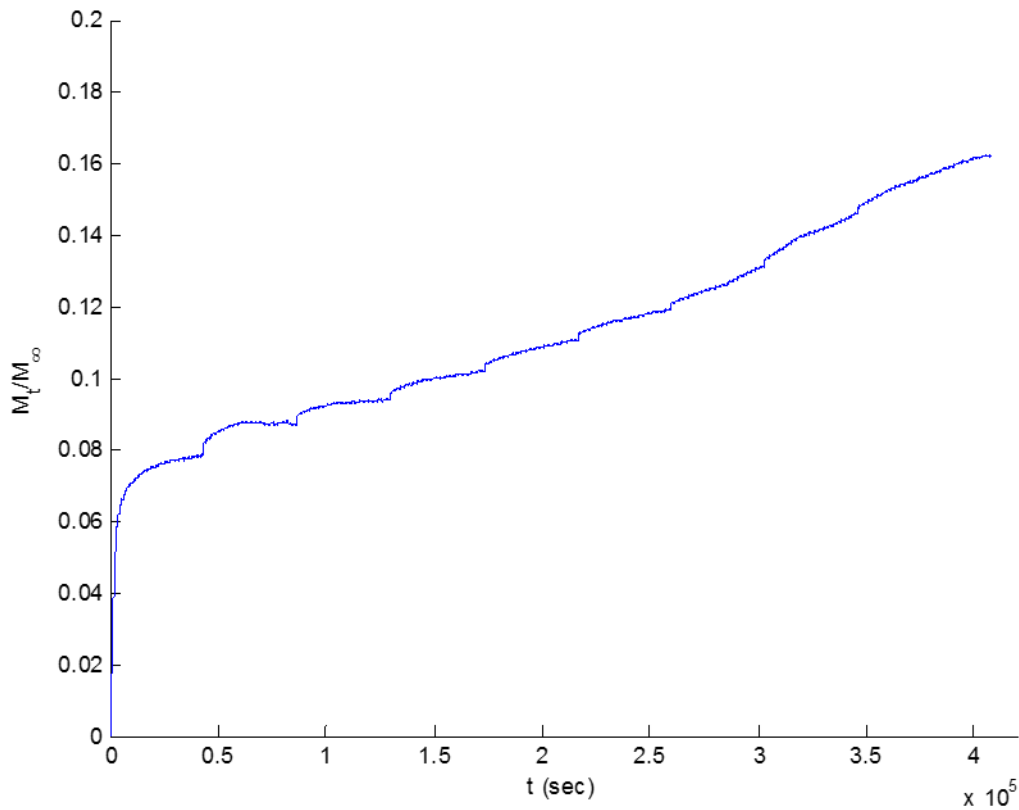
Short time intervals were used for determination of the type of diffusion classification for each sorption step, *i.e.* Case I (Fickian, $n = 0.50$), Anomalous ($0.5 < n < 1.0$), or Case II ($n = 1.0$).

The following is a summary of calculated n values for $M/M_\infty = k t^n$ for each 0.1 activity sorption interval.

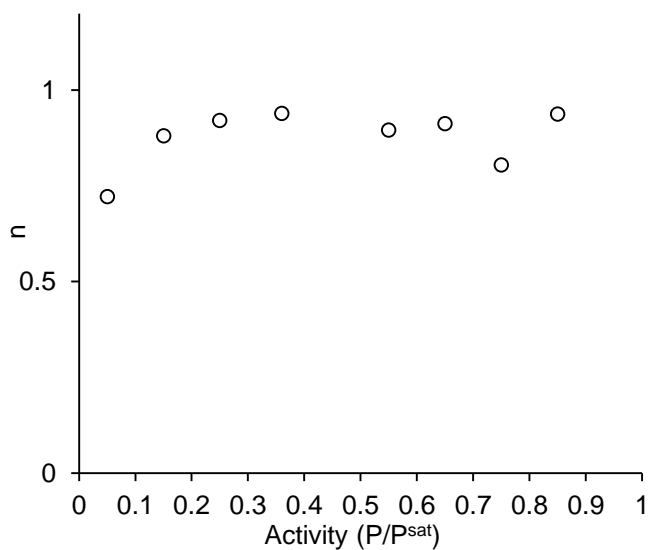


Hexanol

0.1 activity 12 h step intervals up to activity = 0.9, Film thickness = 0.252 μm



Short time intervals were used for determination of the type of diffusion classification for each sorption step, *i.e.* Case I (Fickian, $n = 0.50$), Anomalous ($0.5 < n < 1.0$), or Case II ($n = 1.0$). The following is a summary of calculated n values for $M/M_\infty = k t^n$ for each 0.1 activity sorption interval.



Appendix E - MATLAB Code used in Chapter 4 Data Analysis

The following MATLAB code is a sample from the code written and used to analyze the kinetic sorption data associated with Chapters 4 and 5. It is included primarily to serve as verification of the mathematical equations and MATLAB functions used to analyze the data using non-linear regression methods to extract relevant kinetic sorption parameters, namely diffusion coefficients and relaxation parameters.

```
solvent = 'Methanol';
temperature = '30\circC';
% Load Data
numbers1 = xlsread('Methanol 8-24-15','323');
numbers2 = xlsread('Methanol 8-24-15','324');

f01 = 4999808.5; % Hz, crystal #2, channel #2
f02 = 5000834.0; % Hz, crystal #3, channel #3
fc1 = 4997844.4; % Hz, coated crystal #2, channel #2
fc2 = 4999117.8; % Hz, coated crystal #3, channel #3

freq1 = [numbers1(1:end,2); numbers2(1:end,2)];% numbers3(1:end,2)];
freq2 = [numbers1(1:end,3); numbers2(1:end,3)];% numbers3(1:end,3)];
tmax1 = max(numbers1(1:end,1)); tmax2 = max(numbers2(1:end,1));% tmax3 =
max(numbers3(1:end,1));
time = [numbers1(1:end,1); (numbers2(1:end,1)+tmax1)];%
(numbers3(1:end,1)+tmax1+tmax2)];

for i = 1:length(freq1)-2
    if freq1(i+1) > freq1(i) + 10 || freq1(i+1) < freq1(i) - 10
        freq1(i+1) = NaN;
    end
    if freq1(i+2) > freq1(i) + 10 || freq1(i+2) < freq1(i) - 10
        freq1(i+2) = NaN;
    end
end
for i = 1:length(freq2)-2
    if freq2(i+1) > freq2(i) + 10 || freq2(i+1) < freq2(i) - 10
        freq2(i+1) = NaN;
    end
    if freq2(i+2) > freq2(i) + 10 || freq2(i+2) < freq2(i) - 10
        freq2(i+2) = NaN;
    end
end

rho = 2.648; % g/cm^3
mu = 2.947E11; % g/cm*sec^2
n = 1;
dm1 = ((f01-freq1)*sqrt(rho*mu)./(2*n*(f01^2)))*1E6; % ug/cm^2
dm2 = ((f02-freq2)*sqrt(rho*mu)./(2*n*(f02^2)))*1E6; % ug/cm^2
```

```

mp1 = ((f01-fc1)*sqrt(rho*mu)./(2*n*(f01^2)))*1E6; % ug/cm^2
mp2 = ((f02-fc2)*sqrt(rho*mu)./(2*n*(f02^2)))*1E6; % ug/cm^2
ms1 = ((fc1-freq1)*sqrt(rho*mu)./(2*n*(f01^2)))*1E6; % ug/cm^2
ms2 = ((fc2-freq2)*sqrt(rho*mu)./(2*n*(f02^2)))*1E6; % ug/cm^2
ms_mp1 = (dm1-mp1)/mp1;
ms_mp2 = (dm2-mp2)/mp2;

thickness1 = mp1/123; %um
thickness2 = mp2/123; %um
num2str(thickness1);

%% Diffusion
L = thickness1/10000; % cm
time = time*60; % convert time in minutes to seconds
DiffCoeff = zeros(9,1);
sorption_interval = 43000;
thickness_mod = linspace(1,1.05,10);
%*****
% L = thickness2/10000; % cm
% ms1 = ms2; % switch ms1 and ms2 for crystal #3 analysis
%*****
%% activity 0 - 0.1
index = 1;
beg = 799;
i = beg:(beg+100); h = beg:(beg+sorption_interval);
ms_temp_diffusive = ms1(i);
ms_temp_total_interval = ms1(h);
MFinf =
mean(ms_temp_total_interval((length(ms_temp_diffusive)+10):(length(ms_temp_diffusive)+12))); % Diffusive portion Minf
M_Minf = ms_temp_diffusive/MFinf;
tT = (time(i)-min(time(i))); % total interval time in sec repositioned to begin at t = 0
tT_total = (time(h)-min(time(h))); % total interval time in sec repositioned to begin at t = 0
D_guess = 1E-12; beta0 = [D_guess]; % initial guesses for nonlinear fit solver
modelfunction = @(b,t)((1-(8/(pi^2)))*...
((1./((2*0+1).^2)).*exp((-b(1).*((2*0+1).^2)).*((pi^2)*t/(4*L^2))))+...
((1./((2*1+1).^2)).*exp((-b(1).*((2*1+1).^2)).*((pi^2)*t/(4*L^2))))+...
((1./((2*2+1).^2)).*exp((-b(1).*((2*2+1).^2)).*((pi^2)*t/(4*L^2))))+...
((1./((2*3+1).^2)).*exp((-b(1).*((2*3+1).^2)).*((pi^2)*t/(4*L^2))))+...
((1./((2*4+1).^2)).*exp((-b(1).*((2*4+1).^2)).*((pi^2)*t/(4*L^2))))+...
((1./((2*5+1).^2)).*exp((-b(1).*((2*5+1).^2)).*((pi^2)*t/(4*L^2)))));
[beta, ~, ~, ~, ~] = nlinfit(tT,M_Minf,modelfunction,beta0);
D = beta(1); % fitted model parameters

ms = ms_temp_total_interval;
Minf_total = 1.0*mean(ms((length(ms)-5):(length(ms))));
M_Minf_diffusive = ms_temp_diffusive/Minf_total; % diffusive interval normalized to max of relaxational interval
M_Minf_total = ms/Minf_total;
mF = MFinf/Minf_total; % proportion mass sorbed for diffusive portion of interval
mR1 = 1-mF;
kR1_guess = 1E-6;

```

```

beta02 = [kR1_guess];
modelfunction2 = @(b,t) (mF*(1-(8/(pi^2))*...
    ((1./((2*0+1).^2)).*exp((-D.*((2*0+1).^2)).*(pi^2)*t/(4*L^2))))+...
    ((1./((2*1+1).^2)).*exp((-D.*((2*1+1).^2)).*(pi^2)*t/(4*L^2))))+...
    ((1./((2*2+1).^2)).*exp((-D.*((2*2+1).^2)).*(pi^2)*t/(4*L^2))))+...
    ((1./((2*3+1).^2)).*exp((-D.*((2*3+1).^2)).*(pi^2)*t/(4*L^2))))+...
    ((1./((2*4+1).^2)).*exp((-D.*((2*4+1).^2)).*(pi^2)*t/(4*L^2))))+...
    ((1./((2*5+1).^2)).*exp((-D.*((2*5+1).^2)).*(pi^2)*t/(4*L^2)))))) +
(mR1*(1-exp(-b(1)*t)));
[beta, ~, ~, ~, ~] = nlinfit(tT_total,M_Minf_total,modelfunction2,beta02);
kR1 = beta(1);
t_calc = linspace(0,(max(tT_total)),100001); % sec
ms_model = zeros(1,length(t_calc)); relaxation_contribution1 =
zeros(1,length(t_calc)); % memory preallocation
n = 0:15;
for k = 1:length(t_calc)
    ms_model(k) = (mF*(1-(8/(pi^2))*...
        ((1./((2*0+1).^2)).*exp((-
D*((2*0+1)^2)).*(pi^2)*t_calc(k)/(4*L^2))))+...
        ((1./((2*1+1).^2)).*exp((-
D*((2*1+1)^2)).*(pi^2)*t_calc(k)/(4*L^2))))+...
        ((1./((2*2+1).^2)).*exp((-
D*((2*2+1)^2)).*(pi^2)*t_calc(k)/(4*L^2))))+...
        ((1./((2*3+1).^2)).*exp((-
D*((2*3+1)^2)).*(pi^2)*t_calc(k)/(4*L^2))))+...
        ((1./((2*4+1).^2)).*exp((-
D*((2*4+1)^2)).*(pi^2)*t_calc(k)/(4*L^2))))+...
        ((1./((2*5+1).^2)).*exp((-
D*((2*5+1)^2)).*(pi^2)*t_calc(k)/(4*L^2)))))))+(mR1*(1-exp(-kR1*t_calc(k))));
    relaxation_contribution1(k) = (mR1*(1-exp(-kR1*t_calc(k))));
end
relaxation_parameter1(index) = kR1;
phi(index) = mF; phi2(index) = mR1; % proportion of total sorption process
extended to equilibrium that is diffusive

%% activity 0.1 - 0.2
index = 2;
beg = 43995;
i = beg:(beg+100); h = beg:(beg+sorption_interval);
equilibrium_extension = 1.1;
L = L*thickness_mod(index);
ms_temp_diffusive = ms1(i)-ms1(beg);
ms_temp_total_interval = ms1(h)-ms1(beg);
MFinf =
mean(ms_temp_total_interval((length(ms_temp_diffusive)+10):(length(ms_temp_diffusive)+12)))); % Diffusive portion Minf
M_Minf = ms_temp_diffusive/MFinf;
tT = (time(i)-min(time(i))); % total diffusive interval time in sec
repositioned to begin at t = 0
tT_total = (time(h)-min(time(h))); % total interval time in sec repositioned
to begin at t = 0
D_guess = 1E-12; beta0 = [D_guess]; % initial guesses for nonlinear fit
solver
modelfunction = @(b,t) ((1-(8/(pi^2))*...
    ((1./((2*0+1).^2)).*exp((-b(1).*((2*0+1).^2)).*(pi^2)*t/(4*L^2))))+...
    ((1./((2*1+1).^2)).*exp((-b(1).*((2*1+1).^2)).*(pi^2)*t/(4*L^2))))+...
    ((1./((2*2+1).^2)).*exp((-b(1).*((2*2+1).^2)).*(pi^2)*t/(4*L^2))))+...

```

```

    ((1./((2*3+1).^2)).*exp((-b(1).*((2*3+1).^2)).*(pi^2)*t/(4*L^2)))+...
    ((1./((2*4+1).^2)).*exp((-b(1).*((2*4+1).^2)).*(pi^2)*t/(4*L^2)))+...
    ((1./((2*5+1).^2)).*exp((-b(1).*((2*5+1).^2)).*(pi^2)*t/(4*L^2)))));
[beta, ~, ~, ~, ~] = nlinfit(tT,M_Minf,modelfunction,beta0);
D = beta(1); % fitted model parameters

ms = ms_temp_total_interval;
Minf_total = equilibrium_extension*mean(ms((length(ms)-5):(length(ms))));
M_Minf_diffusive = ms_temp_diffusive/Minf_total; % diffusive interval
normalized to max of relaxational interval
M_Minf_total = ms/Minf_total;
mF = MFinf/Minf_total; % proportion mass sorbed for diffusive portion of
interval
mR1 = 1-mF;
kR1_guess = 1E-6;
beta02 = [kR1_guess];
modelfunction2 = @(b,t) (mF*(1-(8/(pi^2))*...
    ((1./((2*0+1).^2)).*exp((-D.*((2*0+1).^2)).*(pi^2)*t/(4*L^2)))+...
    ((1./((2*1+1).^2)).*exp((-D.*((2*1+1).^2)).*(pi^2)*t/(4*L^2)))+...
    ((1./((2*2+1).^2)).*exp((-D.*((2*2+1).^2)).*(pi^2)*t/(4*L^2)))+...
    ((1./((2*3+1).^2)).*exp((-D.*((2*3+1).^2)).*(pi^2)*t/(4*L^2)))+...
    ((1./((2*4+1).^2)).*exp((-D.*((2*4+1).^2)).*(pi^2)*t/(4*L^2)))+...
    ((1./((2*5+1).^2)).*exp((-D.*((2*5+1).^2)).*(pi^2)*t/(4*L^2)))) +
    (mR1*(1-exp(-b(1)*t))));
[beta, ~, ~, ~, ~] = nlinfit(tT_total,M_Minf_total,modelfunction2,beta02);
kR1 = beta(1);
t_calc = linspace(0,(max(tT_total)),100001); % sec
ms_model = zeros(1,length(t_calc)); relaxation_contribution1 =
zeros(1,length(t_calc)); % memory preallocation
n = 0:15;
for k = 1:length(t_calc)
    ms_model(k) = (mF*(1-(8/(pi^2))*...
        (1/((2*0+1).^2))*exp((-
D*((2*0+1)^2))*((pi^2)*t_calc(k)/(4*L^2)))+...
        (1/((2*1+1).^2))*exp((-
D*((2*1+1)^2))*((pi^2)*t_calc(k)/(4*L^2)))+...
        (1/((2*2+1).^2))*exp((-
D*((2*2+1)^2))*((pi^2)*t_calc(k)/(4*L^2)))+...
        (1/((2*3+1).^2))*exp((-
D*((2*3+1)^2))*((pi^2)*t_calc(k)/(4*L^2)))+...
        (1/((2*4+1).^2))*exp((-
D*((2*4+1)^2))*((pi^2)*t_calc(k)/(4*L^2)))+...
        (1/((2*5+1).^2))*exp((-
D*((2*5+1)^2))*((pi^2)*t_calc(k)/(4*L^2)))))+(mR1*(1-exp(-kR1*t_calc(k))));
    relaxation_contribution1(k) = (mR1*(1-exp(-kR1*t_calc(k))));
end
relaxation_parameter1(index) = kR1;
phi(index) = mF; phi2(index) = mR1; % proportion of total sorption process
extended to equilibrium that is diffusive

```

Appendix F - Membrane reactor and QCM sorption system images

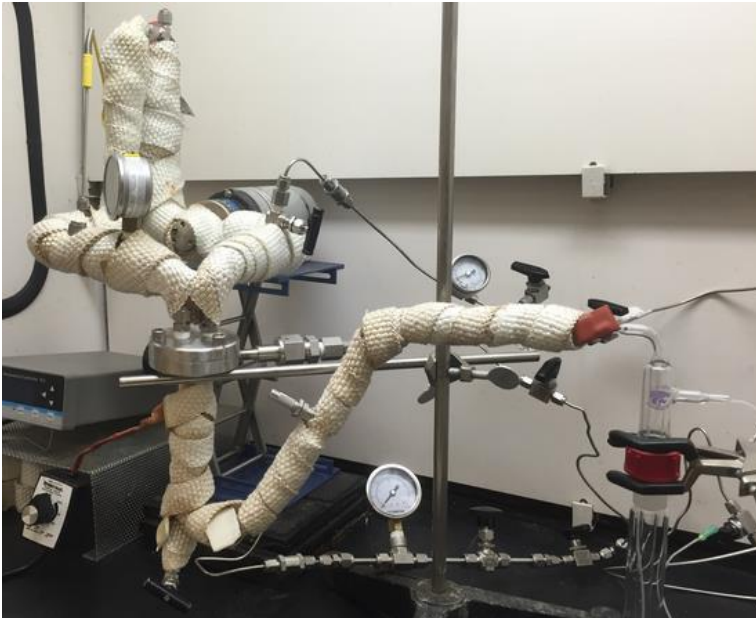


Figure F-1 – Membrane reactor experimental set-up.

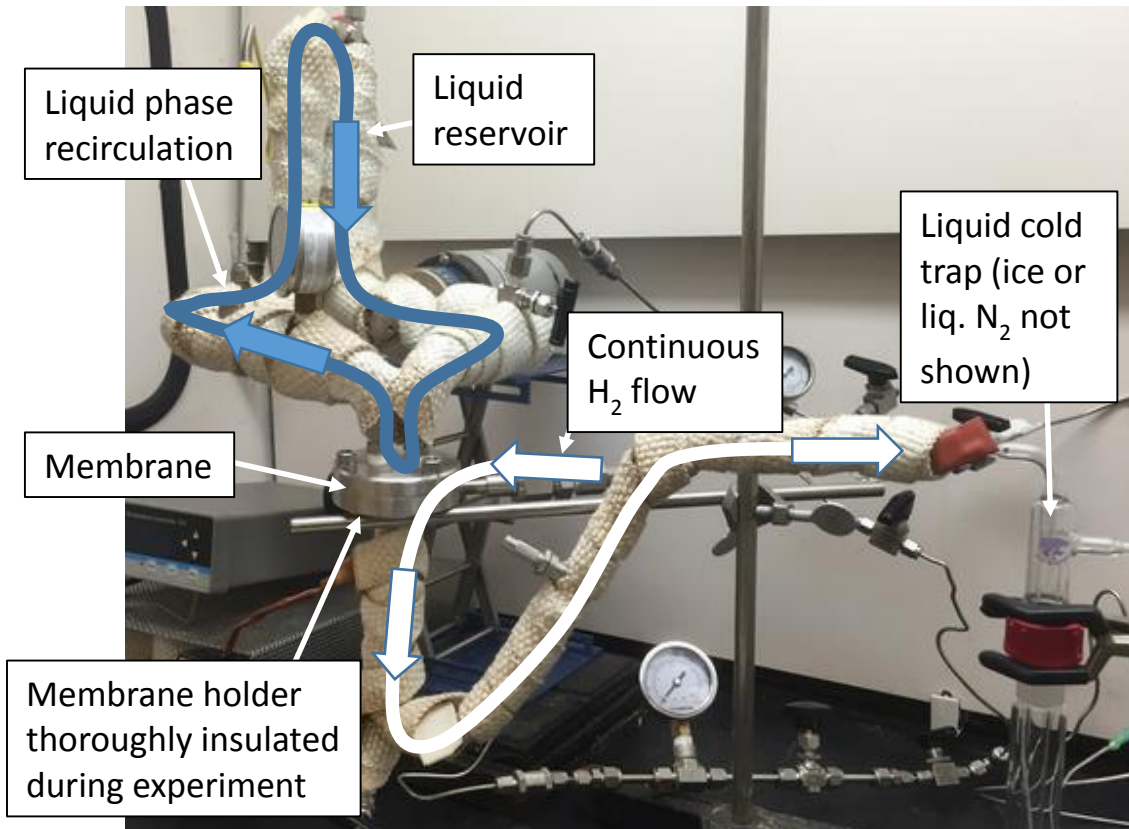


Figure F-2 – Membrane reactor experimental set-up, annotated.

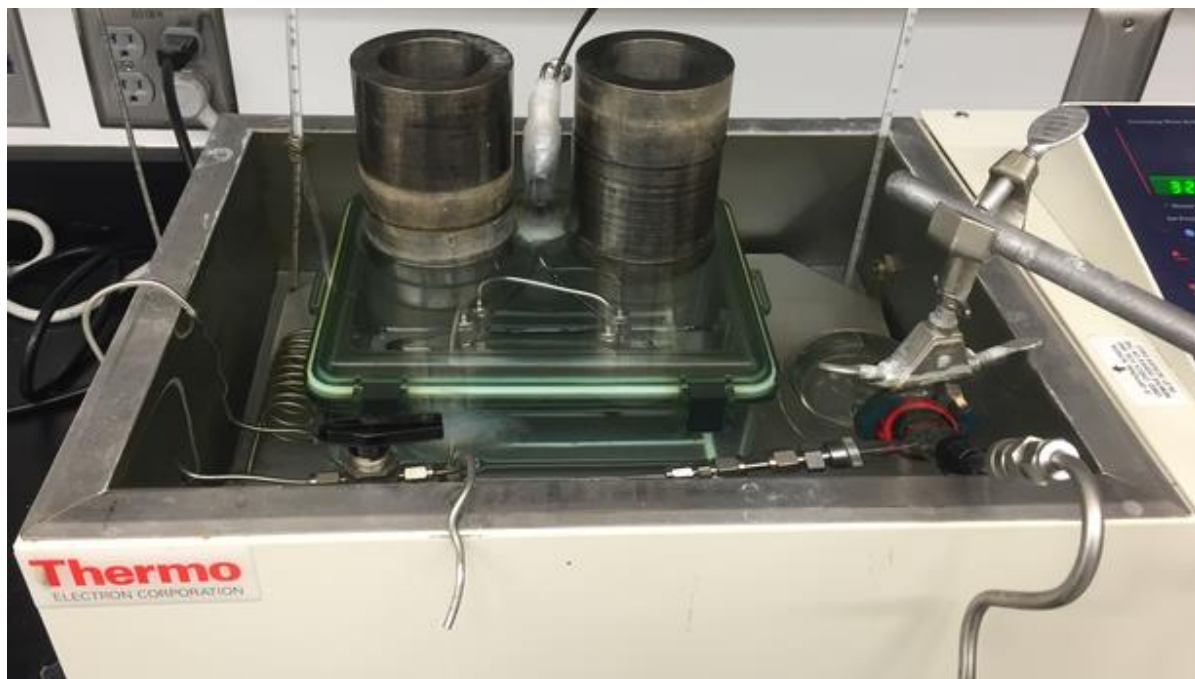


Figure F-3 - Sorption experimental set-up used in Chapters 4 and 5.

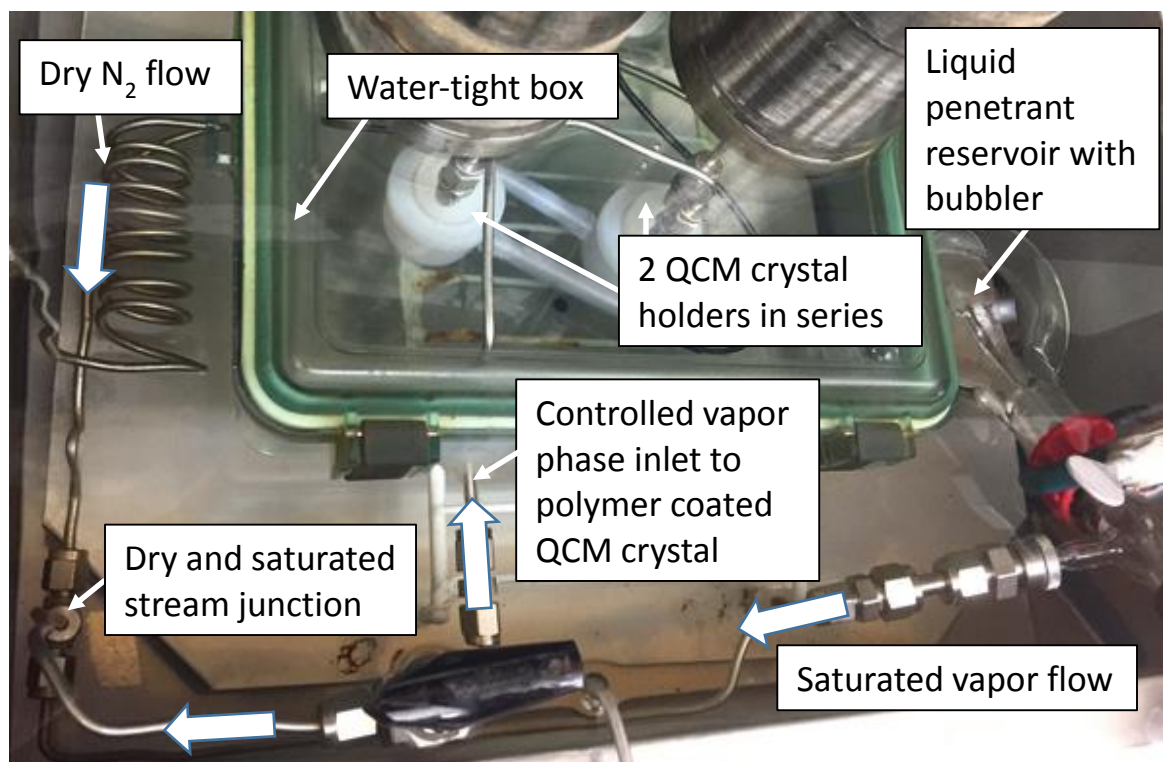


Figure F-4 - Sorption experimental set-up, annotated.